ULTRAFAST TERAHERTZ MICROSCOPY OF ATOMICALLY PRECISE GRAPHENE NANORIBBONS

By

Spencer E. Ammerman

A DISSERTATION

Submitted to
Michigan State University
in partial fulfillment of the requirements
for the degree of

Physics — Doctor of Philosophy

2023

ABSTRACT

Recent developments in bottom-up synthesis of atomically precise graphene nanoribbons (GNRs) [1] are paving the way for new technologies with ångström-scale features that host a myriad of electronic, spin, and topological properties [2]. Studying the ultrafast phenomena relevant to the optoelectronic potential of these GNRs requires extreme spatio-temporal resolution. Conventional techniques for atomic-scale investigation of materials, such as scanning tunneling microscopy (STM) and scanning tunneling spectroscopy (STS), lack the necessary time resolution to investigate ultrafast dynamics. Meanwhile, conventional ultrafast measurements are able to time-resolve the optical excitations of these GNRs, but, they lack the requisite spatial resolution to perform more precise experiments on isolated individual structures. Instead, they act on ensembles and average over many GNR lengths, orientations, and sample qualities [3, 4].

With the development of terahertz scanning tunneling microscopy (THz-STM), coherent control of tunneling electrons on sub-picosecond timescales is now possible in an STM tunnel junction [5–18]. However, to fully empower THz-STM as a scientific tool for materials science, an approach to characterize the electronic properties of new materials and nanostructures without prior knowledge of the sample response is needed. This demands the establishment of terahertz scanning tunneling spectroscopy (THz-STS) with atomic spatial resolution and an approach to analyzing such measurements.

In this thesis, we demonstrate atomic-scale THz-STS for the first time by extracting the differential conductance ($\mathrm{d}I/\mathrm{d}V$) from a model GNR system with ångström-scale resolution in all three spatial dimensions [18]. We utilize bottom-up synthesis to construct atomically precise 7-atom-wide armchair graphene nanoribbons (7-AGNR) on an Au(111) substrate. THz-STM is applied to probe the electronic structure of a 7-AGNR while operating at ultralow tip heights, where the distance between STM tip and GNR is reduced by $\sim 3.0 - 4.0\,\text{Å}$ compared to conventional STM tip heights. We construct a model of the GNR electronic density of states and apply THz-STS to a collection of THz-STM images taken at

different incident THz field strengths to construct $\mathrm{d}I/\mathrm{d}V$ maps of the frontier orbitals on a 7-AGNR segment. Lastly, a set of time-domain measurements are performed in the hopes of observing dynamical effects associated with charging of the GNR during charge injection by the THz-STM. The aforementioned steady-state THz-STS results are sufficient to describe the time-domain measurements without charging, suggesting further sample preparation is needed to decouple the GNR from the Au(111) surface and reveal transient effects.

We further develop and test an algorithm, based on a polynomial representation of the junction I-V curve, for extracting the tunnel junction $\mathrm{d}I/\mathrm{d}V$ accessed by an ultrafast THz-STM probe in both steady-state and optical-pump/THz-STS-probe experiments [19]. We test our algorithm against a set of model systems constructed to represent typical STM samples, e.g., metals, semiconductors, and molecules. Then, we simulate a THz-STS experiment wherein we address systematic error by defining a procedure to determine the algorithm parameters. After setting the stage with steady-state THz-STS, our algorithm is expanded upon, and we show how a dynamic junction $I(V)$ predicted for an optical-pump/THz-STM-probe experiment can be extracted from THz-STS measurements. By applying the cross-correlation theorem in the frequency domain we find that the time-resolution of THz-STS is not limited to the input bandwidth of the ultrafast THz voltage pulse. As a result, our pump-probe THz-STS algorithm reveals dynamics faster than a single oscillation cycle of the THz transient, and in the future may be combined with atomically resolved THz-STS experiments to bridge a new frontier of ultrafast materials science.

ACKNOWLEDGEMENTS

First and foremost, I would like to recognize the amazing opportunity provided by my advisor, **Dr. Tyler L. Cocker**. Being the first to join his research team has been an incredible experience. My time in his group has turned into a life-changing experience. Tyler's passion for research and enthusiasm for teaching and collaboration has been very inspirational. With his guidance, I have accomplished more than I had ever imagined possible. I am grateful for his patience and support while I developed as a scientist and individual.

I owe nearly as much to **Dr. Vedran Jelic**. Our time together building up the THz-STM system was an incredible experience. He is the co-first author of our group's first publication, which came from our work performing THz-STM of 7-AGNRs. His dedication to our research was very motivational and I believe lead to our lab developing as rapidly as it did. I owe much of my technical knowledge to the time working alongside him.

We received gracious support for our STM experiments from **Dr. Reza Loloee**. Our experiments required that our system stays at cryogenic temperatures for extended periods. Reza made sure we had the liquid nitrogen and liquid helium to keep our experiments running.

The department machine shop produced several critical components for our optical setup. I had the fortunate opportunity to learn mechanical skills from **Robert Bennett**. Working closely with Rob and using insight gained from my time in his machine shop course we constructed the dry-air purge box that enables the maximum performance of our THz setup.

Lastly, I want to thank **my friends and family** for their love and support over the years. The road to where I am today started a long time ago. All the lessons I've learned and the experiences I've shared with each of you has shaped me into the person I am today.

PREFACE

The research conducted for this thesis was performed from August 2017 to October 2022 at Michigan State University under the guidance and supervision of Professor Tyler L. Cocker. The work has led to two collaborative refereed publications, of which I am co-first and first author. I have further delivered one invited talk and three contributed talks on these results. For the presentation of my work, I have been awarded first place and runner-up in the student presentation competition at the *45th and 47th (respectively) International Conference on Infrared, Millimeter, and Terahertz Waves: IRMMW-THz*. The publications, along with their corresponding author contributions, are listed below.

S. E. Ammerman, V. Jelic, Y. Wei, V. N. Breslin, M. Hassan, N. Everett, S. Lee, Q. Sun, C. A. Pignedoli, P. Ruffieux, R. Fasel & T. L. Cocker. "Lightwave-driven scanning tunnelling spectroscopy of atomically precise graphene nanoribbons," *Nat Commun* **12**, 6794 (2021).

I constructed the experimental setup with help from V. Jelic, V. N. Breslin, and T. L. Cocker. I conducted the experiments with V. Jelic and T. L. Cocker, with assistance from M. Hassan and S. Lee. I grew the graphene nanoribbon samples with V. Jelic. Precursor molecules were supplied by R. Fasel and P. Ruffieux, who also consulted on nanoribbon preparation and STM characterization of samples. Y. Wei, N. Everett, V. Jelic, T. L. Cocker, and I constructed the model used during data analysis. I performed the data analysis with V. Jelic and T.L. Cocker. Density functional theory calculations were carried out by Q. Sun and C. A. Pignedoli. V. Jelic, T. L. Cocker, and I worked together, with input from the rest of the authorship, to write the manuscript. T. L. Cocker supervised the project. A majority of the experiments were performed in the weeks leading up to the COVID related laboratory shutdowns. Follow-up measurements were unable to be completed until we could safely return to campus. These results are described in chapter 6.

S. E. Ammerman, Y. Wei, N. Everett, V. Jelic, & T. L. Cocker. "An Algorithm for Terahertz Scanning Tunneling Spectroscopy," *Phys. Rev. B* **105**, 115427 (2022).

The project was initiated by T. L. Cocker with first simulations performed by N. Everett. I developed the simulation models with Y. Wei, N. Everett, and T. L. Cocker. I programmed the steady-state algorithm with N. Everett and I programmed the time-dependent algorithm with Y. Wei. I analyzed and interpreted the simulation results with input from V. Jelic and T. L. Cocker. I worked together with V. Jelic and T. L. Cocker to prepare the manuscript. T. L. Cocker supervised the project. The algorithm developed in this work is discussed in chapter 7.

TABLE OF CONTENTS

LIST OF ABBREVIATIONS

GNRs	graphene nanoribbons
STM	scanning tunneling microscopy
STS	scanning tunneling spectroscopy
THz-STM	terahertz scanning tunneling microscopy
THz-STS	terahertz scanning tunneling spectroscopy
7-AGNR	7-atom-wide armchair graphene nanoribbons
AFM	atomic force microscopy
MIR	mid-infrared
EOS	electro-optic sampling
UHV	ultrahigh vacuum
NIR	near-infrared
DFT	density functional theory
DBBA	10,10'-dibromo-9,9'-bianthracene
VB	valence band
CB	conduction band
DSP	digital signal processor
LDOS	local density of states
FFT	fast-Fourier transform
PC	photoconductive switch
OR	optical rectification
SHG	second harmonic generation
DFG	difference frequency generation

SFG	sum frequency generation
TO	transverse optical
WGP	wire-grid polarizer
FWHM	full width at half maximum
CEP	carrier envelope phase
ITO	indium-tin-oxide
YAG	ytterbium aluminum garnet
GDD	group delay dispersion
TOD	third order dispersion
FROG	frequency-resolved-optical-gating
JM-STM	junction-mixing STM
PG-STM	photoconductively gated STM
LA-STM	laser-assisted STM
QPI	quasi-particle interference
ARPES	angle-resolved-photoemission-sampling
PES	ultrafast photoemission sampling
STL	scanning tunneling luminescence
ESR-STM	electron spin resonance STM

Chapter 1
Introduction

Gaining greater insight into the character of nanoscale electronic systems is a cornerstone of materials science and condensed matter physics. For many years, such a pursuit has been held to a convention that one must choose between observations on the systems' natural length scale or their intrinsic timescale. The insight to be gained by investigating new materials has quickly reached a point where behavior at the atomic scale is crucial to device function. Strong confinement of excited electrons on nanometer length scales, well below what they would experience in bulk counterparts (100's of nm), leads to new non-classical phenomena [20]. Measurements on their natural length scale allows them to be integrated into existing or advanced architectures, e.g., field-effect transistors with atomically precise GNRs [21]. Electronic scanning probe techniques such as STM and atomic force microscopy (AFM) allow for robust construction and characterization of nanostructures [22], vibrational spectroscopy of single molecules [23], as well as spatial mapping of intramolecular forces [24]. The extreme spatial resolution of STM is due to the quantum tunneling effect that results in a current developing when an STM tip is brought within approximately one nanometer of a conducting sample surface [25]. Applying a voltage bias between the tip and sample changes the energy level alignment between the two systems and alters the tunneling current between them. Study of the junction's current-voltage characteristic ($I(V)$) as a function of applied bias and extracting a $\mathrm{d}I/\mathrm{d}V$ spectrum is known as STS and is the foundation of materials characterization using STM [26–28]. The energy selectivity of STS allows one to image the real-space distribution of the electronic density of states and has lead to the detection of quasi-particle interference of electrons on surfaces [29–31] and within confined structures [22, 32].

While scanning probe techniques offer the requisite spatial resolution to explore modern materials, they lack access to important dynamical behavior probed by far-field optical

measurements utilizing ultafast light pulses. Far-field techniques such as optical and THz spectroscopies have been indispensable tools for determining conductivity [33–35] and energetic transitions [4], as well as coherent control of molecular rotations [36, 37]. The THz frequency range spans the gap between mid-infrared (MIR) and microwave frequencies. For 1 THz, the wavelength is $\lambda = 300$ μm, which corresponds to a photon energy of just 4 meV (for comparison, $k_B T = 26$ meV at room temperature). Hence, THz light is considered non-ionizing radiation. The THz frequency range is well suited for investigation of low-energy collective excitations in condensed matter systems, e.g., plasmonic modes and phonons [38]. Through the technique of free-space electro-optic sampling (EOS) [39, 40], time-domain measurements of the THz electric field have become standard in materials characterization [38, 41]. It has been shown that THz frequencies have access to the evolution of collective excitations directly on their natural timescales. Integrating a femtosecond (fs, 10^{-15} s) optical pump pulse into a THz spectroscopy setup, time-resolved THz spectroscopy can be performed by recording the time-domain electric field of a free-space propagating THz pulse at a series of time delays relative to sample photoexcitation. For example, the build-up of screening of photoexcitated free-carriers has been observed [42]. Ultrafast optical techniques are also capable of following the evolution of molecular systems, e.g., chemical reactions [43, 44] and molecular reaction dynamics [45]. Access to the natural length and timescale of these processes simultaneously would be groundbreaking in the areas of surface-assisted chemistry [46] and tip-induced chemical reactions [47]. Combining a range of technical concepts from ultrafast THz and optical spectroscopy measurements with the ultimate spatial resolution of STM will allow us to fully characterize a vast array of structure and function on length scales many orders of magnitude smaller than the diffraction limited spot size of a focused ultrafast light pulse, as illustrated in Figure 1.1.

THz-STM builds on the lessons learned in junction mixing STM [48], where light pulses generate fast voltage pulses that couple to the junction via a transmission line. Coupling light pulses directly to the tip apex of an STM from the far-field allows us to generate *ultrafast* voltage pulses across the STM junction. THz-STM utilizes a phase-stable single-cycle THz-frequency light pulse ($\mathbf{E}_{\mathrm{THz}}(t)$) to apply an ultrafast transient bias voltage ($V_{\mathrm{THz}}(t)$) to the tunnel junction of an STM system. Benefiting from an enormous field enhancement ($10^5 - 10^6$) at the scanning probe apex [5, 7, 8, 13], the THz electric-field transient operates in the strong-field regime [17]. The Keldysh parameter (γ) distinguishes between the strong-

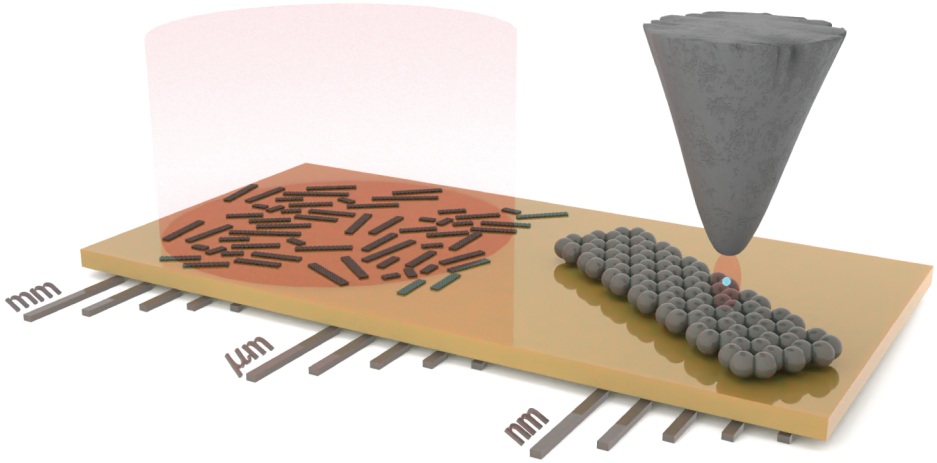

Figure 1.1: Far-field (left) and atomically resolved (right) measurements of GNRs. In the far-field, on the length scale of millimeters to micrometers, light is focused onto sample surfaces containing many different GNRs of various lengths and orientations. At the sub-nanometer scale, scanning probe techniques such as STM investigate individual species with well characterized lengths and structure.

field ($\gamma < 1$) and multi-photon ($\gamma > 1$) regimes by relating the tunnel junction's ionization energy to the pondermotive energy of the driving field. It is on the order of 10^{-3} for THz-STM [49], whereas for optical pulses of the same field strength it is >1. In the strong-field regime, the THz field can be considered a quasi-static voltage transient that changes the energy landscape of the tunnel junction, temporarily opening tunneling pathways on sub-picosecond timescales. This voltage pulse is then rectified by non-linearities of the junction's $I(V)$ to produce a non-zero flow of current between the tip and sample. The resulting THz-induced current pulse far exceeds the bandwidth of traditional STM electronics, with pulse durations of <500 fs. THz-STM measurements often use lock-in detection to measure the average THz-induced current, which is proportional to the charge rectified by each THz pulse at the repetition rate of the laser system. A typical lock-in detection scheme allows high-repetition-rate systems to detect THz driven current on the order of 1 electron per pulse.

The field of THz-STM was first established in 2013, when a THz-driven STM system demonstrated nanometer spatial resolution and sub-picosecond (∼500 fs) temporal resolution [5]. Operating in ambient conditions reduced the stability of the junction, limiting the spatial resolution. Now, THz-STM systems operate in ultrahigh vacuum (UHV) environments and at cryogenic temperatures, which provides the stability required for precision

measurements on the smallest scales. Near liquid helium temperature (<10 K), molecules can be adsorbed onto mono- to few-layer sodium chloride (NaCl) islands and imaged with STM and AFM [24, 50]. Utilizing THz-STM, orbitally selective tunneling out of the highest occupied molecular orbital or into the lowest unoccupied molecular orbital was shown to induce an oscillation of the temporarily charged molecule within the junction, over an insulating NaCl island, in a THz-STM-pump/THz-STM-probe experiment [7].

In addition to resonant tunneling through molecular orbitals, THz-STM can investigate the junction $I(V)$ much like conventional STS. The polarity of $V_{\mathrm{THz}}(t)$ determines the net flow of THz-induced current. Phase and amplitude control of $\mathbf{E}_{\mathrm{THz}}(t)$ allows for the investigation of the $I(V)$ that rectifies the THz voltage [6, 9]. While steady-state experiments may, at times, be approximated by rectification on the $I(V)$ measured in DC-STM, unique circumstances, such as extreme tunnel currents recorded during THz-driven imaging of the metallic-like Si(111)-(7x7) surface [8], will lead to a deviation from DC measurements. Ultimately, for atomic-scale non-equilibrium states induced by photoexcitation, the $I(V)$ of the junction will be unknowable by means other than ultrafast THz-STM. The field is now at a point where the development of a THz-STM analogue to STS is needed. A form of THz-STS capable of extracting both steady-state and time-dependent information will bring THz-STM to the forefront of materials science research. However, with two vital unknowns contributing to the measured signal, i.e., an unknown $I(V)$ and $V_{\mathrm{THz}}(t)$, the problem was nearly intractable. Yet, recent advances in the detection of THz near fields at the apex of an STM tip [10, 11, 15] have allowed us, in this thesis, to develop an approach to extracting the junction's $I(V)$ when the only *a priori* knowledge is $V_{\mathrm{THz}}(t)$.

In this thesis, we pair a custom, commercial STM system operating in UHV and at cryogenic temperatures with a MHz-repetition-rate near-infrared (NIR) laser system and a state-of-the-art, home-built THz generation setup to drive and detect single-electron charge rectification on the scale of 160 fA per pulse with a high-gain (10^9 V/A) current preamplifier and lock-in detection. By operating at cryogenic temperatures, stray signals are reduced and numerous simplifications in STM formalism can be applied [51]. The details of our STM system and the modes of operation used to characterize samples at low temperature under UHV conditions are described in Chapter 2.

The generation of single-cycle, phase stable, free-space THz light pulses was first demonstrated via generation by fast currents in optically-pumped semiconductor photoswitches [52].

New light sources based on efficient nonlinear frequency down conversion in crystals such as lithium niobate ($LiNbO_3$) [53] have lead to higher peak fields [54] suitable for THz-STM. Chapter 3 details (i) our THz generation scheme using the optimized tilted pulse-front geometry established in reference [55], (ii) our setup for performing the aforementioned EOS measurements, and (iii) characterization of the THz pulses produced in our setup.

Though THz-STM is analogous to DC-STM in many ways, understanding subtleties between the techniques is required before meaningful measurements can be performed. Additionally, characterization of $V_{\mathrm{THz}}(t)$ is necessary for the analysis of THz-STM data and, therefore, an implementation of photoemission sampling is needed. In Chapter 4, I discuss how we manipulate $\mathbf{E}_{\mathrm{THz}}(t)$ and sample $V_{\mathrm{THz}}(t)$ in the tip's near field. The principles of THz-STM are described, along with a walkthrough of THz-STM operation for materials characterization. Our new methodology for THz-STS measurement modes are also presented in Chapter 4.

Graphene nanoribbons are an exciting platform for atomic-scale optoelectronic devices, as light is expected to interact strongly with the system's electrons to drive them out of equilibrium [56, 57]. With methods developed for surface-assisted bottom-up synthesis using molecular precursor molecules [1], atomically precise GNRs offer a tunable system compatible with density functional theory (DFT) for first principles calculations of system properties [58–60]. Properties such as magnetism [61], band-gap [62], and topological states [63, 64] are customizable, while heterojunction devices can be directly grown [65, 66]. DFT calculations predict excitonic properties for armchair- [67, 68] and chevron-type [69] GNRs as well as topological phases in cove-edged and chevron GNRs [70]. Far-field THz spectroscopy experiments have reported ultrafast dynamics in GNRs [3, 4, 71, 72], making them an excellent candidate for first atomic-scale THz-STS studies in both steady-state and pump-probe configurations. Chapter 5 describes our growth in UHV conditions and STM characterization of atomically precise 7-AGNRs via bottom-up synthesis using 10,10'-dibromo-9,9'-bianthracene (DBBA) precursor molecules deposited onto an Au(111) surface.

As stated previously, an analogous form of STS is needed for THz-STM to move forward as a tool for materials science. Measurements of the DC $I(V)$ curve, and the corresponding $\mathrm{d}I/\mathrm{d}V$ spectra, for 7-AGNRs exhibit wide band gaps of $\sim 2{-}2.5\,\mathrm{eV}$ [73], which are suitable for optical excitation with visible light pules. The valence band (VB) and conduction band (CB) onsets are located at approximately -0.8 eV below the Fermi level and $+1.5{-}2.0\,\mathrm{eV}$

above the Fermi level, respectively [74–76]. The VB and CB onsets provide nonlinearities in the GNR $I(V)$ curve that will rectify $V_{\mathrm{THz}}(t)$. Due to the bipolar nature of $V_{\mathrm{THz}}(t)$, both positive and negative voltages are sampled during THz-STM. The convolution over $I(V)$ features in the rectified charge poses a significant challenge when interpreting THz-STM data. Chapter 6 describes our THz-STM measurements of single 7-AGNRs and subsequent extraction of the spatially dependent $\mathrm{d}I/\mathrm{d}V$ spectrum probed during THz-STM operation, which establishes atomic-scale THz-STS for the first time.

A significant challenge in performing ultrafast pump-probe THz-STS is the lack of *a priori* knowledge of the junction's non-equilibrium $I(V)$, e.g., following photoexcitation. In order to bring THz-STS forward into a prominent role as a tool for atomic scale surface science, we develop a theoretical framework to analyze THz-STS measurements. Previously, data analysis for THz-STM experiments has largely relied on guess-and-check methods that simulate rectification based on a model system [5, 7, 8]. In Chapter 7, we use measurements of the rectified charge as a function of peak incident electric field strength ($Q_{\mathrm{THz}} - E_{\mathrm{THz,pk}}$) to perform THz-STS. I introduce our inversion algorithm, which combines measurements of the near-field voltage transient [10, 11, 15] with $Q_{\mathrm{THz}} - E_{\mathrm{THz,pk}}$ data to extract the $\mathrm{d}I/\mathrm{d}V$ spectra of model and simulated systems. In a pump-probe experiment, the junction evolves on a femtosecond to picosecond timescale following optical excitation. Nevertheless, our algorithm allows us to extract the transient $\mathrm{d}I/\mathrm{d}V$ with time resolution faster than a single oscillation cycle of the THz probe, thereby accessing an elusive regime of spatio-temporal resolution for materials science. With the advancements in analysis and developments in experimental protocol established in this thesis, we demonstrate a new capacity for THz-STM characterization of nanomaterials with simultaneous ultrafast time resolution and atomic spatial resolution.

Chapter 2
Scanning Tunneling Microscopy

2.1 Tunneling in One Dimension

Theoretical and experimental consideration of the classically forbidden phenomenon of quantum mechanical tunneling dates back to the start of the 20$^{\text{th}}$ century, with work focusing on the emission of electrons from solids [77] and metals subject to intense electric fields [78]. Quantum tunneling arises when an electron is near a material surface, represented in one-dimension by a potential energy, $V(z)$, with a barrier located at $z = 0$ of height $V(0) = V_0$. Figure 2.1 illustrates a free electron, with energy E, bound within a material as a plane wave described by the function,

$$\begin{aligned} \Psi_{\text{e}}(z,t) =& \exp(ikz - \frac{i}{\hbar}Et) \\ =& \psi_{\text{e}}(z)\psi_{\text{e}}(t)\,, \end{aligned} \tag{2.1}$$

where k is the wavevector amplitude, z is distance along the normal of the material, and $\hbar$ is Planck's constant. Application of the time-dependent Schrödinger equation will occur later, in Section 2.3.1. For now, the spatial electron wavefunction comes as a solution to the time-independent Schrödinger equation,

$$\frac{\hbar^2}{2m}\frac{\partial^2}{\partial z^2}\psi(z) = [V(z) - E]\psi(z)\,, \tag{2.2}$$

where m is the electron mass, resulting in a wavevector amplitude,

$$\begin{aligned} k &= \sqrt{\frac{2m}{\hbar^2}[E - V(z)]} && \text{if } E > V(z) \\ k &= \sqrt{\frac{2m}{\hbar^2}E} && \text{if } V(z) = 0 \quad \text{(region I)} \\ k &= \sqrt{\frac{2m}{\hbar^2}[V(z) - E]} = i\kappa && \text{if } V(z) > E \ \text{ (region II)} \end{aligned} \tag{2.3}$$

with different forms depending on the potential and energy. With $V(z) = 0$, the wavefunction forms a standing wave with a complex exponent, characteristic of the energy eigenstates of

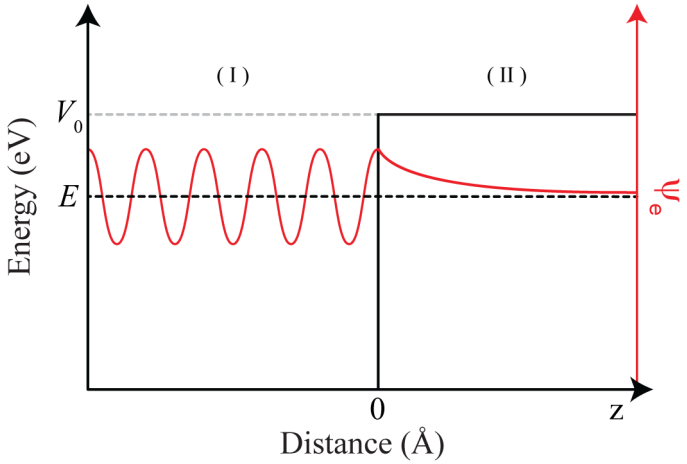

Figure 2.1: Quantum tunneling into a one-dimensional potential $V(z)$. An electron wavefunction, ψ_e, is represented by a complex plane wave in region (I), where $V(z) = 0$, and experiences a real-valued decay within region (II) where $V(0) = V_0$.

the material system. However, when the electron wavefunction encounters the barrier with $E < V_0$ (i.e., bound in the material), k becomes imaginary and the exponent of Equation 2.1 becomes real. The result is an exponential decay of the wavefunction amplitude outside the surface of the material. If another material is introduced within close proximity to the first, such that the potential barrier is narrow, with width $d \sim 1 - 100$nm, we can examine the probability that an electron may tunnel through the barrier by applying Equation 2.2 and Equation 2.1 again. However, to determine the probability amplitude, $|\psi|^2$, of finding an electron in each of the regions in Figure 2.2 we must consider multiple solutions to Equation 2.2. Notably, Equation 2.1 is valid for both $-k$ and $+k$. We define a rightward propagating wave with $k > 0$ and a leftward one with $k < 0$. The electron wavefunction is then described as a superposition of rightward and leftward propagating waves,

$$\psi(z) = \begin{cases} Ae^{ikz} + Be^{-ikz} & z < 0 \quad \text{(region I)} \\ Ce^{-\kappa z} + De^{\kappa z} & 0 < z < d \quad \text{(region II)} \\ Fe^{ikz} & z > d \quad \text{(region III)} \end{cases} \tag{2.4}$$

where A, B, C, D, F are complex amplitudes of the traveling wave components. The probability of the electron tunneling through the barrier and being found in region III is calculated by enforcing continuity of the wavefunction across the potential barrier edges at $z = 0$ and $z = d$. Both ψ and its derivative must match at the boundary, leading to a set of

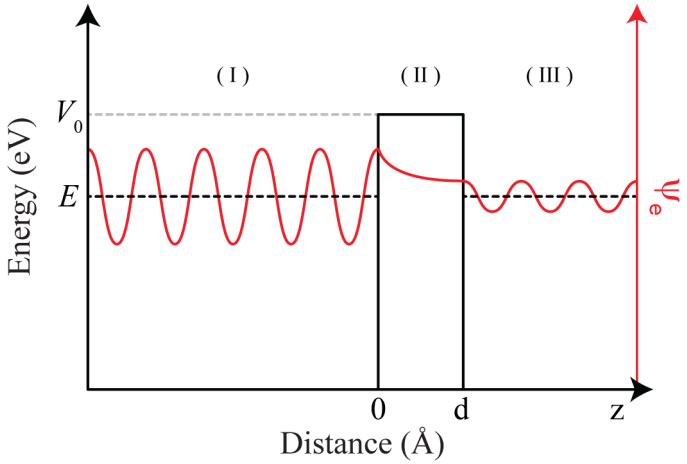

Figure 2.2: Quantum tunneling through a one-dimensional potential barrier with height V_0 and width d. An electron wavefunction, ψ_e, is represented by a complex plane wave in region (I), where $V(z) = 0$, and experiences a real-valued decay within region (II), where $V(z) > E$. The electron is shown to have tunneling through the barrier into region (III), where it forms another complex plane wave with smaller amplitude.

coupled equations that defines the transmission through the barrier as,

$$T = |F|^2 = \frac{16E(V_0 - E)}{V_0^2} \exp\left(-2d\sqrt{\frac{2m}{\hbar^2}(V_0 - E)}\right), \tag{2.5}$$

i.e., the square amplitude of the wavefunction for $z > d$. Despite encountering a potential barrier higher than the energy of the incident particle, the electron wavefunction spreads out through space and leaks into the space past the barrier. The exponential decay of the transmission factor is a hallmark of quantum tunneling and is expanded upon in Section 2.3.1.

The result in Equation 2.5 can be further generalized by allowing the height of the barrier to vary at each boundary. Introducing the Fermi energy, E_F, defines the highest energy fully occupied by electrons on both sides of the barrier and allows us label a material's work function, Φ, as the distance from E_F to the top of the barrier, as shown in Figure 2.3. In Section 2.3.1, I will show how a tunneling picture that involves transmission between two weakly interacting electronic reservoirs, known as the Bardeen model, replaces the transmission amplitude in Equation 2.5 with the square of an energy dependent matrix element,

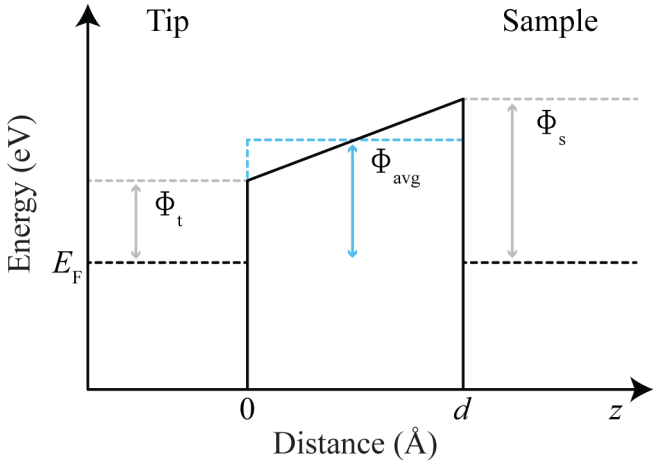

Figure 2.3: Trapezoidal potential barrier diagram. The tip material (left) is characterized by a work function, Φ_t, which is the difference between the Fermi energy, E_F, and the top of the potential barrier at $z = 0$. The sample material (right) is characterized by a work function, Φ_s. Notably, the difference between Φ_t and Φ_s produces a trapezoidal barrier that can be approximated by a rectangular barrier of height $\Phi_{avg} = (\Phi_t + \Phi_s)/2$. The differences in height can arise from a combination of material and geometrical differences.

$|M(E)|^2$. The transmission factor,

$$\begin{aligned} T(E,V,d) \propto \exp(-2\kappa d) &= \exp\left(-2d\sqrt{\frac{2m}{\hbar^2}(V-E)}\right) \\ &= \exp\left(-2d\sqrt{\frac{2m}{\hbar^2}(\Phi_t+\Phi_s)/2}\right) \\ &= \exp\left(-2d\sqrt{\frac{2m}{\hbar^2}\Phi_{avg}}\right) \end{aligned} \tag{2.6}$$

takes the same form as in Equation 2.5 but uses the average barrier height of the junction formed between the materials [79]. This work function was among the first quantities measured after the development of a controllable vacuum gap [80] leading up to the establishment of STM.

2.1.1 Tunneling Microscopy

Observations of tunneling current led to the development of tunneling spectroscopy as a technique for characterizing the electronic properties of materials, leading to notable advances over several decades, e.g., identification of the superconducting energy gap in superconductor-insulator-metal devices [81]. These tunneling spectroscopy measurements deviate from the expected vacuum behavior due to inhomogeneity of the insulating oxide

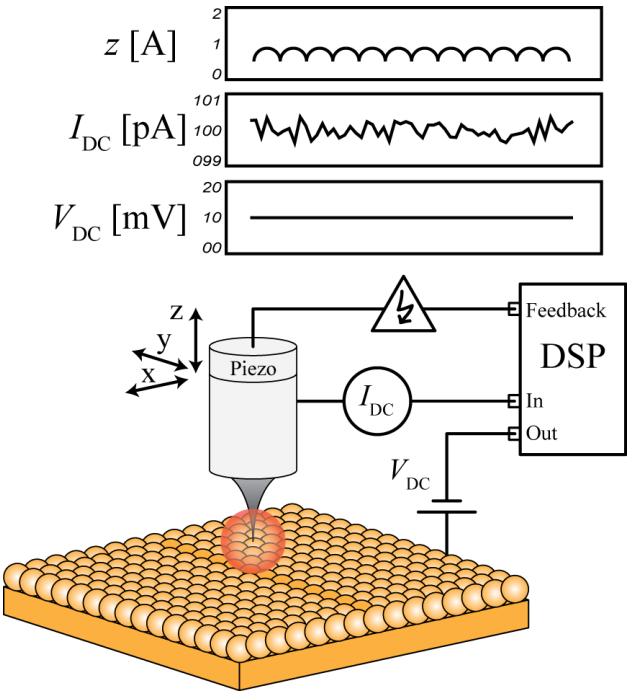

Figure 2.4: Illustration of the basic operational principles of the scanning tunneling microscope.

layer that separates the two conducting elements of the device [82]. A significant advance occurred when the insulating layer of the structure was replaced with a controllable vacuum gap, e.g., it became possible to observe vacuum tunneling based on the exponential dependence of the current with tunnel gap distance, and hence to determine the material work function [80]. With the extreme sensitivity to gap width realized, the tunnel current was quickly utilized to control the height of a scanning probe tip while maintaining a vacuum gap [83].

Due to the extreme sensitivity of the tunnel current on gap distance — tip height changes on the order of 1 Å produce a change in tunnel current of one order of magnitude [27] — precise control of the tip on the sub-Å scale is needed. The implementation of piezoelectric crystals, whose structure deforms under external electric fields, provides picometer spatial precision [51]. This allows for precise control while positioning the probe tip close to the sample surface. A current feedback mechanism is typically employed in a constant-current mode of operation to maintain the tip at a consistent distance from the surface. Figure 2.4 shows the basic operation of an STM system. The STM tip is scanned across the surface and topography is generated as the tip height is modulated to maintain the current setpoint,

I_{DC}, at a voltage, V_{DC}. While the vertical resolution is determined by the vacuum decay of the tunnel current, the atomic lateral resolution comes from the area of the tunnel junction. With this area being related to the radius of curvature of the tip, it becomes important to control the geometry of the probe used to acquire STM images. The wavefunction of an atomic-scale protrusion is typically considered a spherical s-wave with radius, $R < 10$Å, [84, 85] (red sphere in Figure 2.4), though higher order states may be the source of atomic scale resolution [86].

Scanning across the surface in constant-current mode, the tip height traces out a topography of the surface with ångström-scale resolution. Unlike atomic force microscopy [87], the topography in STM does not necessarily correspond to the physical position of atoms but rather to the local density of electronic states (LDOS). This has been shown in theoretical modeling of the density of states for individual atoms: if their contribution to the LDOS is negligible at a particular energy, they are invisible to the tunneling process and thus present no feature in the STM topography [26]. A local minimum in LDOS even leads to a valley in topography [88]. Therefore, the tunnel current depends on more than the transmission factor; the tunnel current also depends on the LDOS of the sample. Scanning tunneling spectroscopy is the investigation of the LDOS via the junction's $I(V)$ and is the principle investigative tool that STM has to offer, in addition to imaging. A detailed discussion of STS measurements is provided in Section 2.3. STM has earned a position among the most common techniques for surface science and is used to study the electronic properties of surfaces [27], nanostructures [22], and molecules [23]. Combining real-space imaging of atomic scale topography with spectroscopic analysis of the surface electronic density of states results in one of the most powerful tools for surface science.

2.2 Atomic Scale Imaging

2.2.1 Tip Preparation

As discussed, the atomic-scale structure of the tip is responsible for imaging the surface features of the sample; careful preparation of the tip micro-structure is therefore necessary. The preparation of tungsten (W) tips begins with electrochemical etching in an electrolyte solution (typically, NaOH or KOH) using an electronic circuit to detect a sudden decrease in the etching current associated with a dramatic change to the tip geometry [89], as illustrated

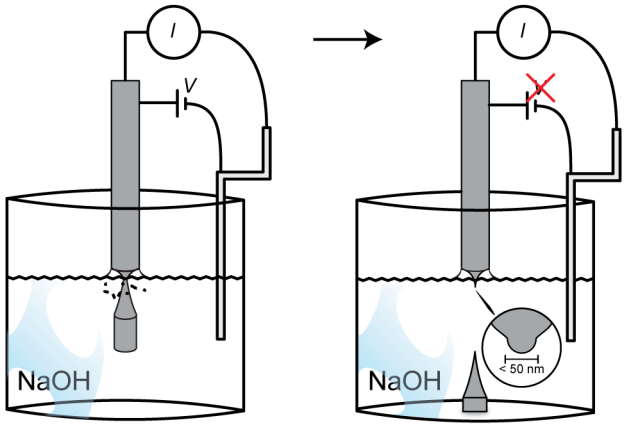

Figure 2.5: Electrochemical etching of a tungsten wire tip. A solid tungsten (W) wire is lowered into a solution of NaOH and adjusted to form a meniscus around the neck of the wire. Negative hydroxide (OH^-) ions react with W to form tungsten oxide (WO_4). The wire surface is preferentially etched at the meniscus due to increased OH^- availability, giving rise to a taper in the lower shank. As the neck of the wire shank thins, the weight of the suspended material will cause the lower shank of wire to separate. This event causes a significant drop in the etch current (I) that will trigger a disconnect of the etch voltage (V) via a switch in the circuit. High current response rates produce a radius of curvature on the 10−100 nm scale.

in Figure 2.5. A bias is applied to the tip while an etching current is measured through a circuit that is designed to shut off when the current drops below a threshold value. The etching process is described by the chemical reaction,

$$\mathrm{W(s) + 2OH^- + 2H_2O \rightarrow WO_4^{-2} + 3H_2(g)\,.} \tag{2.7}$$

The loss of wire material is driven by oxidation of the tungsten surface, forming tungsten oxide (WO_4^{-2}), while a positive voltage (typically, 3.5 V) is applied to the tip [90]. Isolating the effect to the perimeter at the liquid-air interface is crucial to achieving sharp STM tips [91]. A meniscus formed from surface tension in the etching solution enhances the flow of dissolved WO_4 away from the shank, increasing the local etching rate. Preferential etching in the narrow region at the liquid-air interface leads to a relatively large mass of material that is connected to the tip shank by an increasingly narrow bridge. When the weight of the mass overcomes the tensile strength of the tungsten wire, plastic deformation of the bridge reliably produces a sharp tip with radius of curvature below 50 nm [91]. An example is shown in Figure 2.6.

While electrochemical etching is a straightforward method for preparing the macroscopic

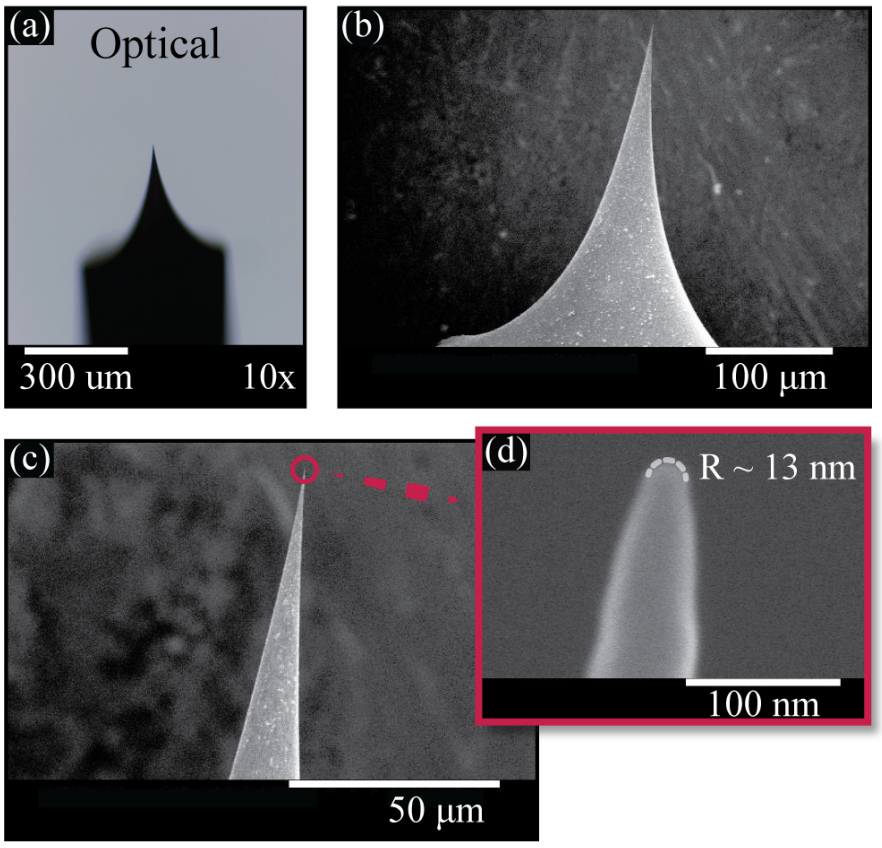

Figure 2.6: An example of successful electrochemical etching of a tungsten wire tip. (a) Optical microscope image at 10x magnification. A single cusp feature formed by the meniscus and 'drop-off' mechanism is present, providing a smooth taper on the scale of 300 µm. (b), (c), and (d) Scanning electron microscope images of the same tungsten tip with increasing magnification. The SEM images indicate a radius of curvature of ∼13 nm.

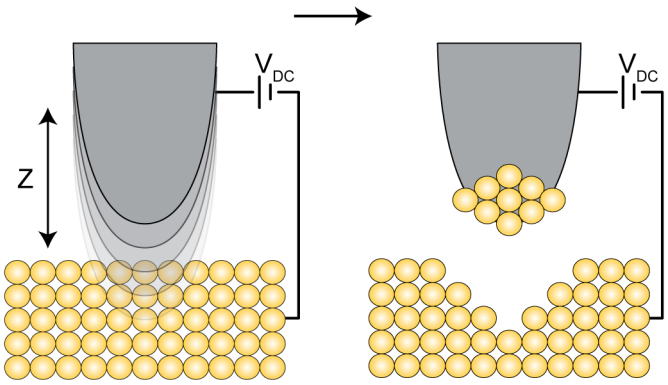

Figure 2.7: Preparation of an atomically sharp tip apex via controlled collision with a gold metal surface. Using the scanning piezo of the STM tip, a controlled motion in the z-direction allows the tip apex to collide with a metal surface. Upon retraction of the tip a cluster of atoms can be extracted from the surface to create a micro-tip. Repeated collisions may be used to further stabilize the tip into a configuration that hosts an atomic protrusion. Applying a bias, V_{DC}, during collisions changes the intensity with which the tip interacts with the sample. Significant changes to both the tip and surface will be achieved when V_{DC} ~ 1 V, while $V_{\mathrm{DC}} \lesssim 100$ mV will do minimal damage to the surface and act as a perturbation to the atomic cluster at the apex.

and mesoscopic structure of the STM tip, *in situ* treatment of the tip apex is the final step to achieving atomic resolution. An accepted limitation of the etching process is a tungsten oxide (WO_3) byproduct that coats the surface with thicknesses up to ~5 nm [92]. Highly technical approaches such as field evaporation during field ion microscopy have shown promise for standardizing the production of atomically sharp STM tips [93]. However, more typical procedures involve multiple techniques to fully prepare the tip. Heating the tip to temperatures upward of 1075 K allows the insulating WO_3 to react with individual W atoms and sublimate from the tip surface. Additionally, biasing the tip with a voltage on the scale of 0.5 kV to 2 kV will drive field emission and can be applied to estimate both the radius of curvature (with Fowler-Nordheim curves [94]), and the cleanliness and stability of the tip apex [95], as well as to further remove oxide and sharpen the apex. The oxide layer can also be removed by sputtering with noble gasses, such as Ar and Ne, and typically leds to a tip radius of curvature below 10 nm [96, 97].

From the conventional techniques, annealing, field-emission, and sputtering remove the oxide layer that acts as an insulator and inhibits the flow of tunnel current. However, after exposing the conductive W tip, a final atomic protrusion must still be formed. Figure

2.7 shows a simple mechanical method to form an atomically sharp tip apex. Starting in constant-current mode with the STM feedback loop establishing a tip height determined by typical parameters of $I_{\mathrm{DC}} = 100$ pA and $V_{\mathrm{DC}} = 100$ mV, the feedback is disengaged and the STM tip is approached to the sample surface until contact occurs. Penetrating the surface causes atoms from the sample to transfer to the tip apex, e.g., forming a gold nanotip on a tungesten wire [98]. The interaction between the tip and surface is governed by the approach distance and the applied DC bias [99]. Both elevated voltages and increased approach distances will cause significant changes to the tip apex and sample location where contact occurs. Break junction measurements and simulations for gold point contacts suggest the lattice temperature is on the order of $100-500$ K at 100 mV, while at 2 V the temperature is expected to reach the melting point [100]. It has been shown that atomic arrangements of the tip apex (e.g. BCC vs FCC) can lead to reproducible changes in the tip DOS [101]. Thus, further approaches at $V_{\mathrm{DC}} \lessapprox 100\,\mathrm{mV}$ can be seen as mechanical annealing of the cluster into a stable crystalline arrangement [102].

2.2.2 Substrate Preparation

Ion bombardment by noble gases, e.g., Ar, also known as sputtering, is a sample preparation technique that cleans a surface at the atomic scale by colliding high energy Ar^+ ions with atoms on the sample surface. Ions in our procedures are typically accelerated with a $1-2$ keV potential. Upon collision, the heavy Ar^+ atoms penetrate into the bulk and transfer kinetic energy through to the top layers of the material, generating a cascading transfer of energy that results in surface layer atoms being ejected from the material [103]. The relatively high energy of the ions may also lead to trapping and capture of the sputter gas, forming defects [104, 105]. To avoid trapping the sputter ions and creating defects in the material, the sputter process is optimized by increasing the sputter yield and decreasing the penetration depth of colliding ions. Adjusting the angle of incidence during sputtering reduces the penetration depth of energized ions and instead enhances the transfer of in-plane momentum into the surface atoms, with increasing sputter yield up to an incident angle of $70-80$ degrees [106]. In our sample preparation, the surface is tilted at 70 degrees relative to the incident ion beam and we operate at an Ar pressure of $\sim 2\times10^{-5}$ mbarr. With an accelerating voltage of 1 keV, we measure a sputter current of $\sim 3\,\mu$A. Nevertheless, bombardment disrupts the crystalline surface. In order to reform the surface structure, we thermally anneal

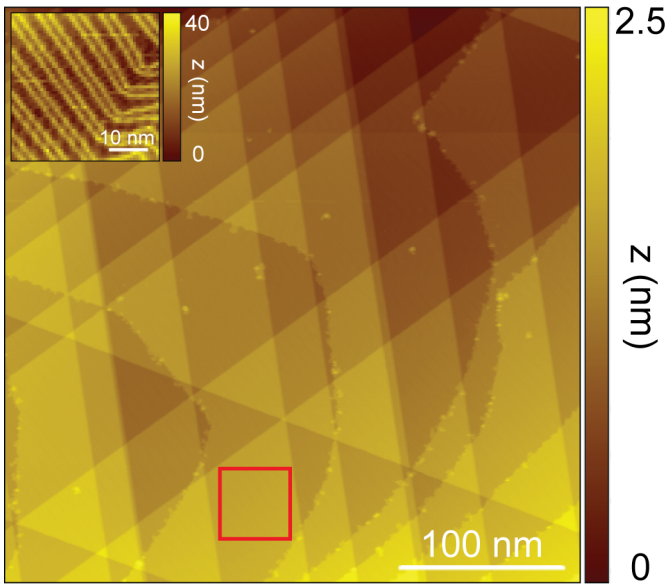

Figure 2.8: Constant-current topography image of a clean, atomically smooth, Au(111) surface. The herringbone surface reconstruction of the (111) crystal orientation is visible in the inset (red box). Preparation of the sample surface was done through cycles of sputtering with 1 keV Ar ions and annealing to 900 K. Imaging conditions: I_{DC} = -50 pA and V_{DC} = -2.0 V.

the sample to high temperatures (e.g., 900 K for gold), allowing the surface atoms to redistribute. Relaxation of the lattice allows for surface reconstruction, such as the herringbone structure visible on the (111) crystal orientation of gold (Au(111)). Figure 2.8 shows an Au(111) surface cleaned by successive cycles of Ar^+ ion bombardment for 30 minutes and annealing to 900 K for 15 min.

2.2.3 Image Calibration

While scanning, the STM tip position is controlled by the deformation of the scanning piezo crystals and the current signal is mapped to coordinates in the image plane. While operating in constant-current mode, the current signal is maintained by precisely varying the tip-sample distance, with significant changes in tunnel current occurring on distances of <1 Å. Therefore, accurate calibration of the STM system is needed to operate the feedback loop and accurately record surface features. Although the current signal recorded during STM measurements does not directly reflect the nuclear positions, the periodicity of lattice sites emerges as a spatial modulation of the electronic density of states. The STM experiments for this thesis were performed on Au(111) surfaces. Scanning a bare gold surface

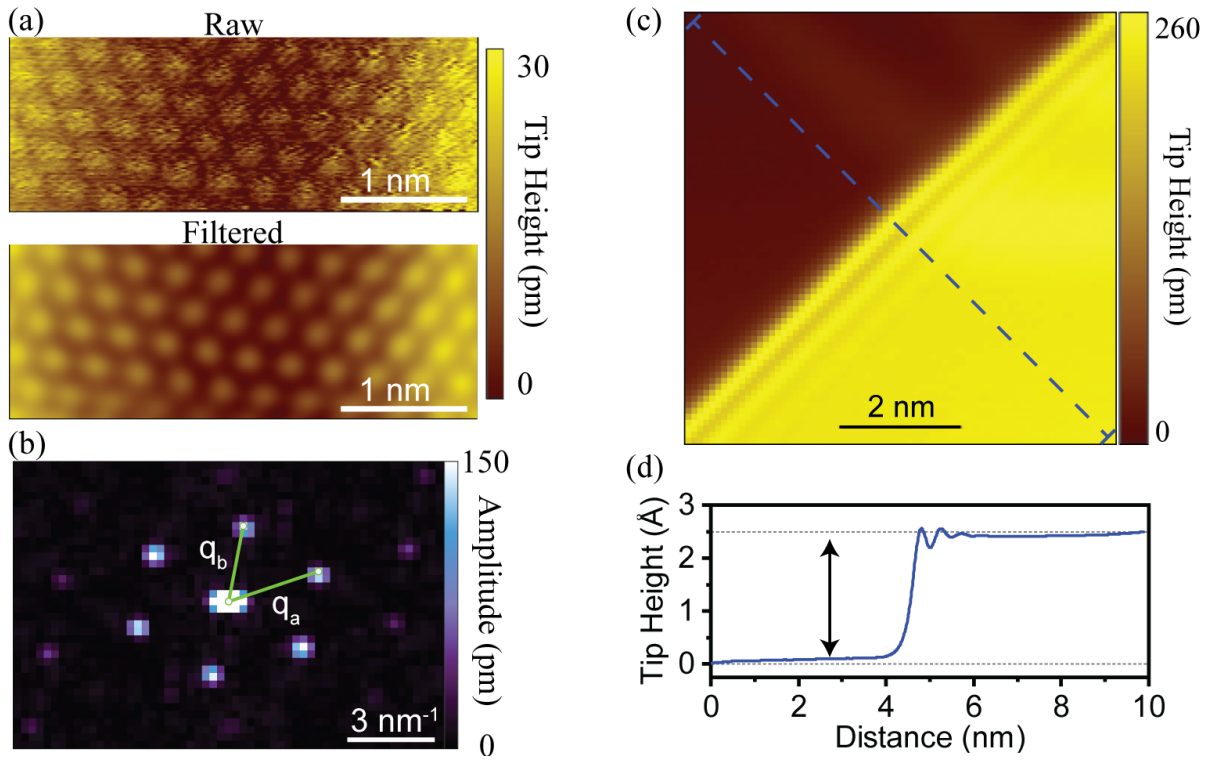

Figure 2.9: Atomic resolution images used to calibrate the STM scanning piezos. (a) Noisy topographic image of an Au(111) surface with atomic resolution (top) and filtered atomic resolution topographic image (bottom). (b) 2D Fast-Fourier transform (FFT) with lattice vectors $r_a = 1/q_a = 2.86\,\text{Å}$ and $r_b = 1/q_b = 2.77\,\text{Å}$. (c) Topographic image of Au(111) terrace edge, including oscillations due to scattering of electrons in the surface state at the step edge. (d) Line cut along the blue dashed line in (c) indicating a step height of 2.5 Å. The filtered image in (a) is the result of isolating the Bragg peaks in the FFT of (b). Topographic images acquired in constant-current mode with setpoints (a) $V_{DC} = -6\,\text{mV}$ and $I_{DC} = -50\,\text{pA}$ at $T_{sample} = 78\,\text{K}$ and (c) $V_{DC} = -400\,\text{mV}$ and $I_{DC} = -300\,\text{pA}$ at $T_{sample} = 7\,\text{K}$.

containing a terrace step-edge allows us to calibrate the vertical (z) axis based on the known step height. Fourier analysis of an atomically resolved Au(111) surface allows us to calibrate the x and y axes. Peaks in the FFT of an atomically resolved surface quantify the periodicity of the surface structure. The inverse of the periodicity should reflect the atomic lattice vectors of the surface. Figure 2.9(a) (top) shows an atomically resolved Au(111) surface where the hexagonal symmetry of the atoms is visible. A 2D FFT (Figure 2.9(b)) shows 6 peaks, which correspond to the lattice arrangement. Isolating these peaks leads to the filtered image, which more clearly shows the hexagonal arrangement of atoms (Figure 2.9(a), Bottom). Adjustment of the piezo constants is performed to compensate for the disagreement between the measured lattice vectors and those found in the literature [107]. The correct constant is

a product of the original value and the ratio of expected lattice vector length to measured lattice vector length,

$$P'_{xyz} = P_{xyz} \frac{r_{\text{expected}}}{r_{\text{measured}}} \,. \tag{2.8}$$

The vertical piezo requires a corresponding feature to perform a calibration. On the Au(111) surface, the in-plane lattice vectors are expected be between 2.7 Å and 2.9 Å. Meanwhile, atomically flat terraces form monolayer step-edges where the topographic height is expected to change by ∼2.4 Å [108]. Analysis of constant-current STM imaging across a clean step-edge (blue dashed line in Figure 2.9(c)) is a simple procedure for determining the z-piezo calibration. Notably, at a bias voltage $V_{\text{DC}} = -400\,\text{mV}$, we see scattering of electrons in the Au(111) surface state at the terrace edge, which appear as standing waves [109]. Repeating these calibration steps is required when changing the operation temperature of the STM system. The piezo crystals deform less as the temperature decreases, requiring adjustment of the constants when cooling down, e.g., from room temperature (RT, 300 K) to liquid nitrogen (LN_2, 77 K) or liquid helium (LHe, 4 K) temperature.

2.3 Tunneling Spectroscopy

Measuring variations in the $I(V)$ at different tip positions allows us to perform STS of the LDOS with ångström-scale precision. The tunneling picture presented in Section 2.1 does not take into account the energy-dependent DOS, $\rho(E)$, that can be combined with the electron wavefunction to generate the energy-dependent LDOS,

$$\text{LDOS} = \rho(\mathbf{r}, E) = \sum_n |\psi_e(\mathbf{r})|^2 \delta(E - E_n) \,, \tag{2.9}$$

that, as we see later, contributes directly to the tunneling current in the Bardeen model. In a neutral configuration, i.e., $V_{\text{DC}} = 0$, electronic states are filled to the energy E_{F} on both sides of the junction. As a result, there is zero net current. Figure 2.10 shows a schematic illustrating the properties of the junction and their contributions to the flow of electrons across the tunnel junction with a positive bias applied to the sample. The occupied density of states of the tip, filled to $E_{\text{F,t}}$, are free to tunnel into unoccupied states of the sample from $E_{\text{F,s}}$ to $E_{\text{F,s}} + \text{e}V$. Elastic tunneling is an energy conserving process, so the electrons in $\rho_t(E)$ must tunnel into unoccupied sample states $\rho_s(E)$. By changing the applied bias, the set of states that are exposed for transport changes, resulting in a change to the total current based on the tip and sample wavefunction overlap at a given energy, $\rho(\mathbf{r}, E) \sim \psi_t(\mathbf{r})\psi_s(\mathbf{r})$.

Recall from Equation 2.6 that the transmission factor depends on the height of barrier. When a bias is applied to the junction, the average barrier height becomes

$$\bar{\Phi} = \Phi_{\text{avg}} + eV/2\,. \tag{2.10}$$

For an electron tunneling from the tip to the sample with energy $E_{\text{F,s}} < E < E_{\text{F,t}}$, the apparent barrier height is largest at $E = 0 = E_{\text{F,s}}$ and is reduced for increasing E, i.e., $\Phi_{\text{app}} = \bar{\Phi} - E$. The barrier height is lowest at the highest occupation energies, $E_{\text{F,t}} = E_{\text{F,s}} + eV$, providing the largest transmission factor due the exponential behavior,

$$T(E, V, d) = \exp\left(-2d\sqrt{\frac{2m}{\hbar^2}[\Phi_{\text{avg}} + \frac{eV}{2} - E]}\right), \tag{2.11}$$

which is illustrated by arrows of decreasing length in Figure 2.10.

In the following section we consider the energy levels introduced as the bias is changed. The positive bias condition, $V_{\text{DC}} > 0$, allow electrons from the occupied states of the tip to tunnel into unoccupied states of the sample. In the negative bias condition, $V_{\text{DC}} < 0$, electrons from the sample tunnel into unoccupied states of the tip. When we consider the energy dependent behavior of $T(E, V, d)$, it is clear that the majority of the current is generated by electrons with $E \simeq \text{e}V$. The transmission factor exclusively allows tunneling into unoccupied states, whether they be of ρ_{s} when $V_{\text{DC}} > 0$ or ρ_{t} when $V_{\text{DC}} < 0$. The reduced barrier height for electrons tunneling at $E = eV$ leads to an asymmetry in the contributions from occupied and unoccupied states of ρ_{s} to the tunneling current. The contribution from the occupied states of the sample, $\rho_{\text{s}}(E < E_{\text{F,s}})$, at $V_{\text{DC}} < 0$ is minimized by the transmission factor because the barrier height is largest for $\rho_{\text{s}}(E = E_{\text{F,s}} - eV_{\text{DC}})$. However, at $V_{\text{DC}} > 0$ the largest contributions to the tunnel current occur at unoccupied states of the sample, $\rho_{\text{s}}(E = E_{\text{F,s}} + eV_{\text{DC}})$. This asymmetry in the tunneling condition as well as other voltage dependent effects has prompted development of extraction methods for ρ_{s} of various complexity [110, 111]. Bias dependent changes in the tunnel current is the basis of STS and the following discussion aims to elucidate the origins of this behavior using the Bardeen model [112] as well as provide an understanding of how STS measurements are performed.

2.3.1 Bardeen Tunneling Model

Bardeen considered the transmission of many electronic states through a one-dimensional

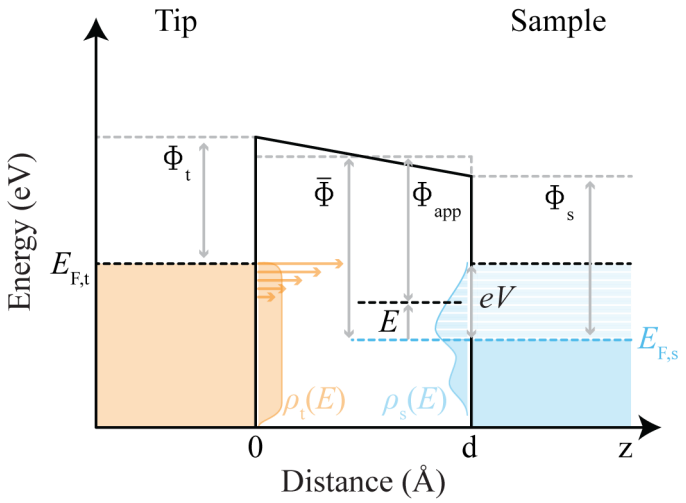

Figure 2.10: Energy level diagram of an STM junction with positive bias applied to the sample. A change in applied bias voltage (eV) alters the Fermi level alignment between the tip ($E_{\mathrm{F,t}}$) and sample ($E_{\mathrm{F,s}}$), promoting tunneling between the two reservoirs. Tunneling is limited to exchanges between occupied states of the tip, $\rho_{\mathrm{t}}(E)$, and empty states of the sample, $\rho_{\mathrm{s}}(E)$. Transmission through the barrier is further emphasized near the Fermi level, where the apparent barrier height, $\Phi_{\mathrm{app}} = \bar{\Phi} - E$, is the lowest.

barrier [112]. This interpretation has seen widespread application in the years since the development of STM [79, 84, 113]. In a many-state picture, all tunneling channels are open simultaneously and we must consider transmission of electrons through the barrier from all occupied states with energies $E_{\mathrm{F}} - e|V| < E < E_{\mathrm{F}}$.

The transmission rate across the barrier is governed by the continuity equation from electrodynamics,

$$\frac{\partial \rho(z,t)}{\partial t} + \operatorname{div} j(z,t) = 0\,, \tag{2.12}$$

where $\rho(z,t)$ is the probability density,

$$\rho(z,t) = \Psi(z,t)\Psi^*(z,t)\,, \tag{2.13}$$

and $j(z,t)$ is the current density flowing between the tip and sample. We can apply the time-dependent Schrödinger equation,

$$i\hbar\frac{\partial}{\partial t}\Psi(z,t) = \left(-\frac{\hbar^2}{2m}\frac{\partial^2}{\partial z^2} + V(z,t)\right)\Psi(z,t)\,, \tag{2.14}$$

to describe the change in $\rho(z,t)$, producing a matrix element for the transmission amplitude from an initial state of the tip ($\psi_{t,i}(0)$) to a final state of the sample ($\psi_{s,f}(d)$), which we

evaluate at a surface located within the barrier above the sample surface,

$$M_{fi}(E) = \frac{\hbar^2}{2m} \int_{z=z_s} \left[\psi_{t,i}(z,E)\frac{\partial}{\partial z}\psi^*_{s,f}(z,E) - \psi^*_{s,f}(z,E)\frac{\partial}{\partial z}\psi_{0,i}(z,E)\right] dS\,. \tag{2.15}$$

We can insert the wavefunctions from Equation 2.4 after applying the proper boundary conditions from Equation 2.3, where the origin of the wavefunctions are at $z = 0$ and $z = d$ for the tip and sample, respectively. Evaluation of the one-dimensional matrix element produces,

$$M_{fi}(E) = \frac{\hbar^2}{2m}\kappa\psi_{t,i}(0)\psi_{s,f}(d)A\exp(-\kappa d)\,, \tag{2.16}$$

where A is the tunneling area of the junction and κ can be defined based on Equation 2.11 or Equation 2.3, depending on that accuracy needed. In the Bardeen model, $I(V)$ is the sum of all allowable electron transmission paths through the vacuum and takes the form,

$$I = \frac{4\pi e}{\hbar}\sum_{i,f}|M_{fi}|^2\delta(E_f - E_i)\,. \tag{2.17}$$

When a bias, V, is applied to the junction the energy levels change, such as in Figure 2.10, and all the states between $E = 0$ and $E = \mathrm{e}V$ contribute to the tunnel current. The initial and final state energies must be the same to conserve energy so M_{fi} reduces to $M(E)$ and the current takes the integral form,

$$I(V) = \frac{4\pi e}{\hbar}A\int_0^{eV}\rho_s(E - eV)\rho_t(E)\exp(-2\kappa(V)d)dE\,, \tag{2.18}$$

where $\rho_s = \Psi_s\Psi_s^*$ is the density of states of the sample and $\rho_t = \Psi_t\Psi_t^*$ is the density of states of tip.

For energies $eV << \bar{\Phi}$, the transmission coefficient simplifies to $T(d)$ (Equation 2.6), where d is the tip-sample separation distance, and can be separated from the integral in Equation 2.18. Rearranging the terms allows I to be written as,

$$I(V,z) \propto I(V)T(z) = I(V)\exp(-2\kappa z)\,, \tag{2.19}$$

with κ the barrier decay coefficient. Determination of κ is achieved through vertical spectroscopy measurements where the current is recorded as a function of tip height ($I(z)$). Analysis of vertical STS measurements involves fitting $I(z)$ with an exponential according to Equation 2.19 and leads to an estimation for the work function according to Equation 2.6.

2.3.2 dI/dV Spectroscopy

Experimental STS is performed by measuring changes in the tunnel current as a function of applied bias. The Bardeen model again offers a concise description of the change in tunnel current, dI, for a change in the bias of dV. If we consider the case of $eV << \bar{\Phi}$ and let $I(V) = \int \partial I/\partial V dV$, then Equation 2.18 produces,

$$\frac{\mathrm{d}I}{\mathrm{d}V} \approx \frac{4\pi e^2}{\hbar} \rho_{tip}(eV)\rho_{sample}(eV)T(d)\,, \tag{2.20}$$

when evaluated at $E = \mathrm{e}V$ so that $T(d) = \exp(-2\kappa d)$. If we assume the Tersoff-Hamman approximation for a spherical (s-wave) tip wavefunction [84], a flat density of states near the Fermi level of ρ_{tip} is reasonable, e.g., $\rho_{tip}(eV) = \rho_{tip}(0)$. With this constant approximation for the tip density of states, measurements of the differential conductance performed at fixed tip-sample distance are proportional to the energy-dependent local density of states in the sample,

$$\frac{\mathrm{d}I}{\mathrm{d}V}(V) \propto \rho_{sample}(eV)\,. \tag{2.21}$$

Under these assumptions, a trace of $\frac{\mathrm{d}I}{\mathrm{d}V}(V)$, such as is shown in Figure 2.11, reveals the sample LDOS.

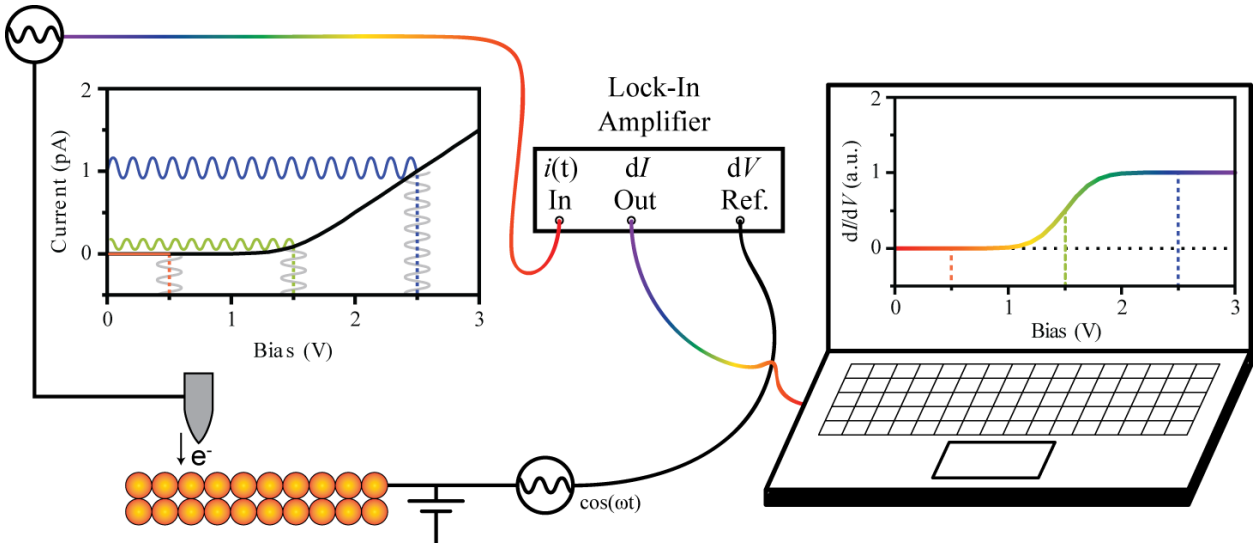

Figure 2.11: Extracting the differential conductance spectrum from the local slope of the $I(V)$. We trace out the local $\mathrm{d}I/\mathrm{d}V$ as a function of applied bias (V) by recording changes in current, dI, for a bias modulation amplitude of dV. An AC current, $i(t)$, is induced by an AC bias modulation, $V_{\mathrm{AC}} = dV\cos(\omega t)$, which can be measured using lock-in detection.

Acquiring a measurement of $\mathrm{d}I/\mathrm{d}V$ is made relatively straightforward through the ap-

plication of a bias modulation and lock-in detection (Figure 2.11). Applying a time-varying voltage results in a periodic change in the tunnel current,

$$i(t) = I(V_{\mathrm{DC}} + dV\cos(\omega t))\,, \tag{2.22}$$

where the instantaneous current, $i(t)$, is the result of modulating the static bias, V_{DC}, by an amount, dV, at an angular frequency, ω. If dV is small compared to the static bias, a Taylor series expansion of Equation 2.22 about V_{DC} becomes a reasonable approximation,

$$i(t) = \sum_{n=0}^{\infty} \frac{\delta V^n}{n!} \frac{d^n I(V_{\mathrm{DC}})}{dV^n} \cos^n(\omega t)\,. \tag{2.23}$$

Using a power reduction identity, each of the cosine terms in Equation 2.23 can be written as a function of the corresponding harmonic frequency, $\omega_n = n\omega$,

$$\begin{aligned}
\cos^2(\omega t) &= \frac{1}{2} + \frac{1}{2}\cos(2\omega t) \\
\cos^3(\omega t) &= \frac{3}{4}\cos(\omega t) + \frac{1}{4}\cos(3\omega t) \\
\cos^4(\omega t) &= \frac{3}{8} + \frac{1}{2}\cos(2\omega t) + \frac{1}{8}\cos(4\omega t)
\end{aligned}$$

Regrouping the terms in order of increasing ω_n,

$$\begin{aligned}
i(t) = \sum_{n=0}^{\infty} \frac{\delta V^n}{n!} \frac{\mathrm{d}^n I(V_{\mathrm{DC}})}{\mathrm{d}V^n} \cos^n(\omega t) = \\
&+ (I(V_{\mathrm{DC}}) + ...) \\
&+ \delta V \cos(\omega t)(\frac{\mathrm{d}I(V_{\mathrm{DC}})}{\mathrm{d}V} + ...) \\
&+ \frac{1}{4}\delta V^3 \cos(2\omega t)(\frac{\mathrm{d}^2 I(V_{\mathrm{DC}})}{\mathrm{d}V^2} + ...) \\
&+ ...\,,
\end{aligned}$$

we find that the lowest order approximation for each $\cos(\omega_n t)$ has an amplitude proportional to the corresponding differential order $\mathrm{d}^n I_{\mathrm{DC}}/\mathrm{d}V^n$. Therefore, recording the lock-in detector signal at frequency ω_n of the modulated current in Equation 2.22 is approximately proportional to recording the direct measurement of $\mathrm{d}^n I(V_{\mathrm{DC}})/\mathrm{d}V^n$. Pairing lock-in detection with a sweep of V_{DC} extracts the energy dependent differential conductance.

The resolution of the STS measurements is controlled by both the oscillation amplitude of V_{AC} as well as the temperature of the measurement. In all $\mathrm{d}I/\mathrm{d}V$ measurements utilizing an oscillating bias voltage the energy resolution takes the form,

$$\Delta E = \sqrt{(2\mathrm{e}V_{\mathrm{RMS}})^2 + (0.28\mathrm{meV/K}T)^2}\,, \tag{2.24}$$

where $V_{\mathrm{RMS}} = \mathrm{d}V/\sqrt{2}$ and the value 0.28 meV/K arrises from the width of the derivative of the Fermi distribution,

$$f(E) = \frac{1}{1 + \exp\left(\frac{E-\mathrm{e}V}{k_B T}\right)}\,, \tag{2.25}$$

with $k_B T$ being Boltzmann's constant [51]. Thermal broadening of the energy resolution plays a significant role in room temperature experiments, where the energy resolution is at least 83 meV and resolution losses due to bias modulation are easily managed by selecting an appropriate modulation amplitude. When investigating samples at lower temperatures ($T \sim 10$ K), thermal broadening is minimal at just 2.8 meV. In this case, careful selection of modulation amplitude is necessary to avoid limiting the energy resolution based on the applied V_{RMS}. Working at lower voltages, where small modulation amplitudes are significant is an advantage, e.g., $V_{\mathrm{DC}} = 10\,\mathrm{mV}$ and $dV = 1\,\mathrm{mV}$, $2\mathrm{e}V_{\mathrm{RMS}} \simeq 2.4\,\mathrm{meV}$ compared to $V_{\mathrm{DC}} = 1\,\mathrm{V}$ and $dV = 20\,\mathrm{mV}$, $2\mathrm{e}V_{\mathrm{RMS}} \simeq 48\,\mathrm{meV}$.

At higher voltages, e.g., $V_{\mathrm{DC}} \simeq 1\,\mathrm{V}$, calculation of the transmission factor suggests significant suppression of contributions to the current in Equation 2.18 by energies less than $\mathrm{e}V$. This implies that the limit of STS resolution on the 1 V scale is largely due to variation in the transmission factor rather than thermal broadening of the energy levels or bias modulation amplitude, so long as they are reasonably smaller than the width of $T(V, d)$.

A practical consideration when performing $\mathrm{d}I/\mathrm{d}V$ spectroscopy is the bandwidth limit of the pre-amplifier necessary to detect pA-scale currents. For modulation frequencies within the bandwidth of the pre-amplifier, the output is measured without distortion. However, there is a frequency-dependent transfer function (i.e., 'roll off curve') that will affect the amplitude of the signal recorded by the STM electronics (Figure 2.12). To determine the transfer function, a known bias modulation (e.g., 100 mV) is used to induce a current oscillation with a linear response (e.g., a resistor with R = 1 GΩ) that is transmitted through the pre-amplifier (with gain set to 10^9 V/A). Using our lock-in as both the detector and the reference, we sweep the modulation frequency and measure the pre-amplifier output. For

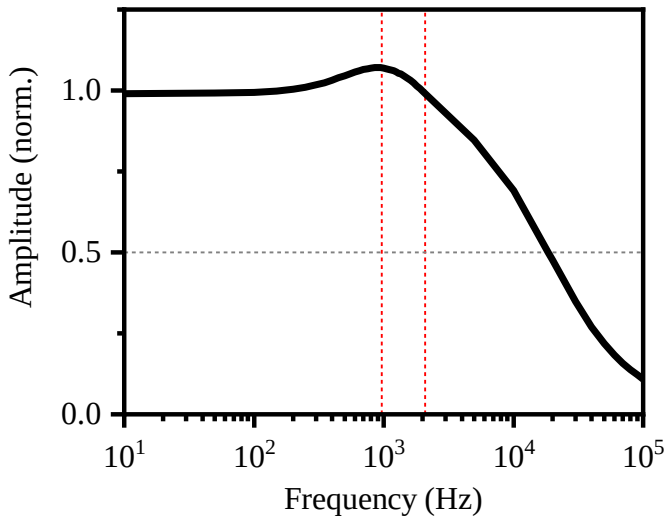

Figure 2.12: Frequency dependent transfer function for our FEMTO low-noise pre-amplifier operating at maximum gain of 10^9 V/A. The response curve is normalized to the modulation amplitude used during the measurement, 100 mV. Red dashed lines indicate commonly used modulation frequencies for THz-STM (963 Hz) and STS (2083 Hz).

frequencies within the bandwidth we expect a signal that accurately reflects the amplitude of the current modulation. When the frequency exceeds the bandwidth, stray capacitance in the pre-amplifier and cabling connecting to the tip leads to a frequency dependent filtering,

$$|V_{\mathrm{OUT}}| = \frac{I_{\mathrm{IN}} R_{\mathrm{FB}}}{\sqrt{1 + (\omega R_{\mathrm{FB}} C_{\mathrm{FB}})}}\,, \tag{2.26}$$

where R_{FB} is the feedback resistor used inside the pre-amplifier and C_{FB} is the parasitic capacitance of the circuit [107]. During imaging experiments, the combination of STM scan speed, scan size, and pixel count define a sampling interval in which the STM electronics records the current signal. Higher modulation rates improve the signal-to-noise ratio (SNR) by increasing the number of $\mathrm{d}I/\mathrm{d}V$ or THz-STM samples obtained within the STM sampling interval. Averaging over an increased number of counts divides noise (e.g., tip motion, junction changes, or voltage fluctuations) across each data point at a characteristic rate of $1/f$. The increased modulation rates also allow STM imaging to be performed at higher speeds, allowing experiments to be performed in less time with sufficient signal. However, a balance must be struck between increased SNR and decreases in the pre-amplifier output.

2.4 LT-UHV STM System

This section covers aspects of the STM system used in the experiments presented later

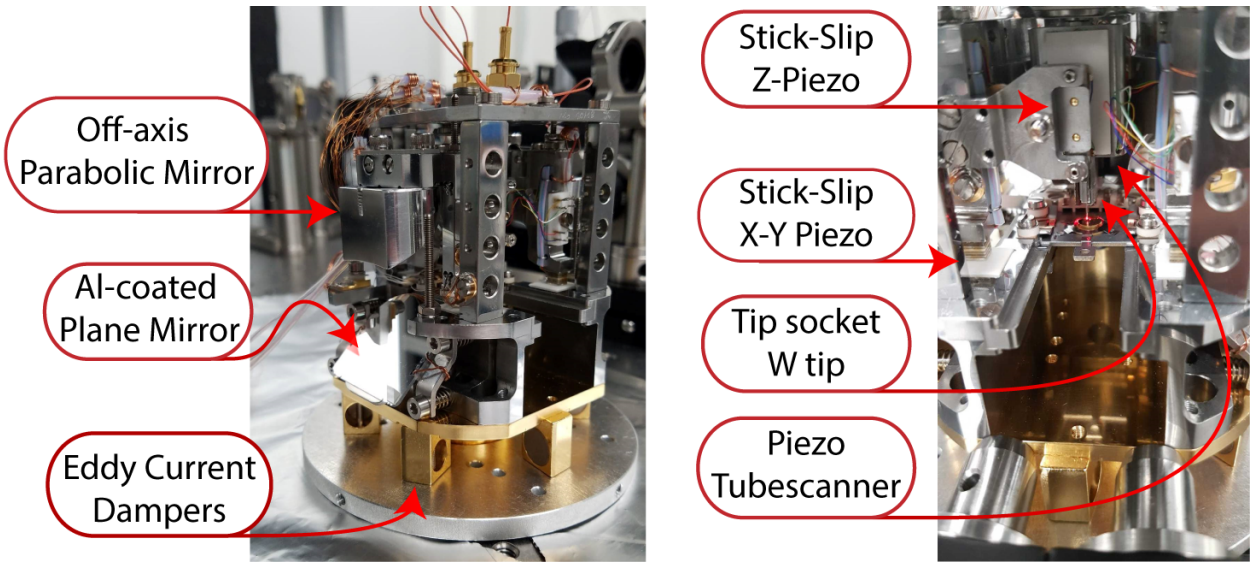

Figure 2.13: Image of the STM scan head with optical elements and pan-scan design.

in this thesis. For course motion, the system implements a stick-slip action, where opposing piezos push and pull each other to walk the tip around the sample surface and move the tip vertically for retraction and approach. Figure 2.13 shows our custom commercial STM system produced through collaboration with Createc GmbH. The system operates in a UHV environment ($P < 10^{-10}$ mbar) at cryogenic temperatures while maintaining optical access. The STM is located in a nested system of cooled shields that provide thermal insulation for operating at cryogenic temperatures. The outermost heat shield is connected to a cryostat that contains 20 L of liquid nitrogen (LN_2) at 77 K. It acts as a thermal barrier for the inner heat shield, which is connected to a helium cryostat containing 4.2 L of liquid helium (LHe) at 4 K. When operating at LHe temperatures, the hold time for the inner cryostat of our microscope is ∼100 hrs when subject to the lowest heat loads, reducing to ∼66 hours when utilizing optical access. When operating at 77 K using LN_2 and under typical heat loads, the inner cryostat hold time increases significantly and lasts longer than the >100 hr hold time of the outer cryostat. For initial cooling purposes, from room temperature, the scan head is brought into physical contact with the helium shield for increased heat conduction. The helium cryostat can hold either LN_2 or LHe for operation at 77 K or <10 K, respectively.

During typical operation, the scan head is mechanically isolated from the thermal shields to increase stability but is kept in thermal contact with the inner cryostat via a braided copper wire. The scan head is suspended from a set of three springs that provide necessary

Open Shutters	Heater	Temperature (K)
0/2	Off	6.6
0/2	On	7.1
1/2	Off	7.7
1/2	On	8.2
2/2	Off	9.0
2/2	On	9.5

Table 2.1: STM base temperatures for different configuration of heat loads. Heater refers to usage of the internal pre-amplifier.

balance and damping against vertical vibrations. Rotational motion of the scan head is damped by an array of magnetic standoffs located around the bottom perimeter of the scan head that generate eddy currents in opposing metallic standoffs on the helium shield. The entire vacuum system is then suspended on pneumatic air legs to dampen building vibrations. For increased current sensitivity, our scan head is equipped with an internal pre-amplifier that offers a gain of 10^{10} V/A while operating at cryogenic temperatures. However, LHe temperature is too cold for normal operation and a heater is used to keep the pre-amplifier from 'freezing'. Using the internal pre-amplifier heater causes the average temperature of the scan head to increase and reduces cryogen hold time. Optical access for the STM is provided by a 6-mm-thick c-cut sapphire vacuum window and a pair of 1-inch-diameter, 3-mm-thick, windows of the same material on each side of the system (one on each heat shield). Illumination is controlled via a pair of shutters located on each side of the nitrogen shield; opening them exposes the windows on the nitrogen and helium shields. Attached to the STM chamber is a preparation chamber used for *in-situ* tip/sample preparation. Finally, a load-lock chamber is coupled to the preparation chamber to facilitate the transfer of samples from ambient conditions into UHV via the preparation chamber, and ultimately to the STM scan head, as seen in Figure 2.14.

Table 2.1 contains the base operating temperatures for the STM while operating in a number of different conditions that subject the scan head to varying heat loads. Two shutters provide line-of-sight access to the STM scan head for optical measurements. These ports allow heat and light to illuminate the system, causing the base temperature to rise. Similarly, the heat load needed to operate the internal pre-amplifier incidentally applies an additional thermal load to the scan head, again resulting in elevated base temperature. A combination of shutter status and internal pre-amplifier engagement leads to variation in the

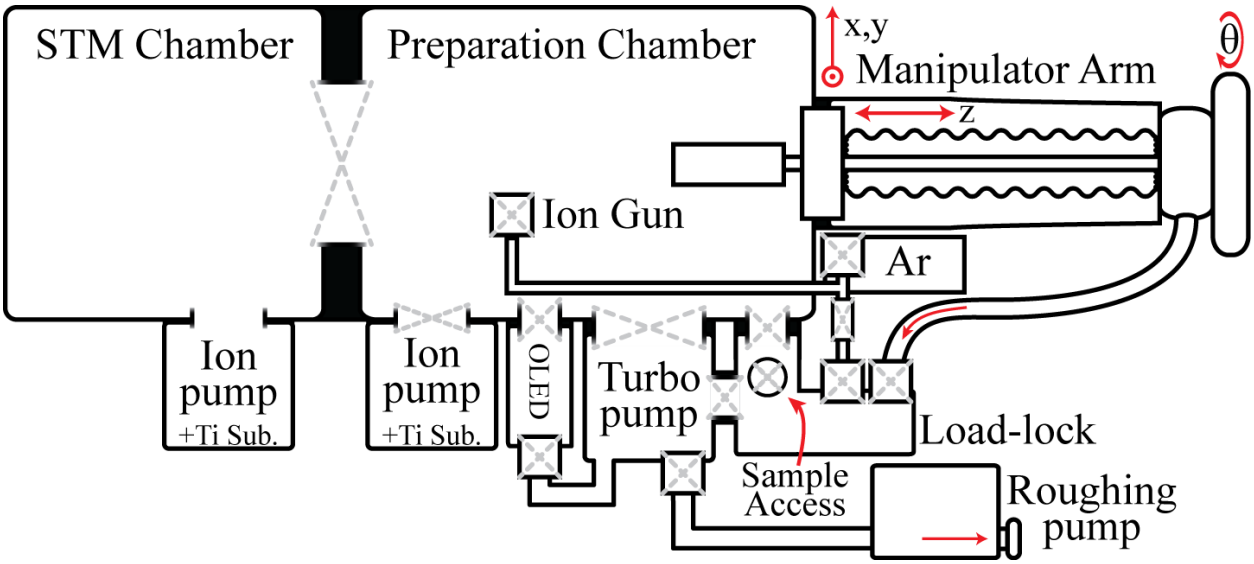

Figure 2.14: Schematic of the STM vacuum chamber. Valves are indicated by pairs of crossed grey dashed lines. Both the STM and preparation chambers are equipped with ion pumps capable of maintaining chamber pressures $< 10^{-10}$ mbar. A turbo molecular pump is connected to the preparation and load-lock chambers and backed by a roughing pump. A leak valve connected to the ion gun is used to incorporate argon gas for ion bombardment. A circular access port is used to exchange tips and samples in/out of the vacuum system through the load-lock chamber. The manipulator arm maintains vacuum while moving in four degrees of motion and is pumped out through the load-lock chamber.

STM base temperature from 6 K to 10 K. Increased heat loads result in reduced hold times for the system's cryogenic liquids.

Regardless of system configuration, the cleanliness of our sample surface is paramount for the proper execution of experiments. To maintain ultrahigh vacuum of $P < 10^{-10}$ mBar, a series of pumps designed to operate in different pressure regimes is implemented. A turbo and roughing pump are primarily used to evacuate the majority of gas from the system and reduce the pressure below 10^{-7} mbar, where water vapor is no longer a significant contribution to the chamber atmosphere. However, below 10^{-7} mbar, out-gassing of adsorbates, specifically water vapor, on the chamber walls prevents the system from achieving UHV pressure. A 'bake-out' of the system is performed by heating the vacuum chamber above the evaporation temperature of water. For our system, a bake-out temperature of $120-135$ °C is maintained for $\sim$72 hrs so that when the chamber returns to room temperature, $P \sim 10^{-8} - 10^{-9}$ mbar is reached. To approach UHV conditions, additional ion pumps are employed that use high potential gradients (several thousand volts) to ionize gas particles within the pump volume and accelerate them into a collection plate made of a highly reactive material (e.g., titanium). At UHV pressure ($\sim 10^{-10}$ mbar), small molecules become the dominant species in the vacuum (e.g., H_2 and CO). A titanium sublimation pump (TSP) can be used to coat the chamber with titanium atoms that react with colliding molecules, capturing them indefinitely, to aid in the adsorption of smaller molecules, which further lowers the base pressure of the microscope. Maintaining ultra low chamber pressure ($P < 10^{-10}$ mbar) reduces adsorbate accumulation rate. The accumulation rate is inversely proportional to the pressure and an estimate for the time it takes to accumulate one monolayer of adsorbates at $P = 10^{-9}$ mbar is 1 hr [106]. For our system this estimate suggests a surface cleanliness on time scales > 10 hrs, sufficiently long to perform experiments.

2.4.1 STM Optics

The STM is a commercial unit designed to provide excellent mechanical, thermal, and electrical stability for high quality measurements. It also provides optical access for THz-STM measurements. A pair of 1-inch-diameter, 60-degree off-axis parabolic mirrors are attached directly to the STM carriage (Figure 2.13, left). The effective focal distance is 33.85 mm and the focal point is fixed to a height of 2.2 mm above the base of the STM sample plate (Figure 2.15). With the parabolic mirrors connected directly to the STM carriage,

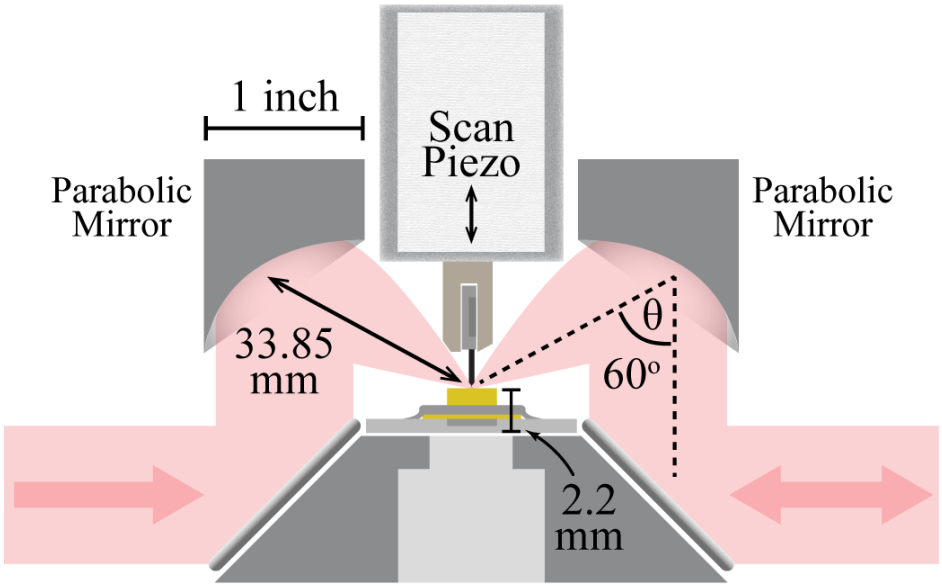

Figure 2.15: Schematic for the optical beam path on our custom Createc GmbH scan head. The scan head is equipped with a pair of 1 inch diameter, 60-degree off-axis parabolic mirrors with effective focal length of 33.8 mm. The scan piezo can be coarsely moved across the sample and vertically. To keep the tunnel junction within the optical focus, the sample + plate must be 2.2 mm in height and the parabolic mirrors are mechanically coupled to the scan piezo. The optical beam is incident from the left to reproduce our experimental setup and the right-side optical path may be used for illumination or collection of light coming from the focus.

the STM tip can be moved anywhere on the sample while maintaining a tip position in the common focus. A pair of flat mirrors fixed to the scan head frame (Figure 2.13(left)) direct light into (or away from) the focusing mirrors (Figure 2.15). Both sets of optical elements are made of aluminum, offering high reflectance across a broad spectral range. The on-board parabolic mirrors offer two significant advantages over traditional optical setups with externally mounted lenses. Positioning them inside the chamber close to the tip (rather than outside the chamber) reduces the focal length, leading to increased numerical aperture when using the same diameter beam,

$$\mathrm{NA} = n_r \frac{D}{2f}\,, \tag{2.27}$$

where the refractive index $n_r = 1$ in vacuum, D is the beam diameter, and f is the focal length of the optical element. With an incident beam diameter of 25.4 mm, the NA of our focusing mirrors is 0.375. A larger numerical aperture reduces the beam waist, i.e., the distance from the center of the focus to the position at which the intensity falls to $1/e^2$. The

beam diameter ($2 \times$ beam waist, w_f) can be expressed as,

$$2w_f = \frac{4\lambda}{\pi \mathrm{NA}}\,, \tag{2.28}$$

where λ is the wavelength of the light being focused. The focal spot size is constrained by diffraction and requires a high NA to achieve effective focusing. For our system and a wavelength of 300 µm (i.e., $f = 1$ THz), the beam diameter at the STM focus is ~ 1 mm.

The second advantage to using parabolic mirrors as focusing optics is avoiding dispersion. It is important to note that reflective optics (mirrors), as opposed to transmissive optics (lenses), do not introduce the same material-related effects to the light pulse being focused, e.g., attenuation, spectral losses, dispersion and chromatic aberration. By limiting the dispersion introduced by the optical components of our setup, the laser pulse duration remains as short as possible and the time resolution is maintained. Using materials with significant frequency dependence impedes experiments by limiting the parameter space that we can explore. The choice of broad-spectrum reflective parabolic mirrors allows us to utilize laser light from the low UV range ($\sim$300 nm) all the way to the terahertz regime ($\sim$300 µm). The diffraction limit as well as the effects of dispersion will be discussed in the following chapter, where the optical setups of this thesis and its experiments are introduced.

Chapter 3
Ultrafast Light Probe

There is an ongoing pursuit to develop new tools for materials science and fundamental research. Electronic transport measurements at microwave frequencies [114] and optical spectroscopy with NIR and visible light have been prominent historical methods for materials characterization [115]. Typically, transport measurements are performed via patterned contacts, but these can limit device design and distort the measured properties, e.g., due to contact morphology [116] and Schottky barriers [117]. Electronic circuits and sources further limit these measurements to microwave frequencies and nanosecond timescales. The development of THz time-domain spectroscopy, with far-infrared light (0.1 to 10 THz), provided a non-contact method for measuring a material's frequency-dependent complex refractive index, permittivity and conductivity with ultrafast time resolution [118]. These measurements access intrinsic electronic properties, such as carrier mobility and scattering rate [33]. Modern THz sources generate broadband pulses with duration ranging from picoseconds to tens of femtoseconds [55, 119–121]. Combining an optical pump with THz spectroscopy measurements in a pump-probe scheme provides access to excited state behavior, e.g., photoinduced carrier [122, 123] and quasiparticle dynamics [124, 125]. Measurements of the THz electric field transient, enabled by electro-optic sampling [39], grant sub-picosecond time resolution. With photon energy of $0.4-40\,\mathrm{meV}$, THz frequency light bridges the gap between electronic and optical measurements without significant disturbance to the system. THz spectroscopy, having the combined capability to investigate materials in steady-state and non-equilibrium conditions, has now grown into a key tool for materials science and ultrafast research [126].

In the early 20^{th} century, it was shown that the physical properties of bulk crystals could be defined by the periodic potential that comes from the organization of the atomic lattice, providing a way to classify insulators, semiconductors, and metals based on the distribution of electronic states [127]. For the non-equilibrium state formed when a semiconductor absorbs

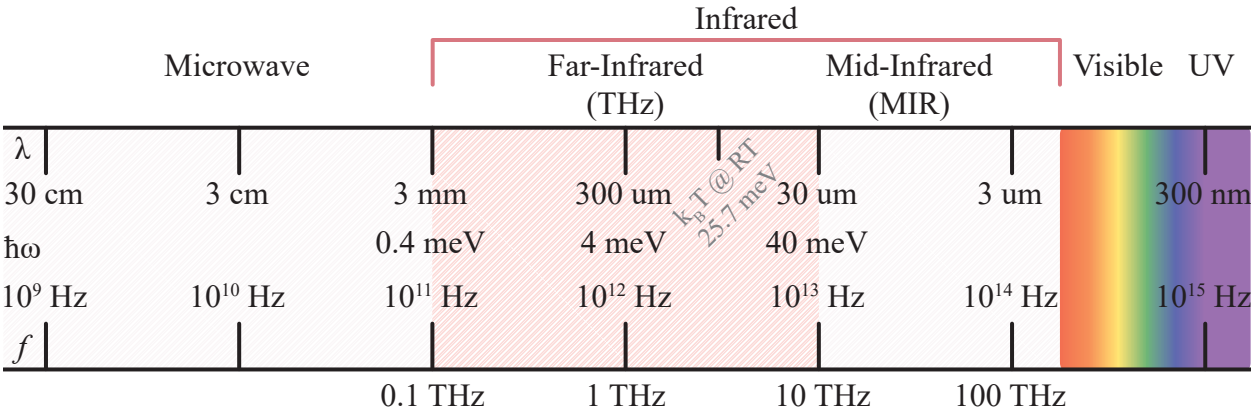

Figure 3.1: Electromagnetic spectrum spanning microwave to visible frequencies. The far-infrared (0.1 - 10 THz) frequency range has become a powerful tool for ultrafast materials science. With photon energies on the order of k_BT at room temperature or below, THz light is non-ionizing and suitable for investigating low-energy and collective excitations in the range of a few meV to several tens meV.

photons with energy above the band gap, the strength of electron-electron and electron-phonon interactions begins to dictate the properties of the system [128]. For example, photoexcited free carriers (i.e., electrons and holes) in GaAs experience strong interactions with longitudinal-optical phonons as they cool to the band edge [129]. The effect is observed in THz spectroscopy on the 1 to 3 ps timescale, while the lifetime of free carriers at the band edge can also be seen and is on the order of 100 ps [130]. Even faster dynamics have also been measured through the THz photoconductivity, such as the sub-picosecond photoinduced phase transition of VO_2 [131, 132]. These measurements have been enabled by EO detection of phase-stable THz (0.1−10 THz) and multi-THz (10−60 THz) probe pulses [34, 133]. By directly detecting the oscillating electric field of the probe pulses in the time domain − analogous to an oscilloscope with THz bandwidth − EO detection achieves time resolution faster than an oscillation cycle of the probe light, allowing for the separation of competing atomic and electronic degrees of freedom.

In modern optoelectronic materials, quasiparticles called excitons are formed when carrier screening is low and binding between electrons and holes is larger than k_BT. Exciton absorption resonances at visible wavelengths are of particular interest for use in next-generation photovoltaic devices [134, 135]. Excitons in two-dimensional semiconductors have gained particular attention because reduced screening out of the material plane leads to strongly bound excitons that are stable at room temperature [136, 137]. The excitons in these systems can

be measured by THz spectroscopy through intra-excitonic transitions [138]. They have been found to form on sub-picosecond timescales and have lifetimes on the order of 100 ps [72].

In this thesis, we investigate GNRs, which are also atomically thin. Additionally, whereas graphene is a semimetal with a Dirac cone dispersion relation, confinement in the lateral direction opens a band gap that is comparable to two-dimensional semiconductors like the transition metal dichalcogenides. We therefore expect dynamics on similar timescales, i.e., the 100 fs − 100 ps range accessible by THz pulses, provided the GNRs are sufficiently isolated from the substrate. Indeed, optical-pump/THz-probe spectroscopy of GNR ensembles in solution reveals picosecond-scale THz photoconductivity dynamics [4, 139], which we aim to resolve on the atomic scale. Thus, for our experiments, we employ single-cycle phase-stable THz light pulses with duration on the order of 1 ps in order to access the intrinsic timescales of electron dynamics in these materials.

3.1 Terahertz Pulse Generation

Early reports of sub-mm-wavelength electromagnetic waves date back to the use of fast arc currents as early as 1920 [140, 141]. However, this method of fast electrical current generation was supplanted by acceleration of photoexcited free carriers generated in photoconductive materials. The photoconductive switch (PC) became the basis for generating free-space-propagating THz light pulses [52, 142]. In THz generation by a PC, femtosecond optical pulses excite a semiconductor substrate, which is subject to an external electric field. It produces THz radiation according to the relationship,

$$\mathbf{E}_{\mathrm{THz}}(z,t) = -\frac{\mu_0 A}{4\pi z}\frac{d\mathbf{J}(t)}{dt}\,, \tag{3.1}$$

where $\mathbf{E}_{\mathrm{THz}}$ is the emitted THz electric field, A is the excited area, $\mathbf{J}$ is the current density produced by photoexcitation, and z is the far-field distance where the emission is detected ($z \gg \lambda$) [143]. The relationship suggests shorter excitation pulses produce higher THz peak fields. However, scattering into satellite valleys of the band structure limits carrier mobility for broadband THz generation when using very short optical excitation pulses [130]. The field strengths generated with this technique is also limited by the mobility of the carriers generated during photoexcitation [144], leading to maximum peak fields on the order of 1 kV/cm when subject to mJ/cm^2 fluences [145].

Ultimately, the experimental goals of this thesis dictate the choice of generation method

used. Although PC switches have been employed for THz-STM [5, 8], the work presented in this thesis requires high peak THz electric fields ($E_{\mathrm{THz,pk}}$) at the source due to the optical losses anticipated for our envisioned new modalities. Additionally, operating at higher repetition rate than past THz-STM setups will enable an improved signal-to-noise ratio. Modern solid-state laser systems offer high average powers and operate at MHz repetition rates [146]. The system used in our experiments is a CARBIDE laser produced by Light Conversion. The laser system is based on an ytterbium-doped KGW crystal (Yb^{3+}:$KGd(WO_4)_2$), with a central emission wavelength of $\lambda = 1030\,\mathrm{nm}$ and a pulse duration, $\tau_p = 232\,\mathrm{fs}$. The Yb-doped crystal family, commonly found in the form Yb:YAG and Yb:KGW, offers high thermal stability and emission cross-section [147], allowing our system to achieve an average power of 40 W with 40 µJ pulse energy at a repetition rate, $f_{\mathrm{rep}} = 1$ MHz. The laser system drives optical rectification in $LiNbO_3$, an all-optical generation method that exploits the electro-optic properties of a non-centrosymmetric medium [148, 149]. THz generation via optical rectification follows from the nonlinear polarization induced by the ultrafast optical pulse. The remainder of this section will discuss the generation of single-cycle phase-stable THz electric field transients via optical rectification in $LiNbO_3$.

3.1.1 Optical Rectification in Lithium Niobate

Optical rectification (OR) is a nonlinear optical effect occurring in non-centrosymmetric media. Bound electrons in a non-centrosymmetric crystal can be treated as harmonic oscillators subject to an anharmonic potential,

$$U^{\mathrm{anh}}(x) = \frac{1}{2}m\omega_0 x^2 + \frac{1}{3}max^3\,, \tag{3.2}$$

where m is the electron mass, ω_0 is the oscillator's resonant angular frequency, and a is strength of anharmonicity. The anharmonic term in $U^{\mathrm{anh}}(x)$ is a consequence of a nonlinear contribution in the restoring force,

$$F = -\frac{dU^{\mathrm{anh}}(x)}{dx} = -m\omega_0^2 x - max^2\,. \tag{3.3}$$

If we introduce a monochromatic electric field,

$$E(t) = E_0\exp(-i\omega t)\,, \tag{3.4}$$

of angular frequency ω, a Lorentzian model for electron displacement, $x(t)$, is formed,

$$\ddot{x}(t) + 2\gamma\dot{x}(t) + \omega_0^2 x(t) + ax^2 = -\frac{e}{m}E(t) \tag{3.5}$$

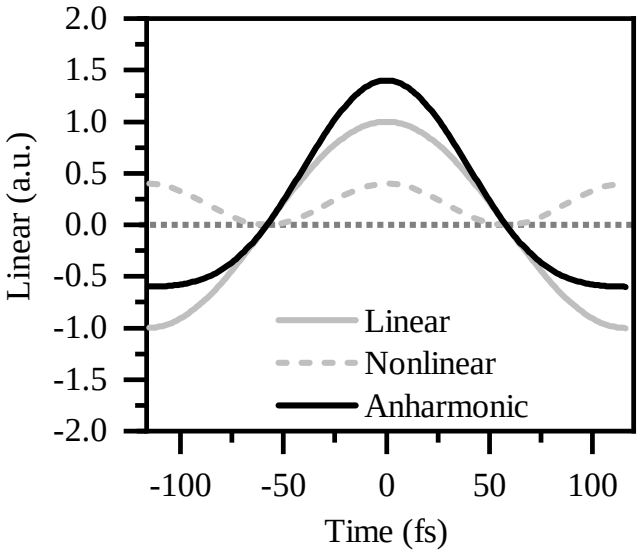

Figure 3.2: One period of an anharmonic oscillation demonstrating the preferential motion in one direction. The anharmonic curve (solid black line) is the sum of linear curve (solid grey line) and the nonlinear curve (dashed grey line).

with $-2\gamma\dot{x}(t)$ representing a damping force.

For weak anharmonicity, $ax^2 \ll \omega_0^2 x$, the solutions for $x(t)$ can be separated into a superposition of harmonic displacements,

$$x(t) = x_{\mathrm{L}}(t) + x_{\mathrm{NL}}(t)\,, \tag{3.6}$$

where $x_{\mathrm{L}}(t)$ is the linear solution and $x_{\mathrm{NL}}(t)$ is the nonlinear solution. A schematic of the electron motion is depicted in Figure 3.2. In a non-centrosymmetric crystal, characterized by $U(x) \neq U(-x)$, electronic motion develops additional harmonic modes when driven by $E(t)$. With $ax^2 \ll \omega_0^2 x$, $x_{\mathrm{NL}}(t)$ can be treated as a perturbation, of magnitude λ, and expanded in a power series,

$$x_{\mathrm{NL}} = \sum_{n=1}^{\infty} \lambda^n x_{\mathrm{NL}}^{(n)}\,. \tag{3.7}$$

After we insert a displacement into Equation 3.5 with the form defined by Equation 3.6 and Equation 3.7 and separate terms by their order in λ, a set of coupled equations is obtained,

$$\begin{aligned}
\ddot{x}^{(1)}(t) + 2\gamma\dot{x}^{(1)}(t) + \omega_0^2 x^{(1)}(t) &= -\frac{e}{m}E(t) \\
\ddot{x}^{(2)}(t) + 2\gamma\dot{x}^{(2)}(t) + \omega_0^2 x^{(2)}(t) &= -a[x^{(1)}]^2 \\
\ddot{x}^{(3)}(t) + 2\gamma\dot{x}^{(3)}(t) + \omega_0^2 x^{(3)}(t) &= -2ax^{(1)}x^{(2)} \quad \text{etc.}
\end{aligned} \tag{3.8}$$

The first expression is the linear variant of Equation 3.5 with a steady-state solution, where $x^{(1)}(t)$ oscillates with amplitude,

$$x^{(1)}(\omega) = \frac{e}{m}\frac{E_0 e^{-i\omega t}}{\omega_0^2 - \omega^2 - i\omega\gamma}\,. \tag{3.9}$$

This term manifests in the material when we look at a single electric dipole, expressed as,

$$p(t) = ex(t)\,, \tag{3.10}$$

such that a volumetric collection of electrons within the system produces a polarization,

$$P(t) = \frac{Ne^2}{m}\frac{E_0 e^{-i\omega t}}{\omega_0^2 - \omega^2 - i\omega\gamma}\,. \tag{3.11}$$

Here, N is the number of electrons per unit volume and may be expressed in a simplified form,

$$P(t) = \epsilon_0 \chi_e^{(1)}(\omega) E_0 e^{-i\omega t}\,, \tag{3.12}$$

where ϵ_0 is the vacuum permittivity and

$$\chi_e^{(1)}(\omega) = \frac{Ne^2}{m}\frac{1}{\omega_0^2 - \omega^2 - i\omega\gamma} \tag{3.13}$$

is the linear electric susceptibility. The polarization can be inserted into the macroscopic electric-displacement-field equation,

$$D(t) = \epsilon_0 E(t) + P(t) = \epsilon_0(1 + \chi_e^{(1)})E(t)\,, \tag{3.14}$$

resulting in the linear dielectric constant, $(1 + \chi_e^{(1)})$, and the dielectric permittivity,

$$\epsilon(\omega) = \epsilon_0(1 + \chi_e^{(1)})\,. \tag{3.15}$$

Now that we have formulated the response for a monochromatic wave we extend our picture to the interaction of two frequency components of a light pulse, ω_1 and ω_2, producing a combined electric field,

$$E(t) = E_1 \exp(-i\omega_1 t) + E_2 \exp(-i\omega_2 t) + c.c.\,, \tag{3.16}$$

where *c.c.* denotes the complex conjugate. Inserting Equation 3.16 into Equations 3.8 reveals a second order response, $x^{(2)}(\omega) \propto [x^{(1)}(\omega)]^2 \propto |E(t)|^2$. The square of the electric field can

be expanded to show it contains terms corresponding to second harmonic generation (SHG), difference frequency generation (DFG), and sum frequency generation (SFG), i.e.,

$$\begin{aligned}\frac{1}{2}|E(t)|^2 = & E_1^2 + E_2^2 \\ & + E_1^2\cos(2\omega_1 t) + E_2^2\cos(2\omega_2 t) \\ & + 2E_1E_2\cos([\omega_1+\omega_2]t) + 2E_1E_2\cos([\omega_2-\omega_1]t)\,.\end{aligned} \tag{3.17}$$

SHG is provided by terms containing $\cos(2\omega t)$, DFG by $\cos([\omega_2-\omega_1]t)$, and SFG by $\cos([\omega_2+\omega_1]t)$. OR is a special case of DFG where $\omega_1 = \omega_2$. Interestingly, for intrapulse OR, frequency mixing necessarily cancels any carrier-envelope-phase offset, ϕ_0, carried by the optical pulse. In general, the cosine arguments in Equation 3.17 carry the full angular dependence of the wave in the form, $\omega t+\phi_0$. In conventional optical or NIR pulsed fs laser, ϕ_0 results in a shot-to-shot change in the carrier envelope phase, ϕ_{CEP}, which specifices the shape of the electric field within the constant pulse envelope. Conversly, the difference calculation removes ϕ_0 leading to a phase-stable THz pulse after generation.

The expression for the second-order nonlinear polarization induced by OR is

$$P_i^{(2)}(0) = 2\epsilon_0 \sum_{j,k} \chi_{ijk}^{(2)}(0,\omega_1,-\omega_1)E_j(\omega_1)E_k^*(\omega_1)\,, \tag{3.18}$$

where the indices i,j,k represent Cartesian components of the susceptibility tensor $\chi_{ijk}^{(2)}$ and the complex field, $E_k^*(\omega_1)$, arises because the polarization is a real observable, as are the fields, and so $E_k(-\omega_1) = E_k^*(\omega_1)$.

The macroscopic electric-displacement-field from Equation 3.14 can be extended to nonlinear media by incorporating the second-order polarization in Equation 3.18. We can then examine the one-dimensional wave equation in a nonlinear medium where, the linear and nonlinear components of D are incorporated as the THz electric field and the second-order polarization,

$$\begin{aligned}\frac{\partial^2 E_{\mathrm{THz}}(z,t)}{\partial z^2} - \frac{n_{\mathrm{THz}}^2}{c^2}\frac{\partial^2 E_{\mathrm{THz}}(z,t)}{\partial t^2} = & \frac{1}{\epsilon_0 c^2}\frac{\partial^2 P_{\mathrm{THz}}^{(2)}(z,t)}{\partial t^2} \\ = & \frac{\chi_e^{(2)}}{c^2}\frac{\partial^2 |E(z,t)|^2}{\partial t^2}\,,\end{aligned} \tag{3.19}$$

where c is the speed of light, n_{THz} is the complex index of refraction at THz frequencies, and $E(z,t)$ is the optical electric field introduced in Equation 3.4. From Equation 3.19 we see that the nonlinear polarization, induced by the optical field $E(z,t)$, becomes a source for the THz wave generated in a non-centrosymmetric medium.

Crystal	$\chi_e^{(2)}$(pm/V)	bandgap (eV)
ZnTe	68.5 [150]	2.26 [151]
$LiNbO_3$	168 [150]	3.8 [152]
GaP	24.8 [153]	2.25 [154]

Table 3.1: Optical properties of common nonlinear crystals.

Optical rectification, like all nonlinear optical processes, is inefficient due to the small nonlinear dielectric coefficients of materials. $LiNbO_3$ is the crystal of choice for high-field THz generation through OR because it has a relatively large $\chi_e^{(2)}$ and bandgap [37]. Table 3.1 lists the second order susceptibility and optical bandgap of common crystals used in THz generation. The nonlinear coefficient in $LiNbO_3$ is an order of magnitude larger than other common materials for THz generation and has a larger bandgap, which prevents saturation at higher fluence due to multi-photon absorption. This leads to significantly higher field strengths over GaP and ZnTe [152].

In our system, we utilize NIR pulses centered at 1030 nm with a pulse duration $\tau_p =$ 232 fs. According to the time-bandwidth product, assuming a Gaussian NIR pulse, $0.44 = \tau\Delta\nu$, where $\delta\nu$ is the NIR pulse bandwidth. Therefore, our estimated THz bandwidth from OR spans from 0 THz to $\Delta\nu_{\mathrm{THz}} = \frac{0.44}{0.232\mathrm{ps}} = 1.9\,\mathrm{THz}$. In practice, the maximum allowable frequency is determined by the frequencies of phonon resonances in the generation medium. $\epsilon(\omega)$ becomes imaginary when ω approaches the frequency of the transverse optical (TO) phonon, ω_{TO}, maximizing the attenuation coefficient,

$$\alpha(\omega) = \frac{\omega}{c}\mathrm{Im}\sqrt{\epsilon(\omega)}\,. \tag{3.20}$$

As a result, THz radiation with frequency near ω_{TO} is strongly absorbed for propagation distances $L > \frac{1}{\alpha}$. In stoichiometric $LiNbO_3$ crystals ($\sim$1:1 ratio Li:Nb), the first TO phonon frequency occurs near 5.3 THz [155]. In the crystal used in our THz generation setup, $LiNbO_3$, the phonon frequency is increased to 7.44 THz [156] by doping with 1.3 mol% magnesium [157].

Additionally, if the THz waves propagate slower than the optical pulse envelope ($n_{\mathrm{THz}} > n_{\mathrm{O}}$) a walk-off of length,

$$l_w = \frac{c\tau_p}{n_{\mathrm{THz}} - n_{\mathrm{O}}}\,, \tag{3.21}$$

will develop. Generation of a secondary THz wave after a distance l_w will lead to destructive interference, while continuous generation through the crystal will result in complete

destructive interference after a distance $l_w \ll l$.

Extending our picture from one dimension to two (or three) dimensions, the interference develops through THz wave generation at all points along the pulse front, i.e., across the spatial extent of the optical pulse. Individual circular waves develop at each point in space to form a unified wavefront − a process known as the Huygen's principle (Figure 3.3(a)). As the optical pulse moves ahead of the THz wavefront, the next THz wavefront is generated before the pre-existing THz wavefront has reached the same position, resulting in destructive interference.

This interference effect can be understood in terms of phase-matching conditions. Consider a plane wave,

$$E_n(z,t) = A_n(z,t)\exp(i(k_n z - \omega_n t)) + c.c.\,, \tag{3.22}$$

where k_n is the amplitude of the wavevector at a frequency ω_n. Referring to Equation 3.19 and considering a pair of frequencies ω_1 and ω_2 that generate $\omega_{\mathrm{THz}} = \omega_2$ - ω_1 without depleting ω_2, we have the following conditions,

$$\begin{aligned} \frac{dA_2}{dz} &= 0 \\ \frac{dA_1}{dz} &= \frac{2i\omega_1\chi_e^{(2)}}{k_1 c^2} A_2 A_{\mathrm{THz}}^* e^{i\Delta k z} \\ \frac{dA_{\mathrm{THz}}}{dz} &= \frac{2i\omega_{\mathrm{THz}}\chi_e^{(2)}}{k_{\mathrm{THz}} c^2} A_2 A_1^* e^{i\Delta k z}\,, \end{aligned} \tag{3.23}$$

where A_1 and A_{THz} are complex and A_2 is constant. Unless the phase-matching condition,

$$\Delta k = k_2 - k_1 - k_{\mathrm{THz}} = 0\,, \tag{3.24}$$

is met, the wave amplitudes A_1 and A_{THz} will be oscillatory and unable to increase, averaging out to zero over long distances. The wavevectors associated with the phase-matching condition are tied to quantum mechanical momentum conservation,

$$\hbar k_{\mathrm{THz}} = \hbar k_2 - \hbar k_1\,, \tag{3.25}$$

that is, in turn, connected to the interaction between the oscillating light and the crystal. The propagation of light through matter is governed by the dispersion relation,

$$k_i = \frac{\omega_i}{c} n(\omega_i)\,, \tag{3.26}$$

where $n(\omega_i)$ is the complex index of refraction. Momentum conservation can then be described as,

$$\omega_{\mathrm{THz}} n(\omega_{\mathrm{THz}}) = \omega_2 n(\omega_2) - \omega_1 n(\omega_1)\,, \tag{3.27}$$

where the right-hand-side can be written in terms of the central frequency of the optical pulse, ω_{O},

$$\omega_2 n(\omega_2) - \omega_1 n(\omega_1) = \left[\frac{\partial k(\omega)}{\partial \omega}\right]_{\omega_{\mathrm{O}}}. \tag{3.28}$$

Therefore,

$$\frac{k_{\mathrm{THz}}}{\omega_{\mathrm{THz}}} = \left[\frac{\partial k(\omega)}{\partial \omega}\right]_{\omega_{\mathrm{O}}}, \tag{3.29}$$

where the ratio, $\frac{k_{\mathrm{THz}}}{\omega_{\mathrm{THz}}}$, defines the phase velocity of the generated THz wave and the expression, $\left[\frac{\partial k(\omega)}{\partial \omega}\right]_{\omega_{\mathrm{O}}}$, defines the group velocity for a pulse with center frequency ω_{O}. Thus, the phase-matching condition has lead to the velocity relationship needed to ensure optimized THz generation,

$$v_{\mathrm{ph}}^{\mathrm{THz}} = v_{\mathrm{gr}}^{\mathrm{O}}\,, \tag{3.30}$$

where the THz waves add constructively throughout the crystal. This can also be written in terms of the index of refraction,

$$n_{\mathrm{ph}}^{\mathrm{THz}} = n_{\mathrm{gr}}^{\mathrm{O}}\,. \tag{3.31}$$

For ZnTe, this condition is met for NIR pulses centered at 812 nm and a generation frequency of 1.7 THz [143]. As femtosecond 800 nm pulses are readily available through Ti:Sapphire lasers, ZnTe has been one of the key materials for THz science for almost thirty years. Conversely, for $LiNbO_3$, which has a higher $\chi^{(2)}$, $n_{\mathrm{ph}}^{\mathrm{THz}} = 5.16$ and $n_{\mathrm{gr}}^{\mathrm{O}} = 2.23$ [53] at 1 THz and 800 nm respectively. The following section will discuss how to account for the velocity mismatch and engineer constructive interference for optimized THz pulse generation.

3.1.2 Phase-Stable Single-Cycle THz Pulses

The last section described the importance of phase matching during nonlinear optical generation of THz waves in a non-centrosymmetric medium. For THz frequencies with $n_{\mathrm{ph}}^{\mathrm{THz}} > n_{\mathrm{gr}}^{\mathrm{O}}$, the wavefront generated by OR moves slower than the nonlinear polarization induced by the intensity envelope of the optical pulse. This phenomenon was observed in lithium tantalate as EO shockwaves [148, 149] before being imaged in $LiNbO_3$ [158–160]. As

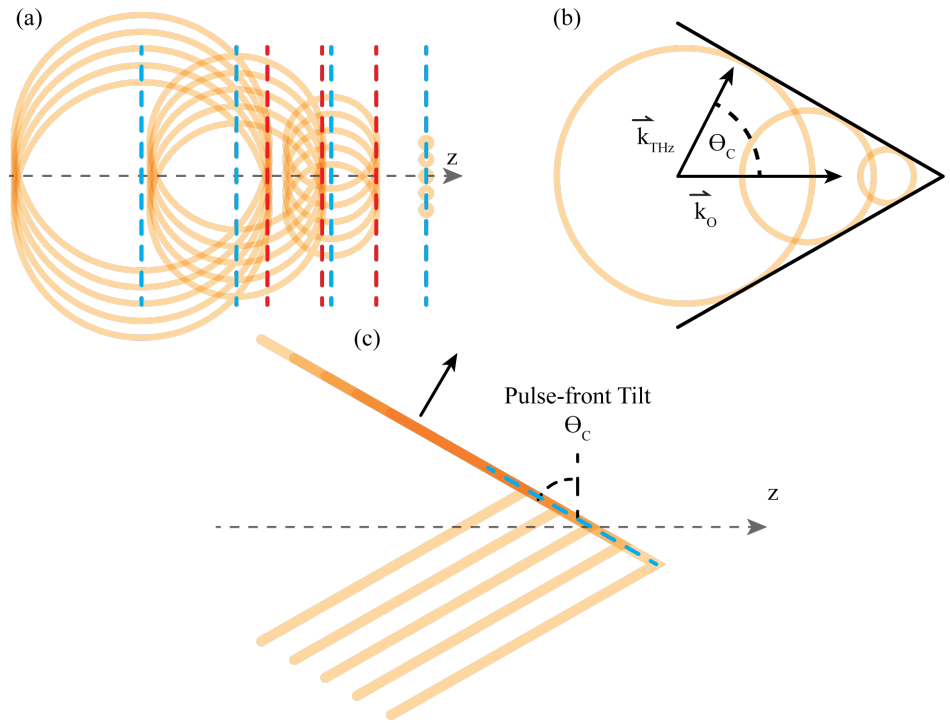

Figure 3.3: An illustration of the Cherenkov cone produced in $LiNbO_3$. (a) An optical pulse with a pulse front perpendicular to the z axis (blue), propagating with wavevector, $\mathbf{k}_O$, generates Huygen's THz wavelets uniformly across the front (orange). Lack of phase matching with the the pulse front prevents the wavelets from different pulse front locations from constructively interfering. (b) Wavelets produced along the optical axis define a THz wavefront at the Cherenkov angle, θ_C. (c) Tilting the optical pulse front at $\theta_C = 64^o$ allows THz wavelets to constructively interfere along $\mathbf{k}_{\mathrm{THz}}$, thereby increasing in amplitude to form a strong THz wave propagating along $\mathbf{k}_{\mathrm{THz}}$ (dark orange).

a result of the differences in their velocity, the THz wave and optical pulse front develops an angular separation,

$$\begin{aligned}\theta_C &= \cos^{-1}\left(\frac{v_{\mathrm{ph}}^{\mathrm{THz}}}{v_{\mathrm{gr}}^{\mathrm{O}}}\right) = \cos^{-1}\left(\frac{n_{\mathrm{gr}}^{\mathrm{O}}}{n_{\mathrm{ph}}^{\mathrm{THz}}}\right) \\ &= \cos^{-1}\left(\frac{2.23}{5.16}\right) = 64.4^o\,.\end{aligned} \tag{3.32}$$

This leads to a THz wavefront propagating with wave vector, $\mathbf{k}_{\mathrm{THz}}$, at an angle θ_C from the optical wave vector (Figure 3.3(b)). θ_C is known as the Cherenkov angle, and is observed in a number of physical situations where an object moves faster than the speed of light in a medium. A tilted optical intensity front allows the individual THz waves to constructively interfere and generate THz efficiently with a pulse front along $\mathbf{k}_{\mathrm{THz}}$ (Figure 3.3(c)) [53].

For our setup, we use a modification to the tilted-pulse-front technique developed in

reference [53], refined based on the 4f geometry in reference [55], and adapted for THz-STM in references [7, 13, 15]. The schematic in Figure 3.4 shows a horizontally polarized (in-plane) NIR pulse (red) incident on a pair of cylindrical lenses (C_1 and C_2) that give the beam shape a vertical ellipticity with a vertical magnification ratio of 150/70 = 2.14. The grating (Thorlabs GR50-0310, 300 lines/mm) has an expected damage threshold of 40 W/cm^2. To minimize damage, our beam is further expanded by a pair of spherical lenses (S_a and S_b) with a magnification ratio of 60/50 = 1.2. For a 3 mm beam diameter, the area of the beam profile is increased from 7.06 mm^2 to 21.2 mm^2, reducing the power density on the grating from 255 W/cm^2 to 85 W/cm^2. We also use an optical chopper at the cylindrical lens focus, reducing the average power incident on the grating to 42.5 W/cm^2. Selection of the grating parameters and 4f telescope design follows from reference [55] and [156]. The magnification ratio of the telescope lenses can be related to (1) the pulse front tilt and (2) the imaging of the grating into the crystal, i.e., the color focus, where there is no spatial chirp. The optimized configuration is obtained when these two magnification ratios, β_1 and β_2, are equal. The first condition leads to,

$$\beta_1(\theta_d, p) = \frac{p\lambda}{n_{\text{gr}}^{\text{NIR}}\cos(\theta_d)\tan(\gamma_C)}\,, \tag{3.33}$$

where θ_d is the diffraction angle of the NIR beam off the grating, p is the groove density in lines/mm, λ is the center wavelength of the NIR pulse, $n_{\text{gr}}^{\text{NIR}}$ is the NIR index of refraction used in Equation 3.32, and γ_C is the final (desired) pulse tilt. The second condition gives,

$$\beta_2(\theta_d) = \frac{\tan(\gamma_C)}{n_{\text{ph}}^{\text{NIR}}\tan(\theta_d)}\,, \tag{3.34}$$

where $n_{\text{ph}}^{\text{NIR}}$ is the index of refraction at NIR frequencies and comes into play at the air-crystal interface due to refraction. Plotting β_1 and β_2 simultaneously allows us to identify a crossing point for each choice of p at different diffraction angles [156]. For a groove density of 300 lines/mm and λ = 1030 nm, the magnification factor β is found to be 0.26 for a diffraction angle of 74.3 degrees, with an incident angle of θ_i = -40.8 degrees. This is close to the magnification factor we use in our setup of 0.25 (50 mm / 200 mm). Following the schematic in Figure 3.4, a stage is used to align the NIR laser onto the grating at angle θ_i = -41 deg without changing the NIR position on the grating. The grating is aligned such that the m = -1 diffraction order is output parallel to the breadboard mounting array at θ_d = 74 degrees. Diffraction of the beam causes the colors in the beam to diverge from each

other while remaining collimated. The diverging color rays are then collimated by the first spherical lens, S_1, at the Fourier plane 400 mm from the grating. At the Fourier plane the colors are spatially separated, but each monochromatic beam is focused.

The beam profile is illustrated in Figure 3.4. The broadband pulse before the grating is shown as a single color. After diffraction it splits into separate ellipses. The rays correspond to individual colors, which diverge upon diffraction, then propagate parallel to one another but spaced apart after S_1. Meanwhile, the beam at a particular wavelength is collimated when it reaches S_1 and then focuses at its focal length away, such that a Fourier plane is created with separated but individually focused colors. Additionally, a half-wave plate ($\lambda/2$) rotates the polarization from horizontal to vertical before the crystal to match its electro-optic axis. The positions of the colors are indicated next to the beam path. The second spherical lens, S_2, is located 50 mm from the Fourier plane and recombines the colors into a color focus while also collimating the beam for each individual color. The $LiNbO_3$ crystal is oriented perpendicular to the NIR beam, 50 mm from S_1, where the color focus coincides with the correct pulse front tilt. The crystal is cut at 63 deg to match the THz emission angle, thereby minimizing refraction losses.

The THz pulse generated inside the crystal originates from an area the same size as the NIR beam profile. The initial NIR beam diameter is approximately 3 mm. Following the series of lenses used in the 4f setup, and the projection onto the emission plane, the focal spot inside the crystal is expected to have dimensions 0.8 mm x 0.45 mm ($A = 1.13\,\mathrm{mm}^2$). The estimated dimensions of the THz beam spot inside the crystal is on the order of the THz wavelength, thus, divergence is expected from the generation due to Rayleigh diffraction,

$$w(z) = w_0\left[1 + \left(\frac{z\lambda}{\pi w_0^2}\right)^2\right]^{\frac{1}{2}}, \tag{3.35}$$

where $w(z)$ is the beam waist (the width at which the intensity drops from maximum to $1/e^2$ of the maximum) hereafter referred to as the beam radius, λ is the THz wavelength, and w_0 is the beam radius at $z = 0$. We can define the the Rayleigh length as,

$$z_0 = \frac{\pi w_0^2}{\lambda}, \tag{3.36}$$

which is the distance traveled before the beam naturally expands to a radius $\sqrt{2}w_0$. We can calculate the expected beam radius, w, at 4 inches (101.6 mm) from the crystal for both axes of the beam spot. The 0.8 mm axis diverges to 12.15 mm (D = 24.3 mm) while the 0.45

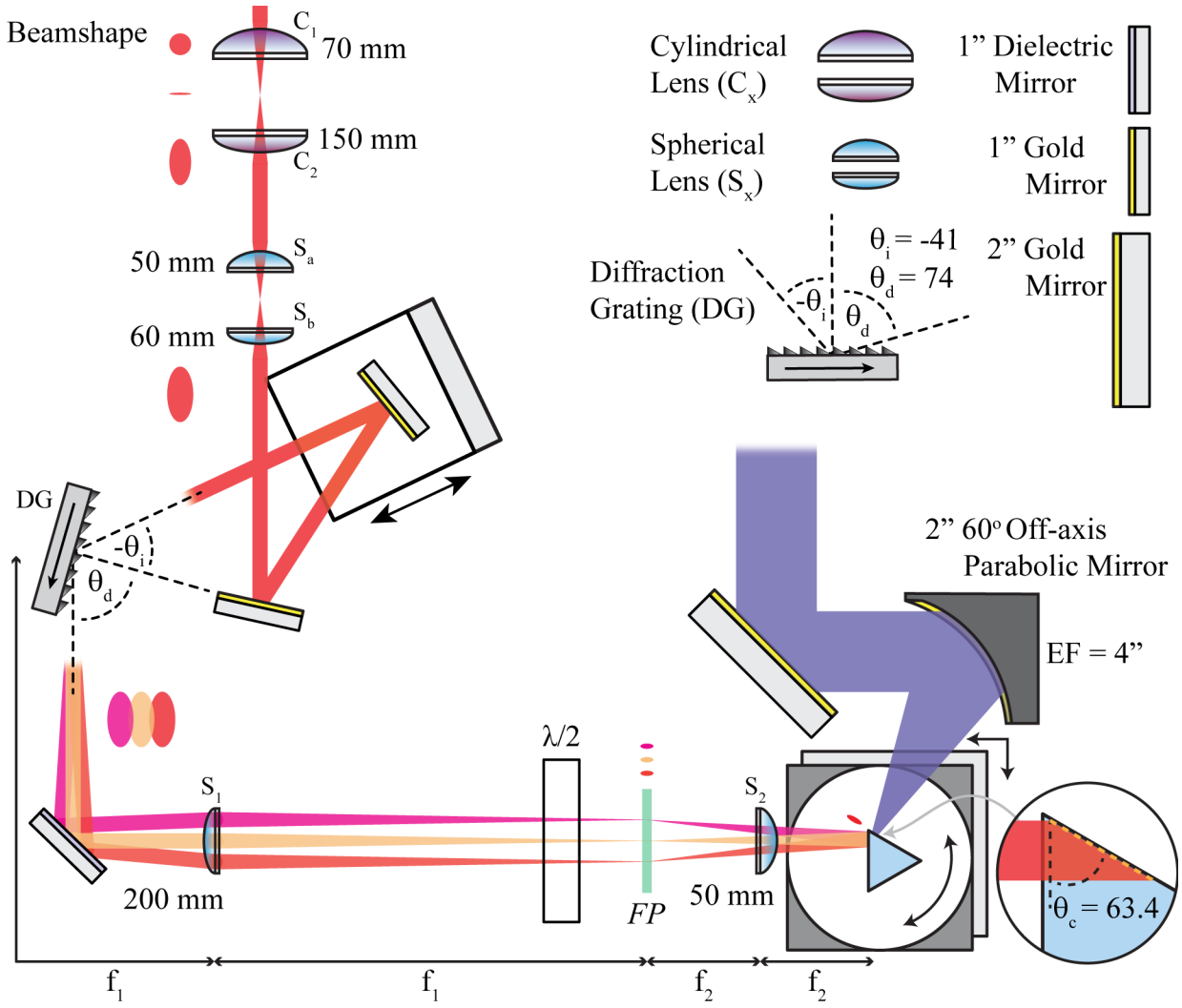

Figure 3.4: A schematic for our 4f tilted-pulse-front setup to generate THz pulses in $LiNbO_3$. The beam shape is indicated by colored ellipses aside the optics along the beam path. A pair of cylindrical lenses (C_1 and C_2) create a vertical ellipticity in our NIR laser beam (red, λ = 1030 nm). The spherical lens pair (S_a and S_b) expand the beam by a factor of 1.2 to decrease the power density on our Thorlabs 300 lines/mm diffraction grating. A stage is used to align the NIR beam into the grating at θ_i = -41 deg. The 'blaze arrow' indicates the direction of the beam diffracted through the m = -1 order at θ_d = 74 deg, leading to diverging colors (multicolored ellipses). The 4f setup is defined by spherical lenses S_1 and S_2 with focal lengths f_1 = 200 mm and f_2 = 50 mm. S_1 collimates the diverging colors and focuses each beam to a spot in the Fourier plane (FP). At the Fourier plane, the colors are focused at different positions. A half waveplate ($\lambda/2$) rotates the polarization to vertical, aligning it with the crystal's electro-optic axis. S_2 recombines the colors at a color focus while simultaneously creating the desired pulse front tilt. Due to the choice of magnification from the 4f telescope and grating density, the NIR pulse front tilt matches the Cherenkov angle, θ_C = 64 deg, inside the $LiNbO_3$ crystal for optimized THz pulse generation.

mm axis expands to 21.6 mm ($D = 43.2$ mm). In practice, we do not observe this degree of ellipticiy in the THz beam profile. Instead, it has a full width at half maximum (FWHM) of approximately 13 mm in the x direction and 15 mm in the y direction. Using 2-inch mirrors allows us to propagate the THz beam with a 1 to 1.5 inch diameter that, using Equation 3.36, has a Rayleigh length on the order of several meters. Ultimately, sufficient Rayleigh length is needed for the extensive optical setup that is used to employ several THz-STM modalities.

After generation, the THz beam propagates through a pair of 2-inch diameter wire-grid polarizers that have an aperture of 34 mm (WGP, Purewave PW010-030-050) for field-strength control. A stationary WGP is fixed and defines the position $\theta_s = 0^o$, where its wires are horizontal. The wires in a WGP are conductive, so THz light aligned parallel to the wires will be absorbed. Therefore, the stationary WGP sets the THz pulse polarization to be vertical for $\theta_s = 0^o$. A second WGP is in a rotation stage and its angle, θ_a, controls the electric field strength through the relation $|E_{\mathrm{THz}}| \propto \cos^2(\theta_a)$. The wires are cross-polarized at $\theta_a = 90^o$, at which point the THz field is minimized.

A pneumatically controlled flip-mirror has two states that can be used to change the number of reflections within the beamline and induce a change of the THz pulse carrier envelope phase (CEP) by π (i.e. it inverts the pulse). The phase change can be explained by examining the interaction between the THz electromagnetic wave and the metallic mirror surface. Assuming a perfect conductor with no transmission, the boundary conditions at the interface forces the amplitude of the reflected wave to be equal and opposite to the incoming wave. Euler's identity then allows us to convert the -1 into a phase of π, i.e., $-1 = \exp(i\pi)$. A 4-inch-diameter 0.5-mm-thick silicon wafer is used as a 50/50 beam-splitter and is the entry point into a Michelson interferometer. The adjustable beamline (Figure 3.5, right) incorporates a pair of 90° off-axis parabolic mirrors with focal lengths of 3 inches; the intermediate focus is used for differential-mode modulation of the THz beam using an optical chopper (Thorlabs MC2000B with MC1F10HP chopper blade). The stationary beamline (Figure 3.5, bottom) incorporates another pneumatic flip mirror and a single 90° off-axis parabolic mirror (focal length of 4 inches). This provides the option to invert only the field of the THz pulse in the stationary arm by utilizing the Gouy phase at the focus, where a 0.5-inch-diameter gold mirror is placed. After recombining at the silicon beam-splitter and propagating out of the interferometer setup, an indium-tin-oxide (ITO)

coated BK7 window is used to direct the THz beam toward our electro-optic detection and STM setups. It serves the additional function that it is transmissive to visible light, so a collinear visible guide beam can be used after the ITO window for alignment.

3.2 THz Pulse Detection

The development of ultrafast lasers created a need for detection methods with time resolution beyond the capabilities of electronics [161]. Conceptually straightforward detection methods include intensity and interferometric autocorrelation measurements that use an interferometer similar the one we have built in our THz setup (Figure 3.5). Interferometric autocorrelation measurements resolve interference fringes resulting from electric field interference that modulates the pulse intensity during a second-order nonlinear process, e.g., second harmonic generation. The technique allows us to estimate a pulse's duration and, with limited accuracy, determine if the pulse is broadened due to dispersion.

For THz power measurements in our lab we use a thermopile detector from Coherent and a large-area pyroelectric detector (Gentec QS9-IL). Conventionally, autocorrelation measurements are uncommon for THz frequencies. Instead, the most common technique for THz pulse detection is EOS in a nonlinear medium containing a second-order nonlinearity [39, 40]. Single-shot EOS detection schemes are now available [162], but challenging. Therefore, the time-domain measurements presented in this thesis are stroboscopic and average over >1000 pulses for each data point, which is the most common approach used for THz spectroscopy. EOS relies on the phase-stability of THz pulses, i.e., their consistent electric field shape in the time domain, which is ensured by intra-pulse DFG in $LiNbO_3$, as will be discussed in the following section.

Interestingly, a critical component to the success of THz spectroscopy in ultrafast science has been the ability to measure the THz electric field transient directly, rather than simply the intensity envelope. EOS of broadband THz pulses allows for the characterization of a material's frequency-dependent complex conductivity, without using the Kramers-Kronig relations, and this can be translated into a description of the dielectric function and index of refraction [163]. Detecting the THz electric field transient also enables subcycle time resolution in pump-probe experiments. The inherent phase stability provided by the techniques used to generate broadband THz pulses is of great benefit to THz science. As we will see

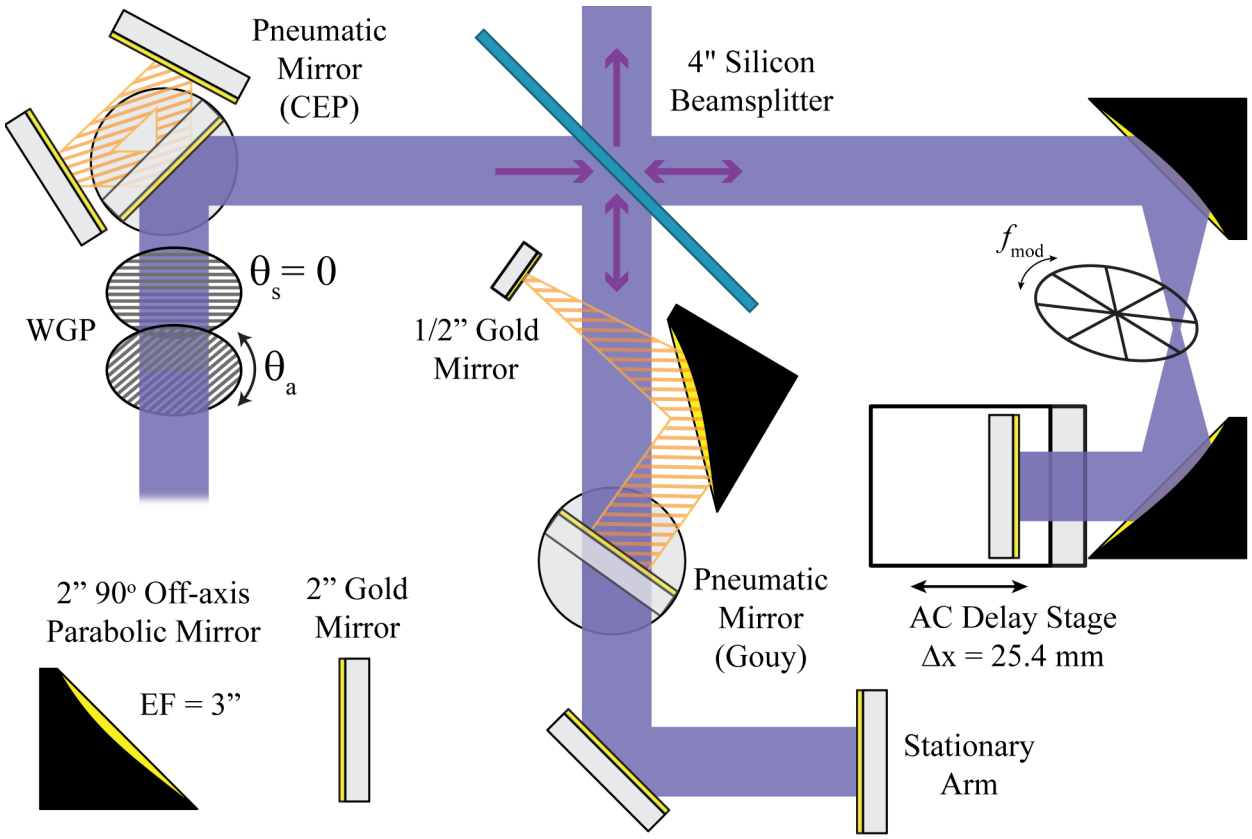

Figure 3.5: THz setup schematic. The THz beam (E_{THz}, purple) enters the setup after generation through a pair of wire-grid polarizers (WGP) containing an array of 10 µm wires spaced at 30 µm. The first WGP controls the THz field strength, $|E_{\mathrm{THz}}| \propto \cos^2(\theta_a)$ with the second WGP held at $\theta_s = 0^o$ to enforce vertical polarization. A pneumatic flip mirror (CEP) changes the number of reflections in the setup by 1 and alters the carrier-envelop-phase (ϕ_{CEP}) by π, controlling the polarity of E_{THz}. A silicon beamsplitter is used to divide the pulse into equal portions and direct them into the two arms of a Michelson-interferometer. The stationary arm has a fixed path length and contains a second pneumatic flip mirror (Gouy) that allows us to change the stationary arm ϕ_{CEP} by π using the reflection off of a 0.5-inch-diameter gold mirror at the focus of a 90^o off-axis parabolic mirror. The adjustable arm contains a delay stage (AC Delay) that controls the path length of the arm and the time-overlap of the two THz pulses. The adjustable arm beam path is equipped with a focus for power measurements or modulation with an optical chopper spinning at frequency f_{mod}.

in the rest of this thesis, phase stability is essential for intrinsically nonlinear processes like lightwave-driven STM.

3.2.1 Electro-Optic Sampling

Continuing the discussion on second-order nonlinear polarization from Equation 3.1.1, crystals that poses a large $\chi_e^{(2)}$ not only allow for OR, but also the Pockels Effect. The second-order nonlinear polarization associated with the Pockels Effect is

$$\begin{aligned} P_i^{(2)} =& 2\sum_{j,k} \epsilon_0 \chi_{ijk}^{(2)}(\omega,\omega,0) E_j(\omega) E_k(0) \\ =& \sum_j \epsilon_0 \chi_{ij}^{(2)}(\omega) E_j(\omega)\,, \end{aligned} \tag{3.37}$$

where the static field, $E_k(0)$, is encoded in a field-induced susceptibility,

$$\chi_{ij}^{(2)} = \chi_{ijk}^{(2)}(\omega,\omega,0) E_k(0)\,. \tag{3.38}$$

This is a similar result to the nonlinear polarization derived for OR. With the static field contributing to the second-order susceptibility, we can say that the Pockels Effect is a field-induced birefringence. Crystals with static birefringence exhibit a polarization-dependent index of refraction, with slow and fast axes that can lead to elliptical polarization. In EOS measurements, the crystal does not have a static birefringence. Instead, the THz field induces a birefringence and measuring this allows the THz field to be determined.

Utilizing a sufficiently short optical pulse, we read out the change to the birefringence of the crystal. The probe pulse must be short enough to treat the THz field as quasi-static. When birefringence is induced, a degree of ellipticity is acquired by the probe pulse that is proportional to the strength of the instantaneous THz electric field. A phase-matched optical pulse will propagate colinearly through the detection setup at a fixed delay-time, τ, accumulating a differential phase retardation,

$$\Delta\phi = \frac{\omega L}{c} n_O^3 r_{41} E_{\mathrm{THz}}\,, \tag{3.39}$$

where r_{41} is the relevant EO tensor coefficient for ZnTe, which is a common material for EOS. Recording the ellipticity imparted onto the probe pulse as a function of τ allows us to trace the transient THz electric field, $E_{\mathrm{THz}}(t)$. Furthermore, we can calculate the strength of the field based on the magnitude of the induced ellipticity,

$$E_{\mathrm{THz}} = \sin^{-1}\left(\frac{A-B}{A+B}\right) \frac{\lambda_O}{2\pi n_{\mathrm{O}}^3 r_{41} T_{\mathrm{ZnTe,THz}} L}\,, \tag{3.40}$$

where A and B are the photodetector responses, $T_{\mathrm{ZnTe,THz}} = 0.48$ is the transmission coefficient of ZnTe at 1 THz, L is the thickness of the crystal used for detection, and $n_{\mathrm{O}} = 2.85$ [164] is the index of refraction for a gate pulse with wavelength $\lambda = 800\,\mathrm{nm}$.

There are several common crystals that exhibit the Pockels Effect, each with distinct phase-matching conditions for NIR and THz frequencies. Notably, ZnTe is phase-matched for frequencies near 800 nm and 1.5 THz. A description of the scheme used to generate < 20 fs NIR probe pulses with central wavelength near 800 nm will be provided in the following section.

In the setup picture shown in Figure 3.6, the THz pulses are focused onto a 100 µm ZnTe(110) detection crystal mounted to another 2-mm-thick ZnTe(100) crystal via a 90° off-axis parabolic mirror. ZnTe is not perfectly phase matched with all the frequencies of a single-cycle THz pulse. Using a thin detection crystal reduces the sampling length during EOS and lowers the impact of walk-off between the pulses. Fresnel reflections at the backside crystal interface lead to a reflection of the THz pulse that is detected at later delay times. For a thin detection crystal, the reflection appears close to the main pulse on the delay-time axis. Mounting the detection crystal to a thicker crystal with the same index of refraction adds a delay time to the reflection. A 2-mm-thick ZnTe crystal is chosen to match the index of refraction of the detection crystal and the (100) crystal orientation has an orthogonal EO axis such that it does not contribute to the EO signal. The index of refraction of ZnTe near 1 THz is ~ 3.2 [143] and would lead to a reflected THz pulse detected 2.13 ps after the main pulse for a 100-µm-thick crystal versus 44.8 ps for a 2.1-mm-thick crystal.

An aperture is drilled through the rear of the mirror surface to allow the probe pulses to propagate colinearly with the THz beam. An important consideration is the spatial overlap between the THz and probe beams. Due to the significant wavelength difference (300 µm vs 800 nm) and the corresponding diffraction limits, we expand the probe beam to match the THz spot size for accurate measurement of the THz electric field strength and waveform. Before focusing, all frequencies within the THz pulse have the same beam radius. Equation 2.28 is proportional to wavelength, indicating that the lower frequencies (longer wavelengths) of the THz pulse will not focus as tightly as the higher frequencies. A typical single-cycle THz pulse generated in $LiNbO_3$ will have a spectrum spanning 0.5 THz to 2 THz, resulting in a factor of four difference in beam radius at the focus. Matching the THz and optical spot size ensures that all frequencies of the broadband single-cycle pulse are sampled.

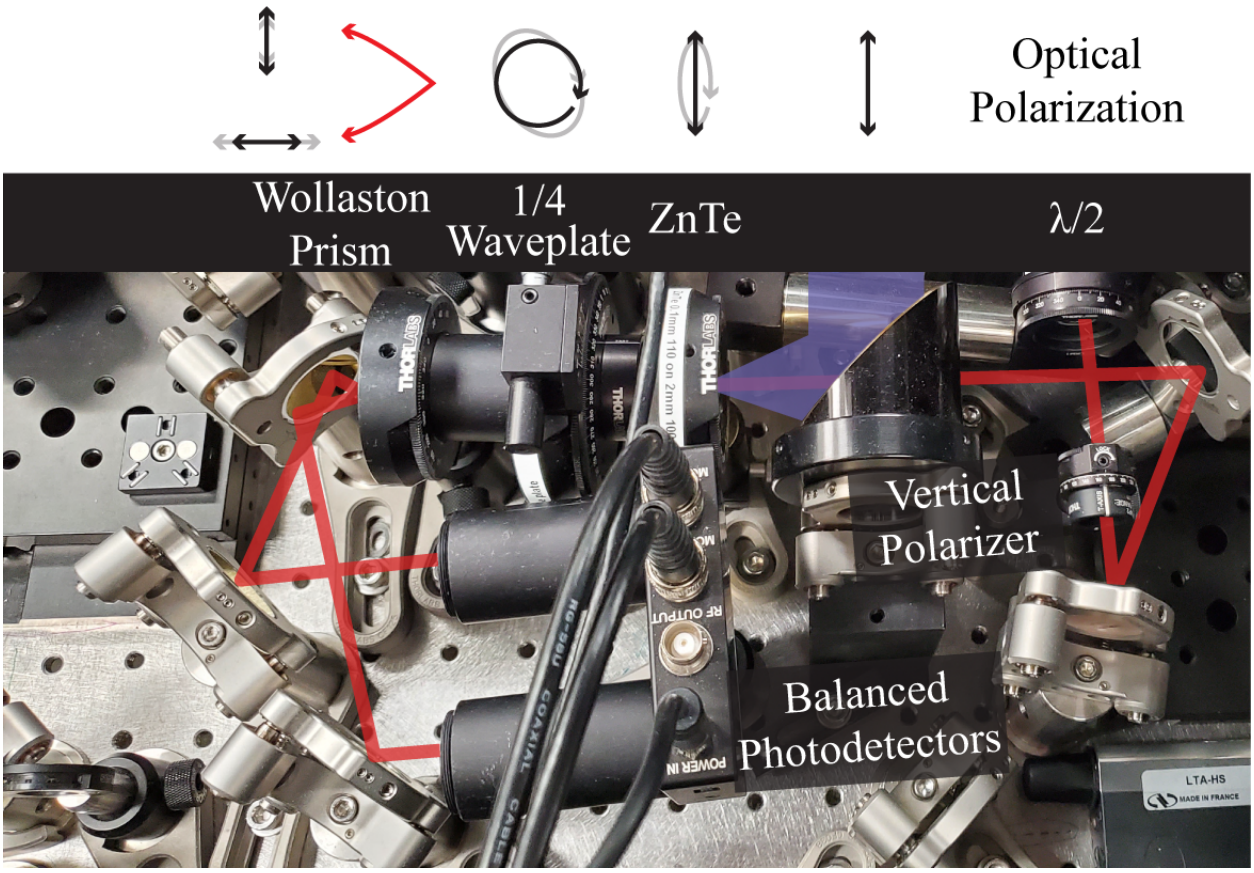

Figure 3.6: Electro-optic sampling setup used to perform time-domain measurements of the THz electric field transient. Optical gate pulses (red beamline, $\lambda = 800$ nm) pass through a waveplate ($\lambda/2$) and vertical polarizer for attenuation and then through an aperture in the back of a 90^o off-axis parabolic mirror. THz pulses (purple beamline) enter along the collimated axis of the parabolic mirror before being focused into a 100 µm ZnTe(110) detection crystal mounted to a 2 mm ZnTe(100) crystal. The gate and THz pulses propagate co-linearly through the ZnTe crystal. The gate pulse ellipticity changes throughout the setup, as illustrated at the top. The ellipticity in the absence of a THz field (black arrows) is initially vertical and is converted to a circular polarization by a $\lambda/4$ waveplate. A Wollaston prism separates the gate pulses into horizontal and vertical polarization components before directing them into a balanced photodetector. In the presence of a THz field, THz-induced birefringence imparts a small ellipticity to the gate pulse, resulting in an imbalance between vertical and horizontal polarization after the $\lambda/4$ waveplate. The gate polarization in the presence of a THz field is illustrated at the top as grey arrows.

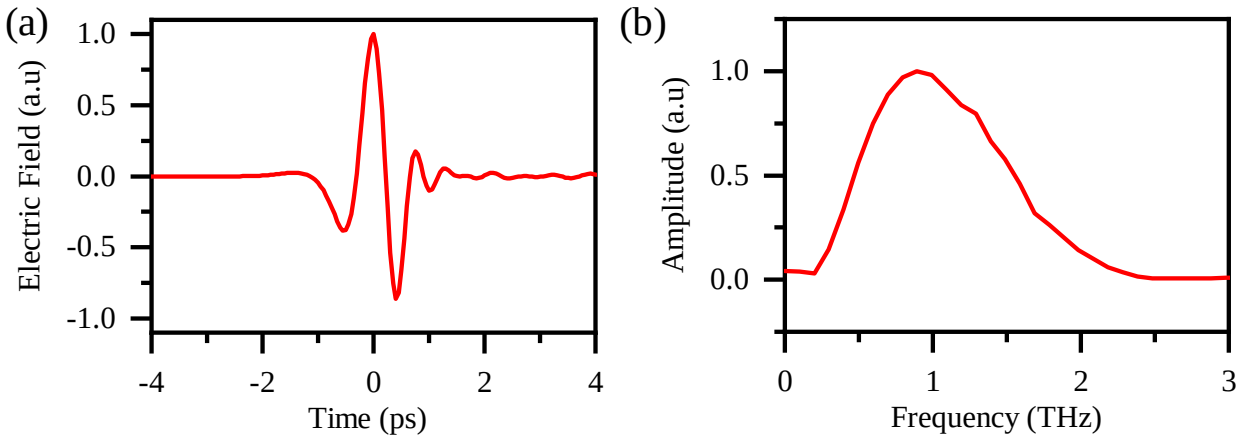

Figure 3.7: Time-domain measurement of a THz electric field transient acquired with EOS. (a) EOS waveform of a THz pulse generated by OR in our 4f setup with $LiNbO_3$. (b) Fast-Fourier transform of the waveform in (a) with bandwidth of 1 THz.

Following the ZnTe crystal is a $\lambda/4$ waveplate that converts the gate pulse from linear to circular polarization. The ellipticity of the optical pulse in the presence of the THz field is read out by separating the orthogonal polarization components of the optical beam with a Wollaston prism. The prism contains an interface between two materials with an index mismatch that preferentially reflects the light polarized parallel to the surface (S-polarized) in one direction and the perpendicular polarization (P-polarized) in the opposite direction. A pair of photodiodes with matched circuit impedance are then used to detect each beam from the Wollaston prism.

With EOS, we trace out the transient THz electric field profile directly in the time domain by changing the pump-gate delay time, i.e., the delay time between the 800 nm probe pulse and the THz pulse. A typical spectrum is shown in Figure 3.7(a) along with the corresponding FFT in panel (b). The bandwidth of the generated THz pulse (FWHM) is approximately 1 THz.

Care must be taken when performing EOS measurements to ensure the highest accuracy. EO detection is sensitive to all environmental impacts on the THz pulse. Figure 3.8(a) shows an EO trace of the same THz beamline under different environmental conditions. The black trace contains many oscillations that arise from water molecules in the atmosphere, which absorb and re-emit at THz frequencies. A set of water line resonances can be seen to impact the THz spectrum at 1.12-1.18 THz, 1.43 THz, 1.68 THz, and 1.86 THz that are consistent with resonances reported in the literature [165]. To avoid unwanted interactions

that would reduce our THz field, we have constructed a dry-air purge box that is capable of maintaining a dry environment with humidity as low as 0.01%. The FFTs plotted in red and shown in Figures 3.7(b) and 3.8(b) are both acquired while the setup is under optimally dry conditions, i.e., after allowing the purge box humidity to stabilize for $>$ 30 minutes. The THz EOS waveforms in 3.8(a) were acquired after the THz purge box was opened and acclimating to a $\sim$40% relative humidity environment for $\sim$45 min. Notably, the symmetry of the waveform changes. The main peak is reduced by 9.6% while the second half-cycle is reduced by 44%. The effects of waveform symmetry on THz-STM measurements will be discussed in Chapters 4$-$7.

The detection crystal has a frequency dependent transfer function that is convoluted with the THz pulse spectrum during EOS measurements. The velocity mismatch in ZnTe between the 800 nm gate pulse and the frequencies in the THz pulse leads to a frequency dependent walk-off that acts as a filter. The cut-off frequency in ZnTe forms at $\sim$2.5 THz for crystal thicknesses $>$100 µm [143]. Additionally, the nonlinear susceptibility of ZnTe is affected by a TO phonon resonance with a frequency of 5.3 THz that limits detection bandwidth above 4 THz for all crystal thicknesses [143]. The frequency filtering effect can be minimized by preparing the crystal as thin as possible while still maintaining measurable EO signal. The EO traces shown were recorded using a 100-µm-thick ZnTe(110) crytal. A reflection can be seen in the EOS trace in Figure 3.8(a) at 10.86 ps. This feature corresponds to THz pulse delayed by a reflection within the 0.5-mm-thick Si beamsplitter. Using the 100-µm-thick ZnTe(110) crytal mounted to an additional 2.0-mm-thick ZnTe(100) increases the delay from the analogous reflection of the THz pulse within the detection crystal. Increasing the delay time between the main pulse and reflected pulses allows for FFT calculations using a wider time window;, the added time increases FFT resolution.

3.2.2 Ultrashort Gate Pulse Generation

One of the assumptions made for EOS is the treatment of the THz electric field as quasi-static. However, this assumption requires that the gate pulse duration be sufficiently short compared to the oscillation time of the THz pulse [166]. Moreover, for the experiments discussed later in the thesis, knowledge of the precise THz field profile plays an important role in understanding our THz-STM measurements. The THz pulse measured by EOS is a convolution between the electric field transient, crystal electro-optic response function, and

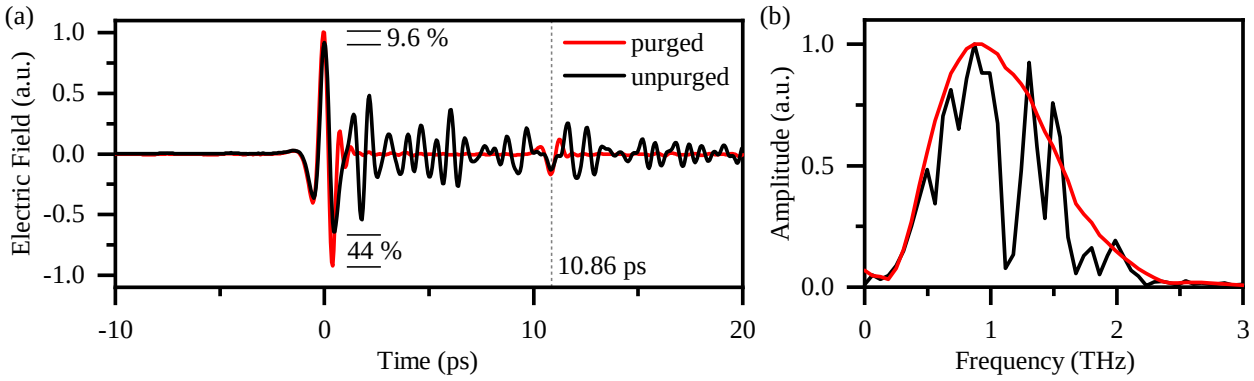

Figure 3.8: EOS measurements of our THz pulses with and without a dry air purge. (a) A pristine EOS trace acquired at < 0.05 % humidity is shown (red) to contrast against a waveform measurement performed under ambient conditions (black). Significant ringing is present as a result of THz absorption by H_2O in the atmosphere. (b) FFTs of the waveforms in (a) in the range -8 to 8 ps. The time window is narrowed to avoid reflections like the one indicated in (a) (a THz reflection from the 0.5-mm-thick Si beamsplitter) that would introduce Fabry-Perot resonances in the FFT. The waveforms in (a) are normalized to the maximum of the purged signal, the resulting changes in field strength are indicated in percent. The amplitude spectra in (b) are normalized to the maximum of the individual data.

gate pulse spectrum [167]. Performing EOS measurements with a broadband gate pulse prevents filtering effects that would reduce the measured bandwidth of the THz pulse. This effect can be mitigated so long as the ratio of gate pulse duration to THz half-cycle time is less than 1/2.7 [166].

To create a gate pulse with a duration $\tau_g < 20$ fs, we exploit the Kerr nonlinearity that produces a third-order nonlinear susceptibility in an ytterbium aluminum garnet (YAG) crystal. This class of materials experiences an intensity-dependent index of refraction, developing a nonlinear polarization,

$$P^{\mathrm{NL}}(\omega) = 3\epsilon_0\chi^{(3)}(\omega = \omega + \omega + \omega)|E(\omega)|^2 E(\omega)\,. \tag{3.41}$$

White-light supercontinuum generation (spectral broadening of an ultrafast pulse) arises from two important contributions, self-phase modulation and self-focusing [168, 169]. Self-focusing spatially confines the light by acting against diffraction, increasing the interaction length in the crystal, over which the effects of self-phase modulation are able to generate significant broadening of the input spectrum. In practice this picture of broadening fails over long distances due to a combination of dispersion and chip that develops due to self-phase modulation, requiring carefully chosen materials with negative dispersion to balance the the

positive dispersion of self-phase modulation, e.g. fibers used for communication [170].

Before discussing our setup for white-light generation, the concept of dispersion should be clarified in the context of a broadband pulse. The dispersion relation can be seen by considering the frequency dependent wavenumber, $k(\omega)$, and a Taylor series expansion about the center frequency of the pulse,

$$k(\omega) = k_0 + \frac{\partial k}{\partial \omega}(\omega - \omega_O) + \frac{1}{2}\frac{\partial^2 k}{\partial \omega^2}(\omega - \omega_0)^2 + \frac{1}{6}\frac{\partial^3 k}{\partial \omega^3}(\omega - \omega_O)^3 + [...]\,. \tag{3.42}$$

Whereas k_0 is the wavevector of the central frequency of the pulse and relates to the phase velocity, each term in the series expansion has a different physical interpretation.

$$\begin{aligned}
\frac{\partial k}{\partial \omega} &= \frac{1}{\nu_{\mathrm{gr}}} \\
\frac{\partial^2 k}{\partial \omega^2} &= \text{group delay dispersion (GDD)} \\
\frac{\partial^3 k}{\partial \omega^3} &= \text{third order dispersion (TOD)}
\end{aligned}$$

The first-order term identifies the average speed of the pulse as it propagates through the medium, while higher-order terms describe the relative speeds of each frequency. Normal dispersion occurs when GDD is positive, resulting in a slowing of the group velocity for higher frequencies. Anomalous dispersion is when the GDD is negative, resulting in larger group velocity at higher frequencies. Relating these concepts to the prism compressor, most materials and processes apply a positive GDD; the compressor is designed to apply negative GDD, allowing the higher frequencies to rejoin the low frequencies, producing time-domain compression of the pulse. In the compressor, the group-velocity-dispersion (GVD, GDD per unit length) is determined by the second derivative of the optical path length (P) with respect to the wavelength ($d^2P/d\lambda^2$) for each light ray propagating along different trajectories [171]. The prism pair within the compressor refracts the incident light within the pulse, separating the frequencies so that they propagate along separate trajectories. The accumulation of GDD during propagation through the compressor is thus controlled by the overall length of the compressor. Adjusting the separation between prism apices, by changing the position of the prism perpendicular to the beam path, provides fine control of pulse dispersion. In general, the optical path length difference can also be described by higher order derivatives, which allows the prism compressor to affect more complex pulse dispersion, e.g., $d^3P/d\lambda^3$ relates to the pulse's TOD.

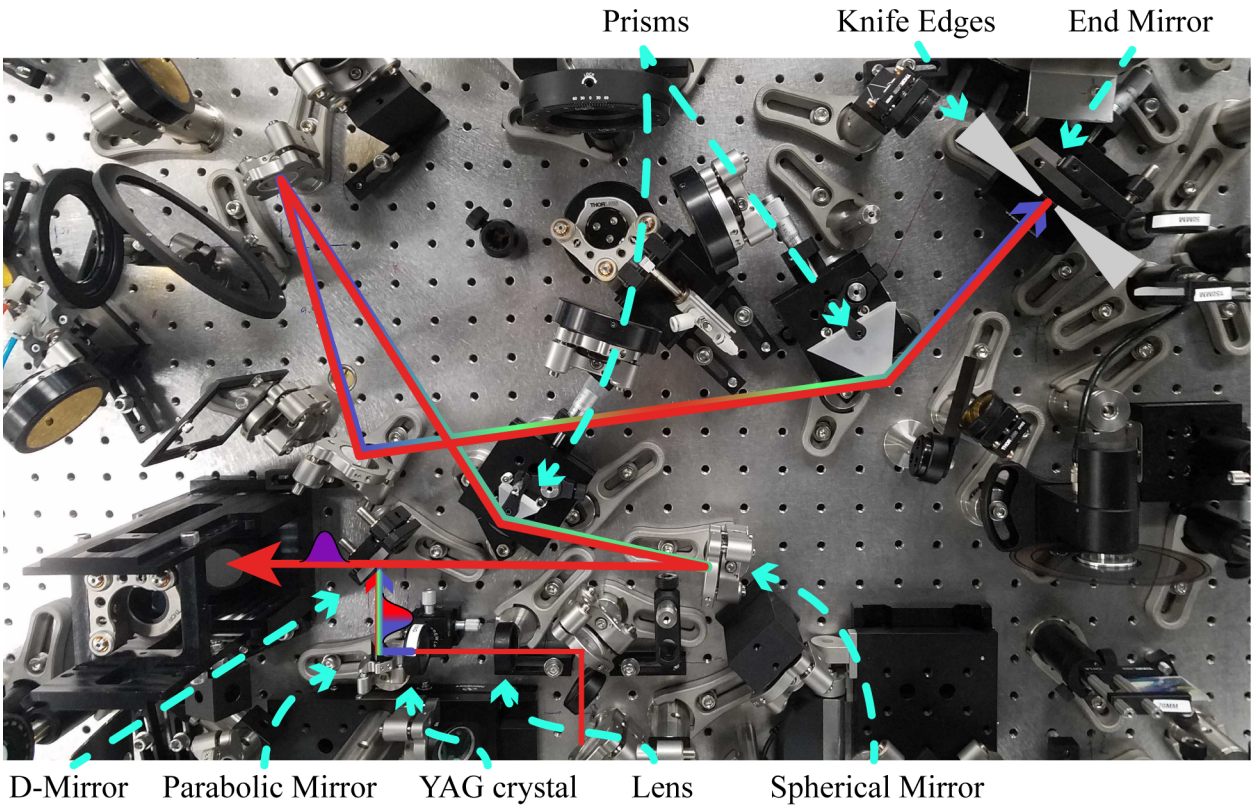

Figure 3.9: Supercontinuum while-light generation and prism compressor. An ultrafast NIR pulse ($\lambda = 1030$ nm) with a pulse energy of $\sim$500 nJ is focused into a 4-mm-thick YAG crystal by a 2-inch-focal-length (50.8 mm) spherical lens. A 0.5-inch-focal-length (12.7 mm) silver 90° off-axis parabolic is used to collimate the white-light and direct it toward a D-mirror. The white light is reflected into a 500-mm focal length spherical mirror that focuses through the prism compressor to a 2-inch-diameter (50.8 mm) square silver mirror. The mirror is on a stage to optimize its position at the Fourier plane generated by refraction through the prisms within the compressor and focusing optics. The white-light pulse propagates through a small prism (BK7) and large prism (BK7) whose separation distance, in combination with the focal length of the spherical mirror, dictate the dispersion compensation of the compressor. The multi-colored beam path indicates the white-light spectrum that enters the compressor and the red beam path indicates the spectrum that is selected by the knife edges at the Fourier plane. Gaussian distributions and white arrows indicate the relative orientation of the colors within the pulse. Positive dispersion is experienced during supercontinuum generation (red followed by blue at the YAG crystal). Refraction through the prisms provides negative dispersion that inverts the orientation of the colors. At the output of the compressor the dispersion is minimized and the colors are evenly distributed throughout the pulse (blue and red are mixed to make purple after the D-mirror).

The gate pulse we use is a white-light supercontinuum produced by self-phase modulation. A high-intensity NIR light pulse induces a nonlinear polarization in the YAG crystal, leading to the development of a phase offset,

$$\phi_{\mathrm{NL}} = -n_2 I(t) \frac{\omega_0 L}{c}\,, \tag{3.43}$$

where $n_2 I(t)$ is the nonlinear contribution to the intensity-dependent refractive index and L is the interaction length. The behavior of ϕ_{NL} dictates how the spectrum is broadened and produces lower frequencies at the beginning of the pulse and higher frequencies at the end of the pulse according to relationship,

$$\delta\omega(t) = \frac{d}{dt}\phi_{\mathrm{NL}}(t)\,. \tag{3.44}$$

The chirp induced by the process prevents the broadband pulse from having a short pulse duration [172]. In order to reduce the pulse duration the dispersion must be compensated.

To achieve significant pulse compression we built the 500-mm-long double-pass 2-prism compressor, pictured in Figure 3.9. Refraction of the light rays through the prisms alters the relative path lengths of the colors through the compressor. Blue wavelengths travel a shorter distance between the spherical focusing mirror and the flat end mirror, allowing positive GDD to be compensated as the pulse travels through the compressor. The effect is visualized by intensity profiles colored in red and blue that overlap to make purple at the output of the compressor in Figure 3.9. A larger separation between prisms enhances the accumulation of negative dispersion. The generating pulse continues to propagate through the compressor alongside the gate pulse. Without separating them, the higher-order dispersion in the NIR pulse will limit the the gate pulse compression. Likewise, the NIR pulse is many orders of magnitude more intense and would render the gate pulse undetectable during EOS. We can isolate the desired spectrum at a Fourier plane. A long, 500-mm-focal-length silver spherical mirror is used to focus the pulse through the prism compressor, leading to a Fourier plane at the focus half-way through the compressor. The white-light pulse (multi-colored beamline in Figure 3.9) is filtered at the Fourier plane by blocking the highest and lowest frequencies with a pair of sharp razor blades. The filtered pulse (red beamline in Figure 3.9) is reflected backward through the prism compressor in order to complete the pulse compression. A Flame spectrometer produced by Ocean Optics was used to measure the gate pulse spectrum, as shown in Figure 3.10(a). We select a range from 700 nm to 950 nm ($\Delta\nu$ = 112 THz).

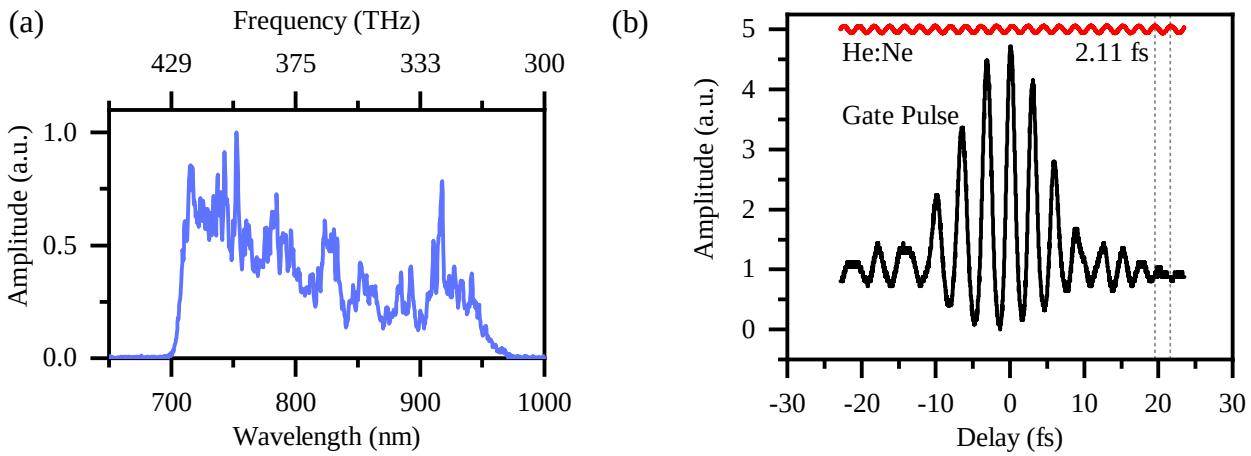

Figure 3.10: Verification of ultrashort gate pulse duration for EOS measurements. (a) Measurement of the 10-mW-average-power gate pulse using a Flame spectrometer from Ocean Optics. The spectrum spans 112 THz, from 700 nm to 950 nm. (b) Interferometric autocorrelation trace of the ultrashort gate pulse (black) produced from a white-light supercontinuum. The time axis is determined by the interference period (2.11 fs) of a CW He:Ne laser (red) with a wavelength of 633 nm.

Removing the NIR spectral components from the pulse significantly reduces the power; the input pulse contained ∼500 nJ and the measured gate pulse power after spectral selection was 10 nJ (10 mW).

To maximize power through the compressor, each prism was aligned to allow transmission at Brewster's angle to minimize reflection losses. Adjusting the prism positions perpendicular to the beam path allow us to optimize the gate pulse compression. Optimization of the gate pulse duration was done while performing interferometric autocorrelation measurements (Figure 3.10(b)). The measurements are performed with a Michelson interferometer setup designed to generate a second harmonic (SH) signal. The SH signal is sensitive to the intensity profile, $|E|^2$, but does not contain sufficient information to deduce the phase of the gate pulse. The SH dependence on E and the pulse intensity leads to interference of signal that should produce a ratio of 8:1, between the maximum and minimum deviation from the baseline. The photodiode detector used in our setup was also sensitive to linear absorption of the gate pulse spectral content. Although the sensitivity was low, a relatively inefficient SH process leads to a mixed character of SH and linear absorption, reducing the ratio in our measurement to ∼5:1. Therefore, only a rough estimation of the pulse duration is possible. The interferometer was built with a continuously oscillating speaker as the delay-time mechanism, and, hence, the time axis needed to be calibrated. Our calibration

was performed via linear interference of a CW He:Ne laser with a wavelength of 633 nm. Modulation of the average power by linear interference was measured as a periodic oscillation (red curve, Figure 3.10(b)), which allowed us to calibrate the time axis using $T = \lambda/c = 2.11$ fs for $\lambda = 633\,\text{nm}$. The ultrabroadband spectrum leads to a few-cycle autocorrelation with a FWHM $< 20\,\text{fs}$. For a Gaussian pulse, the duration is therefore $\frac{20}{1.414} = 14.1\,\text{fs}$. To obtain a more precise measurement, complex reconstruction algorithms can be used to analyze frequency-resolved-optical-gating (FROG) maps acquired for the pulse by measuring spectra produced by intra-pulse second harmonic generation as a function of delay-time. However, due to the relatively large time-scale difference between the optical gate pulse and the EO-detected THz pulse, it was not necessary to pursue such thorough characterization in this case. Conversely, EO characterization of multi-THz pulses (in the MIR) requires precise optimization of the gate pulse duration, e.g., for 30 THz the half-cycle time is expected be around 30 fs, requiring the gate pulse in EO detection be <15 fs [173].

3.2.3 Imaging the THz Focus

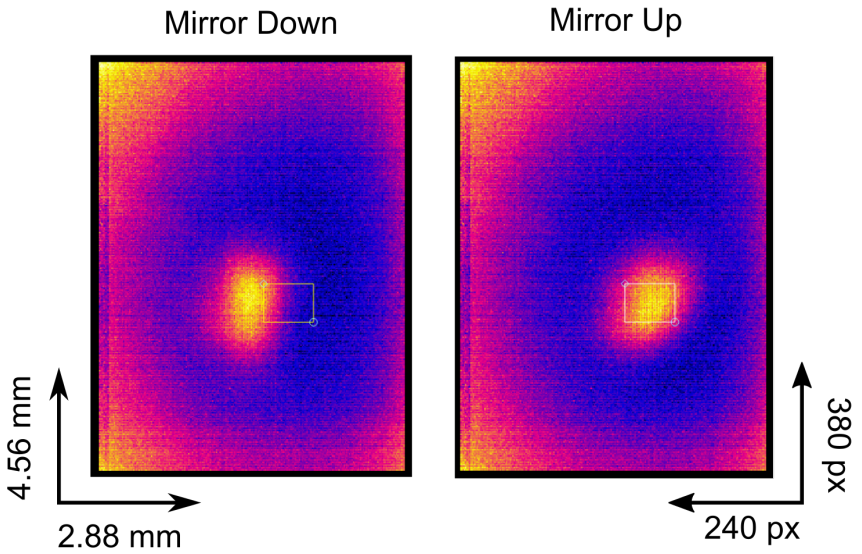

Figure 3.11: Images of the THz beam spot acquired by a SEEK Compact Pro thermal camera. The two images identify 'mirror up', which selects $E_{\text{THz,pk}} > 0$, and 'mirror down' used for $E_{\text{THz,pk}} < 0$. These images are used to optimize the pointing of our THz beam at various points throughout the setup. The contrast around the pulse comes from uneven exposure of the room temperature background.

The THz setup in Figure 3.5 contains many control parameters that can affect the

THz beam alignment. A key parameter for the experiments discussed in Chapter 4 and presented in Chapter 6 is control of the THz polarity, i.e., the direction of the peak THz electric field, $E_{\mathrm{THz,pk}}$. The CEP mirror in Figure 3.5 that flips the THz polarization also changes the beam path by approximately 15 cm. The 2-inch-diameter gold mirror must be repeatable in its positioning, as minor deviations in the pointing will affect the alignment of the beam after several meters of propagation to the STM tip. Additionally, the THz setup is based on a Michelson interferometer geometry containing two separate beam paths, each of which contains adjustable optics, so their collimation after recombination must also be confirmed.

We employ a temperature-sensitive camera (SEEK Compact Pro, manufactured by SEEK Thermal) for THz imaging. The camera uses 12-µm-wide microbolometer pixels made from vanadium oxide, and incorporates these into an electronic circuit constructed to detect the changes in material resistivity as a function of temperature. The thermal camera is low-profile (as it was originally designed for smartphones) and thus fits in many locations throughout the setup. As an example, for testing the alignment of the CEP mirror into the interferometer, the camera was mounted and placed at the focus in the adjustable arm of the THz interferometer (see Figure 3.5). Here, we can see the real-space changes in alignment between CEP mirror configurations. Despite the relatively large focal size of the THz beam, it is still necessary to eliminate alignment changes between THz configurations and hence we performed such characterizations and subsequent optimization alignment for all configurations. This is important because at the STM tunnel junction the tip diameter is on the order of the spot size. Thus, adjustments in the pointing could lead to changes in the coupling efficiency of the incident THz field to the tip and tunnel junction.

Chapter 4
Terahertz Scanning Tunneling Microscopy

Optical experiments utilizing ultrafast light pulses have become an integral approach to materials science research [49, 174]. Ultrafast spectroscopy is the study of photoexcited states of matter and was recognized by the 1999 Nobel prize in chemistry. The award was presented to Ahmed Zewail for using femtosecond optical pulses to probe chemical reactions. Since then, light pulses across the IR, visible, UV, and x-ray spectral ranges have been used extensively to investigate, free-carriers [175], quasi-particles [176], magnetism [177], and complex materials [178]. Pump-probe measurements with sub-picosecond excitation pulses and THz or MIR probe pulses characterize the initialization of non-equilibrium states and their subsequent decay pathways in condensed matter systems. The dynamics of the excited system can be monitored by the spectral signatures of low-energy excitations, e.g. phonons and interband transitions in excitons, which are involved in electron-electron and electron-phonon interactions [179, 180]. A key step in developing our understanding of materials and how to integrate them into next-generation devices is to characterize ultrafast processes locally [181], which requires access to sub-nanometer length scales. This has spurred great interest in developing techniques that allow light to be utilized on increasingly smaller length scales [17]. The push toward the ultimate limits in time and space of condensed matter systems has resulted in THz-STM [5, 6, 9–12, 14, 16, 182–184], which is a marriage between ultrafast THz pulses and atomically resolved STM [7, 8, 13, 15, 18, 185–187].

At the smallest length scales, the arrangement of atomic constituents plays a significant role in the dynamics of the system. This is evident in low-dimensional and correlated electron systems, where electron-electron and electron-phonon coupling, together with their behavior near defects, dominate the mediation of energy transfer and relaxation. Energy harvesting, e.g., for solar cell technology, requires the separation of charge across interfaces, e.g., between materials [188], within nanostructures [189] and across molecules [190]. STM studies of

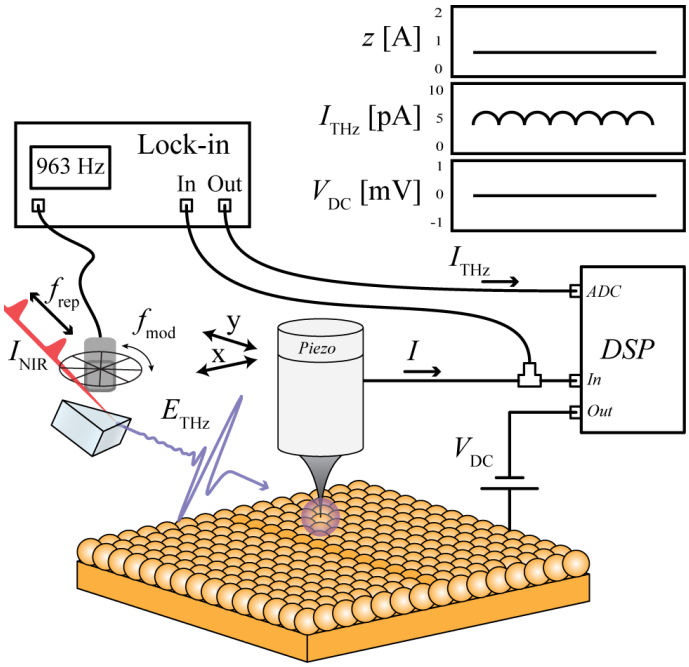

Figure 4.1: Schematic diagram of constant-height THz-STM operation. NIR pulses (I_{NIR}) generate single-cycle THz pulses (E_{THz}) that illuminate the tunnel junction of an STM and induce a tunnel current at a repetition rate, $f_{\mathrm{rep}} = 1$ MHz. The STM tunnel current is fed into a lock-in amplifier that is referenced to an optical chopper, which modulates the NIR pulse train. This turns the THz generation on and off at a modulation rate, $f_{\mathrm{mod}} = 963$ Hz. The lock-in signal is fed into the DSP, where the THz-induced current is recorded. Constant-height THz-STM operates without the feedback loop engaged and typically with $V_{\mathrm{DC}} = 0\,\mathrm{V}$.

isolated individual molecules have shown strong coupling between electronic and photonic degrees of freedom [191] as well as between electronic and vibronic degrees of freedom [192] with extreme spatial sensitivity to charge injection into the system.

In STM experiments, the key to establishing the technique as a *de facto* tool for surface science has been the application of local tunneling spectroscopy. STS measurements extract the LDOS with ångström-scale resolution in both single point measurements and in spatially resolved maps of quasi-particle interference [31, 193]. The latter allows STM to construct a map of the sample's band structure similar to angle-resolved photoemission spectroscopy measurements [194, 195]. The next step in atomic scale surface science is the unambiguous real-space detection of electronic dynamics. However, STM lacks the temporal resolution necessary to resolve the dynamics that are relevant in the next generation of complex electronic materials.

To achieve ultrafast time resolution in THz-STM, the static bias voltage (V_{DC}) is replaced by a time-dependent bias modulation ($V_{\mathrm{THz}}(t)$) created by the electric field of a phase-stable single-cycle THz pulse coupled to the tip (E_{THz}, Figure 4.1). The bias modulation is ultrafast, evolving on sub-picosecond timescales ($< 10^{-12}\,\mathrm{s}$), i.e., many orders of magnitude faster than conventional modulation rates. The THz voltage modulation amplitude is typically $1-2$ orders of magnitude larger than what is used in $\mathrm{d}I/\mathrm{d}V$ spectroscopy [196].

THz-STM probes a unique spatio-temporal regime, but further development of the technique is needed to establish it as a tool for exploring new materials. In this chapter, I will present the principles of THz-STM using analogues to the STM and STS concepts presented in Chapter 2. I will further present a guide to the experimental procedures I have developed for performing THz-STM and THz-STS experiments. Later, in Chapter 6, these methods are used to explore atomically precise graphene nanoribbons. In Chapter 7, I present new analytic tools for analyzing the data from these methods, laying the groundwork for future materials science.

4.1 Ultrafast STM

With the establishment of commercial compact, turn-key ultrafast lasers and the development of commercial low-temperature UHV STM systems, scientific pursuits on ultrafast time scales and of atomic length scales have become commonplace. As our technological age progresses, the demand to combine them has reached a critical point. Device construction has reached the nanometer length scale [197, 198] and device operation speeds are now in the GHz regime [199]. THz-STM now provides simultaneous sub-picosecond time resolution with ångström spatial resolution, and is in the process of maturing as a next-generation tool for ultrafast surface science on the atomic scale.

Two prominent early attempts to incorporate ultrafast time resolution into STM experiments were junction-mixing STM (JM-STM) [48] and photoconductively gated STM (PG-STM) [200]. These developments in the late 1990's were promising, offering temporal resolution on picosecond timescales. However, the spatial resolution of STM is a hallmark of the technique and must be maintained to fully realize ultrafast time-resolved STM measurements. In the case of PG-STM, the origins of the time-resolved signal were capacitive in

nature and therefore extended over several micrometers [201], precluding the technique from achieving atomic-scale spatial resolution. JM-STM was developed to to utilize fast voltage transients generated by photoconductive switches that are launched along pre-patterned transmission lines and detected in the STM tunnel current [202]. The necessity of a transmission line is broadly limiting in terms of sample flexibility and the propagation of the transient voltage limited the time resolution to >10 ps. On the other hand, JM-STM helped inspire the both THz-STM and our THz-STS algorithm presented in Chapter 7.

An alternative route to ultrafast time resolution involves direct illumination of the tunnel gap by ultrafast NIR and optical laser pulses. This leads to photo-assisted tunneling triggered by optical excitation of the tunnel junction, such as was observed in the first demonstration of STM combined with ultrafast pulses [203]. Utilizing femtosecond pulses in laser-assisted STM (LA-STM) leads directly to sub-picosecond current modulation [204], which has allowed for atomic scale investigation of single molecules [205]. However, complications arise when an STM junction is illuminated with laser light that carries enough photon energy to photoexcite electrons in the system, especially when the average power is high. The tunnel current is extremely sensitive to the tip-sample distance, and direct illumination with femtosecond lasers induces thermal expansion of the STM tip [206]. Pulse energies < 1 nJ have been recommended to mitigate these effects, though they still occur [207]. The thermal effects of direct laser illumination are made more technically challenging when considering the stability of the combined laser and STM systems.

Typically, the STM is suspended in vacuum and mechanically isolated from the environment. Illuminating the junction with light originating far the STM (where the systems are ostensibly decoupled from one another) compounds the thermal problems of LA-STM. The focus size of the laser pulses at optical and NIR wavelengths is on the order of a few tens of µm and is often coupled into the junction via a focusing lens from outside the vacuum chamber, leading to significant motion of the focus for small perturbations of either system [208]. While the non-contact approach of LA-STM is appealing, the thermal effects and stability challenges have proven to be difficult to overcome. Recently, a new photo-assisted tunneling technique has been developed to mitigate some of these issues. The introduction of shaken-pulse pair [209] and homodyne mixing of NIR pulses [186] have attempted to alleviate the thermal fluctuations of the STM tip and junction by removing the need for optical chopping. Yet, the shot-to-shot thermal contributions will always be difficult to rule out for

photon energies that are strongly absorbed by the tip and junction.

A key challenge has been to achieve ultrafast time resolution in an STM through a method that operates similarly to conventional STM, i.e., ideally, with a voltage based probe. In STM and STS, a static voltage probe allows us to extract quantitative information about a sample's electronic structure, aiding in the development of new devices and fundamental physics [210]. The models that describe tunneling between the tip and sample are highly dependent on tunnel gap distance, and, thus, these experiments require a high degree of stability. Laser excitation with optical and NIR wavelengths degrades thermal stability, especially when the incident power is high. Conversely, operating at low frequencies (e.g, THz) avoids the shot-to-shot thermal fluctuations that cause the tunneling gap to change width for higher frequency illumination. An equally important aspect is that the THz pulse acts as an ultrafast bias voltage rather than a photoexcitation of the junction, as is discussed below. Thus, THz-STM builds on the developments of previous time-resolved STM techniques and overcomes the challenges they encountered. The rest of this chapter will describe the concepts behind THz-induced tunneling in an STM tunnel junction and the experimental modalities used for science.

4.1.1 Keldysh Parameter

A straightforward definition of the regimes of nonlinear interaction of electromagnetic waves with matter is provided by the Keldysh parameter [211, 212],

$$\gamma = \frac{\omega\sqrt{2m_e\Phi}}{eE}\,, \tag{4.1}$$

where ω is the angular oscillation frequency of the electric field, m_e is the mass of the electron, e is the elementary charge, Φ is the ionization energy or barrier height, and E is electric field strength. The Keldysh parameter distinguishes between the multi-photon regime of optical nonlinearity ($\gamma > 1$) and the nonperturbative, strong-field regime ($\gamma < 1$), where field-driven tunneling dominates (Figure 4.2(a)). For typical STM parameters, e.g., a gap distance of $d = 1\,\text{nm}$ and $V = 1\,\text{V}$ (such that $E = V/d = 10^9\,\text{V/cm}$), the Keldysh parameter at 1 THz is $\gamma = 4.74\times10^{-2}$. Operating in the strong-field regime of light-driven currents, where the THz pulse acts as an ultrafast voltage transient, allows us to maintain the tunneling behavior that gives rise to atomic resolution in STM. The term 'lightwave-driven STM' has been coined to describe this class of experiments [7, 49], which originated in the THz spectral range [5].

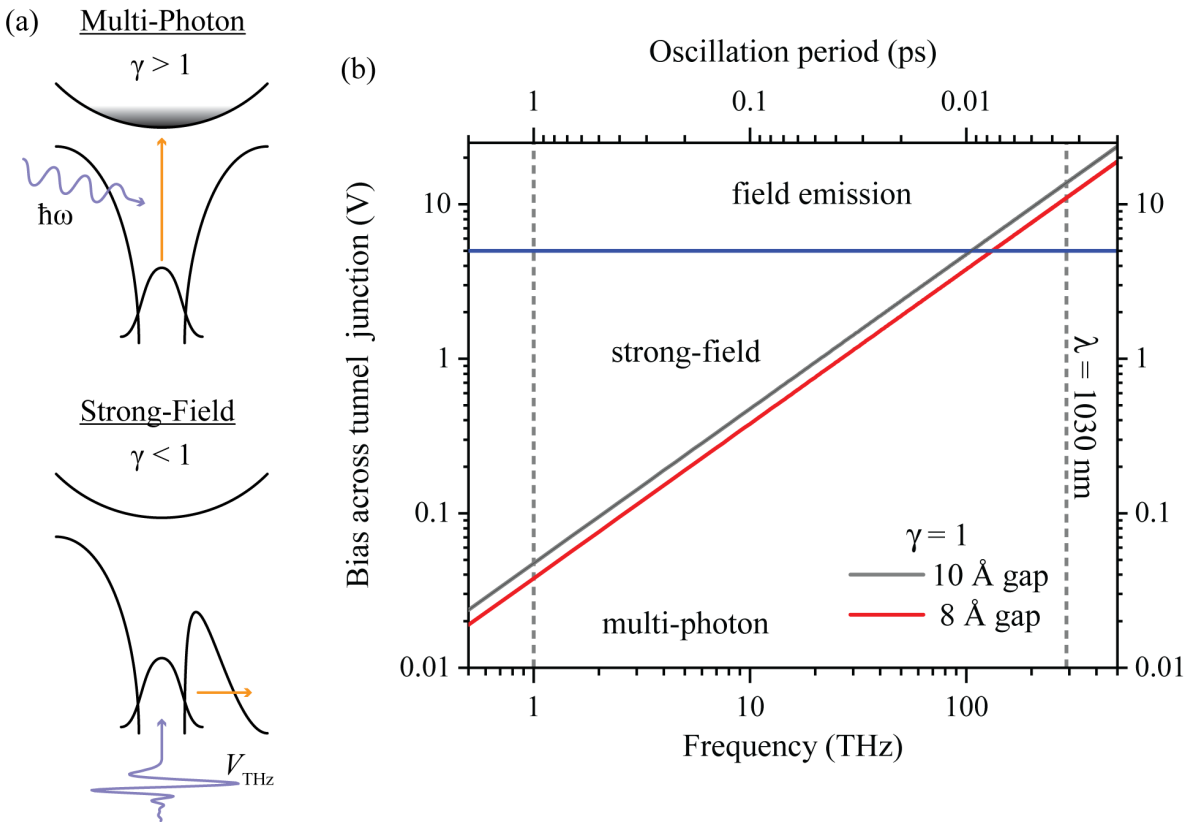

Figure 4.2: Illustration and calculation of the Keldysh parameter, γ, defining the separation between two regimes of nonlinear light-matter interaction, i.e., the multi-photon and strong-field regimes. (a) An illustration of the differences between multi-photon and strong-field regimes. In the multi-photon regime ($\gamma > 1$) the system undergoes an electronic excitation by absorbing a photon with energy, $\hbar\omega$, resulting in a direct excitation into higher energy bands (top). In the strong-field regime ($\gamma < 1$) the electric field of the light acts as a voltage, e.g., V_{THz}, and changes the potential of the system (bottom). Distortion of the energy landscape changes the height of the potential barriers and allows for quantum tunneling. (b) Calculation of applied voltage across an STM tunnel junction for typical gap distances. The region above the diagonal line corresponds to the strong-field regime, while the region below the line corresponds to the multi-photon regime. The blue horizontal line indicates the applied voltage at which field emission occurs for a static bias and $\Phi = 5\,\mathrm{eV}$. A pair of vertical dashed grey lines are provided for reference, denoting the approximate center frequency of our THz pulses (left) and the fundamental frequency of our NIR laser system (right).

Equation 4.1 can be rewritten as $V = d\omega\sqrt{2m_e\Phi}/\gamma$. Figure 4.2(b) shows the minimum applied voltage, $V(\gamma = 1)$, to remain in the strong-field regime for two different tunnel gap widths. At 1 THz, the minimum voltage is ∼50 mV, whereas at the fundamental frequency of our laser (291 THz, 1030 nm), the minimum voltage is $V \sim 14$ V. In conventional STM, when $V_{\mathrm{DC}} \gtrsim \Phi/e$ (5 V in Figure 4.2(b)) the current across the junction is described by field emission, which is less sensitive to gap distance. As a result, the current is no longer concentrated on the atomic cluster at the end of the tip for field emission and the spatial resolution degrades. If the voltage is below the line for a given gap distance and frequency, then the light-matter interaction can be described by a multi-photon process and current is generated by a process such as photon-driven or photo-assisted tunneling [185, 205, 209]. Interestingly, this suggests that THz-driven tunneling uniquely spans mV to V energy scales as a strong-field process while simultaneously maintaining sub-picosecond temporal resolution. The oscillation period shown in Figure 4.2(b) indicates twice the upper limit of time resolution for lightwave-driven STM of a given frequency.

In summary, for a THz pulse coupled to an STM junction, if the electric field is high enough to operate in the strong-field regime (as is the case for all experiments discussed in this thesis), then we can treat oscillation of the tip-coupled electric near-field, E_{THz}, as a quasi-static bias voltage, $V_{\mathrm{THz}}(t)$, applied across a junction of width d.

4.1.2 THz-Induced Current

In THz-STM, an ultrafast voltage transient, $V_{\mathrm{THz}}(t)$, is supplied by a free-space electromagnetic pulse, $E_{\mathrm{THz}}(t)$, that is focused onto the STM tip apex, as shown in Figure 4.3(a). Operating in the strong-field regime allows us to treat the time-dependent voltage as quasi-static, so we can map the voltage onto the $I(V)$ as if we were simply varying V_{DC} in time. The peak electric field, E_{pk}, of the incoupled pulse can be varied without affecting the shape of the electric field waveform, e.g., using a pair of wire-grid polarizers. $E_{\mathrm{THz}}(t)$ can be detected by electro-optic sampling and is related to the THz voltage waveform applied to the tunnel junction by the transfer function of the tip. The transfer function, $H(\omega)$, depends on the incoupling geometry, the macroscopic, mesoscopic, and microscopic shape of the tip, the dielectric function of the tip material, and the spectral content of the pulse [8–11, 15, 182]. In some circumstances, it may also depend on the local dielectric resonse of the sample [173, 213], but that is beyond the scope of this work. Characterization of the waveform is

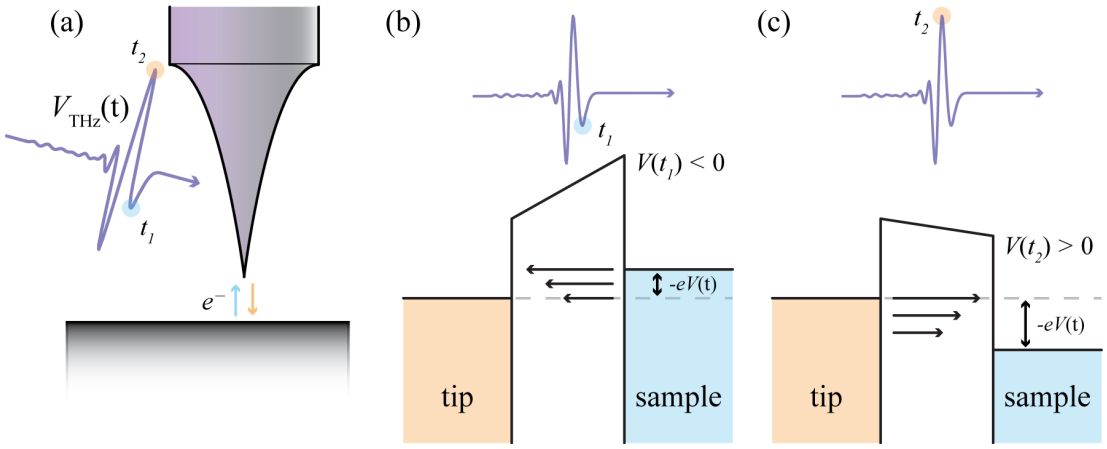

Figure 4.3: THz-induced modification to the potential energy landscape of an STM tunnel junction. (a) A free-space THz pulse is coupled to tip of an STM, where it acts as a quasi-static bias voltage, $V_{\mathrm{THz}}(t)$, and induces a current across the tunnel junction. As the voltage evolves, it opens different tunnel pathways. (b) During negative half-cycles, tunneling is allowed from the sample into the tip, resulting in negative current. (d) During positive half-cycles, a positive current is induced, as electrons are able to tunnel into unoccupied states of the sample.

experimentally feasible [10, 11, 15, 214] and will be discussed later in the chapter. For now, we model the voltage across the junction as,

$$\begin{aligned} V(t) &= V_{\mathrm{THz}}(t) \\ V_{\mathrm{THz}}(t) &= V_{\mathrm{pk}} V_0(t)\,, \end{aligned} \tag{4.2}$$

where V_{pk} is a constant scaling factor proportional E_{pk} and $V_0(t)$ is the trace of the electric near-field transient. $V_{\mathrm{THz}}(t)$ evolves adiabatically, changing the energy level alignment between the tip and sample. Changing between positive and negative half-cycles of the voltage oscillation induces a bipolar current response. A negative current is produced for $V_{\mathrm{THz}}(t) < 0$ when tunneling pathways above the Fermi level of the tip are open, allowing electrons to flow from occupied states of the sample to unoccupied states of the tip (Figure 4.3(b)). Conversely, $V_{\mathrm{THz}}(t) > 0$ results in a positive current, where electrons tunnel from the occupied states of the tip into unoccupied states of the sample (Figure 4.3(c)).

Since $V_{\mathrm{THz}}(t)$ originates from the oscillation of a free-space-propagating electromagnetic field, the time integral must be zero. Charge rectification occurs when $V_{\mathrm{THz}}(t)$ is mapped onto an $I(V)$ with nonlinearities. This rectified charge is responsible for the current detected in THz-STM. As discussed in Chapter 2, STS aims to extract the junction's $I(V)$, which relates to the density of states of the sample. The electronic distribution of features in the

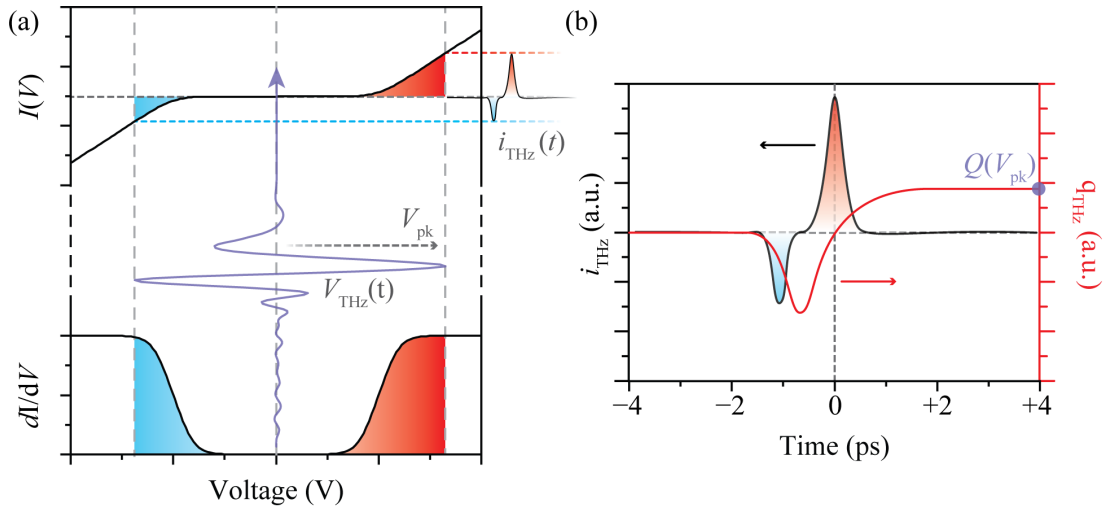

Figure 4.4: Rectification of THz-induced current pulses. (a) An ultrafast voltage transient, $V_{\mathrm{THz}}(t)$, is applied to an $I(V)$ curve. The nonlinearities of the $I(V)$ produce an asymmetry in the current pulse, $i_{\mathrm{THz}}(t)$. (b) The instantaneous rectified charge, $q_{\mathrm{THz}}(t)$, is the running intgral of the current pulse and its final value is the net rectified charge, $Q_{\mathrm{THz}}(V_{\mathrm{pk}})$. Adjusting V_{pk} changes the size of the voltage waveform, thereby sampling different regions of $I(V)$ to produce different values of $Q_{\mathrm{THz}}(V_{\mathrm{pk}})$.

LDOS manifest as nonlinearities of the junction $I(V)$. These nonlinearities are responsible for producing an asymmetric current pulse, $I(V_{\mathrm{THz}}(t)) = i_{\mathrm{THz}}(t)$. This is shown in Figure 4.4(a), where only select portions of $V_{\mathrm{THz}}(t)$ produce a non-zero current response for the example $I(V)$. We can describe the transfer of charge across the junction during the evolution of the voltage pulse as

$$q_{\mathrm{THz}}(t') = \int_{-\infty}^{t'} I(V_{\mathrm{THz}}(t))\, dt \ , \tag{4.3}$$

where $q_{\mathrm{THz}}(t')$ is the instantaneous charge rectified and is shown in Figure 4.4(b). The total charge transferred across the junction by a single THz pulse is the net rectified charge,

$$\begin{aligned} Q_{\mathrm{THz}} &= \int_{-\infty}^{\infty} I(V_{\mathrm{THz}}(t))\, dt \\ Q_{\mathrm{THz}}(V_{\mathrm{pk}}) &= \int_{-\infty}^{\infty} I(V_{\mathrm{pk}} V_0(t))\, dt \ , \end{aligned} \tag{4.4}$$

where the second line in Equation 4.4 comes from the implementation of our representation for $V_{\mathrm{THz}}(t)$ in Equation 4.2. $Q_{\mathrm{THz}}(V_{\mathrm{pk}})$ is the principle signal measured in THz-STM when a THz-field control scheme is implemented.

The femtosecond- to picosecond-scale oscillations of the THz-induced current shown in Figure 4.5(a) are far too fast to be detected directly by the STM electronics (since the

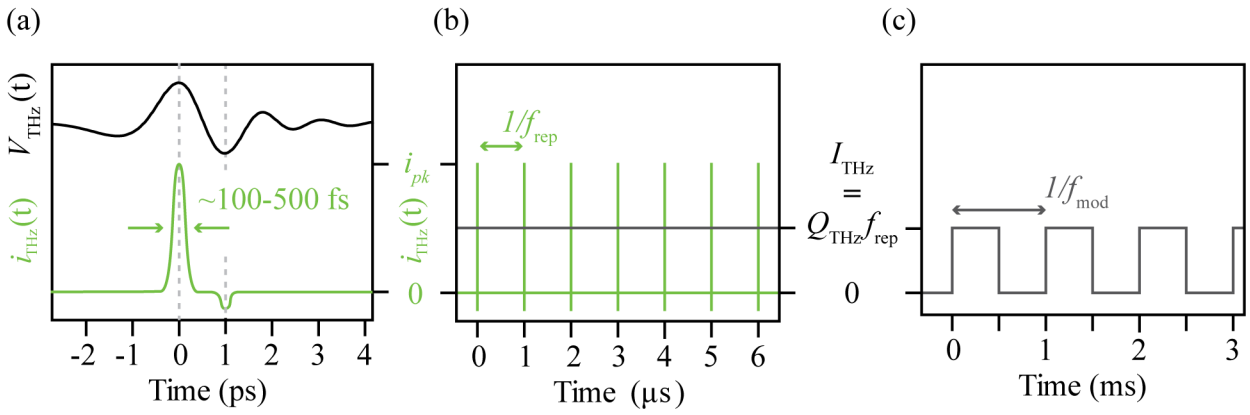

Figure 4.5: Measuring a THz-STM signal with lock-in detection. (a) An ultrafast voltage transient, $V_{\mathrm{THz}}(t)$, induces a sub-picosecond current pulse, $i_{\mathrm{THz}}(t)$. (b) A train of current pulses are generated at the laser repetition rate, f_{rep}, leading to a current detected by the STM that is proportional to the net charge rectified per pulse, Q_{THz}. (c) Using lock-in detection and modulating the THz pulse train at a rate, f_{mod}, the average THz-induced current, I_{THz}, is measured.

bandwidth of a typical STM preamplifier is ≈1 kHz). Instead, the electronics integrate over the duration of the current pulse and output the net rectified charge across the junction. A train of current pulses is produced at the repetition rate of the laser system, as shown in Figure 4.5(b), and each pulse within a time period corresponding to the STM preamplifer bandwidth contributes to the average THz-induced current, $I_{\mathrm{THz}} = Q_{\mathrm{THz}} \times f_{\mathrm{rep}}$. For our system, the repetition rate is 1 MHz and the bandwidth of our preamplifier is 1 kHz at maximum current-to-voltage gain, which is used throughout this thesis. For a standard THz-STM measurement this means 1000 pulses contribute to the signal that comes from the preamplifier. Thus, ultimately, we measure the net rectified charge averaged over many pulses. To reliably detect I_{THz} we employ lock-in detection. As shown in Figure 4.5(c), the NIR laser responsible for THz pulse generation is periodically blocked with an optical chopper at a rate, f_{mod}, and a lock-in amplifier is referenced to the modulation. The lock-in output is then fed into the STM controller (DSP), as shown in Figure 4.1, and recorded along with the STM tip position and various other parameters. The details of experimental procedures will be described in the next section.

4.2 A Guide to THz-STS

STM is well known as one of the few techniques capable of atomic spatial resolution.

However, its ability to extract LDOS with ångström resolution makes it irreplaceable. To elevate THz-STM as a comparable, time-resolved tool for materials science and device characterization, the technique must also be able to extract meaningful, quantitative, and unique information regarding the dynamic LDOS while maintaining atomic spatial resolution, and ideally do so without making *a priori* assumptions about the sample. The treatment presented in the previous section has been used in several THz-STM publications, which have simulated their experimental results [5, 7, 8]. To expand on the basic understanding of THz-STM and advance the technique as a robust tool for ultrafast materials science research, we have developed THz-STS as an ultrfast complement to conventional STS in this thesis. By establishing the procedures for steady-state THz-STS, we set the stage for extracting time-domain information from analogous measurements. In this section, I will cover the modalities of THz-STS that, when combined, are capable of interrogating the sample LDOS probed by the THz voltage in four-dimensions with ultrafast/atomic spatio-temporal resolution. I will also detail key aspects of the experimental setup that make this possible.

4.2.1 Duty Cycle

A critical parameter in controlling our THz-STM signal is tip height, z_{tip}. The exponential dependence of the tunnel current, discussed in Chapter 2, holds equally for THz-driven current. Adjusting the tip height will tune both the average, I_{THz}, and peak, i_{pk}, currents across the junction. Careful control of the STM tip height is necessary to ensure sufficient signal-to-noise ratio while avoiding peak currents that can lead to sample damage or tip changes. Figure 4.6 shows the relationship between average current and peak current for different laser repetition rates.

For our system, $f_{\mathrm{rep}} = 1$ MHz, which means operating in the single electron regime of rectified charge corresponds to $I_{\mathrm{avg}} = 160\,\mathrm{fA}$. Using our preamplifier (FEMTO Low-noise, DLCPA-200) at maximum gain (10^9 V/A), the STM outputs a signal of 160 µV for this current, which is well within the range of standard lock-in detection. However, if you consider that the average current incorporates the time between THz pulses, it becomes clear that the average current is a vast underestimate of the currents generated at the peak of $V_{\mathrm{THz}}(t)$. The peak current, i_{pk}, is roughly proportional to the average number of rectified charges per THz pulse (for cases of unipolar current pulses). The width of the current pulse can be estimated from autocorrelation measurements and 100−500 fs pulse widths have been reported [5, 7,

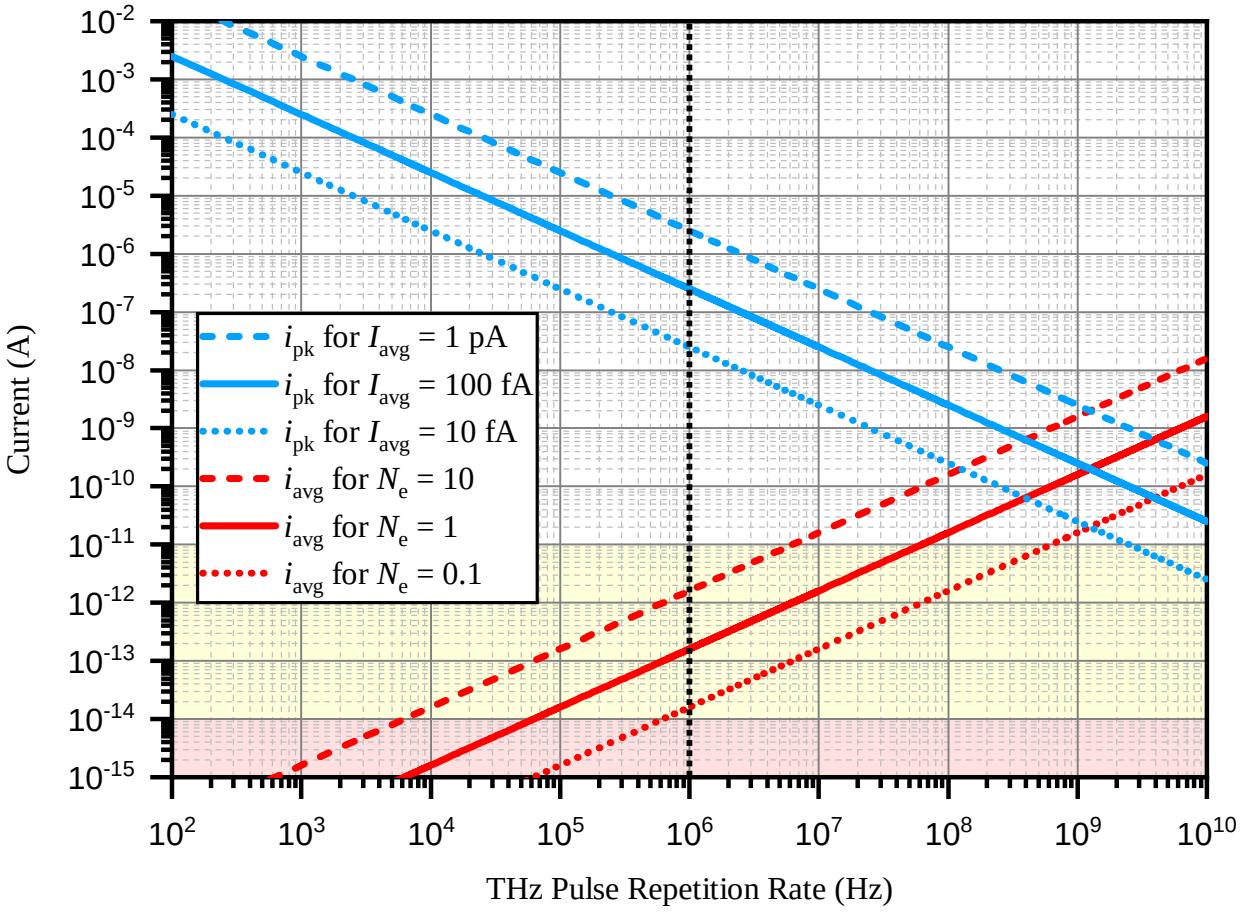

Figure 4.6: Comparison of time-averaged and peak-transient THz-pulse-driven tunnel currents at various repetition rates. For comparison, the laser repetition rate of our system is 1 MHz (vertical dashed line). In red, the average THz-pulse-driven tunnel current (I_{avg}) is shown for a constant number of rectified elementary charges per THz pulse: $N_e = 10$ (dashed red line), $N_e = 1$ (solid red line) and $N_e = 0.1$ (dotted red line). In blue, the peak instantaneous THz-pulse-driven tunnel current (i_{pk}) is shown for a constant average THz-pulse-driven tunnel current: $I_{\text{avg}} = 1$ pA (dashed blue line), $I_{\text{avg}} = 100$ fA (solid blue line) and $I_{\text{avg}} = 10$ fA (dotted blue line). The blue curves assume that the THz pulse voltage is active for 400 fs (an estimation based on past measurements [5, 8]). The shaded box in red shows the typical tunnel current detection limit of conventional (state of the art) STM systems that utilize lock-in detection ($\sim$10 fA), while the shaded box in yellow shows the typical range of the tunnel current for a high gain preamp operating in constant-current mode (active feedback loop).

8, 12]. Assuming a unipolar, square current pulse for the purpose of illustration, for an average rectified charge of one electron per pulse, i.e., $N_e = 1$, the peak current is between 320 nA ($\tau = 500$ fs) [5, 12] and 1.34 µA ($\tau = 120$ fs) [7]. This is because the duty cycle of our THz-induced signal (the ratio of voltage pulse duration to time between laser shots) is 10^{-6} or less.

The duty cycle reduces the average current detected by the STM electronics and poses a challenge to performing THz-STM measurements. In normal operation, while in constant-current mode, the STM feedback loop establishes the tip height based on the DC tunneling parameters and the conductance of the junction. At the same height, the THz-STM current will be undetectable because of the 10^{-6} reduction in average current associated with the duty cycle.

For a solution, we can refer back to Equation 2.18 and recall that $I \propto \exp(-2\kappa z)$. This allows us to increase the average current by ∼1 order of magnitude for each Å of tip approach. If we are performing constant-current STM characterization of a sample at $V_{\mathrm{DC}} = 1$ V and $I_{\mathrm{DC}} = 100$ pA, we will typically decrease the tip height by 3−4 Å to perform THz-STM experiments. At this new tip height, for $V_{\mathrm{pk}} \sim 1$ V, $Q_{\mathrm{THz}} \sim 1 - 10$ electrons/pulse and $I_{\mathrm{THz}} \sim 0.1 - 1$ pA. Alternatively, the feedback loop may be left engaged if instead we reduce V_{DC} such that the tip approaches the surface to maintain the tunneling setpoint. I_{DC} may also be increased to the same effect. We have found success using setpoint parameters of $I_{\mathrm{DC}} = 100$ pA and $V_{\mathrm{DC}} = 10$ mV, which allows us to record THz-STM data for several hours at a time. Similar parameters are reported by Cocker *et al.* [7]. There, they used THz-STM to atomically resolve the LDOS of molecular orbitals of individual pentacene molecules adsorbed on salt (NaCl) monolayers.

4.2.2 THz-STM Setup

In typical THz-STM experiments, the signal being recorded is the THz-induced tunneling current, $I_{\mathrm{THz}} = Q_{\mathrm{THz}}(V_{\mathrm{pk}}) \times f_{\mathrm{rep}}$. The control parameters of interest are the incident THz electric field strength, which we describe by the peak THz field, $E_{\mathrm{THz,pk}}$, and the carrier-envelope-phase, ϕ_{CEP}, of the waveform, which governs the orientation of the peak bias applied to the junction. The level of control we have over ϕ_{CEP} is limited compared to other, more complex, forms of arbitrary THz waveform generation [215]. However, we do have two ways to alter the waveform. (i) ϕ_{CEP} can be changed by a factor $\pm\pi$ to invert the sign of $E_{\mathrm{THz,pk}}$.

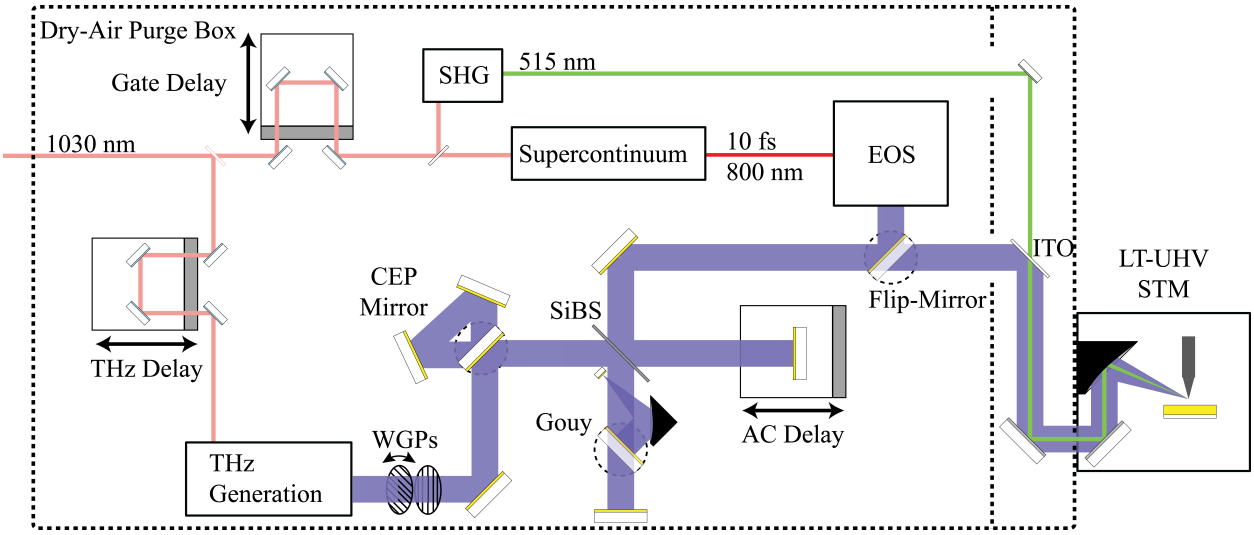

Figure 4.7: Optical setup for THz-STM and THz waveform characterization. SHG – second harmonic generation (in BBO); EOS – electro-optic sampling; AC – autocorrelator; LT-UHV STM – low-temperature ultrahigh-vacuum scanning tunneling microscope; ITO – indium tin oxide, transparent conductor (50Ω/sq) on a BK7 glass substrate; SiBS – silicon beamsplitter; WGPs – wire-grid polarizers (10 µm wire width, 30 µm spacing).

Inversion of the peak field is governed by a set of mirrors that can alter the THz beam path between odd and even number of bounces (Figure 4.7). The current optical setup uses the 'Mirror Up' configuration, defined by an odd number of reflections in the THz beam path, to generate primarily positive current. The 'Mirror Down' configuration is defined by an even number of reflections and typically generates negative current. A pair of wire-grid polarizers (Figure 4.7) are used to attenuate $E_{\mathrm{THz,pk}}$, scaling V_{pk} proportionally. (ii) The Michelson interferometer setup is equipped with a pneumatic mirror in the stationary arm that is capable of inverting ϕ_{CEP} through the use of the Gouy phase shift experienced at an optical focus. By directing the stationary arm into a 90° off-axis parabolic mirror, we focus the THz pulse to a gold end mirror that reflects the pulse back with a phase change of π. Time delaying the adjustable arm of the interferometer will cause the two pulses to interfere. The combination of interference between two pulses of the same phase or two of the opposite allows us a reasonable amount of waveform construction freedom to optimize the shape of $V_{\mathrm{THz}}(t)$ for THz-STS measurements.

4.2.3 THz Tunneling Spectroscopy

Investigation of the sample LDOS with THz-STM follows a similar procedure as it does

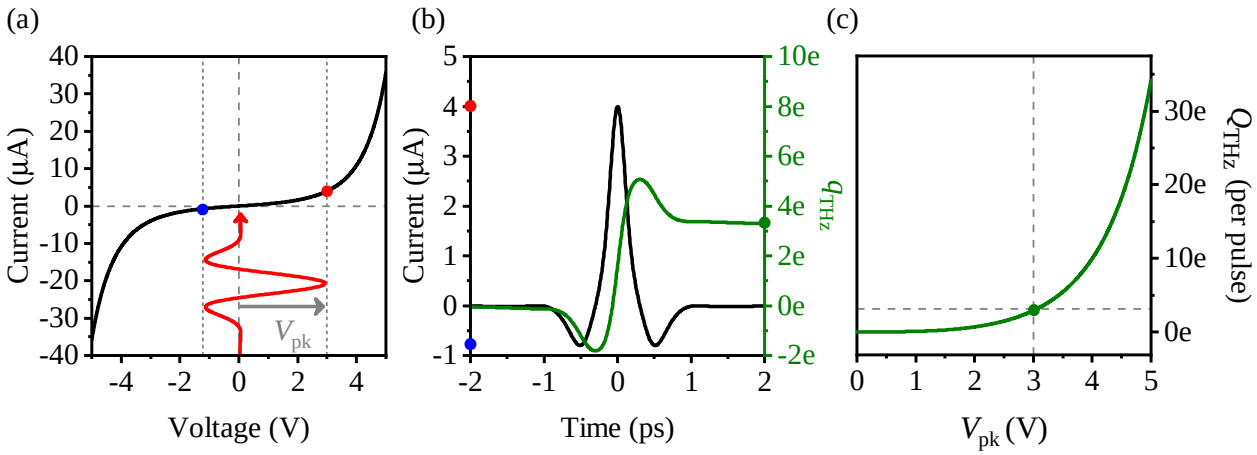

Figure 4.8: Terahertz-induced charge rectification across an STM tunnel junction. (a) Simmons model $I(V)$ (black curve) for a typical THz-STM tip height of z = 4 Å. In THz-STM, a transient voltage pulse $V_{\mathrm{THz}}(t)$ (represented schematically by red curve) acts on the $I(V)$ characteristic. Here, $V_{\mathrm{THz}}(t)$ is defined as a normalized oscillatory component multiplied by V_{pk}. The maximum and minimum voltages sampled by the voltage pulse are indicated by solid red and blue circles, respectively. (b) Ultrafast current pulse (black curve) generated by mapping the transient bias voltage onto the I-V characteristic in (a). Red and blue points indicate the extrema, as in (a). The green curve shows the running integral of the current transient, defined in the text as q_{THz}. The green point denotes the net rectified charge per pulse, defined in the text as Q_{THz}, which is detected in a THz-STM experiment. (c) The simplest spectroscopic measurement for THz-induced tunneling is to sweep V_{pk} and measure Q_{THz}.

for STS, where we define THz scanning tunneling spectroscopy as the method for extracting the energy-dependent distribution of electronic states of the tunnel junction. The typical parameters of interest for STS are replaced by time integrated variations that are concerned with the current pulse, $i_{\mathrm{THz}}(t)$, induced by the THz voltage transient, $V_{\mathrm{THz}}(t)$, rather than the static signal associated with a particular voltage. Developing a full suite of THz-STS modalities that are well understood in the steady-state is necessary to fully realize their time-dependent analogs. The challenges arise from the time integration of $i_{\mathrm{THz}}(t)$. $V_{\mathrm{THz}}(t)$ samples all $I(V)$ configurations along the waveform $V_{\mathrm{THz}}(t)$, so that all nonlinearities in $I(V)$ between $I(V_{\mathrm{THz,max}})$ and $I(V_{\mathrm{THz,min}})$ are sampled in a single THz pulse. The information from each $I(V)$ feature is convoluted together by the STM electronics according to Equation 4.4.

In analogy to conventional STS, where the current is measured as a function of voltage, we record the average rectified charge as a function of peak field strength, $Q_{\mathrm{THz}}(E_{\mathrm{THz,pk}})$. The peak voltage applied to the junction, V_{pk} is directly proportional to $E_{\mathrm{THz,pk}}$, allowing us

to select a region of the $I(V)$ to sample, as shown in Figure 4.8(a). The current induced by $V_{\mathrm{THz}}(t)$ is determined by both the shape of the voltage transient as well as $I(V)$, which often produces both negative and positive current contributions. An example of a bipolar current response is shown in Figure 4.8(b). The minimum and maximum currents are defined by how far $V_{\mathrm{THz}}(t)$ sweeps up and down the $I(V)$. The STM electronics lack the bandwidth to resolve the instantaneous current, and instead are sensitive to only its rectified component. Recording the $Q_{\mathrm{THz}}(E_{\mathrm{THz,pk}})$ signal results in our '$Q_{\mathrm{THz}} - E_{\mathrm{THz,pk}}$ curve' shown in Figure 4.8(c). A complete $Q_{\mathrm{THz}} - E_{\mathrm{THz,pk}}$ curve is typically sampled for both positive and negative $E_{\mathrm{THz,pk}}$. Our procedures for extraction $I(V)$ from $Q_{\mathrm{THz}}(E_{\mathrm{THz,pk}})$ will be detailed later in the thesis.

4.2.4 Double-Pulse THz-STM Measurements

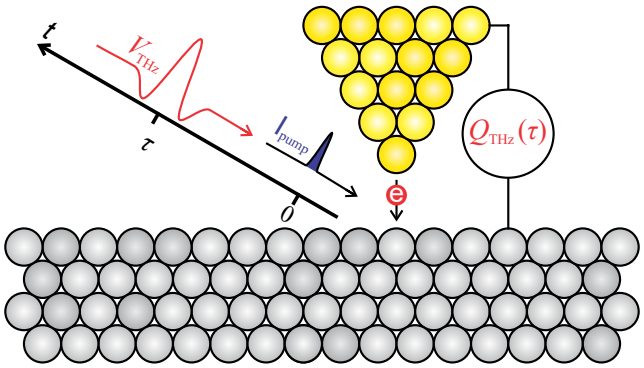

Figure 4.9: Schematic depicting an optical-pump/THz-STM-probe measurement of a transient $I(V)$. The pump pulse is absorbed by the sample at $t = 0$, triggering a modification of the $I(V)$ within the pump intensity envelope ($\mathrm{I_{pump}}$). The evolution of the junction is read out via the rectified current ($Q_{\mathrm{THz}}(\tau)$) generated by a time-delayed THz voltage probe (V_{THz}).

Our primary approach to time-resolved THz-STS in this thesis is optical-pump/THz-probe measurements utilizing femtosecond NIR or optical pump pulses, as shown in Figure 4.9. The femtosecond pump pulse triggers the onset of dynamics in the system. Analyzing these experiments will require a new analytical tool to extract the time-dependent LDOS information. In an excited-state scenario, it will not be sufficient to treat the $I(V)$ as if it matches what would be measured by conventional STM. New features in the density of states may arise and the filling of the LDOS may change to an unknown degree. Ultimately, we aim to extract the time-dependent differential conductance describing the behavior of

electronic populations within sample surfaces, nanostructures, and molecules with atomic spatial resolution.

An additional route to inducing dynamics is to pump the system either via the field of a THz pulse (rather than that of an optical or NIR pulse) or via ultrafast THz-driven charge injection. I have described how the THz pulse meets the criteria for interacting with the junction in the strong-field regime, but that is ultimately a result of having sufficient field strength to achieve $\gamma < 1$ combined with the work function defining the relevant energy scale. However, if the sample is predisposed to low-energy excitations (e.g., phonons) with resonances in the THz frequency range, then resonant or multi-photon pumping may occur that can be explored in THz-pump/THz-STM-probe experiments.

Alternatively, autocorrelation measurements using the Michelson interferometer shown in Figure 4.7 involve controlling the time delay of two identical THz pulses at the STM junction. In these experiments, the first pulse may drive tunneling that perturbs the sample in a way that can be measured in the current stimulated by the second pulse. THz autocorrelation measurements can be used to estimate the duration of the THz-induced current [5], track the vertical oscillations of single molecules [7], and detect coherent acoustic phonons in thin films of Au(111) [216]. Unlike optical-pump/THz-STM-probe experiments, autocorrelation experiments have two THz pulses in the junction simultaneously. The measured current is nonlinearly dependent on field strength and the fields of the two pules will interfere when they are close together in time. Near time-overlap, constructive and destructive interference changes the resulting current pulse. Therefore, extraction of information is typically performed at delay times away from $\tau = 0$ for pump-probe measurements. Alternatively, estimates of the current pulse duration are based on the width of the autocorrelation peak near $\tau = 0$.

In our system we have also used autocorrelation measurements to determine the quality of our THz alignment to the STM junction. The nonlinearity of the tunnel current leads to extreme sensitivity to the strength of the THz field. The strength of the pulse from each arm of the autocorrelator should be the same, such that the autocorrelation, $Q(\tau)$, is symmetric, where τ is the delay between pulses. However, if there is an asymmetry in the field strength between pulses, then the autocorrelation trace will develop an asymmetric temporal response. Our system involves several configurations that allow us to change the peak of the THz electric field; thus, a method for determining the quality of the alignment

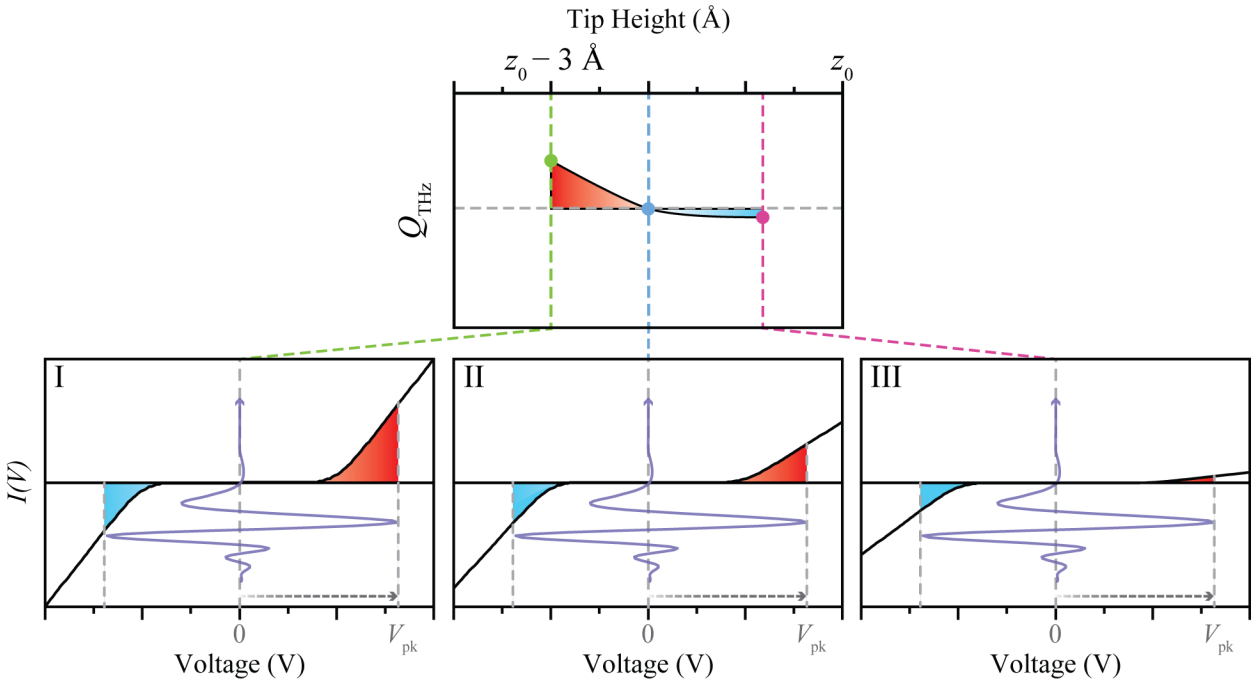

Figure 4.10: Illustration of a THz-STS vertical spectroscopy measurement. The experiment is initialized at a height $z_0 - 3$ Å, then Q_{THz} is recorded while the tip is retracted. In position (I), the positive THz-induced current contribution due to features at positive voltage in $I(V)$ outweighs the negative equivalent, resulting in $Q_{\mathrm{THz}} > 0$. At position (II), the positive nonlinearity of $I(V)$ has decayed more than the negative with increasing z, so the two THz-induced current contributions are equal in weight, producing $Q_{\mathrm{THz}} = 0$. The decay trend continues into position (III), where the positive side of $I(V)$ is almost zero and $Q_{\mathrm{THz}} < 0$.

in these configurations is extremely useful.

4.2.5 Barrier Spectroscopy

STS measurements typically focus on energetic distribution of the LDOS. However, early studies in the development of STM relied on measuring the characteristic exponential decay of the current as proof of tunneling [80]. From these measurements, the barrier decay rate, κ, and the apparent barrier height, Φ, can be extracted [217], where Φ is an intrinsic characteristic of the sample associated with its work function. Measurements of the LDOS acquired at different tip positions in the same tip-height plane and those performed out-of-plane as a function of tip height are complimentary and provide a full three-dimensional picture of the electronic density of states.

In THz-STS, we can perform analogous experiments: we record the THz-induced tunneling current as the tip height is changed, i.e., $Q_{\mathrm{THz}}(z)$, also referred to as a '$Q - z$ curve'.

Recall, for THz-STM experiments, it is typically necessary to approach the tip toward the sample by a substantial distance compared to conventional tip heights ($\sim$3$-$4 Å relative to a typical tip height of approximately 1 nm). The exponentially increasing THz-STM signal comes from the scaling of *individual* features in the LDOS and $I(V)$. Retracting the tip from the surface decreases the steepness of the nonlinear components in $I(V)$, resulting in reduced total signal, despite the THz pulse sampling the same voltage range. In extreme cases, the vertical extension of LDOS features present at THz-STM tip heights may be so localized that they are not visible at the higher tip heights where conventional STM operates [18]. A signature of this effect can be seen in a sign change in some $Q-z$ curves, which occurs at a height where the balance between positive and negative contributions to the THz-induced current switches. An example is shown in Figure 4.10, where the vertical decay distance of the $I(V)$ nonlinearity at positive voltage is much faster than its counterpart at negative bias, leading to a sign change in $Q_{\mathrm{THz}}(z)$. The THz-induced current becomes exclusively negative as the tip approaches the STM-operation height of z_0.

The decay coefficient, κ, may be extracted from THz-STM measurements in conjunction with $Q-E$ spectroscopy and the extraction of $\mathrm{d}I/\mathrm{d}V$. With a numerical representation of $I(V)$, $Q_{\mathrm{THz}}(z)$ can be simulated by multiplying the features in $I(V)$ by $\exp(-2\kappa_n z)$, where κ_n is the decay coefficient of the nth LDOS feature. The simulations of $Q-z$ can then be fit to the experimental data, where the fit parameters are the κ_n. Combining $Q-z$ and $Q-E$ spectroscopy allows THz-STS to be applied across all three spatial dimensions of the LDOS. An example on how we applied these two techniques is presented in Chapter 6.

4.2.6 Multi-Image Analysis

In STS, the differential conductance can be mapped out spatially by applying a modulation, dV, on top of the bias, V_{DC}, during an STM scan and recording the corresponding current modulation image. When surface defects are present, scanning large regions reveals standing waves associated with surface electrons scattering off of defects and constructively (or destructively) interfering on the length scale associated with the Fermi surface-momentum at the energy level of V_{DC}. These quasi-particle interference (QPI) maps [193] give STM the tools required to extract momentum information from a sample's surface electrons, thereby gaining access to information typically reserved for techniques like angle-resolved-photoemission-sampling (ARPES).

While scanning the tip across the sample surface to create a THz-STM image, the rectified current measured at each pixel, p_n, contains information regarding the LDOS in the voltage range probed by the THz pulse. At each tip location in the image, the junction LDOS may change, while the shape of V_{THz} is assumed to remain constant. (As an aside, potential changes to the waveform may be used as another type of probe, but are beyond the scope of this work [19]). As the the tip moves to new locations over the sample, the distribution and filling of unoccupied and occupied states dictates the net THz-induced current detected at a given pixel, which may be either positive or negative. This is unique to THz-STM, which applies a bi-directional voltage pulse that drives both positive and negative currents.

Multi-image analysis can be performed by acquiring many images, i.e., image$^{(o)}$ ... image$^{(i)}$, of the same region at different incident $E_{\mathrm{THz,pk}}$, denoted by $E^{(i)}_{\mathrm{THz,pk}}$ and $V^{(i)}_{\mathrm{pk}}$. The data in the pixels, $p^{(i)}_n$, of the image set form a series of curves, $Q(V^{(i)}_{\mathrm{pk}}, p_n)$ at fixed pixel position p_n that can be used to extract the LDOS at each pixel. The resulting three-dimensional map contains $\mathrm{d}I/\mathrm{d}V$ across the entire V_{pk} axis, allowing the LDOS to be imaged over a large voltage range at ultralow tip-sample distances, revealing previously inaccessible LDOS distributions with extremely short vertical decays. Moving the imaging plane vertically and performing constant-height THz-STM imaging enables a type of THz-STM tomography, where the weighting of the LDOS features (e.g., electronic orbitals) decay at different rates. By applying the methodology of multi-image analysis, a 4-dimensional map of the LDOS would be generated, revealing the spatially dependent barrier height. If the description of κ is expanded to included the in-plane electron momentum, $\kappa = \sqrt{2m\Phi/\hbar^2 + k_{\parallel}^2}$, the same data set could also lead to a map of the energy-momentum landscape within the Brillouin zone [218]. A multi-image analysis approach to THz-STS is compelling as the technique becomes more developed and the overall stability of the measurements is improved. Extending THz-STM imaging to large length scales, on the order of $10-100\,\mathrm{nm}$, could lead to THz-driven measurements of the surface energy-momentum relationship (analogous to QPI) that could then be explored in ultrafast pump-probe measurements.

4.2.7 THz Voltage Characterization

Photoemission Sampling

Broadband phase-resolved detection of the THz pulse temporal profile at the tip apex was performed using ultrafast photoemission sampling [10, 11] (PES; Figure 4.11). A 230 fs

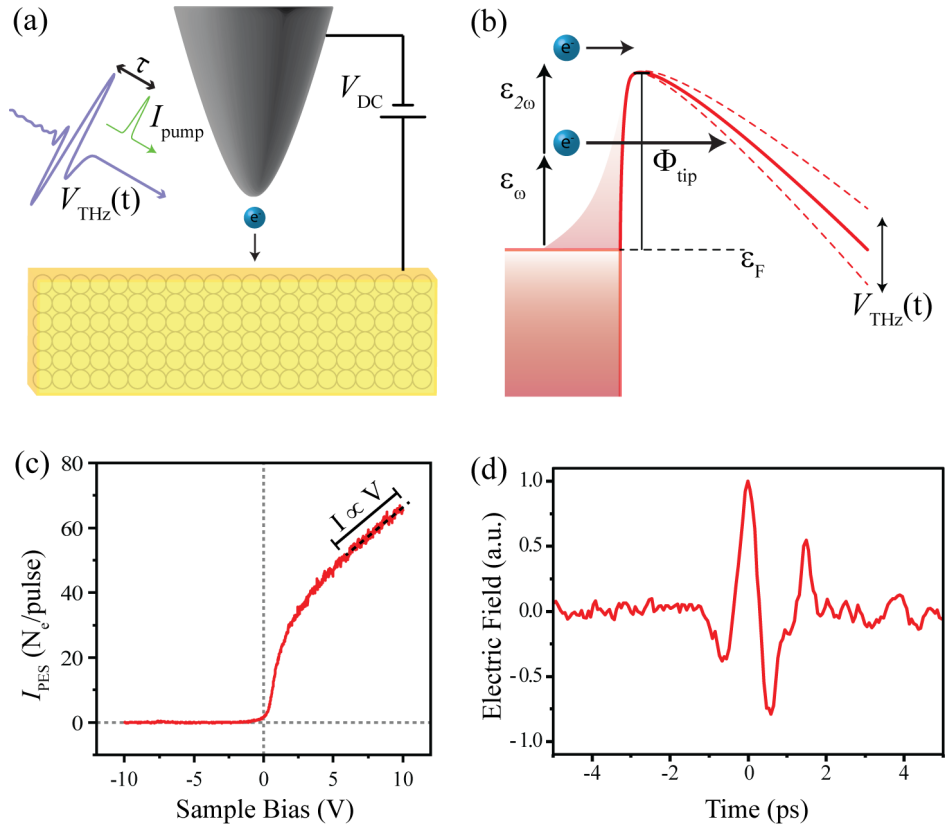

Figure 4.11: THz near-field waveform measurement by PES. (a) PES measurement geometry in which an optical pulse (I_{pump}, $\lambda = 515$ nm) photoexcites free-carriers in an STM tip held at postive bias, V_{DC}, producing an ultrafast photocurrent. A THz probe pulse follows at a delay-time, τ, and couples to the STM tip. (b) Barrier schematic of the photoexcited junction. Multi-photon absorption promotes electrons from the Fermi level to higher energy levels of the tip, allowing for tunneling and photoemission. The THz probe pulse simultaneously applies a bias modulation that affects the total current generated during photoemission by changing the energy landscape proportional to $V_{\text{THz}}(t)$. (c) Average ultrafast PES current, I_{PES}, measured as a function of V_{DC}. A region of linear slope is identified near $V_{\text{DC}} = 10$ V. (c) THz near-field waveform measured with PES at $V_{\text{DC}} = 10$ V with an optical pulse energy of 30 nJ and a pulse duration of < 230 fs.

duration (FWHM) photoexcitation pulse was picked off from the regenerative amplifier laser system and frequency doubled in a β-BBO crystal to a center wavelength of $\lambda = 515$ nm before being sent to the STM tip (Figure 4.11(a)). The photoexcitation pulse and THz pulse propagate collinearly to the STM tip. For PES, the tip is retracted by $\sim$10 nm$-$1 µm from the sample surface with $V_{\mathrm{DC}} = +10V$. At this bias voltage, the $I(V)$ of the STM junction is approximately linear (Figure 4.11(b)). In the linear regime, modulation of the tunneling barrier is directly proportional to the near-field THz voltage transient (Figure 4.11(c)), enabling direct mapping of the near-field waveform at the tip apex. Recent measurements of the THz near field by PES [10, 11] attempt to determine the absolute voltage applied across the junction during THz-STM experiments. However, the results of Abdo *et al.* suggest the atomic structure of the tip apex is what ultimately determines the field enhancement. Our experiences corroborate their observation that the field enhancement depends on the microscopic tip structure. In preparation for the experiments presented in Chapter 6, many hours of minor tip-form crashes were performed to carefully prepare the last atoms of the tip. Assuming the tip is mesoscopically sharp (radius of curvature $<$ 100nm), fine tip shaping can be performed with 20 Å approaches at $V_{\mathrm{DC}} = 0$. More recently, we have also found success while performing tip forms while the THz illuminates the junction, with the field strength set to at least 50% of maximum (V_{pk} on the order of 5V).

The PES photoexcitation pulse is sufficiently short to omit convolution effects when sampling the THz near-field waveform [166]. Comparing to far-field EOS measurements (Figure 4.12(a)), the measured asymmetry between the main peaks of the THz near-field waveform (Figure 4.12(b)) remains the same at approximately 20%. If no asymmetry were present, analysis of THz-STM data (discussed further in Chapters 6 and 7) would be more challenging, if not impossible. For the modeling performed in Chapter 6, the 20% asymmetry was sufficient. The spectral amplitude and phase of the EOS waveform is shown in Figure 4.12(c). In the region between 0.2 and 2.5 THz (where sufficient spectral amplitude is observed), the spectral phase is well behaved and agrees with THz spectroscopy measurements performed by other members of the lab (specifically, in time-resolved THz spectroscopy of GaAs in the range 0.5$-$2.5 THz that agreed with the literature). The extra oscillation cycle in the PES measurement is consistent with a loss of spectral width, as seen in Figure 4.12(d). It may indicate a tip resonance, or equivalently, a reflection of the THz wave off structure on the scale of the wavelength. An optical image of the tip taken at 10$\times$ magnification (Figure

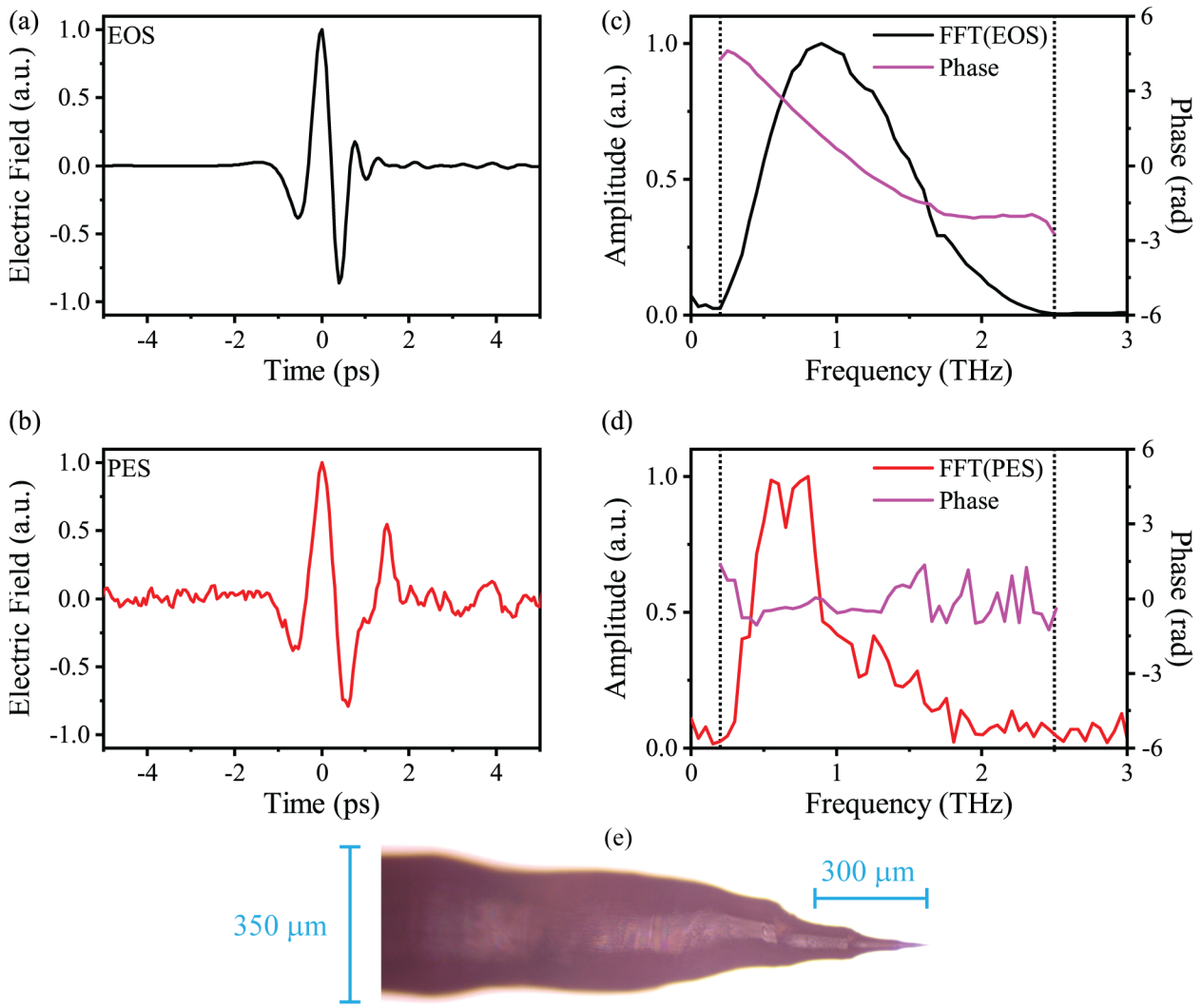

Figure 4.12: Comparison between THz electric far-field transient and near-field voltage transient. (a) EOS measurement of the THz far-field waveform. (b) PES measurement of the THz near-field waveform. (c) EOS spectral amplitude (solid black curve) and phase (solid purple curve) calculated by FFT. (d) PES spectral amplitude (solid red curve) and phase (solid purple curve) calculated by FFT. (e) Optical image of the tungsten-wire STM tip used to record the THz-STM data presented here and in Chapter 6. The tip was ~3 mm long with a diameter of 350 µm, and hosted a number of features on the scale of the THz wavelength. Dashed vertical lines in panels (c),(d) indicate the boundaries to the region of most trustworthy data: 0.2 THz to 2.5 THz, defined by the EOS spectral amplitude.

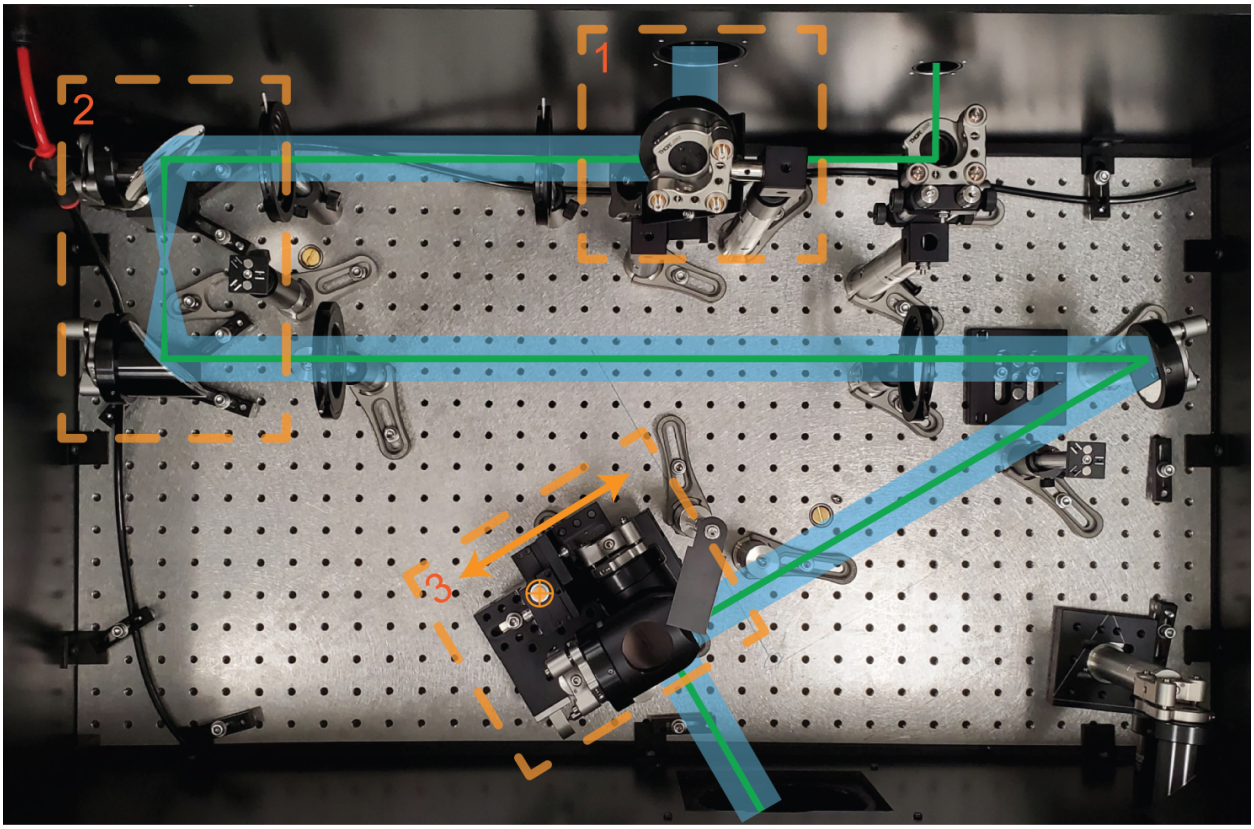

Figure 4.13: An overhead image of the THz-STM coupling setup. The THz beam path is indicated in blue and the optical beam path is shown in green. The setup is enclosed in a purge box with dry air supplied via the red inlet located at the left edge. Orange indicators show the final stage motion: an arrow for translation along the input beam direction and circles with a cross for vertical translation. The setup is constructed on a 24-inch by 48-inch optical breadboard (Newport PG-24-4-ML) and is removed during microscope bakeouts.

4.12(e)) indicates some apex structure from the etching process, e.g., several shallow cusps separated by distances of ∼150 µm. In the future, a systematic approach for tip preparation could be beneficial for THz-STM experiments, as it may lead to reproducible voltage transients.

Coupling Setup

The coupling setup is the final stage between THz and optical light generation and STM scan head illumination. An illustration of the beamline is shown in Figure 4.13 with major elements highlighted. In box 1, a periscope directs the THz pulses downward onto an optically transparent BK7 glass substrate coated with an optically transparent conductive ITO layer that acts as a broadband THz reflector. The ITO-coated window is used as

a beam combiner for the THz, which is reflected, and the optical pump for PES, which is transmitted. The ITO-coated window causes a slight loss in optical power but allows the majority of the optical beam power to transmit through. Following transmission, the optical pulses propagate collinearly with the THz pulses. A pair of parabolic mirrors (box 2) are used to recollimate the THz beam, compensating for Rayleigh diffraction (discussed in Chapter 3). The focus between the parabolic mirrors can also be used during initial alignment to ensure overlap of the optical and THz beamlines. The input apertures to the parabolic mirrors were placed as guides, e.g., to reintroduce the THz and optical pulses to the coupling setup after the breadboard it is built on has been removed and replaced during an STM bakeout event. The THz beamline hosts many configurations (see Figure 4.7); to achieve optimal performance during THz-STM experiments it was important to ensure that the pointing of the THz is stable when changing between setup configurations. The parabolic mirror focus is thus also used in combination with the THz camera introduced in Chapter 3 to visualize the alignment of beamlines in all the configurations. The final set of optics is a periscope (box 3) with both vertical and perpendicular translation stages. The stages allow the beam path to be optimized for alignment into the STM scan head by providing a means to translate the beam without affecting its pointing. Course alignment of the coupling mirror can be performed by imaging the STM tip through the parabolic mirrors on the scan head or by translating the beam onto the reference plane of the scan head. For finer adjustments, the STM tip can be imaged through the right-hand-side of the scan head using a camera (see Figure 2.15 for scan head beam path). The scan head is illuminated by the coupling mirror and provides light for the camera to image the STM tip and junction. The alignment apertures provide a reference for the center of the beamline and are visible to the camera. Using the camera, the coupling stage alignment can be adjusted to center the STM tip within the aperture. Alignment in this way provides a repeatable starting position for fine tuning the input pointing. Final optimization of the input alignment is done by adjusting the tilt of the final coupling mirror to achieve peak THz-STM signals, and requires that the STM be in tunnel contact. Not pictured is the setup lid, which includes an access port above the coupling mirror for direct access to the stage and mirror controls and encloses the coupling setup for dry-air purging.

Chapter 5
Atomically Precise Graphene Nanoribbons

5.1 Surface-Assisted Bottom-Up Assembly

Synthesis of graphene nanoribbons (GNRs) via bottom-up surface-assisted growth produces near-defect-free atomically precise nanographenes [1]. If a GNR is considered a macromolecule separable into an array of repeating units, then engineering its molecular building-blocks gives control over the atomic arrangement of the GNR lattice [2]. Figure 5.1 illustrates the process of growth with molecular building blocks, e.g., DBBA, where a collection of free molecules on an Au(111) surface are assembled into a 7-atom-wide armchair-edge GNR (7-AGNR). In this case, the DBBA precursor molecule contains two bromide (halogen) atoms that experience a catalytic interaction with the metal surface, resulting in a reduction of the dehalogenation barrier by several eV. This leads to the cleavage of the bromide atoms, exposing a carbon on both sides of the molecule. Other halogen atoms, such as iodine, and other metal surfaces, such as Ag and Cu, have different dehalogenation barriers and catalytic strengths that provide a degree of tunablility in the growth process [219, 220]. The growth process progresses by heating the surface to 200 °C, at which point the molecule intermediates gain enough thermal energy to diffuse across the surface. The halogen-free DBBA form single carbon-carbon bonds at the radical site along the center axis of the molecule via an Ullmann coupling reaction [221–223], forming linear polymers of repeating DBBA molecules. The final stage of growth occurs at 400 °C, where the hydrogen atoms that separate polymer units are removed through surface-assisted cyclodehydrogenation to allow a network of carbon-carbon bonds to form.

There are several factors that contribute to the growth process, some of which we can optimize to meet our needs. The precursor molecules migrate about the surface randomly, due to thermal diffusion, and the likelihood that they meet a fellow precursor or a polymer is at the heart of controlling the length of the GNRs. Several coinage metals have been used as

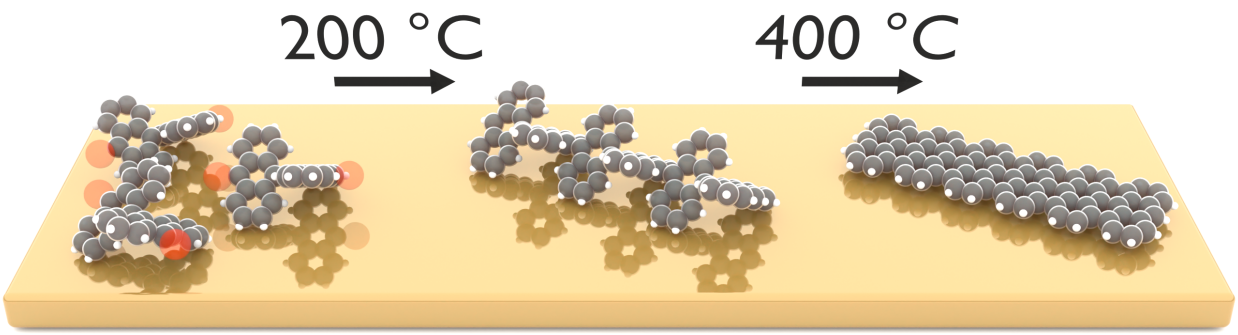

Figure 5.1: The three stages of surface-assisted bottom-up assembly of graphene nanoribbons. From left to right: precursor molecules deposited onto a metallic surface, polymer chains formed after thermal diffusion, and atomically precise graphene nanoribbons formed via cyclodehydrogenation.

the catalytic surface in the bottom-up fabrication strategy for GNRs [224–226]. The choice of metal surface plays a significant role in the growth process by altering the mobility of precursor molecules and polymer chains. If the molecule is unable to link to another molecule it may become passivated by hydrogen from the chamber or surface [227]. The molecule mobility can be limited by its interaction with the surface, which can be dictated by the surface reconstruction. Distinctly different growth results have been observed for DBBA deposited onto different Cu crystal faces, polymer structures on Cu(111) and self-assembled monolayers on Cu(110). The differences are attributed to the anisotropic surface of Cu(111) that leads to a combination of early temperature onset for dehalogenation and a significant adsorption energy between carbon atoms and the Cu surface atoms [228]. Similarly, anisotropic interactions with surface features have been observed to promote preferential growth along the rows of Au(110) [224] and terrace edges of Au(111) [229] and Au(788) [230]. Temperature plays a significant role in the GNR formation process by allowing the molecules and polymer chains to overcome energetic barriers that lead to the next stages of the process. The metal surface acts as a catalyst for dehalogenation and cyclodehydrogenation, but a minimum thermal energy is required to initiate the processes. On the Au(111) surface, partial dehalogenation occurs at 380 K−450 K. In this state, DBBA dimer formation is thermodynamically favored and can limit the formation of longer chains. Increasing the temperature to 600 K−720 K induces cyclodehygenation of neighboring anthracene subunits [231]. The formation of dimer structures and cyclodehydrogenation between neighboring anthracene begins to play a signfi-

cant role at low deposition coverages compared to higher densities, where polymer formation is more likely and fusion of anthracenes is less favorable between neighboring polymers and ribbon structures [229, 232].

5.1.1 Deposition

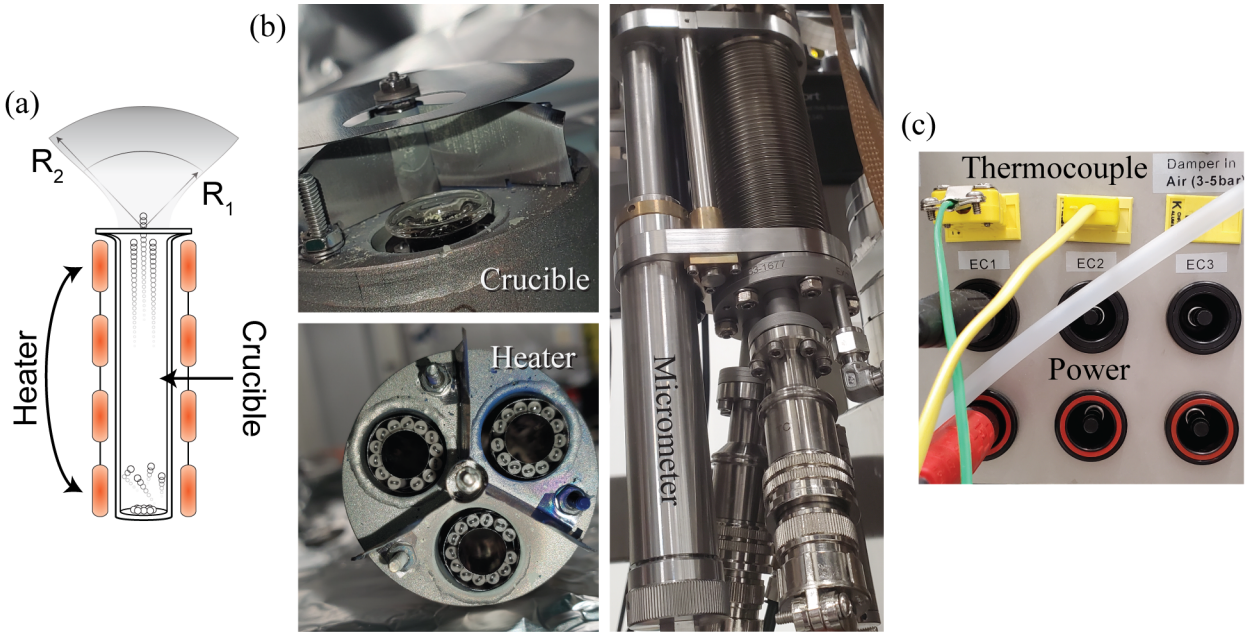

Figure 5.2: (a) Schematic for a Knudsen-type effusion cell, wherein a quartz crucible is heated to evaporate material with a well defined trajectory. (b) In our triple-OLED evaporator, each cell chamber has an individual heater, allowing for isolated evaporation of the material from each crucible. A bellows, equipped with a micrometer, is attached to give control over the radial position of the cell during sample production. (c) Media panel for connecting external power supply and K-type thermocouple. The power supply and thermocouple temperature monitor (green) must be manually moved to whichever cell going to be used.

Thermal evaporation of precursor molecules is performed using a Knudsen-type effusion cell while under ultrahigh vacuum conditions. Figure 5.2(a) shows a cartoon schematic of such an evaporator cell. A heater is used to indirectly heat the precursor material held inside a quartz crucible, as shown in Figure 5.2(b). Under ultrahigh vacuum conditions, the mean free path of the gas-phase material is expected to be much larger than the opening of the crucible, resulting in ballistic-like motion for material leaving the evaporator, as illustrated in Figure 5.2(a). Over the macroscopic distances that separate the evaporator and the substrate surface, the cloud of precursor vapor is described by the density of material

occupying the surface of a sphere with radius R.

$$\rho = \Gamma 4\pi R^2 \quad \text{at const}\, T_{\text{ev}}\,, \tag{5.1}$$

where T_{ev} is the evaporation temperature, Γ is the deposition rate, and R is the distance from the crucible exit. Determination of Γ is achieved using a quartz microbalance (QMB) resonator circuit positioned at the sample location using a retractable arm. Misalignment of the QMB with respect to the substrate position for deposition would misrepresent the deposition rate according to the change in radial position. The corrected rate is proportional to the ratio of the two surface areas,

$$\Gamma_{\text{sample}} = \Gamma_{\text{QMB}} \frac{R_{\text{QMB}}^2}{R_{\text{sample}}^2}\,, \tag{5.2}$$

where R_{sample} represents the substrate position and R_{QMB} the QMB position. The relationship is nonlinear, leading to significant changes in deposition rate as the radial position is changed. The material properties determine the evaporation temperature and the amount of material placed in the crucible governs the density of molecules that are evaporated, resulting in the substrate position being the only means of controlling Γ. Several measurements of the deposition rate acquired at different evaporator temperatures are listed in Table 5.1. An important observation is the reduction in deposition rates that were experienced as evaporation was performed on consecutive days without adding new material to the crucible. Rates of $\sim$3$-$5 Å/min with a deposition times of $\sim$3$-$8 seconds resulted in reasonable submonolayer coverage; however, the temperature for a given rate varied as crucible material was evaporated, consistent with a lower density being evaporated at a given temperature. Alternatively, lower quality material (i.e., a source with more molecular contaminants) could have a lower evaporation temperature and thus higher evaporation rates above T_{ev}. This may lead to a subsequent decrease in material available for evaporation (i.e. lower deposition rates in later trials). Increasing T_{ev} could potentially degrade the precursor molecules and should be avoided, therefore, the evaporation rate should be measured each time a sample is being produced to determine a deposition time to achieve target thickness. The evaporation temperatures for DBBA are reported to be between 150°C$-$200°C [231, 233]. However, the temperature calibration for each evaporation cell is different and deposition rates are the most reliable means of reproducing sample growth.

3-31-2022		4-01-2022		4-09-2022	
T (°C)	Γ (Å/min)	T (°C)	Γ (Å/min)	T (°C)	Γ (Å/min)
87.5	1.87	96.1	7.02	89.0	0.49
92.5	3.75	97.5	7.49	90.0	1.18
94.0	5.62	98.5	9.37	91.2	1.64
94.8	7.49	99.7	10.0	93.5	2.11
		99.9	11.24	94.0	3.55

Table 5.1: QMB Measurements of DBBA deposition rate as a function of temperature across multiple days. Temperature calibration between effusion cells very. We assume that our deposition temperatures are scaled relative to the expected deposition temperature between 150−200 °C.

5.1.2 Growth Conditions and Results

Sample production has two primary goals: first, GNR growth of sub-monolayer samples with coverages of less than 30% and, second, production of isolated GNRs with a variety of lengths. Low surface coverage is needed to ensure significant exposure of the Au(111) surface for STM tip preparation. A clean, sharp STM tip leads to STS characterization of the surface and GNR electronic properties that are comparable to those found in the literature. Meanwhile, isolated ribbons reduce unintentional interactions between neighboring GNRs during THz-STM measurements. To achieve the desired sample quality, the substrate annealing rate, monomer density, and growth temperatures were optimized. Growth is controlled by the temperatures used to initiate the first and second GNR growth stages as well as the annealing rate used to heat the sample between temperature setponts. In our system, we use a radiative heater stage that is feedback-controlled using either the heater monitor or an external low temperature pyrometer (T_{limits}: 100°C−600°C). Initial growth settings included annealing to the sample temperatures listed in Figure 5.1 using the temperature reported by the heater stage thermocouple. The results from this procedure are shown in Figure 5.3(a), which was typical for successful growths where a waiting period of 5−15 min was implemented at each growth stage. Unsuccessful samples grown with this procedure yielded large networks of ribbons fused together in irregular ways (Figure 5.3(b)). Following a heater repair that changed the thermocouple temperature calibration, another procedure was developed to utilize continuous annealing from room temperature to max temperature and yielded more consistent results but required fine tuning of the temperature setpoint to achieve complete growth of GNRs. Figure 5.3 (c) and (d) illustrate the effect of successive

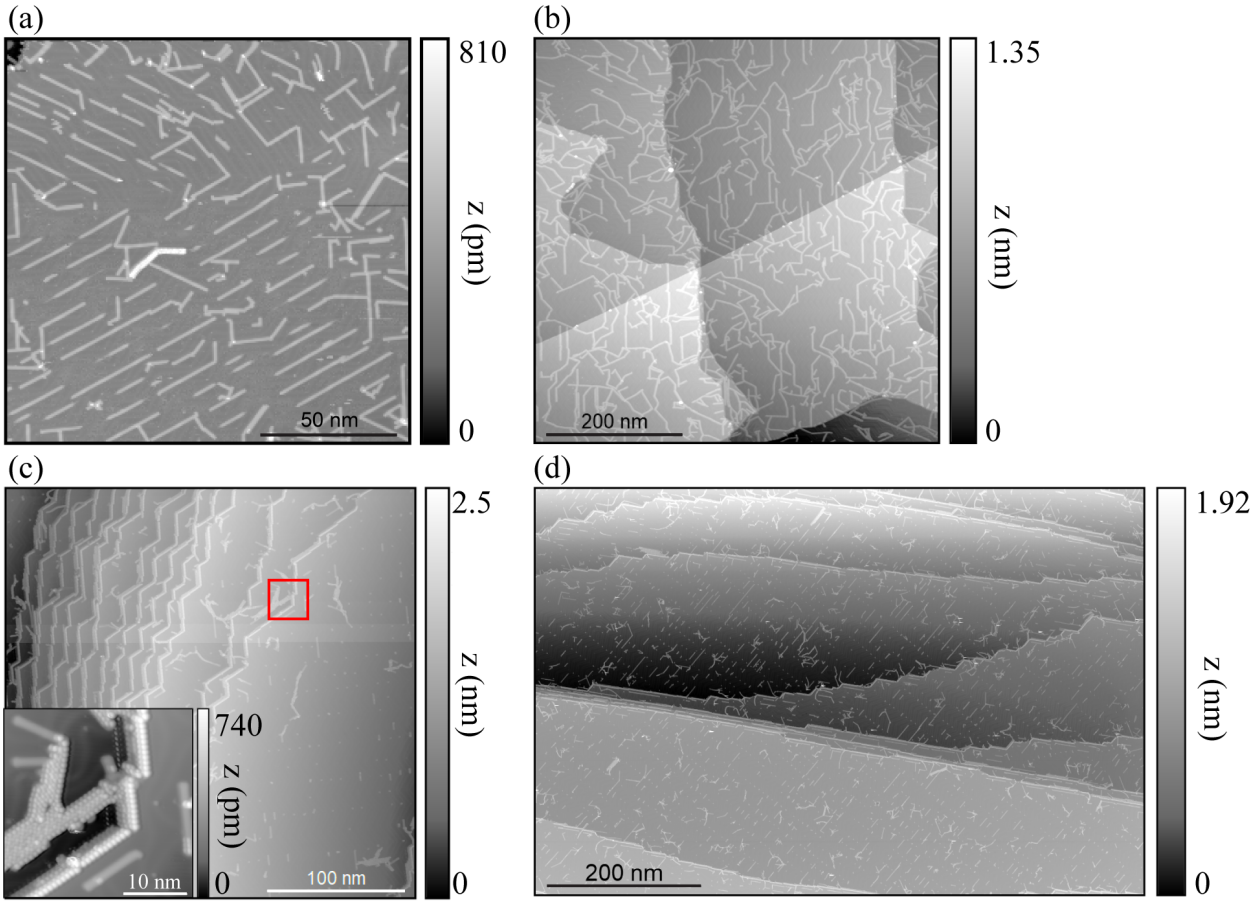

Figure 5.3: GNR samples produced under different growth conditions and procedures. (a) and (b), Results from using a slow annealing rate to transition between temperature setpoints where the temperature was held constant for several minutes. Results in (a) were deemed successful with long disconnected ribbons while the result in (b) are considered a failure due to the formation of large ribbon networks. (c) and (d), Results from a fast anneal rate from room temperature to final temperature setpoints (c, 370 K and d, 440 K). The sample in (c) showed significant clustering at the substrate step-edges and only produced polymers (inset). Results in (d) are considered successful with the formation of long disconnected ribbons spread across the sample surface. All images acquired in constant-current mode with parameters (a):, V_{DC} = -1 V and I_{DC} = -50 pA; (b): V_{DC} = -2 V and I_{DC} = -50 pA; (c): and inset, V_{DC} = 1.5 V and I_{DC} = 100 pA; (d): V_{DC} = 1.5 V and I_{DC} = 100 pA.

annealing cycles, each with a higher final temperature. While using a low-temperature pyrometer aligned to measure the sample plate temperature, the initial growth in Figure 5.3(c) showed significant clustering of GNRs in the intermediate polymer phase along the Au(111) terrace edges with a setpoint temperature of 390 °C. Annealing the sample multiples times (increasing the setpoint in 20 °C increments) up to a max temperature of 440 °C (with an annealing rate of 48 K/min) showed significant displacement of complete GNR products away from the step edges and into alignment across the terrace surface.

5.2 Scanning Tunneling Spectroscopy of 7-AGNRs

Electronic measurements of 7-AGNRs have been well documented across several publications [71, 233] and reviews [2]. The electronic band structure as well as the real-space distribution of the density of states have been calculated via DFT [71] and corroborated via STM and STS measurements [74]. Furthermore, dI/dV spectroscopy performed along a 7-AGNR has been used to investigate band dispersion via QPI [74], while GNR arrays have been investigated with ARPES [234, 235] and optical spectroscopy [71, 236]. In this section, electronic measurements of 7-AGNR samples grown in our system are presented and compared to those found in the literature. STS measurements are performed to characterize the electronic properties of our 7-AGNR samples, with measurements being performed in two modes: $\mathrm{d}I/\mathrm{d}V$ spectroscopy and $I(z)$ spectroscopy.

With the tip placed over a GNR, the applied bias is swept while applying an oscillating voltage bias with a peak-to-peak amplitude of 50 mV. Both the current ($I(V)$) and lock-in ($\mathrm{d}I/\mathrm{d}V(\mathrm{V})$) channels are recorded. A full picture of the $I(V)$ requires sweeping the applied bias across several ranges to capture the features at both low and high applied bias voltage. To avoid saturation of the current signal when increasing the bias scan range, the tip height was increased. Figure 5.4(a) shows $|I(V)|$ measured across several bias ranges from ± 0.6 V to ± 2.5 V.

The exponential dependence of the current on tip height (Equation 2.19) causes the current at increased tip height to be reduced more than it is increased by going to higher voltages. As a result, the features of the individual curves do not align by default. To ensure continuity of features in $|I(V)|$ at different tip heights, we measure the apparent barrier

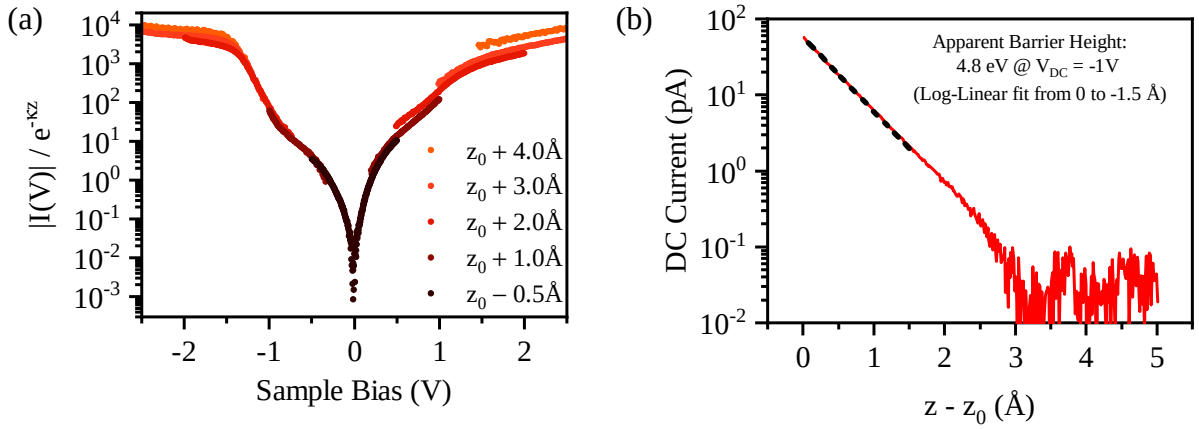

Figure 5.4: Tunneling spectroscopy of a 7-AGNR. (a) Wide-range $|I(V)|$ comprised of several curves acquire with increasing voltage ranges and tip heights. (b) Log-linear plot of the height-dependent current (solid red line) with corresponding logarithmic fit (dashed black line), $I(z) = \exp\big(-1.028\sqrt{\Phi_{\text{app}}}z\big)$. The $\mathrm{d}I/\mathrm{d}V$ spectra in (b) are acquired with bias modulation $V_{\text{mod}} = 50\,\text{mV}$ (peak-to-peak). In (a) and (b) the initial tip height, z_0, is set by the STM feedback loop with $I_{\text{DC}} = -50\,\text{pA}$ and $V_{\text{DC}} = -1\,\text{V}$.

height via an $I(z)$ measurement,

$$\begin{aligned} I(z) &= \exp(-2\kappa z) \\ I(z) &= \exp(-A\sqrt{\Phi_{\text{app}}}z) \end{aligned} \tag{5.3}$$

where $A = 1.028\text{eV}^{-1/2}\text{Å}^{-1}$. With the applied bias at -1 V and a current setpoint of -50 pA, the current is measured while the tip is retracted from the surface. Figure 5.4(b) shows the exponential decay of the tunnel current for increasing tip-sample distance. A fit to the data using Equation 5.3 resulted in $\Phi_{\text{app}} = 4.8$ eV. Our result is consistent with work function measurements of single layer graphene using tungsten tips [237]. Determination of the barrier decay allows each $|I(V)|$ trace in Figure 5.4(a) to be scaled to the relative tip height. After scaling the $I(V)$ curves, features appear at -0.7 V and +1.5V that correspond to the valence band (VB) and conduction band (CB) onsets. The onsets and transport gap of $\sim$2.3 eV are consistent with those reported in reference [74, 234]. The significant current present between the VB onset and 0 applied bias can be attributed to the Shockley surface state of Au(111), as has been reported by several publications [18, 75, 234].

Utilizing the atomic resolution of STM, we further acquire constant-current topographic maps of a 7-AGNR on Au(111) at applied bias voltages near the VB energy level (Figure 5.5(a)) and CB energy level (Figure 5.5(b)). Simultaneously, we record a $\mathrm{d}I/\mathrm{d}V$ signal to produce a map proportional to the real-space distribution of electronic density of states at

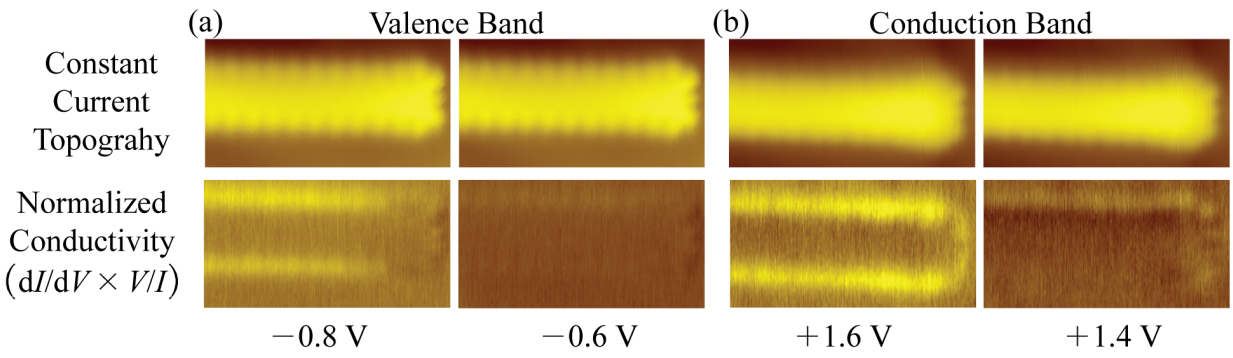

Figure 5.5: Constant-current topography and dI/dV imaging of 7-AGNR frontier bands. (a) Imaging with $V_{\mathrm{DC}} = -0.8$ V, just above the valence band resonance and $V_{\mathrm{DC}} = -0.6$ V, just below the onset. (b) Imaging with $V_{\mathrm{DC}} = +1.6$ V, just above the conduction band resonance and $V_{\mathrm{DC}} = +1.4$ V, just below the onset. dI/dV imaging performed with a bias modulation, $V_{\mathrm{mod}} = 50$ mV, measured peak-to-peak. Images acquired with $I_{\mathrm{DC}} = -50$ pA.

each bias voltage. The dI/dV maps show strong spatial localization of the current to the armchair edges of the GNR. Yet, scanning with the STM feedback loop engaged forces the tip height to adjust for any changes in current, e.g., compensating for the height of the GNR. Tip height adjustments during scanning may contribute to the signal recorded in the dI/dV channel. To rule out artifacts contributing to the spatial dependence of the dI/dV images, we perform a second set of scans that are below resonance. Significant suppression of the band signature at the ribbon edges is observed when the applied bias is moved 200 mV closer to 0 V, ruling out the possibility of significant artifacts contributing to the dI/dV signal.

To determine the origins of the localization observed at the CB and VB energy levels, we use DFT to calculate the VB, VB-1 and CB, CB+1 electron wavefunctions for a 7-AGNR in gas phase [238–241] (DFT calculations performed by our collaborators, see Methods of Reference [18]). The planar cross-sections in Figure 5.6 are calculated at a distance of 2.0 Å above the atomic lattice of the GNR. STM tip heights are expected to be on the order of 1 nm while the feedback loop is engaged. The red and blue regions of Ψ indicate a complex phase in the DFT calculation that the STM is insensitive to. Instead, the STM current detects changes in the probability density, $|\Psi(x, y, V)|^2$.

While the gas phase calculations are informative regarding the intrinsic spatial structure of Ψ, such as symmetry in the complex phase of the VB and CB+1, STM measurements require the GNR be adsorbed onto a surface. Bottom-up synthesis of GNRs on non-metallic substrates is still an on-going effort [2, 242]. Therefore, interactions with the substrate surface

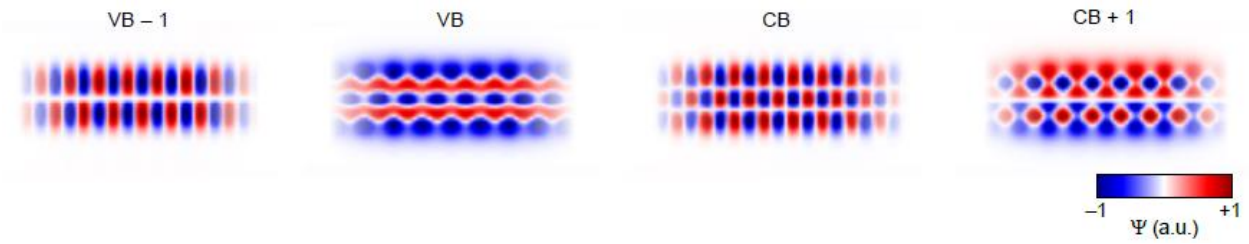

Figure 5.6: Simulated planar cross-sections of the electron wavefunction at several energy band resonances. The spatial distribution of the electron wavefunction, Ψ, for energies near the second valence band (VB–1), valence band (VB), conduction band (CB) and second conduction band (CB+1) is shown, calculated using density functional theory at a tip–sample distance of z = 2.0 Å. The calculation was performed with the 7-AGNR in the gas phase and the height is in reference to the atomic lattice of the 7-AGNR.

must be taken into account. In our experiments, GNR growth is performed on Au(111) surfaces, so further DFT simulations are performed. Calculations of $|\Psi|^2$ incorporating adsorption of the GNR onto an Au(111) surface are shown in Figure 5.7. In our calculations, the GNR is constructed with finite length and an extra hydrogen bound to the zigzag edge (CH_2) acts to terminate the wavefunctions. The calculations are performed across a range of energies, including across band edges, at positive and negative bias voltages. The heights of the cross-sections extend from 2.0 Å, the same height used to calcute the wavefunctions in Figure 5.6, to a more STM-accessible height of 5.0 Å. As a note on heights used in DFT calculations: the exact height is an extrapolation used to correct the artificial decay in vacuum of the charge density due to the localized basis [243] and therefore is reduced compared to experimental heights, likely by a factor ∼2.

$\mathrm{d}I/\mathrm{d}V$ imaging at band onsets near -0.8V and +1.6V in Figure 5.5 show a spatial distribution of signal matching the DFT simulations of $|\Psi|^2$ at elevated tip heights of 5.0 Å. Reference [74] attributes the difference in $|\Psi|^2$ between 2.0 Å and 5.0 Å to destructive spatial interference between complex phases of Ψ that alternate laterally across the ribbon. In particular, the VB and CB+1 exhibit rapid alternation at the center of the ribbon. The wavefunctions expand into the vacuum above the ribbon, leading to suppression of $|\Psi|^2$ at the interior of the ribbon, where interference is spatially symmetric. Consequently, the amplitude of the LDOS decreases as a combination of barrier decay and destructive interference. The exponential dependence of the tunnel current on tip height makes exploration of this

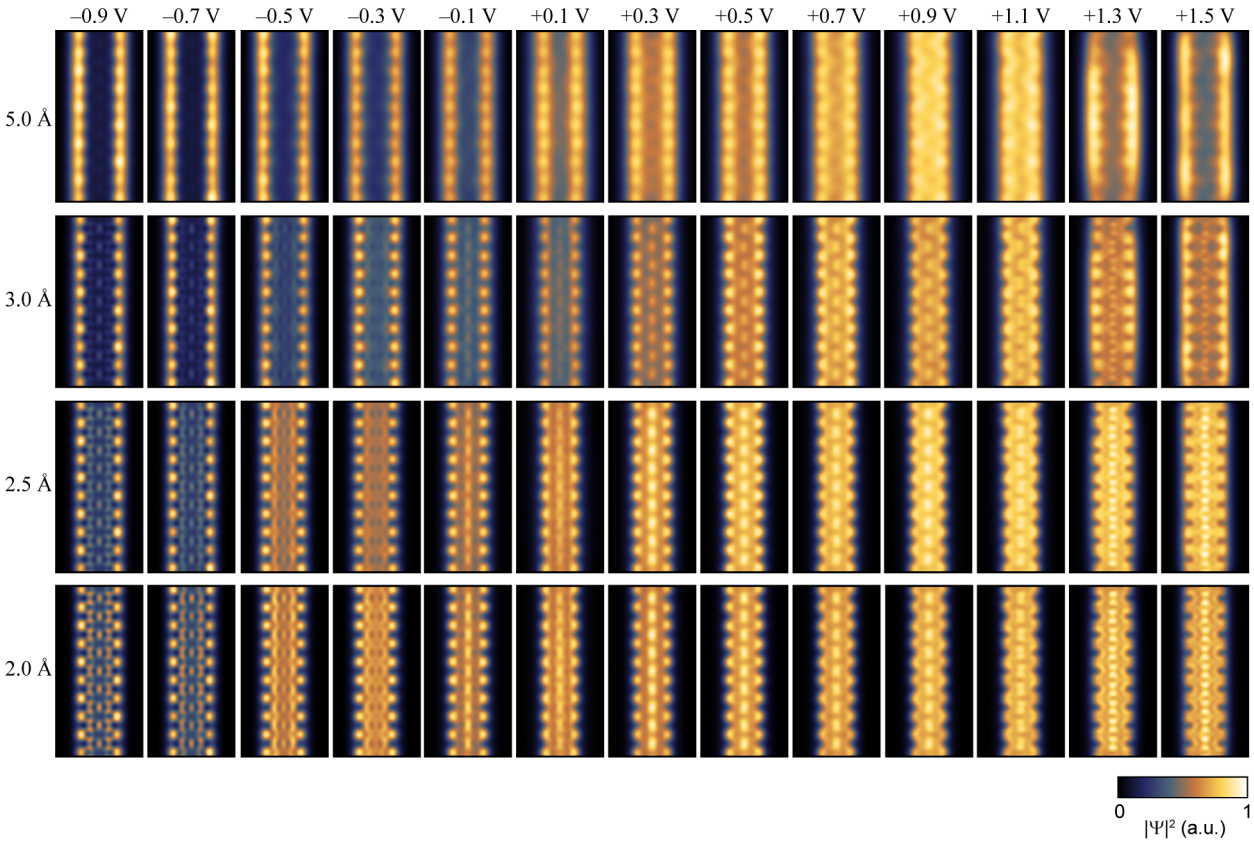

Figure 5.7: Simulated planar cross-sections of the probability density for a 7-AGNR as a function of distance and energy. The spatial distribution of the electron probability density, $|\Psi|^2$, is calculated for energies ranging from 0.9 eV below to 1.5 eV above the Fermi level (see also Reference [19] Methods). Image size 2 nm $\times$ 4 nm. The height of the planar cross-section is referenced to the atomic lattice of the 7-AGNR. The colormap was set independently for each image. The calculation was performed with the 7-AGNR adsorbed on an Au(111) surface.

transition difficult to accomplish at the bias voltages needed to reach band resonance using conventional STM techniques. However, the following chapter will show how THz-STM can leverage this exponential $I(z)$ relationship to explore a 7-AGNR at ultralow tip heights.

5.3 Tip-Induced GNR Modifications

The DFT simulations of electron probability density in Figure 5.7 incorporate a passivization of the GNR end states. The ends of the 7-AGNR are perpendicular to the armchair axis, resulting in a zigzag structure. Termination of the armchair structure results in a sublattice imbalance that localizes an electronic state along the zigzag end, known as a Tamm state. These states have lower energy than the electronic energy levels of their armchair counterparts and thus form as in-gap states [160]. A possible cause for the suppression of the Tamm state at the zigzag edge is with CH_2 termination [73, 227]. A consequence of the CH_2 termination is a decrease in the electronic band gap attributed to an increase of the effective length [73]. The extra hydrogen is expected to be loosely bound with a binding strength of 1 eV [227]. Figure 5.8(a) illustrates a possible modification process using the STM tip. The STM tip is positioned above a featureless GNR terminus and the applied bias voltage is ramped between typical values of -1 V to -4 V. During this time the feedback loop maintains the current setpoint of $I_{\mathrm{DC}} = -100$ pA. To do so, the tip height is increased as the magnitude of the bias increases. Dehydrogenation is thought to occur when a sudden decrease in tip height is observed [227]. Although the initial formation of a CH_2 structure may be unlikely, the observed modification is consistent with the literature. Constant-current scans before (Figure 5.8(b)) and after (Figure 5.8(c)) modification show a significant change in topographic appearance of the terminus. A comparison between the schematics in Figure 5.8(b) and (c) show how the CH_2 termination has been converted into a conventional CH structure that hosts the expected Tamm state distributed across the zigzag structure.

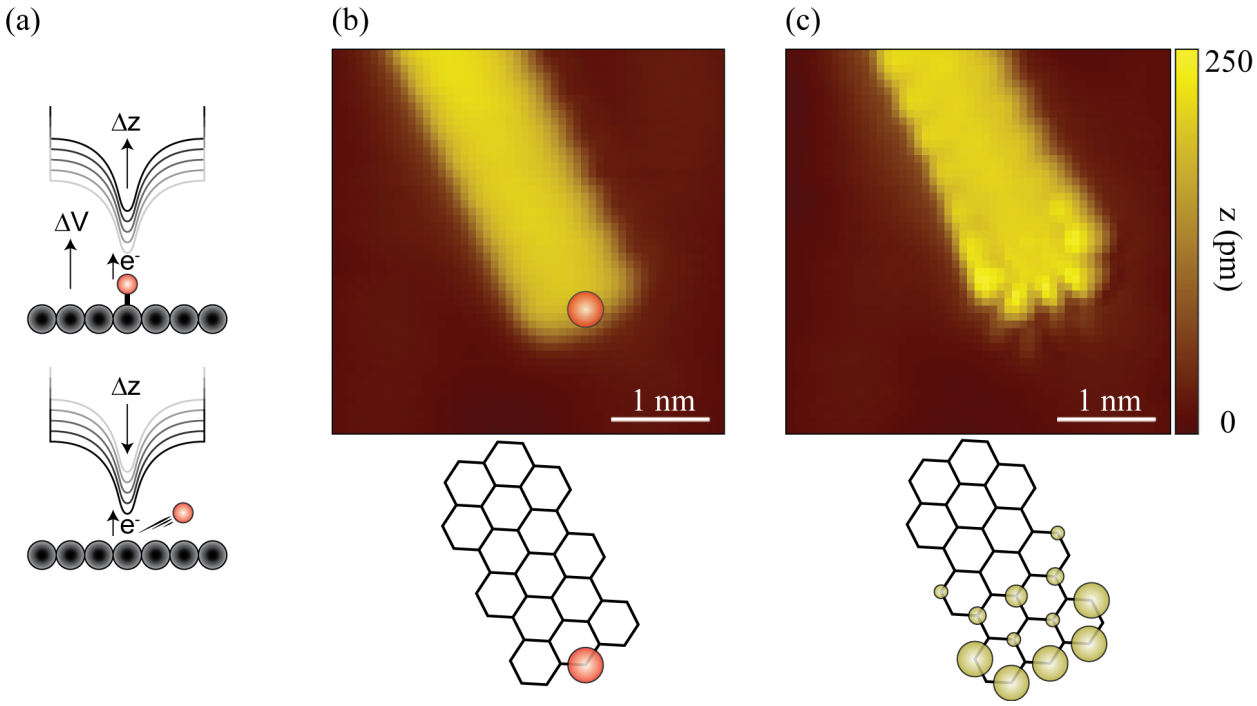

Figure 5.8: STM tip-induced modification of a 7-AGNR terminus. Dehydrogenation from a CH_2 to CH state is a possible mechanism, suggested in the literature [227]. (a) Cartoon illustration of the tip-induced modification strategy. (b) (top) Topogrphic image of a 7-AGNR exhibiting a featureless termination. (bottom) Carbon structure schematic. The red circle represents the location of the extra hydrogen, bonded to the structure as CH_2. (c) (top) Topographic image of the same 7-AGNR after tip-induced modification in constant-current operation. (bottom) Carbon structure schematic with yellow circles indicting the location and relative magnitude of the Tamm state exposed after tip-induced modification [227]. The topographic images were acquired with parameters $I_{DC} = 200$ pA and $V_{DC} = 1$ V (b) and $I_{DC} = 100$ pA and $V_{DC} = 100$ mV (c).

Chapter 6
THz-STM of 7-atom-wide Armchair Graphene Nanoribbons

The previous chapters laid the foundation for performing THz-STM and THz-STS measurements using similar principles to those that would be applied for STM and STS. The natural next step is to bring these capabilities to bear on material systems to inform design and synthesis. Successfully applying our understanding of THz tunneling spectroscopy and performing atomically resolved THz-STS is a necessary validation of our models and will set the stage for further refinement of our approach to THz-STS. Here, we investigate the promising material platform of atomically precise GNRs [2] on the ångström scale with THz-STM and THz-STS. The low duty cycle of THz-driven tunneling facilitates measurements at ultralow tip heights, where the GNR electronic wavefunctions feature far richer spatial structure than at conventional STM tip heights. Operating at $T = 77\,\mathrm{K}$, we perform THz-STS as a function of three-dimensional position above the GNR, allowing us to extract the differential conductance sampled by THz-driven tunneling with ångström horizontal and sub-ångström vertical resolution. Our measurements show that the vertical decay of the differential conductance is remarkably sensitive to lateral position and electronic orbital. Inspired by this observation, we introduce THz-driven scanning tunneling tomography, where constant-height THz-STM images illustrate a transition from tunneling dominated by the occupied states in GNR valence bands to tunneling dominated by unoccupied states in the GNR conduction bands within a tip-sample distance increase of just 1 Å. The THz-STM and THz-STS experiments described in the remainder of this chapter were published in Reference [18].

6.1 THz-STM at Ultralow Tip Heights

The GNRs studied in this chapter were grown from molecular precursors [1] on a clean Au(111) substrate by on-surface synthesis [2] (see Chapter 5 Section 5.1). We select 7-AGNRs

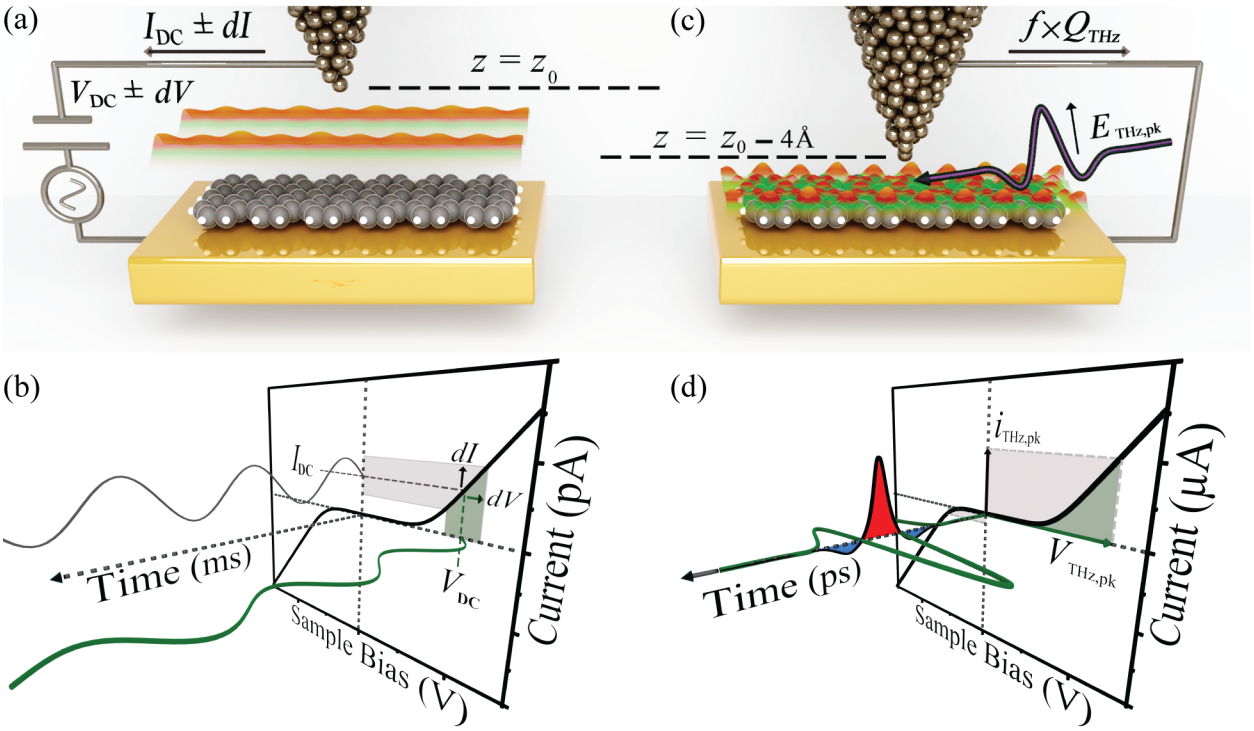

Figure 6.1: Comparing THz-STS to conventional STS. (a) Schematic diagram of the tunnel junction during STM and STS of a 7-AGNR. The tip height, z_0, is set by the tunnel current feedback conditions, e.g. with steady-state bias voltage $V_{DC} = -1$ V and steady-state tunnel current setpoint $I_{DC} = -50$ pA. (b) Schematic $I(V)$ of a 7-AGNR (solid black line) with the time axis of the millisecond sine-wave modulation for conventional STS projected out-of-plane. In STS, the steady-state bias voltage is modulated by a sine-wave of amplitude dV (solid green curve), generating a tunnel current modulation of amplitude dI (solid grey curve). (c),(d) In THz-STM and THz-STS, a phase-stable single-cycle THz pulse with a peak electric field of $E_{THz,pk}$ is coupled through free space to the STM tip apex, where it acts as an ultrafast transient bias with a peak voltage of V_{pk}. The tip height is reduced by approximately 4 Å to account for the reduced duty cycle of the bias compared to conventional STM. At this reduced tip height, the 7-AGNR LDOS features far richer spatial structure than at STM and STS tip heights (orange and green overlays in (a) and (c)). A THz voltage transient induces a sub-picosecond current pulse, $i_{THz}(t)$, defined by the $I(V)$, with peak current, i_{pk}, reaching the μA scale, compensating for the low duty cycle of THz-STS. The average rectified component of the current pulses, $Q_{THz} = eN_e = \int i_{THz}(t)dt$, is measured as a steady-state current, $I_{THz} = f \times e \times N_e$, where e is the elementary charge, f is the repetition rate of the laser and N_e is the average number of rectified elementary charges per THz pulse. The red and blue shadings underneath the sub-picosecond current transient in (d) emphasize the rectification process for a single pulse. The green and gray shaded regions in (b) and (d) highlight the range of the voltage modulation and resulting instantaneous tunnel current.

for the current study, as depicted in Figure 6.1(a). For conventional STM imaging, the tip height $z = z_0$ is defined by the bias voltage V_{DC} and current setpoint I_{DC}. As discussed in Chapter 2, conventional STS is performed by disengaging the feedback loop, applying an additional sinusoidal voltage of perturbative amplitude $\mathrm{d}V$ (e.g. with millisecond oscillation period) and detecting the sinusoidal current amplitude $\mathrm{d}I$ as a function of V_{DC} (Figure 6.1(b)). This yields the slope of the $I(V)$ (i.e. $\mathrm{d}I/\mathrm{d}V$), which is approximately proportional to the energy-dependent LDOS of the sample (see Chapter 2 Section 2.3.2).

In contrast, in THz-STM and THz-STS, the THz voltage probe is nine orders of magnitude faster than conventional voltage modulation and only a single oscillation cycle long. As the THz pulses are generated by an ultrafast NIR laser (see Chapter 3 Section 3.1.2 and Figure 4.7), a train of THz pulses is delivered to the junction. Each THz pulse stimulates a sub-picosecond rectified current pulse through THz-driven tunneling, thereby producing a train of current pulses with a duty cycle equal to the current-pulse duration divided by the time between THz pulses ($\sim$1 ps / 1 µs = 10^{-6}). Only the average THz-induced current can be measured, so the peak current must compensate for the duty cycle by far exceeding I_{DC}, as summarized in Figure 4.6. Consequently, the conventional method of STS is incompatible with the key aspect of THz-driven tunneling that makes ultrafast time resolution possible, and an alternate approach is required for THz-STS.

In the THz-STM and THz-STS experiments reported here, the initial tip height is set using the conventional STM feedback loop. The feedback loop is then disengaged, the bias is reduced to 0 V, and the tip is approached $3 - 4$ Å closer for THz-driven imaging and spectroscopy, e.g., to $z = z_0$ – 4 Å (Figure 6.1(c)). On clean surfaces the tunneling rate increases by one order of magnitude for each ångström of approach, effectively rescaling the $I(V)$ (Figure 6.1(d)). This not only compensates for the $\sim 10^{-6}$ duty cycle of THz-driven tunneling, but also enables measurements at ultralow tip heights. We define ultralow tip heights as distances at which orbitally selective imaging by conventional STM with an s-wave tip is unfeasible because the DC current would either damage the tip apex or surface under investigation or lead to the tip picking up the GNR [233]. Conversely, THz-driven STM is possible because sub-picosecond current pulses of the same peak magnitude consist of only a few electrons.

In practice, single-cycle, phase-stable THz pulses are coupled through free space to the STM tip apex, where they act as ultrafast voltage transients on the junction's $I(V)$, as

depicted in Figures 6.1(c) and 6.1(d). The temporal integral of the THz-driven current, i.e., the rectified charge Q_{THz}, is registered through a shift in the average current of $I_{\mathrm{THz}} = f \cdot Q_{\mathrm{THz}} = f \cdot e \cdot N_e$, where e is the elementary charge, f is the repetition rate of the amplified NIR laser system used to generate the THz pulse train and N_e is the average number of rectified elementary charges per THz pulse (see Chapter 4 for further detail). Notably, the peak of the ultrafast THz-induced current, i_{pk}, can reach the microamp scale within a sub-picosecond oscillation cycle (Figure 6.1(d) and Figure 4.6). The chemical structure of the 7-AGNR is depicted in Figure 6.2(a). Differential conductance mapping of the 7-AGNR valence band in constant-height mode reveals that the LDOS is primarily located outside the atomic frame at a tip height of z_0 (Figure 6.2(b)), consistent with previous observations [74, 234] and Figure 5.5. For comparison, we have calculated the 7-AGNR electron density as a function of energy and height above the atomic plane (see Figure 5.7) using density functional theory (DFT). The DFT tomographic cut through the valence band at $z = 5$ Å agrees with the $\mathrm{d}I/\mathrm{d}V$ map (compare Figures 6.2(b) and 6.2(c)), as has been demonstrated previously [74], where the DFT height is lower than the experimental tip height due to an artifact of the exchange correlation functional and basis set approximations adopted in DFT. Conversely, the DFT cut through the valence band at lower height, e.g., at $z = 2$ Å as shown in Figure 6.2(d), predicts the spatial structure probed in THz-driven experiments. The image is notably richer in detail, since the wavefunction in the interior of the 7-AGNR is composed of lobes of alternating sign that destructively interfere at higher tip heights [74] (see Figure 5.6). These lobes influence STM images recorded with CO functionalized tips [244], but the mixed s- and p-wave character of the tip makes the corresponding microscopy and spectroscopy difficult to interpret [245], while conventional STM with an s-wave tip cannot access the necessary ultralow tip heights. In general, lowering the bias allows the tip to be moved closer (e.g., as is the case for bond-resolved STM using a CO functionalized tip [246]) but the tunneling electrons are not resonant with the molecular orbital LDOS at low bias and the in-gap LDOS is probed instead.

Interpreting THz-driven images can also be non-trivial, since the voltage transient sweeps through both polarities, acting on all LDOS features in the voltage window defined by V_{pk} and the waveform symmetry (Figure 6.1(d)). Precisely characterizing the temporal structure of the voltage waveform at the tip apex is therefore essential. Electro-optic sampling in the far-field provides the THz electric-field transient focused onto the STM tip

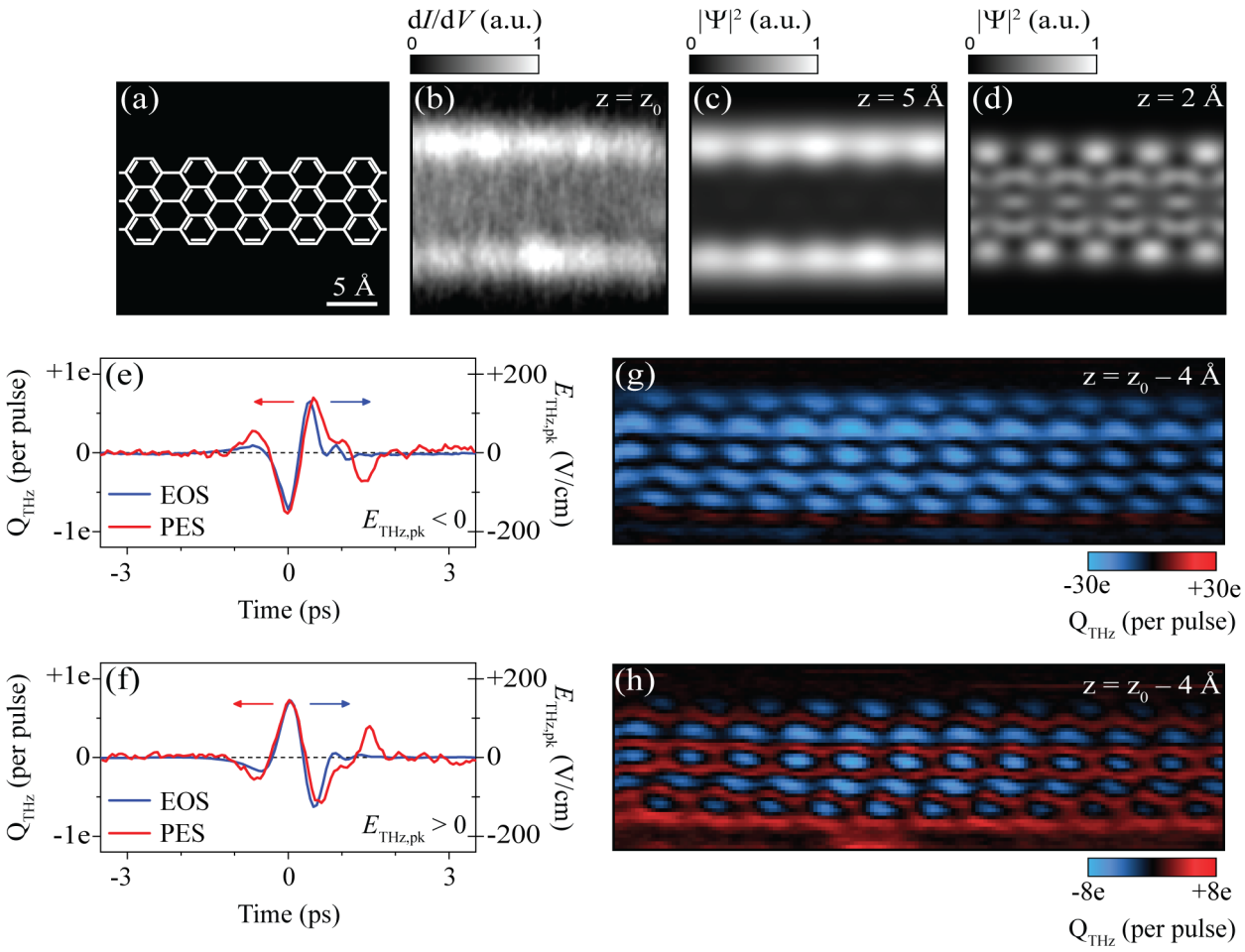

Figure 6.2: THz-STM of seven-atom-wide graphene nanoribbons on Au(111). (a) The chemical sketch of a 7-AGNR segment. The scalebar applies to all images in the figure. (b) Measured steady-state STM constant-height dI/dV acquired at $V_{\mathrm{DC}} = -1$ V. The initial tip height, z_0, was set with the tip located at the center of the nanoribbon at $V_{\mathrm{DC}} = -1$ V and $I_{\mathrm{DC}} = -50$ pA. (c),(d) Electron probability density, $|\Psi|^2$, at $V = -0.9$ V calculated using DFT at a tip height of (c) 5 Å and (d) 2 Å. (e),(f) THz-pulse waveforms measured via free-space electro-optic sampling (EOS, blue curves) and photoemission sampling at the tip apex (PES, red curves). The carrier-envelope-phase shift between (e) and (f) is 180°. (g),(h) THz-STM constant-height rectified charge maps, $Q_{\mathrm{THz}}(x, y)$, acquired at $E_{\mathrm{THz,pk}} = -180$ V/cm (g) and $E_{\mathrm{THz,pk}} = +180$ V/cm (h), with $V_{\mathrm{DC}} = 0$ V and $z = z_0 - 4$ Å for both images.

(Figures 6.2(e) and 6.2(f)), but antenna effects [8, 11, 15] and geometrical features on the scale of the THz wavelength [9, 10, 12, 15] can modify its shape. Therefore, *in-situ* characterization of the near-field waveform is needed [10, 11, 15, 214], e.g. photoemission sampling (PES, see Chapter 4 Section 4.2.7). As THz field enhancement is affected by the microscopic tip profile [15, 182] – which must be carefully prepared over the substrate for high-resolution THz-STM imaging – we use PES to measure the waveform shape but determine the THz voltage calibration from THz-STM and THz-STS. We select between an even or odd number of THz-pulse reflections before coupling the pulses to the tip, and hence invert the polarity of the THz voltage transient at the apex without changing its temporal shape or amplitude, as confirmed by PES in Figures 6.2(e) and 6.2(f). We refer to the electric field transient in which the largest field is negative as $E_{\mathrm{THz,pk}} < 0$ (and vice versa), where the field direction is consistent with the STM bias voltage.

Figure 6.2(g) shows a constant-height THz-STM image of a 7-AGNR recorded for $E_{\mathrm{THz,pk}} < 0$ at $z = z_0$ – 4 Å. Remarkably, it is almost identical to the DFT calculation of the electron density at z = 2 Å, V = –0.9 V (Figure 6.2(d)), which is dominated by the valence band (see Figures 5.6 and 5.7), and features exquisite, ångström-scale detail not observable in the conventional differential conductance image (Figure 6.2(b)). The rectified charge is predominantly negative, consistent with THz-driven tunneling of electrons from the GNR to the tip. Conversely, the THz-STM image for $E_{\mathrm{TH,pk}} > 0$ is significantly more complicated (Figure 6.2(h)). The anti-nodes of negative rectified charge persist, but the previously nodal regions in the interior of the ribbon are replaced by areas of positive rectified charge, i.e., electrons that have moved from the tip into the sample. The mixture of positive and negative rectified charge in Figure 6.2(h) signifies that the $E_{\mathrm{THz,pk}} > 0$ waveform probes considerable sample LDOS on both sides of the Fermi level. The relative weighting between these spectral features depends sensitively on ångström-scale tip position, manifesting as fine local detail in Figure 6.2(h).

6.2 THz-STS With Ångström Resolution

We apply spatially dependent THz-STS to disentangle the intrinsic properties of the 7-AGNR at ultralow tip heights from the THz-driven tunneling process. As a roadmap, conventional $\mathrm{d}I/\mathrm{d}V$ spectra are recorded for the edge of a 7-AGNR and for the substrate at

a tip height of z_0 (Figure 6.3(a)). These measurements are consistent with previous reports [74, 234]. We then select two characteristic locations for THz-STS (Figure 6.3(b)), which we label the node (green circles in Figure 6.3(b)) and anti-node (red diamonds in Figure 6.3(b)) based on the THz-STM image for $E_{\mathrm{THz,pk}} < 0$. The corresponding positions above the atomic structure are determined by comparison with the DFT calculation in Figure 6.2(d). THz-STS spectra are recorded by sweeping the peak field strength of the incident THz pulse (i.e. $E_{\mathrm{THz,pk}}$) while maintaining a uniform waveform shape, then inverting the polarity and repeating [6, 8, 10, 13], as introduced in Chapter 4 Section 4.2.3. Figures 6.3(c) and 6.3(d) show the rectified charge measured at the anti-node and node, respectively, for tip heights of $z = z_0 - 4$ Å and $z = z_0 - 3.5$ Å.

To extract the differential conductance sampled by THz-driven tunneling at each tip position, we adopt a model in which the 7-AGNR band onsets at positive and negative voltages are described by error functions and the Au(111) surface state is described as a Gaussian,

$$\frac{\mathrm{d}I}{\mathrm{d}V} = A_{+}\mathrm{erf}(c_{+}[eV - E_{+}]) + A_{-}\mathrm{erf}(c_{-}[eV - E_{-}]) + A_{\mathrm{Au}}\mathrm{exp}(-c_{\mathrm{Au}}[eV - E_{\mathrm{Au}}]^2)\,, \qquad (6.1)$$

where c_+, c_-, and c_{Au} are coefficients that determine the shape of the function and E_+, E_-, and E_{Au} are the positions of these features. These six parameters are determined by fits to the measured $\mathrm{d}I/\mathrm{d}V$ in Figure 6.3(a) which constraints the energetic positions and widths of the spectral features. Meanwhile, A_+, A_-, and A_{Au} are free parameters that control the amplitude of each feature. We then simulate charge rectification by a voltage pulse matching the THz near-field waveform (Figures 6.2(e) and 6.2f), allowing the amplitude of the three LDOS contributions to vary until the simulation optimally fits the measured $Q_{\mathrm{THz}} - E_{\mathrm{THz,pk}}$ data (lines in Figures 6.3(c) and 6.3(d)). The THz voltage calibration is used as a global fit parameter for all data recorded without a tip change (see Chapter 4 Section 4.2.7). The extracted $\mathrm{d}I/\mathrm{d}V$ curves at the anti-node and node (Figures 6.3(e) and 6.3(f), respectively) are consistent with THz-STM imaging (Figures 6.2(g) and 6.2(h)).

We next combine THz-STS with THz-STM to extract spatial maps of the $\mathrm{d}I/\mathrm{d}V$ amplitudes (multi-image analysis, as introduced in Chapter 4 Section 4.2.6). THz-STM images are recorded as a function of $E_{\mathrm{THz,pk}}$ for both positive (Figure 6.4(b)) and negative polarity (Figure 6.4(b)), allowing $Q_{\mathrm{THz}} - E_{\mathrm{THz,pk}}$ curves to be plotted for every pixel. Applying our model to each pixel individually (with the THz voltage calibration as a global parameter)

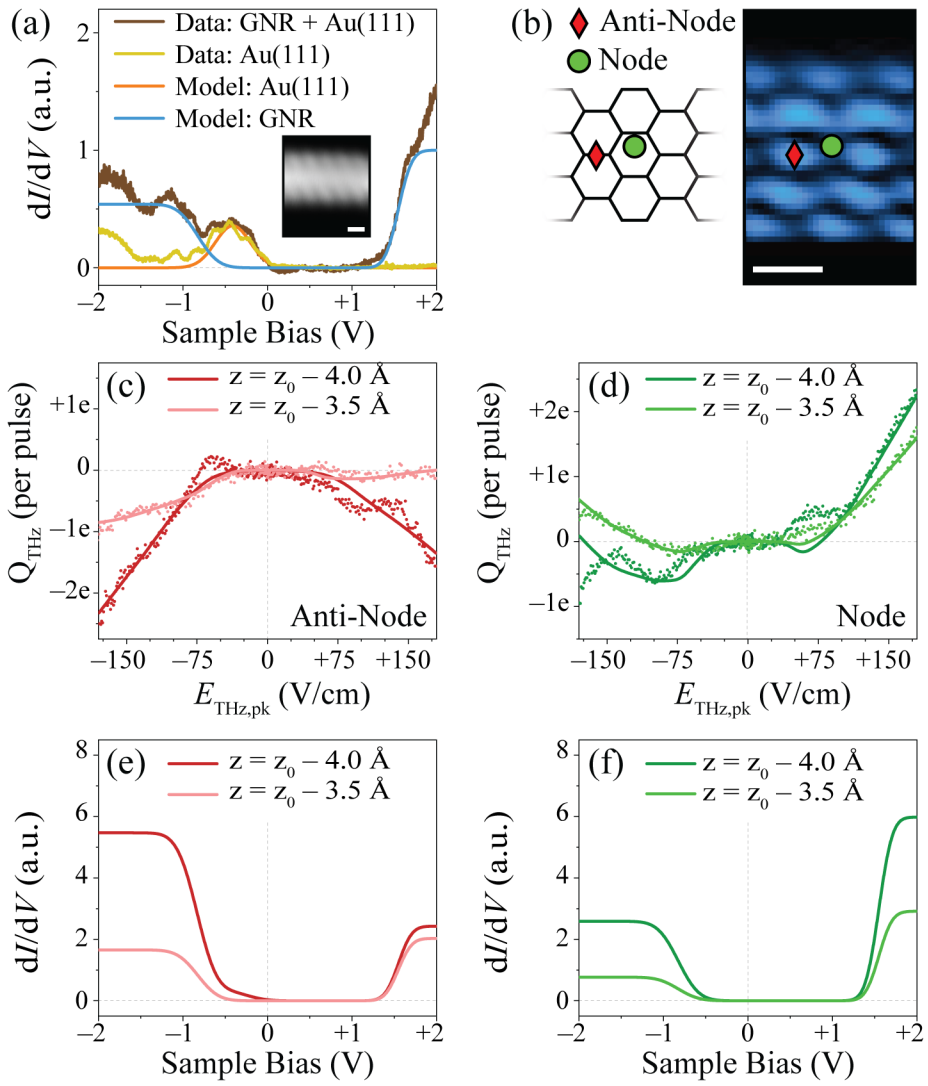

Figure 6.3: THz scanning tunneling spectroscopy of a 7-AGNR with ångström-scale resolution. (a) Conventional STS of a 7-AGNR adsorbed onto an Au(111) surface (solid brown line) and the Au(111) surface state (solid yellow line). The differential conductance of the gold surface state is modeled by a Gaussian centered at –0.4 V (solid orange line), while the differential conductance of the 7-AGNR is modeled as two error functions near the band edges (solid blue line). Inset: typical steady-state constant-height STM image showing the tip positions for tunneling spectroscopy. (b) Tip positions for THz-STS overlayed on a diagram of the physical structure of a 7-AGNR (left) and the Q_{THz} map from Figure 6.2(g) (right). Diamonds: anti-node position; circles: node position. (c),(d) Measured (circles) and simulated (solid lines) $Q_{\mathrm{THz}} - E_{\mathrm{THz,pk}}$ curves at $z = z_0 - 4$ Å (dark lines and symbols) and $z = z_0 - 3.5$ Å (light lines and symbols) with the tip positioned at the anti-node (c) and node (d); $V_{\mathrm{DC}} = 0$ V. (e),(f) $\mathrm{d}I/\mathrm{d}V$ extracted from the fits in (c) and (d) for the anti-node (d) and node (f) tip positions, respectively. The dashed lines in (c) – (f) represent the origin. The scalebars in (b) and the inset of (a) are 5 Å.

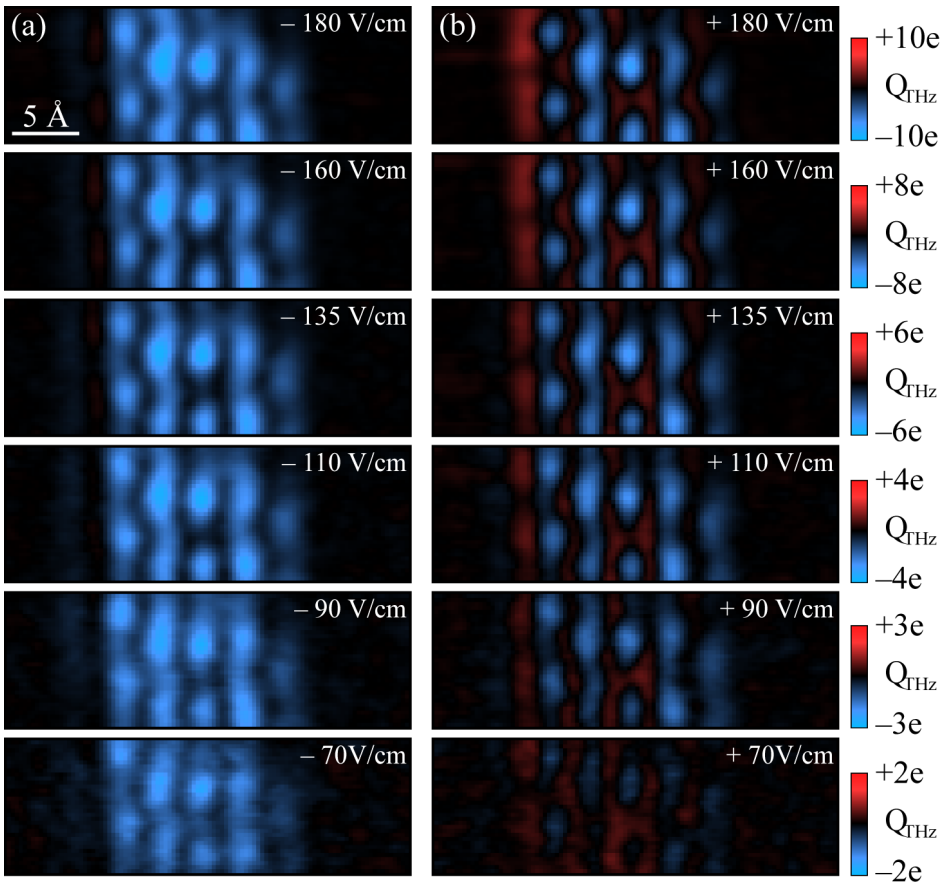

Figure 6.4: THz-STM field-dependent imaging. (a),(b) THz-STM constant-height rectified charge maps acquired at several $E_{\mathrm{THz,pk}}$ using a negative-field-dominant THz pulse (a) and a positive-field-dominant THz pulse (b). The images were acquired with the tip at $z = z_0$ – 4 Å. A 5×5 smoothing filter was applied to the dataset.

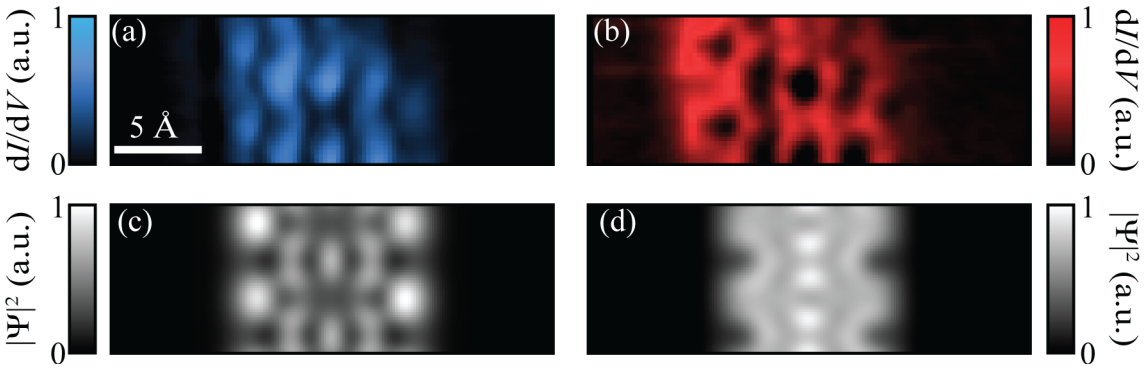

Figure 6.5: Atomically resolved dI/dV maps extracted from THz-STS. (a),(b) Model dI/dV maps at negative (a) and positive (b) bias extracted pixel-by-pixel from field-dependent $Q_{\mathrm{THz}}(x, y)$ images in Figure 6.4. (c),(d) Electron probability density at z = 2 Å and V = –0.9 V (c) and V = +1.3 V (d) calculated by DFT. The scalebar in (a) applies to (a) – (d).

yields the extracted dI/dV amplitude maps at negative (Figure 6.5(a)) and positive (Figure 6.5(b)) bias. They agree with the corresponding DFT images at z = 2 Å, V = –0.9 V (Figure 6.5(c)) and z = 2 Å, V = +1.3 V (Figure 6.5(d)), respectively, which account for the closely spaced [74] VB and VB – 1 at negative bias and the CB and CB + 1 at positive bias.

As further corroboration of our model and the fidelity of the PES waveform, and as a test for multi-electron and dynamic effects, we perform autocorrelation measurements [5, 7–9, 12, 182]. As introduced in Chapter 4 Section 4.2.4, the THz pulses are split in half, a delay is introduced, and Q_{THz} is recorded as a function of delay time for three different $E_{\mathrm{THz,pk}}$ values at both the anti-node (Figure 6.6(a)) and node (Figure 6.6(b)). A single differential conductance curve is sufficient to reproduce the data (Figures 6.6(c) and 6.6(d)) at a given tip position (with a constant THz voltage calibration), indicating that the dI/dV model (Figures 6.6(e) and 6.6(f)), combined with the measured PES waveform, sufficiently captures the details of THz-induced tunneling for this system. Finally, we record an additional THz-STS dataset for a different tip apex and 7-AGNR (Figures 6.7(a) and 6.7(b)). In this case, the higher order oscillations in the THz-STS data are absent and the agreement with the model is even better (Figures 6.7(c) and 6.7(d)). Changes in the tip apex may change the THz field enhancement and lead to a different voltage region being sampled for the same $E_{\mathrm{THz,pk}}$, as discussed in Chapter 4 Section 4.2.7.

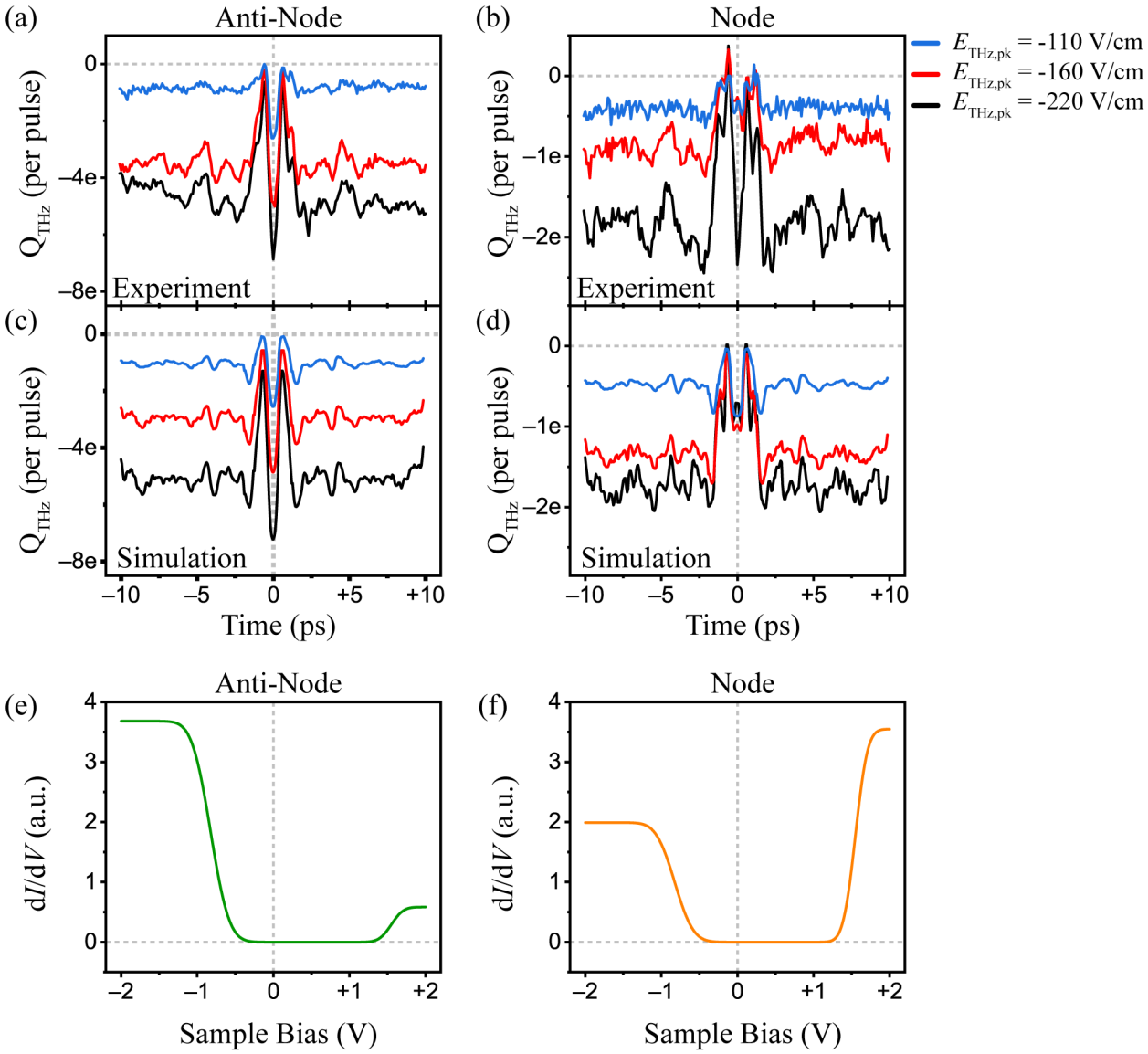

Figure 6.6: THz-STM autocorrelations of a 7-AGNR on Au(111). (a),(b) Experimental THz pulse autocorrelations acquired at zero DC bias ($V_{\mathrm{DC}} = 0$ V) and at constant height ($z = z_0 - 4$ Å) with the tip positioned at the anti-node (a) and node (b). (c),(d) Simulated THz pulse autocorrelations for the the anti-node (c) and node (d) tip positions using the PES waveform in Figure 6.2(e)/(f). The nonlinearity of the $I(V)$ that rectifies the THz pulse within the model was determined from the $t = 0$ ps and $t = 10$ ps values of the experimental autocorrelations. (e),(f) Model dI/dV for the anti-node (e) and node (f) tip positions.

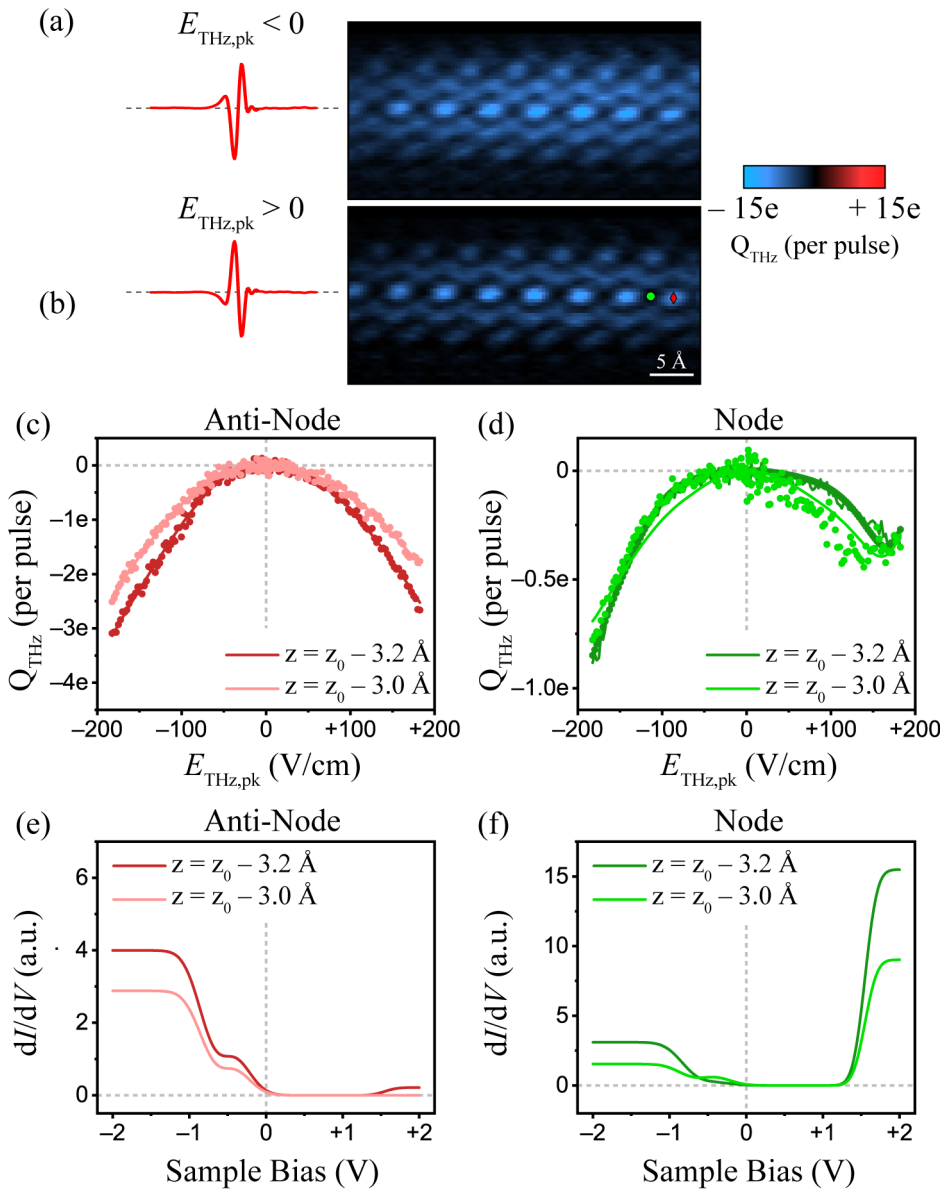

Figure 6.7: THz-STM imaging and spectroscopy of another 7-AGNR with a different tip apex. (a),(b) THz-STM constant-height rectified charge maps acquired at $E_{\mathrm{THz,pk}} = -135$ V/cm (a) and $E_{\mathrm{THz,pk}} = +135$ V/cm (b), with $V_{\mathrm{DC}} = 0$ V and $z = z_0 - 3.0$ Å for both images. The red triangle and green circle indicate the THz-STS locations for the anti-node and node, respectively. (c),(d) Measured (circles) and simulated (solid lines) $Q_{\mathrm{THz}} - E_{\mathrm{THz,pk}}$ curves at $z = z_0 - 3.2$ Å (dark lines/symbols) and $z = z_0 - 3.0$ Å (light lines/symbols) with the tip positioned at the anti-node (c) and node (d) of the valence band LDOS ($V_{\mathrm{DC}} = 0$ V). (e),(f) Model dI/dV extracted from the fits in (c) and (d) for the anti-node (e) and node (f) tip positions, respectively.

Across all datasets, the $\mathrm{d}I/\mathrm{d}V$ curves at the anti-node and node are significantly different from one another, even though they are laterally separated by only ∼2 Å, a distance comparable to the carbon-carbon bond length (Figure 6.3(b)). Retracting the tip by just 0.5 Å at either position (i.e., from $z = z_0 - 4$ Å to $z = z_0 - 3.5$ Å) leads to a drastic change to both the measured $Q_{\mathrm{THz}} - E_{\mathrm{THz,pk}}$ curve (Figures 6.3(c) and 6.3(d)) and the extracted $\mathrm{d}I/\mathrm{d}V$ (Figures 6.3(e) and 6.3(f), respectively). Our measurements thus show spatially dependent THz-STS on the ångström scale and illuminate a rich spatial structure to the LDOS of 7-AGNRs at ultralow tip heights. Most remarkably, we observe that the amplitude of the extracted $\mathrm{d}I/\mathrm{d}V$ at the anti-node position changes far more at negative voltages than positive voltages with increasing tip-sample distance (Figure 6.3(e)). In contrast, at the node position, the z-dependent change to the $\mathrm{d}I/\mathrm{d}V$ at positive and negative voltages is similar (Figure 6.3(f)). Hence, at ultralow tip heights, the vertical decays of the wavefunctions at positive and negative bias depend sensitively on in-plane position and can be significantly different from one another. We explore this further in the next section.

6.3 THz-driven $\mathrm{d}I/\mathrm{d}V$ Tomography

We explore the vertical decays of the 7-AGNR wavefunctions in further detail by recording the rectified charge as a function of tip height above the anti-node (Figure 6.8(a)) and node (Figure 6.8(b)), as introduced in Chapter 4 Section 4.2.5. For each position, the $Q_{\mathrm{THz}}(z)$ measurement is repeated for THz pulses of each polarity with identical $|E_{\mathrm{THz,pk}}|$. We apply our model to fit the $Q_{\mathrm{THz}} - z$, with the z dependence encompassed by an independent exponential decay for each of the three $\mathrm{d}I/\mathrm{d}V$ features (i.e., for the error functions at positive and negative bias and the gold surface state). Measurements recorded with positive and negative $E_{\mathrm{THz,pk}}$ for a given position are fit simultaneously, yielding $\mathrm{d}I/\mathrm{d}V$ as a function of height at the anti-node (Figure 6.8(c)) and node (Figure 6.8(d)). We find that the decay of the error function at negative bias is consistently faster than that at positive bias. This is partially explained by different tunneling barrier heights, since the onset of the LDOS is closer to the Fermi level at negative bias (Figure 6.3(a)). The dependence of the vertical decay rate on horizontal tip position, meanwhile, can be traced back to the complex spatial structure of the wavefunctions at ultralow tip heights. Interference between the probability amplitude lobes of positive and negative sign in an individual wavefunction introduces an

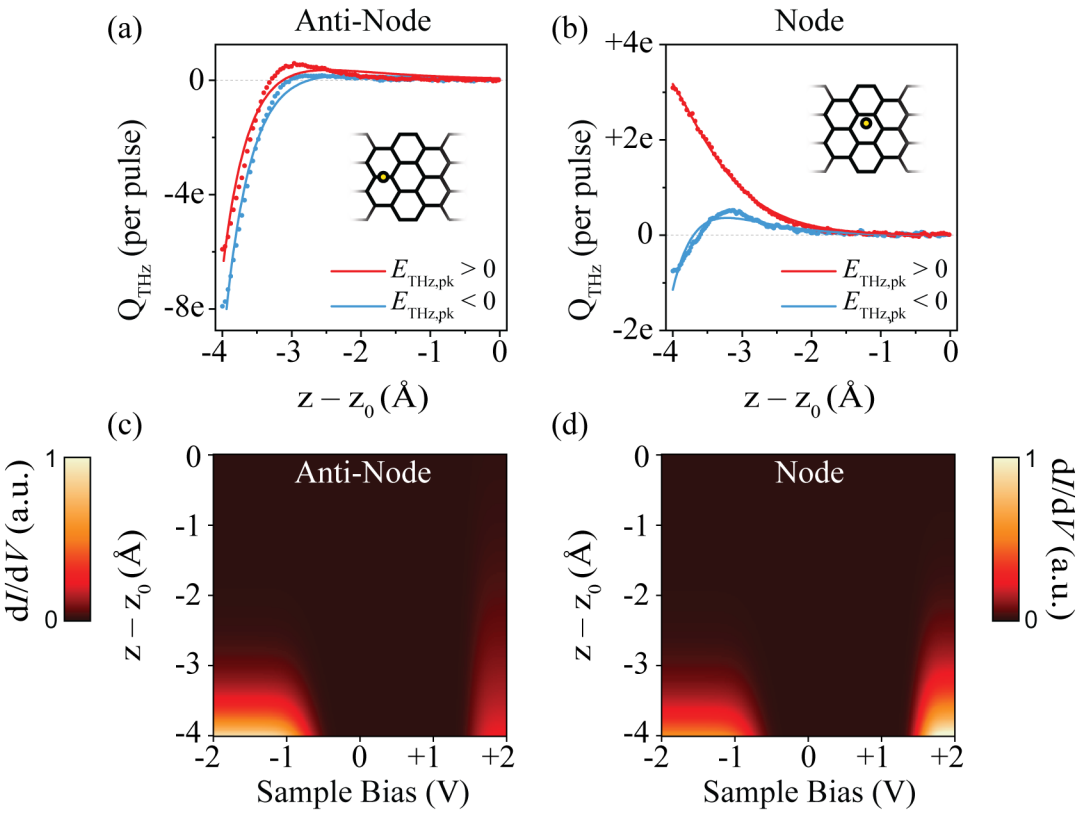

Figure 6.8: Tip-height-dependent THz-STM of a 7-AGNR on Au(111). (a),(b) Measured (circles) and simulated (solid lines) tip retraction scans at the anti-node (a) and node (b) positions (see inset) acquired at V_{DC} = 0 V, $E_{THz,pk}$ = –180 V/cm (blue) and $E_{THz,pk}$ = +180 V/cm (red). (c),(d) Differential conductance at the anti-node (c) and node (d) spatial positions for tip heights, z, ranging from z_0 to z_0 – 4 Å extracted from the fits in (a) and (b), respectively. The orbital decays are modeled using the expression $\exp(-2\kappa z)$. Negative bias fit parameters: κ = 1.3 Å^{-1} at the anti-node and κ = 1.2 Å^{-1} at the node. Positive bias fit parameters: κ = 0.4 $\mathring{A}^{-1}$ at the anti-node and κ = 0.9 Å^{-1} at the node.

additional vertical decay to the LDOS that is wavefunction specific [74] (Figure 5.6). This effect is not observed with conventional STM because destructive interference between the lobes is complete at standard tip heights.

Whereas DFT calculations of the LDOS at constant height agree with our THz-STM and THz-STS measurements (e.g. Figure 6.5(a) to 6.5(d)), the vertical LDOS decays predicted by DFT are not reliable due to the fast decay of the Gaussian basis set and limitations of the exchange correlation functional. Therefore, we compare the experimental decays to tight-binding calculations (Figure 6.9; calculations performed by our collaborators; see Reference [18] Methods). Unlike our DFT calculations, the tight-binding approach considers the wavefunctions separately and does not account for the gold substrate. Nevertheless, reasonable agreement is obtained, albeit under the assumption that each experimental decay can be associated with a particular band (VB – 1, VB, CB, or CB + 1) that dominates the decay at that tip position and energy.

Interestingly, the Q_{THz}–z decay curves for $E_{\mathrm{THz,pk}} > 0$ at the anti-node (Figure 6.8(a)) and $E_{\mathrm{THz,pk}} < 0$ at the node (Figure 6.8(b)) feature prominent sign changes between $z = z_0$ – 4 Å and $z = z_0$ – 3 Å. These sign changes are explained by a competition between the asymmetry of the THz waveform (Figures 6.2(e) and 6.2(f)) and the relative strengths of the valence and conduction bands in the height-dependent $\mathrm{d}I/\mathrm{d}V$ maps (Figures 6.8(c) and 6.8(d)). We investigate the spatial dependence of this competition further with constant-height THz-STM images as a function of tip height, $Q_{\mathrm{THz}}(x, y)$ vs. z, which we call THz-driven scanning tunneling tomography. Figure 6.10(a) shows tomography images for $E_{\mathrm{THz,pk}} < 0$, while Figure 6.10(b) shows the complementary dataset for $E_{\mathrm{THz,pk}} > 0$. The transition from $Q_{\mathrm{THz}} < 0$ to $Q_{\mathrm{THz}} > 0$ is most evident in Figure 6.10(b), where the asymmetry of the THz voltage waveform compensates for the asymmetry of the LDOS onsets relative to the Fermi level. In Figure 6.10(b), the THz-STM image at $z = z_0$ – 4 Å largely matches the spatial structure observed for the opposite polarity (Figure 6.10(a) at $z = z_0$ – 4 Å), albeit with positive rectified charge at the nodal positions. By $z = z_0$ – 3.25 Å, the THz-STM image is entirely composed of positive rectified charge (Figure 6.10(b), right).

To complete our tomography analysis (introduced in Chapter 4 Section 4.2.6), we assemble $Q_{\mathrm{THz}}(z)$ curves for every pixel in Figure 6.10(a),(b) and apply our model, as in Figure 6.8(a),(b), to reveal two-dimensional cross-sections through the differential conductance as a function of tip height at positive and negative bias (Figures 6.11(a) and 6.11(b)). In addition

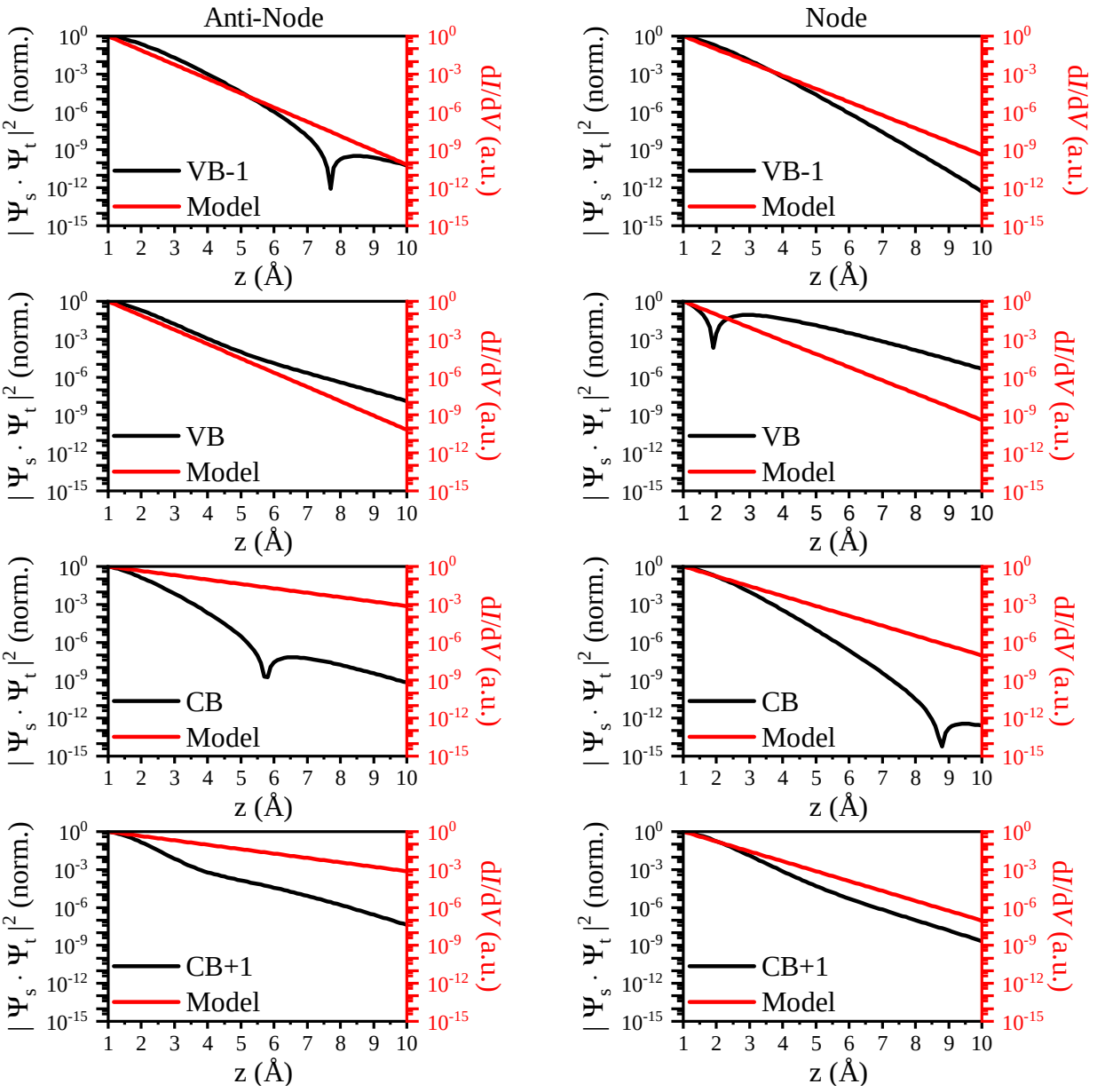

Figure 6.9: Comparison of the theoretical and experimental vertical decays at the anti-node and node positions. For each orbital and tip position, the theoretical vertical decay (solid black line) was calculated using a tight-binding model for the sample wavefunction (Ψ_s) that was convoluted with an s-wave tip (Ψ_t) following the Tersoff-Hamann approximation [84]. The theoretical decay is shown alongside a vertical cut through the extracted dI/dV of Figures 6.8(c) and 6.8(d) (solid red line) in each panel. The theoretical decays and extracted dI/dV decays are artificially normalized to the extracted dI/dV at z = 0 Å for easier comparison. The VB and VB-1 decays are compared to dI/dV at V = –0.9 V while the CB and CB+1 decays are compared to dI/dV at V = +1.3 V.

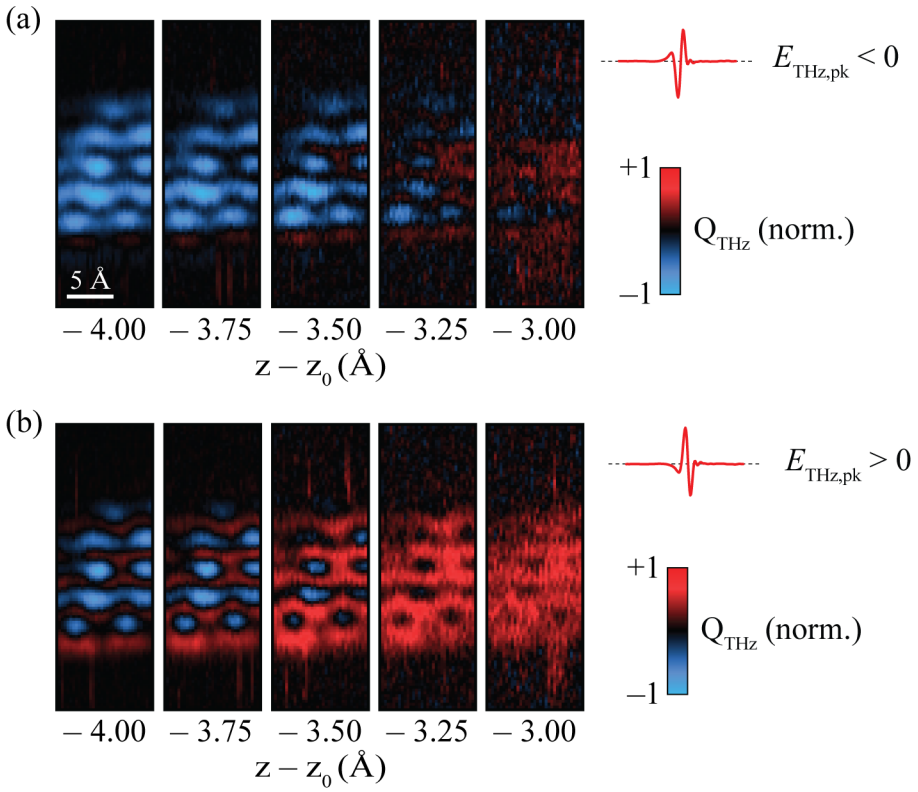

Figure 6.10: Variable-height THz-STM of a 7-AGNR on Au(111). (a),(b) THz-STM imaging tip-height dependence, $Q_{\mathrm{THz}}(x, y)$ vs. z, i.e., THz-driven scanning tunneling tomography, acquired at $E_{\mathrm{THz,pk}} = -180$ V/cm (a) and $E_{\mathrm{THz,pk}} = +180$ V/cm (b) with $V_{\mathrm{DC}} = 0$ V. The scalebar in (a) applies to both (a) and (b).

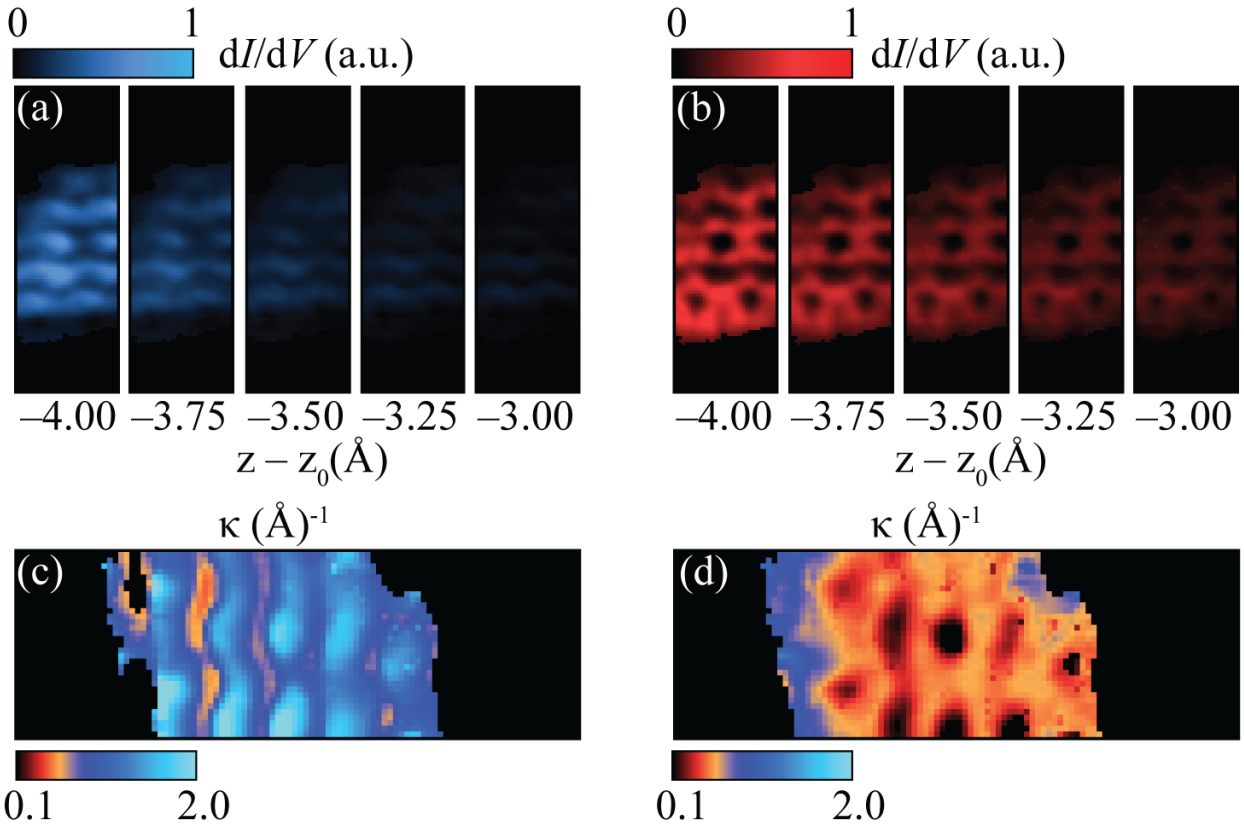

Figure 6.11: Tomographic dI/dV reconstruction from THz-STM tomography. (a),(b) Differential conductance for occupied (a) and unoccupied (b) states. (c),(d) Map of the inverse decay constant, κ, at negative (c) and positive (d) bias. Using the height-dependent $Q_{\mathrm{THz}}(x, y)$ data shown in Figures 6.10(a) and 6.10(b), we create a $Q_{\mathrm{THz}}(z)$ curve at each pixel. We fit the $Q_{\mathrm{THz}}(z)$ curves by incorporating an exponential decay into each term of Equation 6.1. Then, we use the field-dependent image data from Figure 6.4 to create a dI/dV map at $z = z_0$ - 4 Å used to initialize the model. The κ maps are spatially dependent decay coefficients for the dI/dV features at positive and negative bias. The regions within (c) and (d) that are represented by zero on the colormap (black) are artificially inserted because the local value for Q_{THz} and/or the dI/dV amplitude at the corresponding bias is negligible and κ cannot be determined.

to these tomographic reconstructions, we also extract the spatial dependence of the vertical decay parameters with ångström in-plane resolution (Figures 6.11(c) and 6.11(d)). These maps are consistent with our point-spectroscopy analysis in Figure 6.8(a)-(d).

6.4 Conclusions

Looking ahead, THz-driven scanning tunneling microscopy, spectroscopy, and tomography of atomically precise GNRs sets the stage for a new era of ångström-scale ultrafast science in novel material systems. On-surface [2] and solution synthesis [247] of GNRs enable wide-ranging design possibilities, including doping, edge functionality, and even topological electronic states [246, 248]. With pump-probe THz-STM and THz-STS, the optoelectronic properties [4, 71, 72, 249, 250] of individual GNRs will soon come into clearer view, visualized through atomically resolved movies of sub-picosecond population [251, 252] and wavefunction [253] dynamics. Our THz-pulse autocorrelation measurements (Figure 6.6) indicate that a dielectric decoupling layer will likely be needed to unveil the intrinsic GNR dynamics. This is consistent with preliminary optical-pump/THz-STM experiments performed as part of this thesis, which yielded a null result (i.e., no time-dependent THz-STM signal) when the GNRs were illuminated by $\sim$230 fs, $\lambda = 515\,\mathrm{nm}$, pump pulses. However, established manipulation of GNRs with the STM tip [253] provides a clear roadmap for constructing optimized prototypes of atomically precise optoelectronics, including substrate decoupling. In the final chapter, I will discuss the implications of the technical developments presented here and how they can be combined with the analytical framework presented in the following chapter.

Chapter 7
An Algorithm for Terahertz Scanning Tunneling Spectroscopy

The previous chapter demonstrated atomic resolution THz-STS for the first time by extracting the LDOS of a 7-AGNR in all three spatial dimensions. Ultrafast measurements were attempted in the form of THz-STM-pump/THz-STM-probe autocorrelation scans, but the resulting data could be described solely with the steady-state $\mathrm{d}I/\mathrm{d}V$ extracted from THz-STS. These observations suggest interactions between GNRs and a gold surface prevent us from observing the intrinsic dynamics of the GNR with our setup. Likely, a decoupling strategy is needed to take the next step.

More generally, simulated THz rectification on a model DC $I(V)$ curve is sufficient when the junction response is not frequency dependent, i.e., THz and DC voltages act on the same $I(V)$. However, what has not been discussed so far is how the approach in Chapter 6 falls short when the THz $I(V)$ is unknown. For example, a difference between STM and THz-STM $I(V)$ curves has been shown when investigating Si(111)-7x7 [8]. There, the THz-induced tunnel current could not be explained by the stationary picture available to conventional STM. Instead, the finite plasma frequency of the surface state led to a unique THz response. A yet more challenging scenario arises during photoexcitation when the $I(V)$ becomes dynamic. Our approach to THz-STS applied in Chapter 6 will not work for such ultrafast measurements because the STM junction will be driven out of equilibrium during excitation and into a transient state. There, the LDOS will be characterized by an unknown distribution and filling of electronic states that is accessible only to THz-STM.

Investigating ultrafast dynamics is made more challenging when the duration of the THz probe pulse is comparable to the lifetime of the non-equilibrium state, which is expected to be the case for many interesting systems. Our discussion on the limited detection bandwidth of STM electronics in Chapter 4 led to an integral expression for THz-driven charge rectification (Equations 4.3 and 4.4). As the instantaneous THz-induced current is obscured, a systematic

approach to identifying and extracting the hidden $I(V)$ information is necessary for THz-STS on new materials and in non-equilibrium conditions. In particular, in this chapter, we focus on optical-pump/THz-STM-probe experiments where optical photoexcitation occurs much faster than an oscillation of the THz voltage.

We present a THz-STS algorithm for recovering the differential conductance in steady-state or pump-probe experiments with sub-THz-cycle (i.e., subcycle) temporal resolution. Our algorithm requires as input only the THz voltage waveform and Q_{THz} as a function of peak THz voltage and pump-probe delay, i.e., no *a priori* knowledge of the sample LDOS is needed. The chapter is structured as follows. In Section 7.1, we show that modeling the steady-state $I(V)$ as a power series allows us to determine the differential conductance from a polynomial fit to the rectified charge. The efficacy of this algorithm is demonstrated for some examples, each of which corresponds to a model physical system. In Section 7.2, we extend the algorithm to pump-probe THz-STS: We describe the time-dependent $I(V)$ as a power series in which each coefficient is time dependent, allowing us to deconvolve the decay of the differential conductance from the THz voltage waveform using the cross-correlation theorem. We further define the time resolution of pump-probe THz-STS and explore the possibility of extracting sample dynamics that are faster than the bandwidth of the THz probe pulse. Finally, in Section 7.3, we discuss the limitations of the algorithm, the physics that may be investigated, and potential experiments. These results were published in Reference [19] and was developed after the 7-AGNR investigation presented in Chapter 6.

7.1 Steady-State Inversion Algorithm

In the THz-STM simulations presented here, the THz voltage transient defined in Equation 4.2 acts on the tunnel junction $I(V)$ as shown in Figure 4.8(a). Notably, the differential conductance sampled by $V_{\mathrm{THz}}(t)$ may differ from the differential conductance measured by conventional STS even in the absence of photoexcitation [8]. One common difference is that the peak instantaneous current generated in THz-STM experiments tends to exceed typical STM currents by orders of magnitude, e.g. reaching the µA or even mA scale [5, 6, 8, 9, 12]. Figure 4.8(b) shows the current transient generated by the situation depicted in Figure 4.8(a), where the THz voltage transient is applied to a junction defined by the Simmons model [79, 254]. In calculating the Simmons model $I(V)$, the STM tip height has been

reduced compared to conventional STM tip heights, leading to a larger peak current. Such parameters are used in practical THz-STM experiments to account for the relatively low duty cycle (e.g. 10^{-6}) of the train of THz-induced current pulses, as shown in Chapter 6.

7.1.1 Theory

Inspired by junction-mixing STM [48, 202], we model the tunnel current as a polynomial,

$$I(V) = \sum_{n=1}^{N} A_n V^n, \tag{7.1}$$

where the A_n terms are constant coefficients. A key difference compared to junction-mixing STM is that THz-driven tunneling (usually) explores relatively wide voltage ranges at both positive and negative polarity rather than just the local nonlinearity of the $I(V)$. Hence, the high-order terms of the polynomial series are more important, and can even dominate depending on the voltage and the shape of the $I(V)$ curve.

We next consider the rectified charge generated by the THz voltage pulse defined in Equation 4.2 acting on the junction (with no DC bias voltage),

$$Q_{\mathrm{THz}}(V_{\mathrm{pk}}) = \sum_{n=1}^{N} A_n V_{\mathrm{pk}}^n \int_{-\infty}^{\infty} [V_0(t)]^n \, dt. \tag{7.2}$$

Knowing the shape of $V_{\mathrm{THz}}(t)$ is essential, as it allows us to calculate a set of coefficients,

$$B_n = \int_{-\infty}^{\infty} [V_0(t)]^n \, dt, \tag{7.3}$$

that encapsulate the continuous and bipolar nature of the voltage pulse. Notably, the temporal integral of the free-space electromagnetic pulse that generates $V_{\mathrm{THz}}(t)$ is zero, so $B_1 = 0$. Thus, the contribution to Q_{THz} from the Ohmic part of the conductance is $A_1 B_1 = 0$ and

$$Q_{\mathrm{THz}}(V_{\mathrm{pk}}) = \sum_{n=2}^{N} C_n V_{\mathrm{pk}}^n, \tag{7.4}$$

where $C_n = A_n B_n$.

$Q_{\mathrm{THz}}(V_{\mathrm{pk}})$ can be measured directly in a THz-STS experiment. A simulated example is shown in Figure 4.8(c). Inverting the polarity of V_{pk} and repeating this sweep allows the full function to be mapped out. Within the algorithm introduced here, $Q_{\mathrm{THz}}(V_{\mathrm{pk}})$ is simply fit with a polynomial to extract the coefficients C_n, which can subsequently be combined with

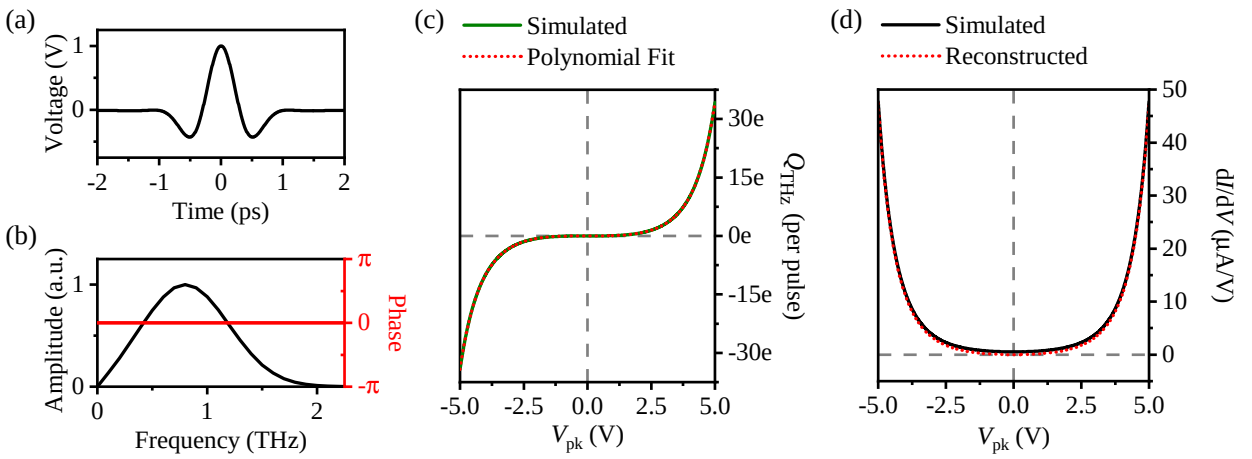

Figure 7.1: Reconstructing a Simmons model differential conductance. (a) Simulated THz voltage waveform, $V_0(t)$ and (b) corresponding spectral amplitude (black curve) and phase (red curve). The amplitude is zero at 0 THz, i.e., the temporal integral of $V_0(t)$ is zero. (c) Simulated rectified charge (green curve) for a Simmons model with $\Phi_s = \Phi_t = 5$ eV and polynomial fit of order $N = 22$ (dotted red curve). (d) Simmons model differential conductance (black curve) and reconstructed differential conductance (red curve) obtained from the steady-state inversion algorithm.

the B_n coefficients determined by numerical integration of the measured voltage transient to yield the $I(V)$,

$$I(V_{\mathrm{pk}}) = A_1 V_{\mathrm{pk}} + \sum_{n=2}^{N} \frac{C_n}{B_n} V_{\mathrm{pk}}^n. \tag{7.5}$$

A limitation of steady-state THz-STS is that the Ohmic part of the conductance does not produce a rectified charge, and therefore the A_1 term is inaccessible. However, calculating the differential conductance,

$$\frac{\mathrm{d}I}{\mathrm{d}V_{\mathrm{pk}}}(V_{\mathrm{pk}}) = A_1 + \sum_{n=2}^{N} n \frac{C_n}{B_n} V_{\mathrm{pk}}^{n-1}, \tag{7.6}$$

reduces the missing Ohmic contribution to a constant offset. For simplicity, we set $A_1 = 0$ in the following.

7.1.2 Demonstration

Here, we demonstrate the steady-state algorithm's effectiveness by recovering the differential conductances of model systems from simulated THz-STS data. The simple THz voltage waveform shown in Figure 7.1(a) is used for the THz-STS simulations. The spectral amplitude and phase of the pulse are shown in Figure 7.1(b).

The algorithm is, in principle, independent of the precise shape of the waveform, but we note that a perfectly symmetric waveform (i.e. sine-like, with $\phi_{\mathrm{CEP}} = \pm\pi/2$) leads to ambiguity, since changing the polarity does not impact Q_{THz}, i.e. $Q_{\mathrm{THz}}(V_{\mathrm{pk}}) = Q_{\mathrm{THz}}(-V_{\mathrm{pk}})$. This can be seen by isolating the even and odd order terms in Equation 7.4. In general, $Q_{\mathrm{THz}}(V_{\mathrm{pk}}) + Q_{\mathrm{THz}}(-V_{\mathrm{pk}})$ can be fit by a polynomial with only the terms of even n, while $Q_{\mathrm{THz}}(V_{\mathrm{pk}}) - Q_{\mathrm{THz}}(-V_{\mathrm{pk}})$ can be fit by a polynomial with only the terms of odd n. However, for a perfectly symmetric pulse, $Q_{\mathrm{THz}}(V_{\mathrm{pk}}) - Q_{\mathrm{THz}}(-V_{\mathrm{pk}}) = 0$ for any $I(V)$ curve, so the odd order terms of the polynomial are inaccessible. In other words, inverting the waveform does not change the weighting between $I(V)$ features at positive and negative V, so the $I(V)$ asymmetry and curvature cannot be disentangled. Optimistically, any asymmetry in $V_{\mathrm{THz}}(t)$ introduces sensitivity to the odd order terms in Equation 7.4, but, realistically, the asymmetry should significantly exceed the noise level. The waveform shape, $V_0(t)$, in Figure 4.8(a) can therefore be considered ideal in that it is optimally asymmetric ($\phi_{\mathrm{CEP}} = 0$).

The first example considered is a Simmons model with material and tip work functions of $\Phi_s = 5$ eV and $\Phi_t = 5$ eV, respectively. The rectification process for this scenario is sketched in Figure 4.8. To apply the steady-state inversion algorithm, the V_{pk} sweep is performed for both V_{pk} polarizations and the complete $Q_{\mathrm{THz}}(V_{\mathrm{pk}})$ (solid green curve) is fit by a polynomial (with $C_1 = 0$; dotted red curve) to obtain the $C_{n>1}$ coefficients, as shown in Figure 7.1(c). Meanwhile, the B_n coefficients are calculated by numerical integration of the THz voltage waveform raised to the n^{th} power, as defined in Equation 7.4. Finally, the differential conductance extracted through the algorithm can be computed directly based on the C_n and B_n coefficients via Equation 7.6. As noted above, we set $A_1 = 0$ because this term cannot be determined from the algorithm when $B_1 = 0$. Figure 7.1(d) shows a comparison between the differential conductance of the Simmons model used in the simulation (solid black curve) and the differential conductance reconstructed from the algorithm (dotted red curve). We note that the voltage axis of Figure 7.1(d) is labelled V_{pk} for consistency with the algorithm, whereas the original is plotted as $\mathrm{d}I(V_{\mathrm{pk}})/\mathrm{d}V_{\mathrm{pk}}$ for comparison, but is, strictly speaking, a function of V. The agreement is near perfect aside from a vertical offset corresponding to A_1.

In general, the algorithm performs exceptionally well for any $I(V)$ that can be well described by a low-order polynomial. Furthermore, for polynomials with $A_1 = 0$, the offset disappears and the reconstructed differential conductance matches the original. However,

experimental differential conductances are often non-monatonic, e.g. due to resonances in the sample LDOS, and can require higher polynomial orders to reasonably reproduce them. Therefore, we next test the algorithm for highly nonlinear $I(V)$s corresponding to model physical systems.

We first model a semiconducting sample with band onsets at -1.5 V and $+1.5$ V bias. Figure 7.2(a) shows the $I(V)$ (top, solid black curve) and differential conductance (bottom, solid black curve). The latter is modeled as the sum of two error functions, one for each band. Simulating charge rectification by the THz waveform in Figure 7.1(a) yields the dotted red curve in Figure 7.2(a), top, which qualitatively resembles the $I(V)$ curve. Applying the steady-state inversion algorithm, i.e. determining B_n and C_n and then calculating $\mathrm{d}I(V_{\mathrm{pk}})/\mathrm{d}V_{\mathrm{pk}}$ using Equation 7.6, yields a reconstructed differential conductance (Figure 7.2(a), bottom, dotted red curve) that matches the original.

Figure 7.2(b) shows another example, this time corresponding to peaks in the sample LDOS such as those observed for single molecules adsorbed on salt islands [7, 13, 15, 50]. We model the differential conductances as Gaussians peaked at ± 2 V (Figure 7.2(b), bottom, solid black curve), and hence the $I(V)$ is the sum of two error functions (Figure 7.2(b), top, solid black curve). The rectified charge (Figure 7.2(b), top, dotted red curve) diverges more strongly from the shape of the $I(V)$ curve in this case, but the algorithm once more accurately reconstructs the differential conductance (Figure 7.2(b), bottom, compare dotted red and solid black curves).

7.1.3 Simulated Experiment

To test our algorithm's robustness and stability, we introduce noise and simulate an experimental THz-STS measurement. We model noise based on pulse-to-pulse energy fluctuations in a NIR laser system that generates THz pulses through optical rectification. Since the emitted THz field is proportional to NIR pulse energy, these fluctuations produce a pulse-to-pulse variation in the strength of the THz voltage applied across the junction. We model this by $V_{\mathrm{THz}}(t) = (1 \pm \epsilon)V_{\mathrm{pk}}V_0(t)$, where ϵ is a random number chosen from within a range defined by the NIR pulse fluctuations. For our simulations, $\epsilon_{\mathrm{max}} = 0.05$. The absolute voltage uncertainty grows with V_{pk}, e.g., for $|V_{\mathrm{pk}}| = 3$ V the uncertainty range is 0.3 V. Notably, the entire THz voltage waveform scales with the NIR pulse energy, as it is expected to retain its temporal shape in an experiment provided the nonlinear generation crystal does not change.

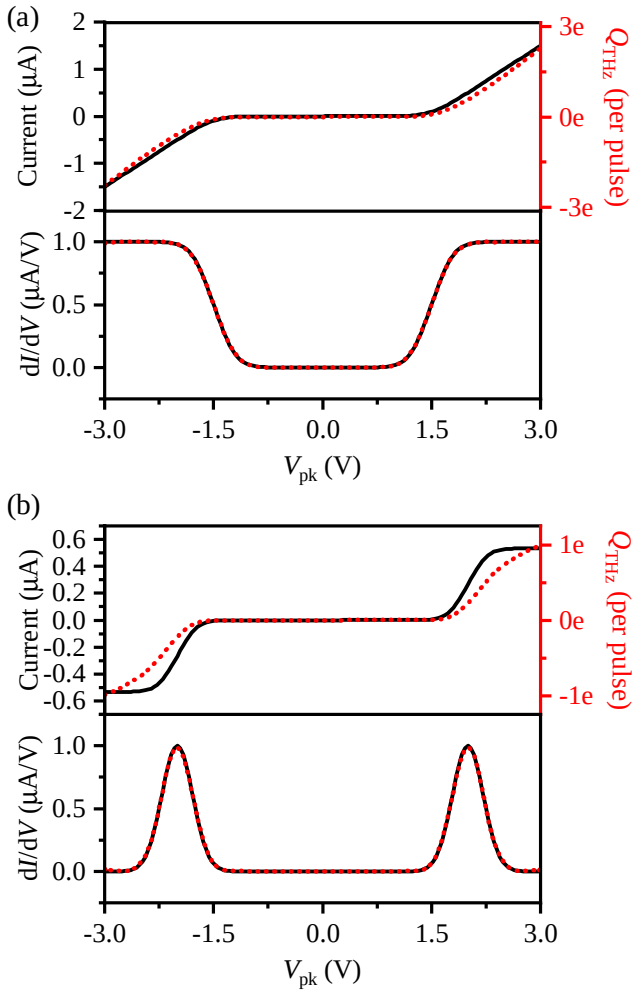

Figure 7.2: Reconstructing highly nonlinear differential conductances. (a) Top: $I(V)$ for a simple model of a semiconducting sample with band onsets at -1.5 V and $+1.5$ V (black curve) and corresponding rectified charge (dotted red curve) produced by the THz voltage waveform in Figure 7.1(a). Bottom: differential conductance for the semiconductor model (black curve) and reconstructed differential conductance (dotted red curve). (b) Top: $I(V)$ for a simple model of a molecule adsorbed on a salt film on a metal substrate with electronic orbitals centered at ± 2 V (solid black curve) and corresponding rectified charge (dotted red curve) produced by the THz voltage waveform in Figure 7.1(a). Bottom: differential conductance for the molecular system (solid black curve) and reconstructed differential conductance (dotted red curve). Fitting of $Q_{\mathrm{THz}}(V_{\mathrm{pk}})$ in each system was performed with a polynomial of order $N = 38$.

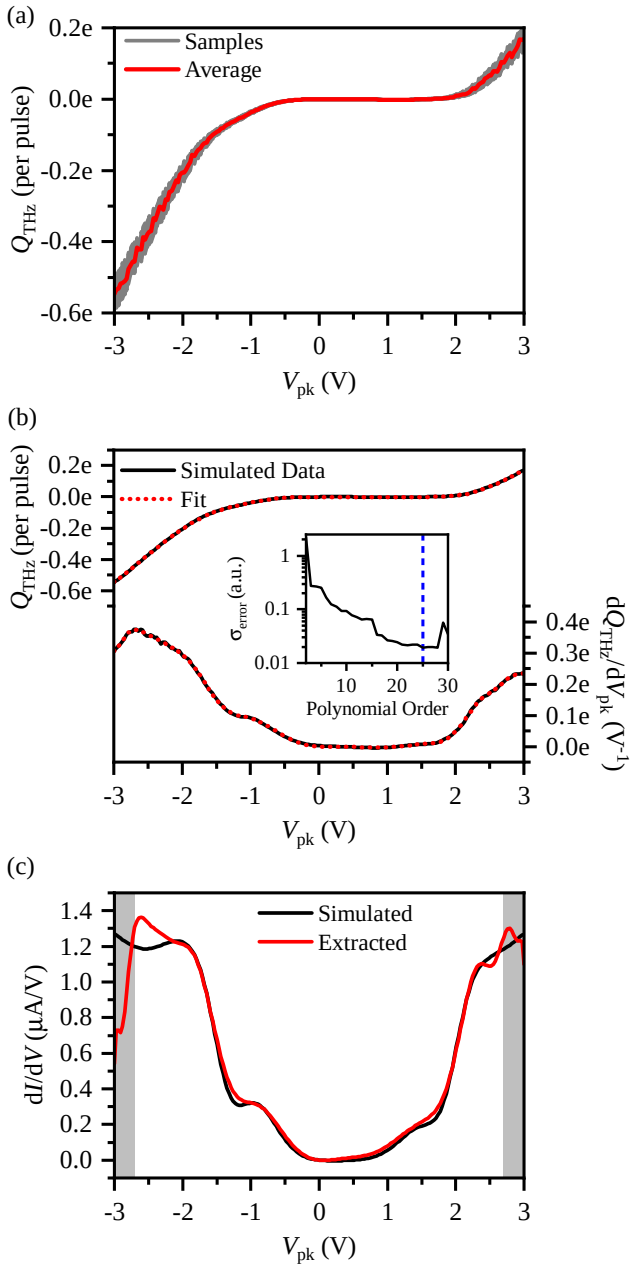

Figure 7.3: Reconstructing an arbitrary differential conductance in the presence of noise. (a) In a simulated THz-STS experiment, charge rectification is calculated for a voltage waveform with a randomly fluctuating field strength ($\epsilon_{\max} = 0.05$; 10 calculations per $V_{\rm pk}$). The gray region shows the simulated experimental data and the red curve is the average. (b) $Q_{\rm THz}(V_{\rm pk})$ (top black curve) and $\mathrm{d}Q_{\rm THz}(V_{\rm pk})/\mathrm{d}V_{\rm pk}$ (bottom black curve) after a Savitzky-Golay filter of order 1 has been applied with a window of 0.27 V (∼5% of the $V_{\rm pk}$ axis width). Red dotted curves: simultaneous fit. Inset: standard deviation of the fit to $Q_{\rm THz}(V_{\rm pk})$. Blue dashed line: polynomial order used for the fits in (b) and extraction in (c). (c) Comparison between the simulated differential conductance (black curve) and the algorithm result (red curve) for polynomial of order $N = 25$. Gray vertical bars: $\sim 5\%$ of the axis width, where the filters break down.

An example simulated experiment is shown in Figure 7.3(a), where ten noisy $Q_{\mathrm{THz}}(V_{\mathrm{pk}})$ curves are overlaid, forming the gray region, which expands with increasing $|V_{\mathrm{pk}}|$. This effect is mitigated by standard measurement techniques, where the rectified charge of many pulses is averaged by a lock-in amplifier. The average of the ten $Q_{\mathrm{THz}}(V_{\mathrm{pk}})$ curves is shown as the red curve in Figure 7.3(a). Its roughness is comparable to similar datasets from the literature [8] and Chapter 6. Unfortunately, the noise in even the average curve leads to spurious weighting of high-order polynomial terms in the fitting step of the algorithm. This, in turn, can result in unphysical oscillations in the extracted differential conductance. Therefore, it is necessary to develop a procedure to obtain a reliable result.

While it is possible to employ an arbitrarily large number of polynomial orders, limiting the number of terms to avoid over-fitting noisy data can suppress oscillations in the extracted $\mathrm{d}I/\mathrm{d}V$ curve. Nevertheless, we find that polynomials with order greater than five tend to develop undesirable $\mathrm{d}I/\mathrm{d}V$ oscillations at the edges of the voltage range when the algorithm is applied as described in the previous section to noisy $Q_{\mathrm{THz}}(V_{\mathrm{pk}})$ data. However, we have discovered that simultaneously fitting both $Q_{\mathrm{THz}}(V_{\mathrm{pk}})$ and $\mathrm{d}Q_{\mathrm{THz}}(V_{\mathrm{pk}})/\mathrm{d}V_{\mathrm{pk}}$ when finding C_{n} better constrains the behavior at the boundaries. To obtain a well-behaved numerical derivative, a smoothing function is applied to $Q_{\mathrm{THz}}(V_{\mathrm{pk}})$ prior to calculating $\mathrm{d}Q_{\mathrm{THz}}(V_{\mathrm{pk}})/\mathrm{d}V_{\mathrm{pk}}$. A second smoothing function is applied to $\mathrm{d}Q_{\mathrm{THz}}(V_{\mathrm{pk}})/\mathrm{d}V_{\mathrm{pk}}$ to reduce the noise that is introduced when calculating the derivative. The smoothed data (Figure 7.3(b), black curves) are produced by applying a Savitzky-Golay filter in each step [255] that convolutes a linear polynomial with a moving window that is $\sim$5% of the total V_{pk} range (i.e., $\sim$0.3 V).

To determine an appropriate number of polynomial fit terms, we calculate the standard deviation, σ_{error}, between the fit result and $Q_{\mathrm{THz}}(V_{\mathrm{pk}})$ as a function of fit order. The polynomial fits in Figure 7.3(b) (red curves) use a polynomial in the lowest plateau region of σ_{error} (marked by a dashed blue line in the inset of Figure 7.3(b)). Although limiting the number of polynomial orders used in the fit reduces the voltage resolution in the extracted differential conductance, it also increases the stability and reliability of the result.

In Figure 7.3(c), we compare the simulated differential conductance (black curve) to the extracted differential conductance (red curve) following this procedure. We have used a more structured model $\mathrm{d}I/\mathrm{d}V$ here than those shown in the previous section to better approximate a real experiment (and a similar $\mathrm{d}I/\mathrm{d}V$ to that measured for the 7-AGNR in Chapter 6). It is important to note the smoothing filters overshoot at the boundaries of

$Q_{\mathrm{THz}}(V_{\mathrm{pk}})$ and $\mathrm{d}Q_{\mathrm{THz}}(V_{\mathrm{pk}})/\mathrm{d}V_{\mathrm{pk}}$, so the extracted $\mathrm{d}I/\mathrm{d}V$ in this region (gray shaded area) may still contain oscillations, as is the case here. The tradeoff between polynomial order and resolution is apparent in the features near $\pm$1V, both of which are broadened. Nevertheless, the adapted algorithm outlined in this section successfully reproduces the salient features of the differential conductance in the presence of noise while mostly constraining artifacts to the $\sim$5% of the voltage range nearest the boundaries.

Including more derivatives in the simultaneous fit can further suppress oscillations, but further smoothing is also required for each additional derivative order. Employing a more sophisticated technique to handle the derivatives of noisy data (e.g., regularization) may improve this approach. We have also explored other procedures (e.g., matrix multiplication, frequency filtering, etc.), but their compatibility with the time-dependent algorithm of the next section has not yet been shown, so it is difficult to comment on their effectiveness at this time.

7.2 Time-Dependent Inversion Algorithm

7.2.1 Theory

The previous section outlined an algorithm to reconstruct static differential conductances from THz-STS measurements. However, a THz voltage pulse can also probe the ultrafast evolution of the junction following photoexcitation by a femtosecond optical or near-infrared pump pulse, as illustrated in Figure 4.9.

In such an experiment, absorption of the pump pulse modifies the junction, changing the $I(V)$ on the timescale of its intensity envelope. The $I(V)$ curve subsequently decays back to the ground state on a timescale defined by the material system. The time-delayed THz probe pulse samples this evolution by adiabatically sweeping through voltage configurations. In this section, we assume THz-driven tunneling does not affect the time-dependence of the $I(V)$. Meanwhile, our treatment of the THz probe as quasi-static is justified by the Keldysh parameter ($\gamma << 1$).

Figure 7.4(b) depicts the projection of $V_{\mathrm{THz}}(t)$ onto a time-dependent $I(V)$ curve defined by a Simmons model that appears at $t = 0$ and decays exponentially for $t > 0$ with a $1/e$ time of 1 ps. We define the delay time τ as the time from photoexcitation (at $t = 0$) to the arrival of the THz voltage peak. The dynamics are encoded in the resulting THz-induced

current transient, which depends on t and τ, while detection via the rectified charge (after integration over t) further obscures the sample dynamics. We note that the rectified charge retains its dependence on τ, since the pump-probe experiment can be repeated for different τ to generate $Q_{\mathrm{THz}}(\tau)$. In the following, we introduce an algorithm to reconstruct the time-dependent differential conductance of a tunnel junction from $Q_{\mathrm{THz}}(V_{\mathrm{pk}}, \tau)$ in a pump-probe experiment.

We begin by generalizing the static $I(V)$ polynomial from Section III to a dynamic polynomial with arbitrary temporal structure. This is done through time-dependent series coefficients, i.e.,

$$I(V,t) = \sum_{n=1}^{N} A_n(t) V^n \,. \tag{7.7}$$

Substituting $I(V,t)$ into the expression for rectified charge (analogous to Equation 7.2 in the previous section) yields

$$Q_{\mathrm{THz}}(V_{\mathrm{pk}}, \tau) = \sum_{n=1}^{N} V_{\mathrm{pk}}^n \int_{-\infty}^{\infty} A_n(t+\tau)[V_0(t)]^n \, dt \,. \tag{7.8}$$

Unlike in the static case, the coefficients of the polynomial cannot be moved outside the temporal integral. Nevertheless, the rectified charge $Q_{\mathrm{THz}}(V_{\mathrm{pk}}, \tau)$ can still be written as a polynomial,

$$Q_{\mathrm{THz}}(V_{\mathrm{pk}}, \tau) = \sum_{n=1}^{N} C_n(\tau) V_{\mathrm{pk}}^n \,. \tag{7.9}$$

We highlight that the series in Equation 7.8 and Equation 7.9 begins at $n = 1$, whereas the static $Q_{\mathrm{THz}}(V_{\mathrm{pk}})$ polynomial in Section III began at $n = 2$ (Equation 7.4), because a nonzero rectified charge can be generated by an Ohmic component that changes with time.

The experimental protocol for pump-probe THz-STS is to record a $Q_{\mathrm{THz}}(V_{\mathrm{pk}}, \tau)$ map. For each sweep of V_{pk} (i.e., for each τ), $Q_{\mathrm{THz}}(V_{\mathrm{pk}})$ is fit by a polynomial, similar to the procedure in the steady-state algorithm. Repeating this process as a function of τ allows $C_n(\tau)$ to be determined experimentally, where

$$C_n(\tau) = \int_{-\infty}^{\infty} A_n(t+\tau)[V_0(t)]^n \, dt \,. \tag{7.10}$$

Here, we note that $C_n(\tau)$ is a cross-correlation of $A_n(t)$ and $[V_0(t)]^n$, and therefore these functions can be isolated using the cross-correlation theorem (which is similar to the convolution theorem). Specifically,

$$\mathcal{F}\{C_n(\tau)\}(\nu) = \mathcal{F}\{A_n(t)\}(\nu) \cdot \mathcal{F}\{[V_0(t)]^n\}(\nu) \,. \tag{7.11}$$

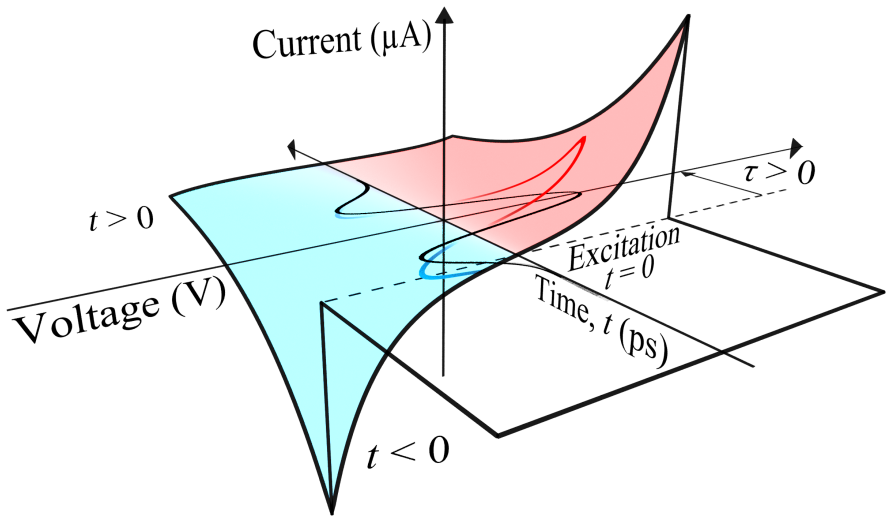

Figure 7.4: Visualizing pump-probe THz-STS of a transient $I(V)$. In an example pump-probe THz-STS experiment, a Simmons model $I(V)$ curve is initialized at $t = 0$ by optical excitation and subsequently decays with a decay time of 1 ps. A THz voltage pulse (black curve) arrives at the tunnel junction after a delay time τ, where τ is defined as the time from excitation to the peak of $V_{\mathrm{THz}}(t)$ and is positive (negative) when the optical pulse arrives first (second). Red and blue shading denotes positive and negative current, respectively. The THz voltage pulse (red and blue curve) is mapped onto the time-dependent $I(V)$ curve, indicating the THz-induced trajectory through three-dimensional $I - V - t$ space. Notably, the THz-induced current is larger for oscillations occuring soon after photoexcitation.

Utilizing a numerical fast Fourier transform algorithm allows $\mathcal{F}\{C_n\}(\nu)$ and $\mathcal{F}\{V_0^n\}(\nu)$ to be extracted from the experimental $C_n(\tau)$ and $V_0(t)$, respectively. Thus, $A_n(t)$ can be obtained by

$$A_n(t) = \mathcal{F}_\nu^{-1}\left\{\frac{\mathcal{F}\{C_n\}(\nu)}{\mathcal{F}\{V_0^n\}(\nu)}\right\}, \tag{7.12}$$

where each n term is calculated separately. A consequence of Equation 7.12 is that the accessible $A_n(t)$ bandwidth depends on the bandwidth of $[V_0(t)]^n$, which in turn is a function of n. This impacts the time resolution of THz-STS, especially in the subcycle regime, as discussed in the following sections.

Within the bandwidth limits, Equation 7.12 directly yields the coefficients of the time-dependent polynomial in Equation 7.7, including the Ohmic term. The time-dependent differential conductance can be obtained from

$$\frac{\mathrm{d}I}{\mathrm{d}V_{\mathrm{pk}}}(V_{\mathrm{pk}}, t) = \sum_{n=1}^{N} nA_n(t)V_{\mathrm{pk}}^{n-1}. \tag{7.13}$$

In contrast to the steady-state algorithm, Equation 7.13 includes even the $n = 1$ term, which is independent of voltage, because its time dependence brings it into view for THz-STS. In the following section, we will demonstrate the algorithm's efficacy by extracting the time-dependent differential conductance from simulated pump-probe THz-STS experiments.

7.2.2 Demonstration

We demonstrate the time-dependent algorithm's effectiveness by recovering a dynamic differential conductance, which we conceive as a model for a photoexcited semiconductor. We describe the differential conductance of the unexcited sample with two error functions, representing conduction and valence bands, with onsets at +2 V and −2 V, respectively. We then introduce ultrafast optical excitation at $t = 0$: a pump pulse with photon energy of ∼4 eV redistributes electrons from the VB to the CB. The subsequent decay dynamics are imprinted on the time-dependent $I(V)$, but the precise behavior is non-trivial and depends on the sample. For the simple case considered here, we speculate that the dominant change may arise from field-emission of electrons from the CB. We therefore incorporate a transient, one-sided Simmons model with a sample work function of $\Phi_{\mathrm{s}} = 3$ eV that appears instantaneously at $t = 0$ ps and decays with a $1/e$ time of 1 ps. The value of Φ_{s} is chosen to model field emission from states well above the Fermi level, i.e., Φ_{s} is smaller than a typical material

work function, while the decay time represents a generic reduction in electrons available for field emission over time, for example through a combination of electron-hole recombination, carrier trapping, and depletion layer formation at the surface [173].

Although the $I(V,t)$ considered here is an example created to demonstrate the time-dependent algorithm's effectiveness, it may be informative to add a few general comments: (i) Optical excitation will likely produce photocurrent even for zero bias voltage, which corresponds to a finite $n = 0$ term in $I(V,t)$. However, this photocurrent is neglected here because THz-STS measurements recorded via lock-in detection, where the THz pulse is modulated, are insensitive to currents that do not depend on $V_{\mathrm{THz}}(t)$. (ii) Tunneling into the CB and out of the VB will presumably also be modulated to some extent by photoexcitation, but we assume that the corresponding impact on the differential conductance will be minor because the fraction of electrons that are photoexcited is likely to be small. Yet, this assumption may break down if the sample contains only a few electrons. (iii) Our time-dependent Simmons model incorporates photo-assisted field emission only from the sample and neglects a similar process from a photoexcited tip. Meanwhile, field emission at the sample and tip work functions is considered to be present, but it is assumed to be negligible here and is therefore left out of the model.

Figure 7.5(a) shows $Q_{\mathrm{THz}}(V_{\mathrm{pk}},\tau)$ generated in a simulated pump-probe THz-STS experiment based on the $I(V,t)$ described above and the waveform in Figure 7.1(a). Interestingly, whereas the shape of $Q_{\mathrm{THz}}(V_{\mathrm{pk}})$ for the static semiconductor model in Figure 7.2(a) resembled that of $I(V)$, their time-dependent shapes in the pump-probe simulation can strongly differ. At $V_{\mathrm{pk}} = 4$ V (Figure 7.5(b)), $Q_{\mathrm{THz}}(\tau)$ features two prominent negative peaks spaced by 1 ps and an approximately exponential decay for $\tau > 2$ ps (red circles), despite there being no time dependence in $I(t)$ at $V_{\mathrm{pk}} = 4$ V at all (black circles). Conversely, at $V_{\mathrm{pk}} = -4$ V (Figure 7.5(c)), the $Q_{\mathrm{THz}}(\tau)$ transient (red circles) is similar to $I(t)$ (black circles), i.e., the decay of the rectified charge is a reasonable proxy for the inherent dynamics of the junction. Together, Figure 7.5(b) and 7.5(c) illustrate that although THz-STS can in some circumstances directly capture the dynamics of the junction, convolution of the THz voltage waveform with those dynamics can also produce misleading features in the experimental data. Furthermore, the parameter space in which each effect dominates is not obvious *a priori*, meaning there is significant uncertainty whether $Q_{\mathrm{THz}}(V_{\mathrm{pk}},\tau)$ shows the intrinsic behavior of the junction for a particular choice of V_{pk}. An algorithm that reveals $I(V,t)$ using the entire $Q_{\mathrm{THz}}(V_{\mathrm{pk}},\tau)$

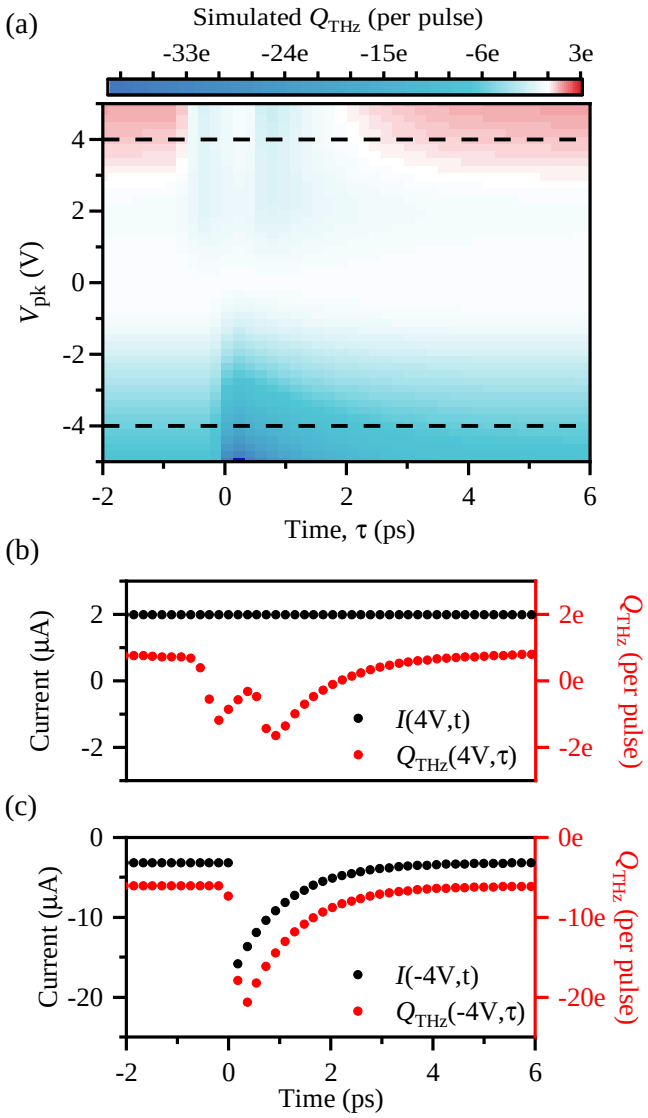

Figure 7.5: Simulated pump-probe THz-STS data. The simulation is performed using the THz voltage waveform in Figure 7.1(a) and the time-dependent differential conductance model described in the text, where the definition of the delay time τ is shown in Figure 7.4(b). (a) Rectified charge map produced by the simulation. The algorithm was applied to a τ window from -5 ps to 15 ps; a cropped region is presented to highlight detail on the subpicosecond timescale. Dashed lines are guides indicating the cross-sectional cuts shown in (b) and (c). (b) Cut through the rectified charge map at $V_{\mathrm{pk}} = 4$ V (red circles) and simulated $I(t)$ at $V = 4$ V for comparison (black circles). (c) Cut through the rectified charge map at $V_{\mathrm{pk}} = -4$ V (red circles) and simulated $I(t)$ at $V = -4$ V for comparison (black circles).

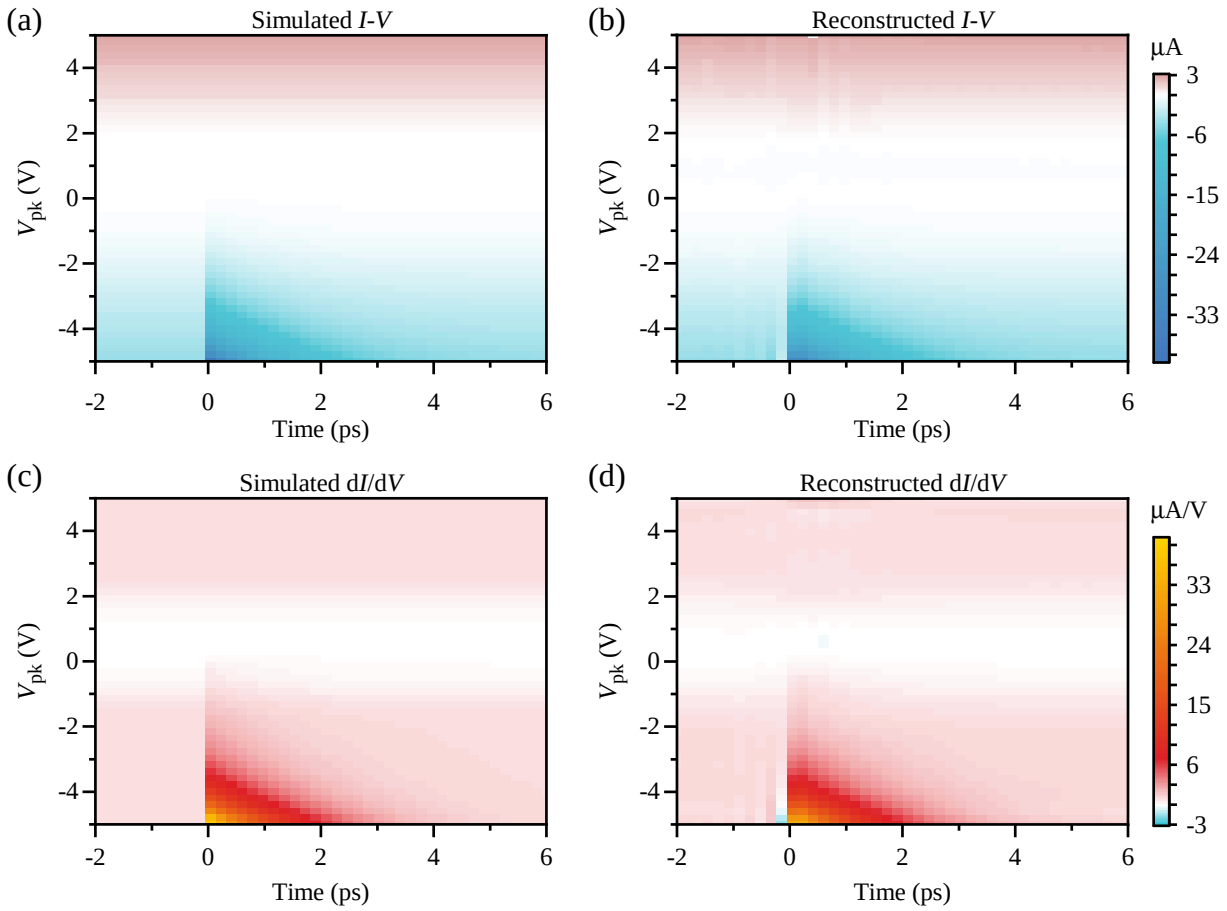

Figure 7.6: Reconstructing a transient $I(V)$ curve and differential conductance with the time-dependent inversion algorithm. (a) Original $I(V)$ used to simulate the THz-STS data shown in Figure 7.5(a). (b) Reconstructed $I(V)$ obtained using the time-dependent inversion algorithm. (c) Differential conductance for the model tunnel junction in (a). (d) Reconstructed differential conductance determined alongside (b) using the inversion algorithm. Fitting of $Q_{\mathrm{THz}}(V_{\mathrm{pk}})$ in the algorithm was performed with a polynomial of order $N = 21$. All plots are cropped along the time axis from the original bounds of -5 ps to 15 ps.

map is therefore essential for pump-probe THz-STS.

Here, we apply the pump-probe THz-STS inversion algorithm introduced in the previous section to the $Q_{\mathrm{THz}}(V_{\mathrm{pk}}, \tau)$ map in Figure 7.5(a). The original $I(V,t)$ used to generate the map is shown in Figure 7.6(a). The procedure is as described in the previous section. Briefly, $Q_{\mathrm{THz}}(V_{\mathrm{pk}})$ is fit by a polynomial at each time step, as defined in Equation 7.9. The n^{th}-order coefficients form a time-dependent function, $C_n(\tau)$. The Fourier transform of $C_n(\tau)$ is divided by the Fourier transform of $[V_0(t)]^n$, and the inverse Fourier transform of the result yields the $A_n(t)$ coefficients of the polynomial. In practice, we also employ an amplitude cutoff for $\mathcal{F}\{V_0^n\}(\nu)$ to avoid divergences, which we set to 5×10^{-4}. For any $\mathcal{F}\{V_0^n\}(\nu)$ below the cutoff, $\mathcal{F}\{A_n\}(\nu)$ is set to 0. The resulting reconstructed $I(V,t)$ obtained through the algorithm is shown in Figure 7.6(b). It agrees remarkably well with the original. The simulated and reconstructed differential conductances are shown in Figure 7.6(c) and 7.6(d), respectively, where the agreement is once more exemplary.

We have further tested the time-dependent algorithm for decay times of 10 ps and 100 ps and found the accuracy of the reconstruction to be similar or better. Alternatively, the steady-state algorithm may be applied to transient $I(V)$s with decay times greater than 10 ps to similar effect (provided the region near $\tau = 0$ ps is excluded) since the differential conductance changes slowly during the oscillations of the THz voltage pulse. For yet longer decay times, greater that 100 ps, the steady-state algorithm is recommended, as the sample dynamics are dominated by frequency components below the THz pulse bandwidth. These frequencies are excluded from the inversion calculation through the $\mathcal{F}\{V_0^n\}(\nu)$ amplitude cutoff.

7.2.3 Subcycle Time Resolution

The time-dependent inversion algorithm is capable of extracting dynamics faster than a single oscillation cycle of the THz voltage probe. This subcycle time resolution is evident in Figure 7.6, where the algorithm reproduces the stepwise onset of the transient at $t = 0$, in addition to the exponential decay for $t > 0$. The onset of the simulated transient occurs in a single 200 fs timestep, i.e., at a rate exceeding the 2 THz bandwidth of the voltage probe (Figure 7.1(b)).

We explore the time resolution of the algorithm further using a simple symmetric Simmons model ($\Phi_{\mathrm{s}} = \Phi_{\mathrm{t}} = 5$ eV) that appears at $t = 0$ and decays exponentially for $t > 0$, as

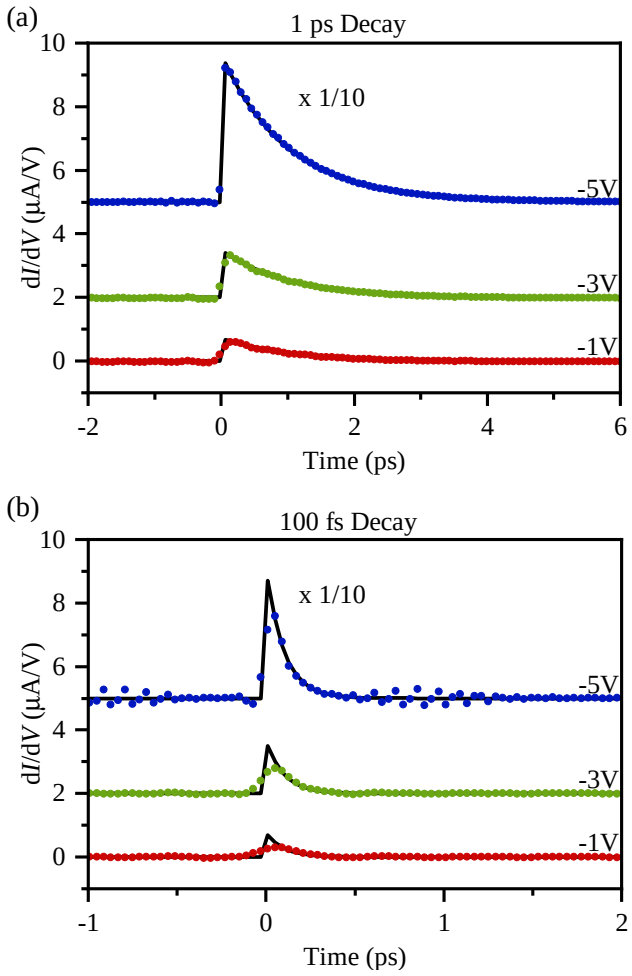

Figure 7.7: Resolving subcycle dynamics with the time-dependent inversion algorithm. The simulated $I(V)$ is defined by a Simmons model that appears at $t = 0$ and subsequently decays away exponentially for $t > 0$, as described in the text. For $t < 0$, $I = 0$ and $\mathrm{d}I/\mathrm{d}V = 0$. (a), (b) Simulated transient differential conductance at $V = -5\,\mathrm{V}$, $V = -3$ V, and $V = -1$ V (black curves, offset for clarity) for a decay time of (a) 1 ps and (b) 100 fs. The reconstructed transient differential conductance is shown for the same voltages ($V = -5\,\mathrm{V}$: blue circles; $V = -3\,\mathrm{V}$: green circles; $V = -1$ V: red circles). Fitting $Q_{\mathrm{THz}}(V_{\mathrm{pk}})$ in the time-dependent algorithm was performed with a polynomial of order $n = 21$ for both 1 ps and 100 fs calculations. In both panels, the plots are cropped from the original time axis of -5 ps to 15 ps that was used in the time-dependent algorithm. Panel (b) was calculated using 500 points along the time axis compared to 250 points for panel (a) to facilitate analysis at higher frequencies.

illustrated in Figure 7.4(b). For $t < 0$, $I = 0$ for all V. We consider the case of a 1 ps decay time and an onset that occurs in one 80 fs timestep. Figure 7.7(a) shows slices through $\mathrm{d}I(V,t)/\mathrm{d}t$ at constant voltages of -5 V, -3 V, and -1 V along with the corresponding cuts through the reconstruction result. The algorithm reproduces the 1 ps exponential decay of the differential conductance at all voltages. Conversely, the 80 fs onset of the transient is only well reproduced for the highest magnitude bias (-5 V), whereas the onset is broadened for voltages closer to 0 (-3 V, -1 V). Interestingly, this means that the step width is better resolved for larger step heights.

The algorithm's time resolution at a given voltage is linked to the nonlinearity of the $I(V)$ at that voltage. Conceptually, this can be understood by considering the THz-induced current pulse. For the case of the Simmons model, the current rapidly increases (decreases) as the voltage reaches the work function of the tip (sample). Therefore, for V_{pk} approaching a work function, the full width at half maximum of the current produced by the main $V_{\mathrm{THz}}(t)$ oscillation cycle narrows. Meanwhile, within the time-dependent algorithm, the fit to $Q_{\mathrm{THz}}(V_{\mathrm{pk}}, \tau)$ (see Equation 7.9) is dominated at low V_{pk} by low polynomial orders and at high V_{pk} by high polynomial orders. The result is faster time resolution for the higher order terms in the inversion algorithm and, similarly, faster time resolution for the parts of the reconstructed differential conductance at higher $|V|$. This explains why the reconstructed step widths in Figure 7.7(a) narrow with increasing $|V|$. It further implies that yet faster time resolution can be achieved for highly nonlinear $I(V)$ curves.

We explore the limits of the algorithm's subcycle time resolution by examining a transient Simmons model that appears within one 40 fs timestep (1/40 fs = 25 THz) and decays with a time constant of 100 fs (1/100 fs = 10 THz). For comparison, the spectral amplitude of the THz voltage pulse is negligible above 2 THz (Figure 7.1(b)). Figure 7.7(b) shows cuts through the differential conductance at -1 V, -3 V, and -5 V alongside cuts through the reconstructed differential conductance at the same voltages. As expected, the time resolution improves for increasing $|V|$, with the result at -5 V close to matching the onset and decay rate, though with lower overall amplitude. However, the reconstructed curve for -5 V also, surprisingly, includes oscillations at both negative and positive times that are not present in the original curve.

The relative accuracy of the reconstructed differential-conductance transients can be understood by considering how subcycle time resolution arises in Equation 7.12. The band-

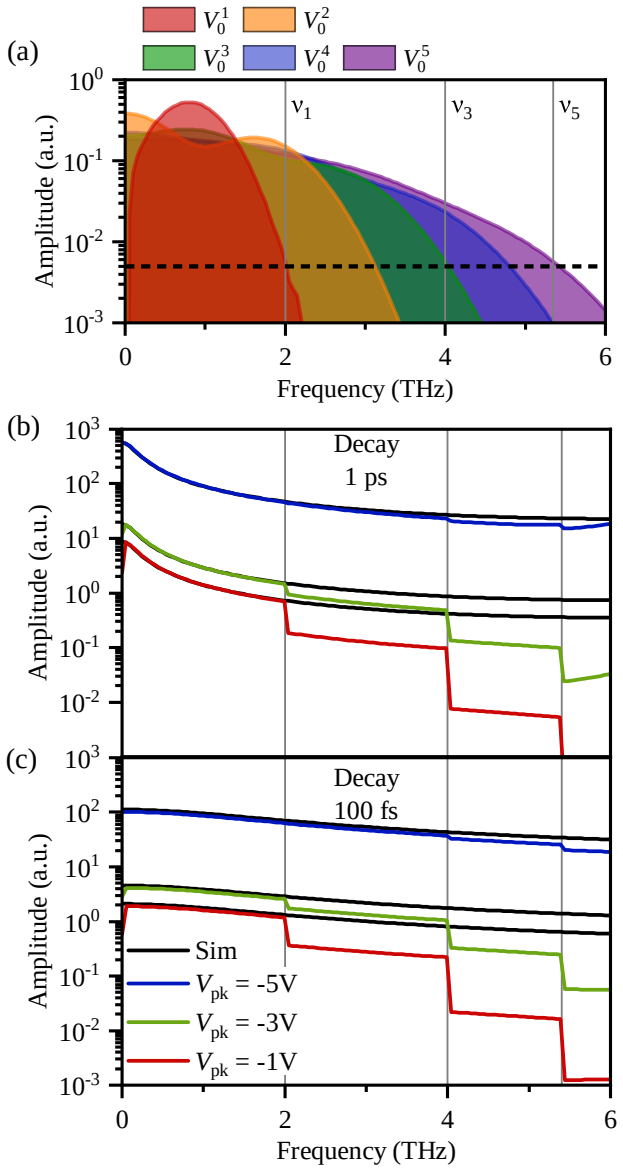

Figure 7.8: Defining the time resolution of THz-STS. (a) Fast Fourier transform amplitude of $[V_0(t)]^n$, indicating the bandwidth of the corresponding order in the time-dependent inversion algorithm. Dashed black line: cutoff amplitude of 5×10^{-4} applied in Equation 7.12. (b), (c) Fast Fourier transform amplitude of the simulated transient differential conductance in Figure 7.7(a): 1 ps decay (b) and Figure 7.7(b): 100 fs decay (c). In each panel, top black curve: -5 V, middle black curve: -3 V, bottom black curve: -1 V. The legend in panel (c) applies to both (b) and (c), where the blue, green, and red curves in each plot are the amplitude of the fast Fourier transform of the reconstructed differential conductance for the corresponding V_{pk} (see legend) and decay time. Gray vertical lines: frequency at which the amplitude of the Fourier transform of $V_0(t)$, $[V_0(t)]^3$, and $[V_0(t)]^5$ crosses the amplitude cutoff, leading to a loss of information in the reconstructed differential conductance (ν_1, ν_3, and ν_5, respectively).

width of $[V_0(t)]^n$ increases for increasing n, as shown in Figure 7.8(a). The spectral amplitude above the cutoff (dashed black line in Figure 7.8(a)) defines the maximum frequency (ν_n) that can be resolved at a given n. Within the time-dependent algorithm, $\mathcal{F}\{A_n\}(\nu)$ is set to zero for frequencies above ν_n, so the reconstructed differential conductance contains the corresponding order only for frequencies below ν_n. This loss of information is visualized in Figure 7.8(b) and 7.8(c), which show the spectral amplitudes of the cuts through the simulated and reconstructed differential conductances from Figure 7.7(a) and 7.7(b), respectively. At the frequencies indicated by the gray lines, the amplitude of $\mathcal{F}\{[V_0]^n\}(\nu)$ crosses the cutoff threshold (Figure 7.8(a)) and that order is dropped from the reconstructed differential conductance (discontinuities in Figure 7.8(b) and 7.8(c)). Only odd orders have a significant impact in this example because the $I(V)$ curve is anti-symmetric and therefore composed of only odd-order terms.

The loss of information is most impactful for the reconstructed curves at low V_{pk} (e.g. -1 V in Figure 7.8(a) and 7.8(b)), since the $A_{n<5}$ coefficients dominate. Conversely, at -5 V, the $I(V)$ is more nonlinear, and hence is composed primarily of higher order terms, so dropping A_1, for example, does not lead to much deviation from the simulated amplitude. Meanwhile, the 1 ps decay curve is better reproduced in the time domain than the 100 fs decay curve (compare Figure 7.7(a) to 7.7(b)). This is because the amplitude of the simulated differential conductance is weighted more strongly at frequencies within the bandwidth of $V_0(t)$ for the 1 ps decay (Figure 7.8(b)) than for the 100 fs decay (Figure 7.8(c)). In other words, when the spectral weight of the simulation is concentrated in a frequency region where all $[V_0(t)]^n$ have sufficient spectral amplitude, the algorithm achieves near perfect reconstruction. As the speed of the dynamics is increased, the spectral weight redistributes from low to high frequency (compare Figure 7.8(b) to 7.8(c)), leading to inaccuracies in the reconstruction, especially at low V_{pk}. Still, even for dynamics far above the bandwidth of the THz voltage pulse, the algorithm recovers the majority of the spectral content for voltages at which the $I(V)$ is highly nonlinear.

7.3 Discussion

Subcycle THz-STS is a potentially powerful tool for ultrafast nanoscience. In anticipation of the wide range of experimental studies that may be enabled, we provide some

comments below on the scope of the steady-state and time-dependent inversion algorithms.

The algorithms as they are currently formulated are not compatible with a static bias voltage, V_{DC}. Specifically, the simplifications in Equation 7.2 and Equation 7.8 cannot be made because cross-terms arise when $V_{\mathrm{total}} = V_{\mathrm{DC}} + V_{\mathrm{THz}}(t)$ is raised to a power of n. We believe this issue can be solved by redefining the polynomial that the THz voltage pulse acts on. In short, when a static bias is present without $V_{\mathrm{THz}}(t)$, it produces a current

$$I_{\mathrm{DC}} = \sum_{n=1}^{N} A_n V_{\mathrm{DC}}^n \,. \tag{7.14}$$

Due to lock-in detection, THz-STS measures only THz-induced current, which we label I'. A new I'-V' characteristic can be defined in which the origin is shifted from $V = 0$, $I = 0$ to $V = V_{\mathrm{DC}}$, $I = I_{\mathrm{DC}}$. The THz voltage pulse acts on this new I'-V' curve, such that

$$I' = \sum_{m=1}^{M} A'_m (V')^m \,, \tag{7.15}$$

and $V' = V_{\mathrm{THz}}(t)$. Critically, the A'_m coefficients are *different* from the A_n coefficients of the original $I(V)$ curve defined in Equation 7.1. We caution that $I'(V_{\mathrm{pk}})$ should be considered a new intrinsic characteristic of the junction sampled by the THz voltage pulse, with V_{DC} as an external control parameter, rather than a translation of the original $I(V)$, since the differential conductance may be frequency dependent and moving the origin will mix the inaccessible linear term of the polynomial with other orders.

Another adaptation to the algorithm could be to use a different basis set for the $I(V)$ curve (i.e., not a polynomial). Other basis sets could prove well-matched to certain shapes and be employed accordingly.

The time-dependent algorithm may be further improved by optimizing how the loss of information at the cutoff amplitude is managed. We have demonstrated one option, which is to set $\mathcal{F}\{A_n\}(\nu)$ to zero when the amplitude of $\mathcal{F}\{[V_0]^n\}(\nu)$ is below threshold. Another approach, which reduces discontinuities, is to set $\mathcal{F}\{A_n\}(\nu)$ equal to its value just above threshold for all frequencies where $\mathcal{F}\{[V_0]^n\}(\nu)$ is below threshold. Regardless, any choice will involve assumptions because information is inaccessible outside of the order-dependent bandwidth.

An important future prospect is to develop an inversion algorithm for THz-pump/THz-probe experiments. The steady-state and time-dependent algorithms introduced here both

assume that the THz voltage pulse does not change the differential conductance. However, it has been shown experimentally that a THz voltage transient can excite sample dynamics, for example molecular motion triggered by THz-induced tunneling [7, 13, 15] or by the local force of the THz field transient [13, 15]. Another scenario is Coulomb blockade dynamics, where the THz-induced tunneling of one electron alters the potential energy landscape encountered by subsequent electrons. This change could occur within the oscillations of the THz voltage and depend on the waveform shape and field strength. It should be possible to identify such behavior from THz-pulse autocorrelation measurements, but an analysis algorithm beyond what is shown in this work will be needed to disentangle it.

For the algorithms presented here, it is also important to consider the material properties that are probed. Following [51], in conventional STS the local density of states of the sample can be approximated as

$$\rho_{\text{sample}}(V) = \frac{\hbar}{4\pi^2 \rho_{\text{tip}} T(V)} \left[\frac{\mathrm{d}I}{\mathrm{d}V} + \frac{ed\sqrt{2m}}{2\hbar\sqrt{\bar{\Phi}}} I(V) \right], \tag{7.16}$$

where ρ_{sample} is the sample LDOS, ρ_{tip} is the tip DOS, $T(V)$ is transmission probability, d is the tunnel barrier width, m is the electron mass, and $\bar{\Phi} = (\Phi_{\text{t}} + \Phi_{\text{s}})/2$. We note that this expression is often further approximated as $\rho_{\text{sample}} \propto \mathrm{d}I/\mathrm{d}V$ in the literature (and in Chapter 2). The steady-state THz-STS inversion algorithm provides $I(V)$ through Equation 7.5 and $\mathrm{d}I/\mathrm{d}V$ through Equation 7.6, with the notable exception of the Ohmic contribution to $I(V)$ and $\mathrm{d}I/\mathrm{d}V$. Yet, Equation 7.16 may not hold for THz-STS. As has been shown for silicon [8], the physical response of a tip-sample junction can significantly differ for a THz voltage probe compared to a DC one, emphasizing the need for a THz-STS inversion algorithm. A reformulation of Equation 7.16 may therefore be necessary for some steady-state THz-STS experiments. It will certainly be required to model pump-probe THz-STS. Optical excitation can transiently modify ρ_{sample}, ρ_{tip}, and $T(V)$ within Equation 7.16, create a non-equilibrium filling of ρ_{sample} and ρ_{tip}, or stimulate more complex dynamics.

In addition to ρ_{sample}, conventional STM can also resolve surface band structure through QPI imaging [31, 193]. Differential conductance images are recorded near a defect or step edge, showing oscillatory (interference) features. The interference can be associated with electron scattering vectors between different points of the surface band structure in the Fourier transform of the $\mathrm{d}I/\mathrm{d}V$ image [193]. Repeating this procedure as a function of bias reveals cross-sections of the surface band structure at different energies. The THz-STS

inversion algorithm introduced here should make QPI imaging possible for THz-STM as well. A spatial map of $Q_{\mathrm{THz}}(V_{\mathrm{pk}})$ could be used to reconstruct the differential conductance at each tip location, and hence extract differential conductance images for each V_{pk}. Yet more excitingly, applying a similar procedure to $Q_{\mathrm{THz}}(V_{\mathrm{pk}}, \tau)$ should yield ultrafast QPI images of optical-pump/THz-probe dynamics, though the experimental stability of THz-STM may need to be improved before this is feasible. Conversely, the stability required for both of the algorithms presented in this paper has been demonstrated in Chapter 6. There, minutes-long constant-height THz-STM imaging shows that present machines are capable of acquiring the data for time-dependent THz-STS. It will, however, be a challenge to acquire a dataset of the same magnitude at each pixel of a QPI image.

We have also successfully tested the steady-state algorithm using an experimental THz voltage waveform recorded by PES [10, 11, 214], specifcally the PES waveform shown in Figures 6.2(e) and 6.2(f). It is worth noting that this test assumes the waveform measured by PES accurately describes the voltage applied across the tunnel junction. Our successful modeling of THz-STS data using this PES waveform shows this is (at least) a good approximation for 7-AGNRs on Au(111). However, other samples may contain further subtleties, making the broad applicability of PES a key experimental question, since the accuracy of the inversion algorithm hinges on knowing the correct waveform shape. For example, very recently, it has been observed that local THz resonances can depend on the tip position for H_2 molecules over a polarized salt at low THz fields [213]. The THz field enhancement is another important parameter, and has been reported to change with the microscopic tip apex [15, 182]. *In situ* voltage waveform characterization may therefore be necessary in some cases. This has been demonstrated for a single-molecule switch [15], and adaptations of this approach could be adopted for other sample systems.

Another possibility is to use multi-messenger detection to corroborate and complement THz-STS measurements. For example, THz-induced luminescence has been measured in conjunction with THz-STM of metal surfaces [14]. THz-STM could also be combined with near-field microscopy, though the spatial resolution of THz near-field microscopy has so far been limited to the $10-100$ nm scale [17]. To overcome this limitation, we propose a new experimental concept inspired by our algorithm that can be summarized in three points: (i) The bandwidth of the current pulse induced by a THz voltage transient is far larger than the input bandwidth. (ii) A transient current emits a field $E_{\mathrm{emit}} \propto \mathrm{d}i_{\mathrm{THz}}(t)/\mathrm{d}t$. (iii) The

THz field scattered from the junction at frequencies well above the input bandwidth carries atomic-scale information if no other frequency broadening effects are present. Detecting these fields may be challenging, but they should directly relate to the time-dependent current across the junction and could enable atomically resolved near-field microscopy.

Finally, inversion algorithms of the type presented here may be of interest for other research fields. We stress that the algorithms only apply when the light-matter interaction is in the strong-field regime. Yet, we anticipate that they are adaptable to THz-STM at higher frequencies for experimental parameters when this is the case [11, 185]. The algorithms should be similarly applicable to other experimental geometries in which strong-field coherent control of current is read out through rectified charge [256–262]. In the interest of clear communication between research fields, we note that for light coupled to a sharp tip near a surface, the geometric asymmetry is sometimes considered in terms of an asymmetric field enhancement that results in an asymmetric near-field waveform and nonzero temporal integral. Conversely, we assume here that the geometric asymmetry can be embedded in the $I(V)$, e.g., through a reduced work function of the tip, as is commonly done in the STM literature. Similarly, we treat the voltage waveform as an input rather than as a net field (i.e., it is independent of the resulting current) so rectified charge does not affect the temporal integral of the voltage waveform either.

7.4 Conclusions

In conclusion, we have introduced a new algorithm to invert THz-STS data recorded in steady-state and pump-probe experiments. From an experimental perspective, the key is to record the rectified charge as a function of peak THz voltage and, in the time-dependent case, optical-pump/THz-probe delay. Polynomial fits to these data are used as the input to the algorithm. The algorithm yields the differential conductance sampled by the THz voltage pulse and achieves subcycle time resolution. By alleviating the need for guess-and-check modeling, the algorithm advances THz-STS as a diagnostic tool for novel ultrafast nanoscience. Experimental tests are still needed to confirm the effectiveness of the algorithm and will, in turn, guide further algorithm refinement. In general, we expect the algorithm introduced here will serve as a launching point for subcycle THz-STS by both enabling a new level of experimental analysis and motivating future theoretical development.

Chapter 8
Summary and Outlook

In this thesis, I have presented the foundations of two distinct disciplines of physics research: ultrafast THz science and atomically resolved surface science. THz spectroscopy and scanning tunneling microscopy have independently been developed into robust techniques for investigating and extracting the electronic properties of condensed matter systems. More recently, the field of THz-STM has brought them together to access the best of both worlds, i.e., ultrafast time resolution and atomic spatial resolution. In this thesis, we have construed a state-of-the-art THz-STM system and further advanced the technique, including the demonstration of the first atomically resolved THz-STS.

Operating in ultrahigh vacuum and at cryogenic temperatures, we coupled broadband phase-stable single-cycle THz pulses to an atomically sharp STM tip. I have shown how we can use THz-STM to investigate atomically precise 7-AGNR at ultralow tip heights and extract the three-dimensional LDOS. Following this experimental demonstration of atomically resolved THz-STM and THz-STS, I have presented a theoretical methodology for going beyond the steady-state to perform time-resolved THz-STS. The developments I have presented in this thesis provide a platform to push THz-STM into the forefront of materials science research, where we will be able to explore new materials, nanostructures, and molecules on the intrinsic time scales of electron dynamics with ångström-scale spatial resolution.

The initial chapters of the thesis present the individual components of our THz-STM system. In Chapter 2, I introduced the principles of STM and STS, followed by the details of a custom commercial STM system that has been designed to facilitate the coupling of light pulses into the STM junction. I discussed the advantages that are provided by a LT-UHV environment, e.g., that it allows us to perform long-duration experiments in a stable environment, with a high degree of reproducability. I introduced the design of the STM scanhead's beam path and the optical elements that allowed us to illuminate the STM

junction. The optical path has been designed to maximize our THz field strength without sacrificing waveform shape or time resolution.

In Chapter 3, I introduced THz and ultrafast science as well as the generation and detection of THz pulses through optical rectification in $LiNbO_3$. The THz generation scheme was chosen to provide THz pulses with sufficient energy to propagate through an extensive optical setup, which has been designed for both characterizing the free-space-propagating THz field and performing THz-STM experiments with new modalities. We have combined a high-repetition-rate laser source with a cutting edge, home built THz generation scheme. Coupling these THz pulses to the STM described in Chapter 2 allows us to perform THz-STM experiments in a tunneling regime of one electron per THz pulse.

The underlying principles of THz-STM and the operation of our THz-STM system was presented in Chapter 4. I introduced the regime of strong-field light-matter interaction, defined by the Keldysh parameter, and explained how the THz electric field acts on the STM junction as an ultrafast bias voltage. The effect results from the relatively low photon energy of THz radiation and the extreme THz field enhancement provided by the STM tip ($\sim 10^6$ within the junction). I introduced the concept of THz-STS, a critical development in THz-STM that allows the technique to extract quantitative information about the LDOS. I developed a suite of supplementary experimental modalities that combine THz-STM with THz-STS, for example to extract two-dimensional maps of the local barrier decay for individual LDOS features. Finally, I outline an approach for characterizing the near-field THz voltage transient − photoemission sampling (PES) − which is needed for THz-STS of technologically relevant materials.

The primary material system studied in this thesis is 7-AGNRs grown via bottom-up synthesis with molecular precursors. This growth technique produces atomically precise structures isolated on an Au(111) surface, where we can study their intrinsic electronic properties − free of defects and with known morphology. The details of the 7-AGNR growth procedures and our initial characterization with conventional STM and STS was presented in Chapter 5. Chapter 6 detailed our investigation of the 7-AGNRs grown in our system with THz-STM. Here, we leveraged the exponential dependence of the tunnel current on tip height to overcome the duty cycle of ultrafast THz-driven current pulses in our system ($\sim 10^{-6}$). This allowed us to enter a tip-height regime not typically accessible by conventional STM. While operating at ultralow tip heights, we demonstrated atomically resolved

THz-STS for the first time and extracted the LDOS of the 7-AGNR in all three spatial dimensions. Investigating the spatial distribution of the LDOS, we performed constant-height THz-STM imaging throughout the vertical expanse of the 7-AGNR. Our measurments confirmed density functional theory predictions that the VB probability density at the interior of the ribbon decays faster than the exponential decay predicted by traditional tunneling theory. In order to explore dynamics that could be associated with charging, we performed THz-STM-pump/THz-STM-probe time-domain measurements using our THz autocorrelation setup. As we could simulate the measurements using the steady-state LDOS extracted from THz-STS measurements, we concluded that further sample preparation to decouple the 7-AGNRs from the metallic surface is necessary before dynamics will be observable with our time resolution.

In the final chapter of the thesis, I provided a broadly applicable model for THz-STS that can be applied to both steady-state and optical-pump/THz-STM-probe experiments. The development is a significant step toward establishing THz-STM as a versatile technique for ultrafast surface science. The algorithms presented require no prior knowledge of the junction $I(V)$ response and are capable of extracting both the steady-state and time-dependent density of states with the only input being the voltage transient evolving within the junction. We simulated a number of experimental scenarios and demonstrated the effectiveness of the algorithm. In the case of optical-pump/THz-STM-probe experiments, we discovered that the time resolution of THz-STM is not limited to the bandwidth of the input pulse. Rather, it scales with the nonlinearity of $I(V)$. We demonstrate this aspect by extracting a 100 fs decay from a simulated pump-probe experiment using an input voltage pulse with a duration of 1 ps. Our algorithm provides a means for THz-STM experiments to be performed across timescales from 100 fs to steady state. We believe the development of THz-STS will prove to be as important for THz-STM as STS has been for STM − that is, essential for its maturation into a tool for exploring new materials.

THz-STM is a budding technique with almost 10 years of development since the inaugural publication in 2013. Since then, several groups across the globe have joined the field. However, having a method for extracting the sample LDOS without advance knowledge of the tunnel junction has remained outstanding, which presented a roadblock to THz-STM achieving its full potential, especially in pump-probe studies of non-equilibrium electron dynamics. The development of our algorithm for THz-STS opens the door for thorough

characterization of new materials both spatially and, critically, in the time-domain with subcycle temporal resolution. Extracting the LDOS in large area snapshots following pump excitation may lead to time-resolved QPI, where the sample's energy-momentum relationship can be extracted on sub-picosecond timescales. This could allow THz-STM to observe the dynamics of material band structure hitherto reserved for ARPES [263], but with the added benefit that nanostructures and atomic defects can be investigated. The time resolution predicted by our simulations suggests that THz-STM may also be used to observe the finest details of photo-induced phase transitions in correlated electron materials [132, 264, 265] and the optically driven formations of quasi-particles [266].

Ultrafast imaging of wavefunction dynamics created by THz-STM-induced charging or photoexcitation is an outstanding goal of THz- STM. Optical excitation of GNRs is believed produce free-carriers that form excitonic states [72] on ps timescales [4]. The excitons formed in narrow GNRs are expected to have a Frenkel-like nature and exhibit strong localization. Comparing to other 2D materials (e.g., transition metal dichalcogenides), we anticipate lateral confinement of the excitons in GNRs [72, 267]. Imaging at ultralow tip heights with THz-STM should reveal the electronic structure, which may be compared with the exciton wavefunction predicted by DFT calculations [71].

Performing time-dependent imaging of the photoexcited GNR, with sub-ps time resolution, may reveal the formation of spatially delocalized hot electons ($\tau < 1$ ps) that cool to the CB edge and localize as they bind into excitons ($\tau \sim$10 ps). In 7-AGNRs, the excited-state electrons may eventually be transported to the ends of the ribbon, where an in-gap state may act as a trap. For GNRs adsorbed directly onto the gold surface, excited electrons appear to tunnel to the substrate on $\sim$10 fs timescales, obscuring these dynamics. Conversely, for GNRs decoupled from the substrate, e.g., by few-layer salt islands, we expect tunneling to the substrate to be suppressed, allowing THz-STM to observe dynamics within the GNR.

Using THz-STM to study engineered GNR structures (e.g., doped or edge-functionalized) will lead to ultrafast movies of a plethora of excited state dynamics. Furthermore, if we combine THz-STM with other unconventional STM techniques, it may become possible to time-resolve light emission from the STM junction, e.g., from radiative biexcitonic states [249]. Measurements of scanning tunneling luminescence (STL) are strongly impacted by the coupling of radiative states to the environment (like the tip) [268]. Therefore, implementing height-dependent THz-STM to perform tomographic investigations of light-emitting nanos-

tructures may provide access to coupling regimes that STL with conventional STM systems find challenging to access. Similarly, electron spin resonance STM (ESR-STM) measurements benefit from tuning via tip height control [269]. Combining THz-STM with ESR-STM may even lead to ultrafast characterization of spin excitations and quantum coherence properties in unique tip height regimes.

REFERENCES

1. Cai, J., Ruffieux, P., Rachard, J., *et al.* Atomically precise bottom-up fabrication of graphene nanoribbons. *Nature* **466,** 470–473 (2010) (cit. on pp. ii, 5, 87, 100).

2. Talirz, L., Ruffieux, P. & Fasel, R. On-Surface Synthesis of Atomically Precise Graphene Nanoribbons. *Advanced Materials* **28,** 6222–6231 (2016) (cit. on pp. ii, 87, 93, 95, 100, 118).

3. Chen, Z., Wang, H. I., Teyssandier, J., *et al.* Chemical Vapor Deposition Synthesis and Terahertz Photoconductivity of Low-Band-Gap N = 9 Armchair Graphene Nanoribbons. *Journal of the American Chemical Society* **139,** 3635–3638 (2017) (cit. on pp. ii, 5).

4. Jensen, S., Ulbricht, R., Narita, A., *et al.* Ultrafast Photoconductivity of Graphene Nanoribbons and Carbon Nanotubes. *Nano Letters* **13,** 5925–5930 (2013) (cit. on pp. ii, 2, 5, 35, 118, 147).

5. Cocker, T. L., Jelic, V., Gupta, M., *et al.* An ultrafast terahertz scanning tunnelling microscope. *Nature Photonics* **7,** 620–625 (2013) (cit. on pp. ii, 2, 3, 6, 36, 62, 66, 72–74, 78, 109, 120).

6. Yoshioka, K., Katayama, I., Minami, Y., *et al.* Real-space coherent manipulation of electrons in a single tunnel junction by single-cycle terahertz electric fields. *Nature Photonics* **10,** 762–765 (2016) (cit. on pp. ii, 4, 62, 106, 120).

7. Cocker, T. L., Peller, D., Yu, P., *et al.* Tracking the ultrafast motion of a single molecule by femtosecond orbital imaging. *Nature* **539,** 263–267 (2016) (cit. on pp. ii, 2, 4, 6, 44, 62, 66, 72, 74, 78, 109, 124, 141).

8. Jelic, V., Iwaszczuk, K., Nguyen, P. H., *et al.* Ultrafast terahertz control of extreme tunnel currents through single atoms on a silicon surface. *Nature Physics* **13,** 591–598 (2017) (cit. on pp. ii, 2, 4, 6, 36, 62, 68, 72, 73, 105, 106, 109, 119, 120, 127, 141).

9. Yoshioka, K., Katayama, I., Arashida, Y., *et al.* Tailoring Single-Cycle Near Field in a Tunnel Junction with Carrier-Envelope Phase-Controlled Terahertz Electric Fields. *Nano Letters* **18,** 5198–5204 (2018) (cit. on pp. ii, 4, 62, 68, 105, 109, 120).

10. Yoshida, S., Hirori, H., Tachizaki, T., *et al.* Subcycle Transient Scanning Tunneling Spectroscopy with Visualization of Enhanced Terahertz Near Field. *ACS Photonics* **6,** 1356–1364 (2019) (cit. on pp. ii, 4, 6, 62, 68, 69, 81, 83, 105, 106, 142).

11. Müller, M., Sabanés, N. M., Kampfrath, T. & Wolf, M. Phase-Resolved Detection of Ultrabroadband THz Pulses inside a Scanning Tunneling Microscope Junction. *ACS Photonics* **7,** 2046–2055 (2020) (cit. on pp. ii, 4, 6, 62, 68, 69, 81, 83, 105, 142, 143).

12. Luo, Y., Jelic, V., Chen, G., *et al.* Nanoscale terahertz STM imaging of a metal surface. *Physical Review B* **102,** 205417 (2020) (cit. on pp. ii, 62, 72, 74, 105, 109, 120).

13. Peller, D., Kastner, L. Z., Buchner, T., *et al.* Sub-cycle atomic-scale forces coherently control a single-molecule switch. *Nature* **585,** 58–62 (2020) (cit. on pp. ii, 2, 44, 62, 106, 124, 141).

14. Kimura, K., Morinaga, Y., Imada, H., *et al.* Terahertz-field-driven scanning tunneling luminescence spectroscopy. *ACS Photonics* **8,** 982–987 (2021) (cit. on pp. ii, 62, 142).

15. Peller, D., Roelcke, C., Kastner, L. Z., *et al.* Quantitative sampling of atomic-scale electromagnetic waveforms. *Nature Photonics* **15,** 143–147 (2021) (cit. on pp. ii, 4, 6, 44, 62, 68, 69, 105, 124, 141, 142).

16. Yoshida, S., Arashida, Y., Hirori, H., *et al.* Terahertz scanning tunneling microscopy for visualizing ultrafast electron motion in nanoscale potential variations. *ACS Photonics* **8,** 315–323 (2021) (cit. on pp. ii, 62).

17. Cocker, T. L., Jelic, V., Hillenbrand, R. & Hegmann, F. A. Nanoscale terahertz scanning probe microscopy. *Nature Photonics* **15,** 558–569 (2021) (cit. on pp. ii, 2, 62, 142).

18. Ammerman, S. E., Jelic, V., Wei, Y., *et al.* Lightwave-driven scanning tunnelling spectroscopy of atomically precise graphene nanoribbons. *Nature Communications* **12,** 6794 (2021) (cit. on pp. ii, 62, 80, 94, 95, 100, 114).

19. Ammerman, S. E., Wei, Y., Everett, N., *et al.* Algorithm for subcycle terahertz scanning tunneling spectroscopy. *Physical Review B* **105,** 115427 (2022) (cit. on pp. iii, 81, 97, 120).

20. Leonard, F. & Tersoff, J. Novel Length Scales in Nanotube Devices. *Physical Review Letters* **83,** 5174–5177 (1999) (cit. on p. 1).

21. Llinas, J., Fairbrother, A., Barin, G. B., *et al.* Short-channel field-effect transistors with 9-atom and 13-atom wide graphene nanoribbons. *Nature Communications* **8,** 633 (2017) (cit. on p. 1).

22. Crommie, M. F., Lutz, C. P., Eigler, D. M. & Heller, E. J. Quantum corrals. *Physica D: Nonlinear Phenomena* **83,** 98–108 (1995) (cit. on pp. 1, 12).

23. Stipe, B. C., Rezaei, M. A. & Ho, W. Single-Molecule Vibrational Spectroscopy and Microscopy. *Science* **280,** 1732–1735 (1998) (cit. on pp. 1, 12).

24. Gross, L., Mohn, F., Moll, N., *et al.* The Chemical Structure of a Molecule Resolved by Atomic Force Microscopy. *Science* **325,** 1110–1114 (2009) (cit. on pp. 1, 4).

25. Binnig, G., Rohrer, H., Gerber, C. & Weibel, E. Tunneling through a controllable vacuum gap. *Applied Physics Letters* **40,** 178 (1982) (cit. on p. 1).

26. Lang, N. D. Spectroscopy of single atoms in the scanning tunneling microscope. *Physical Review B* **34,** 5947–5950 (1986) (cit. on pp. 1, 12).

27. Stroscio, J. A., Feenstra, R. M. & Fein, A. P. Electronic Structure of the Si(111)2 x I Surface by Scanning-Tunneling Microscopy. *Physical Review Letters* **57,** 2579–2582 (1986) (cit. on pp. 1, 11, 12).

28. Lauhon, L. J. & Ho, W. Direct Observation of the Quantum Tunneling of Single Hydrogen Atoms with a Scanning Tunneling Microscope. *Physical Review Letters* **85,** 4566–4569 (2000) (cit. on p. 1).

29. Crommie, M. F., Lutz, C. P. & Eigler, D. M. Imaging standing waves in a two-dimensional electron gas. *Nature* **363,** 524–527 (1993) (cit. on p. 1).

30. Hasegawa, Y. & Avouris, P. Direct Observation of Standing Wave Formation at Surface Steps Using Scanning Tunneling Spectroscopy. *Physical Review Letters* **71,** 1071–1074 (1993) (cit. on p. 1).

31. McElroy, K., Simmonds, R. W., Hoffman, J. E., *et al.* Relating atomic-scale electronic phenomena to wave-like quasiparticle states in superconducting $Bi_2Sr_2CaCu_2O_{8+\delta}$. *Nature* **422,** 592–596 (2003) (cit. on pp. 1, 63, 141).

32. Freeney, S. E., Borman, S. T. P., Harteveld, J. W. & Swart, I. Coupling quantum corrals to form artificial molecules. *SciPost Physics* **9,** 085 (2020) (cit. on p. 1).

33. Van Exter, M. & Grischkowsky, D. Carrier dynamics of electrons and holes in moderately doped silicon. *Physical Review B* **41,** 12 140–12 149 (1990) (cit. on pp. 2, 33).

34. Ulbricht, R., Hendry, E., Shan, J., *et al.* Carrier dynamics in semiconductors studied with time-resolved terahertz spectroscopy. *Reviews of Modern Physics* **83,** 543–586 (2011) (cit. on pp. 2, 34).

35. Joyce, H. J., Boland, J. L., Davies, C. L., *et al.* A review of the electrical properties of semiconductor nanowires: insights gained from terahertz conductivity spectroscopy. *Semiconductor Science and Technology* **31,** 103003 (2016) (cit. on p. 2).

36. Fleischer, S., Zhou, Y., Field, R. W. & Nelson, K. A. Molecular Orientation and Alignment by Intense Single-Cycle THz Pulses. *Physical Review Letters* **107,** 163603 (2011) (cit. on p. 2).

37. Kampfrath, T., Tanaka, K. & Nelson, K. A. Resonant and nonresonant control over matter and light by intense terahertz transients. *Nature Photonics* **7,** 680–690 (2013) (cit. on pp. 2, 40).

38. Spies, J. A., Neu, J., Tayvah, U. T., *et al.* Terahertz Spectroscopy of Emerging Materials. *The Journal of Physical Chemistry C* **124,** 22335–22346 (2020) (cit. on p. 2).

39. Wu, Q. & Zhang, X.-C. Free-space electro-optic sampling of terahertz beams. *Applied Physics Letters* **67,** 3523 (1995) (cit. on pp. 2, 33, 48).

40. Jepsen, P. U., Winnewisser C. Schall, M., Schyja, V., *et al.* Detection of THz pulses by phase retardation in lithium tantalate. *Physical Review E* **53,** R3052–R3054 (1996) (cit. on pp. 2, 48).

41. Hangyo, M., Tani, M. & Nagashima, T. Terahertz Time-Domain Spectroscopy of Solids: A Review. *International Journal of Infrared and Millimeter Waves* **26,** 1661–1690 (2005) (cit. on p. 2).

42. Huber, R., Tauser, F., Brodschelm, A., *et al.* How many-particle interactions develop after ultrafast excitation of an electron-hole plasma. *Nature* **414,** 286–289 (2001) (cit. on p. 2).

43. Rosker, M. J., Dantus, M. & Zewail, A. H. Femtosecond Clocking of the Chemical Bond. *Science* **241,** 1200–1202 (1988) (cit. on p. 2).

44. Zewail, A. H. Femtochemistry: Atomic-Scale Dynamics of the Chemical Bond. *The Journal of Physical Chemistry A* **104,** 5660–5694 (2000) (cit. on p. 2).

45. Ischenko, A. A., Weber, P. M. & Dwayne Miller, R. J. Capturing Chemistry in Action with Electrons: Realization of Atomically Resolved Reaction Dynamics. *Chemical Reviews* **117,** 11066–11124 (2017) (cit. on p. 2).

46. Treier, M., Pignedoli, C. A., Laino, T., *et al.* Surface-assisted cyclodehydrogenation provides a synthetic route towards easily processable and chemically tailored nanographenes. *Nature Chemistry* **3,** 61–67 (2010) (cit. on p. 2).

47. Hla, S.-W., Bartels, L., Meyer, G. & Rieder, K.-H. Inducing All Steps of a Chemical Reaction with the Scanning Tunneling Microscope Tip: Towards Single Molecule Engineering. *Physical Review Letters* **85,** 2777–2780 (2000) (cit. on p. 2).

48. Nunes Jr., G. & Freeman, M. R. Picosecond Resolution in Scanning Tunneling Microscopy. *Science* **262,** 1029–1032 (1993) (cit. on pp. 2, 64, 121).

49. Lloyd-Hughes, J., Oppeneer, P. M., Pereira dos Santos, T., *et al.* The 2021 ultrafast spectroscopic probes of condensed matter roadmap. *Journal of Physics: Condensed Matter* **33,** 353001 (2021) (cit. on pp. 3, 62, 66).

50. Repp, J., Meyer, G., Stojković, S. M., *et al.* Molecules on Insulating Films: Scanning-Tunneling Microscopy Imaging of Individual Molecular Orbitals. *Physical Review Letters* **94,** 026803 (2005) (cit. on pp. 4, 124).

51. Voigtländer, B. *Scanning Probe Microscopy. Atomic Force Microscopy and Scanning Tunneling Microscopy* (Springer-Verlag Berlin Heidelberg, 2015) (cit. on pp. 4, 11, 25, 141).

52. Fattinger, C. & Grischkowsky, D. Terahertz beams. *Applied Physics Letters* **54,** 490 (1988) (cit. on pp. 4, 35).

53. Hebling, J., Stepanov, A. G., Almási, G., *et al.* Tunable THz pulse generation by optical rectification of ultrashort laser pulses with tilted pulse fronts. *Applied Physics B* **78,** 593–599 (2004) (cit. on pp. 5, 42–44).

54. Yeh, K.-L., Hoffmann, M. C., Hebling, J. & Nelson, K. A. Generation of 10 μJ ultrashort terahertz pulses by optical rectification. *Applied Physics Letters* **90,** 171121 (2007) (cit. on p. 5).

55. Hirori, H., Doi, A., Blanchard, F. & Tanaka, K. Single-cycle terahertz pulses with amplitudes exceeding 1 MV/cm generated by optical rectification in LiNbO3. *Applied Physics Letters* **98,** 091106 (2011) (cit. on pp. 5, 33, 44).

56. Cocchi, C., Prezzi, D., Ruini, A., *et al.* Optical Excitations and Field Enhancement in Short Graphene Nanoribbons. *The Journal of Physical Chemistry Letters* **3,** 924–929 (2012) (cit. on p. 5).

57. Vo, T. H., Gayani, U., Perera, E., *et al.* Nitrogen-Doping Induced Self-Assembly of Graphene Nanoribbon-Based Two-Dimensional and Three-Dimensional Metamaterials. *Nano Letters* **15,** 5770–5777 (2015) (cit. on p. 5).

58. Nakada, K. & Fujita, M. Edge state in graphene ribbons: Nanometer size effect and edge shape dependence. *Physical Review B* **54,** 17954–17961 (1996) (cit. on p. 5).

59. Son, Y.-W., Cohen, M. L. & Louie, S. G. Half-metallic graphene nanoribbons. *Nature* **444,** 347–349 (2006) (cit. on p. 5).

60. Son, Y.-W., Cohen, M. L. & Louie, S. G. Energy Gaps in Graphene Nanoribbons. *Physical Review Letters* **97,** 216803 (2006) (cit. on p. 5).

61. Shinde, P. P., Gröning, O., Wang, S., *et al.* Stability of edge magnetism in functionalized zigzag graphene nanoribbons. *Carbon* **124,** 123–132 (2017) (cit. on p. 5).

62. Chen, Y.-C., de Oteyza, D. G., Pedramrazi, Z., *et al.* Tuning the Band Gap of Graphene Nanoribbons Synthesized from Molecular Precursors. *ACS Nano* **7,** 6123–6128 (2013) (cit. on p. 5).

63. Gröning, O., Wang, W., Yao, X., *et al.* Engineering of robust topological quantum phases in graphene nanoribbons. *Nature* **560,** 209–213 (2018) (cit. on p. 5).

64. Rizzo, D. J., Jiang, J., Joshi, D., *et al.* Rationally Designed Topological Quantum Dots in Bottom-Up Graphene Nanoribbons. *ACS Nano* **15,** 20633–20642 (2021) (cit. on p. 5).

65. Cai, J., Pignedoli, C. A., Talirz, L., *et al.* Graphene nanoribbon heterojunctions. *Nature Nanotechnology* **9,** 896–900 (2014) (cit. on p. 5).

66. Costa, P. S., Teeter, J. D., Enders, A. & Sinitskii, A. Chevron-based graphene nanoribbon heterojunctions: Localized effects of lateral extension and structural defects on electronic properties. *Carbon* **134,** 310–315 (2018) (cit. on p. 5).

67. Yang, L., Cohen, M. L. & Louie, S. G. Excitonic Effects in the Optical Spectra of Graphene Nanoribbons. *Nano Letters* **7,** 3112–3115 (2007) (cit. on p. 5).

68. Prezzi, D., Varsano, V., Ruini, A., *et al.* Optical properties of graphene nanoribbons: The role of many-body effects. *Physical Review B* **77,** 041404(R) (2008) (cit. on p. 5).

69. Wang, S. & Wang, J. Quasiparticle Energies and Optical Excitations in Chevron-Type Graphene Nanoribbon. *The Journal of Physical Chemistry C* **116,** 10193–10197 (2012) (cit. on p. 5).

70. Lee, Y.-L., Zhao, F., Cao, T., *et al.* Topological Phases in Cove-Edged and Chevron Graphene Nanoribbons: Geometric Structures, Z2 Invariants, and Junction States. *Nano Letters* **18,** 7247–7253 (2018) (cit. on p. 5).

71. Denk, R., Hohage, M., Zeppenfeld, P., *et al.* Exciton-dominated optical response of ultra-narrow graphene nanoribbons. *Nature Communications* **5,** 4253 (2014) (cit. on pp. 5, 93, 118, 147).

72. Tries, A., Osella, S., Zhang, P., *et al.* Experimental Observation of Strong Exciton Effects in Graphene Nanoribbons. *Nano Letters* **20,** 2993–3002 (2020) (cit. on pp. 5, 35, 118, 147).

73. Talirz, L., Söde, H., Kawai, S., *et al.* Band Gap of Atomically Precise Graphene Nanoribbons as a Function of Ribbon Length and Termination. *ChemPhysChem* **20,** 1–7 (2019) (cit. on pp. 5, 98).

74. Söde, H., Talirz, L., Gröning, O., *et al.* Electronic band dispersion of graphene nanoribbons via Fourier-transformed scanning tunneling spectroscopy. *Physical Review B* **91,** 045429 (2015) (cit. on pp. 6, 93, 94, 96, 103, 106, 109, 114).

75. Deniz, O., Sánchez-Sánchez, C., Dumslaff, T., *et al.* Revealing the Electronic Structure of Silicon Intercalated Armchair Graphene Nanoribbons by Scanning Tunneling Spectroscopy. *Nano Lett* **17,** 2197–2203 (2017) (cit. on pp. 6, 94).

76. Wang, S., Kharche, N., Costa Girão, E. C., *et al.* Quantum Dots in Graphene Nanoribbons. *Nano Letters* **17,** 4277–4283 (2017) (cit. on p. 6).

77. Schottky, W. Über kalte und warme Elektronenentladungen. *Zeitschrift für Physik* **14.1,** 63–106 (1923) (cit. on p. 7).

78. Fowler, R. H. & Nordheim, L. Electron Emission in Intense Electric Fields. *Proceedings of the Royal Society of London. Series A, Containing Papers of a Mathematical and Physical Character* **119,** 173–181 (1928) (cit. on p. 7).

79. Simmons, J. G. Electric Tunnel Effect between Dissimilar Electrodes Separated by a Thin Insulating Film. *Journal of Applied Physics* **34,** 2581 (1963) (cit. on pp. 10, 21, 120).

80. Binnig, G., Rohrer, H., Gerber, C., *et al.* Tunneling through a controllable vacuum gap. *Applied Physics Letters* **40,** 178 (1982) (cit. on pp. 10, 11, 79).

81. Giaever, I. Energy Gap in Superconductors Measured by Electron Tunneling. *Physical Review Letters* **5,** 147–148 (1960) (cit. on p. 10).

82. Fisher, J. C. & Giaever, I. Tunneling Through Thin Insulating Layers. *Journal of Applied Physics* **32,** 172 (1961) (cit. on p. 11).

83. Binning, G., Rohrer, H., Gerber, C. & Weibel, E. Surface Studies by Scanning Tunneling Microscopy. *Physical Review Letters* **49,** 57–61 (1982) (cit. on p. 11).

84. Tersoff, J. & Hamann, D. R. Theory and Application for the Scanning Tunneling Microscope. *Physical Review Letters* **50,** 1998–2001 (1983) (cit. on pp. 12, 21, 23, 115).

85. Garcia, N., Ocal, C. & Flores, F. Model Theory for Scanning Tunneling Microscopy: Application to Au(110) (1x2). *Physical Review Letters* **50,** 2002–2005 (1983) (cit. on p. 12).

86. Chen, C. J. Origin of Atomic Resolution on Metal Surfaces in Scanning Tunneling Microscopy. *Physical Review Letters* **65,** 448–451 (1990) (cit. on p. 12).

87. Pavlicek, N. & Gross, L. Generation, manipulation and characterization of molecules by atomic force microscopy. *Nature Reviews Chemistry* **1,** 0005 (2017) (cit. on p. 12).

88. Lang, N. D. Apparent Size of an Atom in the Scanning Tunneling Microscope as a Function of Bias. *Physical Review Letters* **58,** 45–48 (1987) (cit. on p. 12).

89. Bryant, P. J., Kim, H. S., Zheng, Y. C., *et al.* Technique for shaping scanning tunneling microscope tips. *Review of Scientific Instruments* **58,** 1115 (1986) (cit. on p. 12).

90. Oliva, A. I., A. Romero, G. & Peña, J. L. Electrochemical preparation of tungsten tips for a scanning tunneling microscope. *Review of Scientific Instruments* **67,** 1917–1921 (1996) (cit. on p. 13).

91. Ju, B. F., Chen, Y. L. & Ge, Y. The art of electrochemical etching for preparing tungsten probes with controllable tip profile and characteristic parameters. *Review of Scientific Instruments* **82,** 013707 (2011) (cit. on p. 13).

92. Biegelsen, D. K., Ponce, F. A., Tramontana, J. C., *et al.* Ion milled tips for scanning tunneling microscopy. *Applied Physics Letters* **50,** 696 (1987) (cit. on p. 15).

93. Ahmed, R., Urban, R., Salmons, M., *et al.* Field Assisted Reactive Gas Etching of Multiple Tips Observed using FIM. *Ultramicroscopy* **223,** 113216 (2021) (cit. on p. 15).

94. Lucier, A.-S., Mortensen, H., Sun, Y. & Grütter, P. Determination of the atomic structure of scanning probe microscopy tungsten tips by field ion microscopy. *Physical Review B* **72,** 235420 (2005) (cit. on p. 15).

95. Hagedorn, T., El Ouali, M., Paul, W., *et al.* Refined tip preparation by electrochemical etching and ultrahigh vacuum treatment to obtain atomically sharp tips for scanning tunneling microscope and atomic force microscope. *Review of Scientific Instruments* **82,** 113903 (2011) (cit. on p. 15).

96. Albrektsen, O., Salemink, H. W. M., Mørch, K. A., *et al.* Reliable tip preparation for high-resolution scanning tunneling microscopy. *Journal of Vacuum Science & Technology B: Microelectronics and Nanometer Structures Processing, Measurement, and Phenomena* **12,** 3187 (1994) (cit. on p. 15).

97. Schmucker, S. W., Kumar, N., Abelson, J. R., *et al.* Field-directed sputter sharpening for tailored probe materials and atomic-scale lithography. *Nature Communications* **3,** 935 (2012) (cit. on p. 15).

98. Pascual, J. I., Mendez, J., Gomez-Herrero, J., *et al.* Quantum Contact in Gold Nanostructures by Scanning Tunneling Microscopy. *Physical Review Letters* **71,** 1852–1855 (1993) (cit. on p. 16).

99. Chang, C. S., Su, W. B. & Tsong, T. T. Field Evaporation between a Gold Tip and a Gold Surface in the Scanning Tunneling Microscope Configuration. *Physical Review Letters* **72,** 574–577 (1994) (cit. on p. 16).

100. Agraït, N., Yeyati, A. L. & van Ruitenbeek, J. M. Quantum properties of atomic-sized conductors. *Physics Reports* **377,** 81–279 (2003) (cit. on p. 16).

101. Vazquez de Parga, A. L., Hernan, O. S. & Miranda, R. Electron Resonances in Sharp Tips and Their Role in Tunneling Spectroscopy. *Physical Review Letters* **80,** 357–360 (1998) (cit. on p. 16).

102. Tewari, S., Bastiaans, K. M., Allan, M. P. & van Ruitenbeek, J. M. Robust procedure for creating and characterizing the atomic structure of scanning tunneling microscope tips. *Beilstein Journal of Nanotechnology* **8,** 2389–2395 (2017) (cit. on p. 16).

103. Kashi, S. R., Kang, H., Sass, C. S. & Rabalais, J. W. Inelastic Processes in Low-Energy Ion-Surface Collisions. *Surface Science Reports* **10,** 1–104 (1989) (cit. on p. 16).

104. Coratger, R., Claverie, A., Ajustron, F. & Beauvillain, J. Scanning Tunneling Microscopy of Defects Induced by Carbon Bombardment on Graphite Surfaces. *Surface Science* **227,** 7–14 (1990) (cit. on p. 16).

105. Hahn, J. R. & Kang, H. STM study of Ar^+-induced defects produced by near-threshold energy collision. *Surface Science* **357-358,** 165–169 (1996) (cit. on p. 16).

106. Oura, K., Lifshits, V. G., Saranin, A. A., *et al. Surface Science - An Introduction* (Springer-Verlag Berlin Heidelberg, 2004) (cit. on pp. 16, 30).

107. Chen, C. J. *Introduction to Scanning Tunneling Microscopy* (Oxford University Press, 1993) (cit. on pp. 18, 26).

108. Barth, J. V., Brune, H. & Ertl, G. Scanning tunneling microscopy observations on the reconstructed Au(111) surface: Atomic structure, long-range superstructure, rotational domains, and surface defects. *Physical Review B* **42,** 9307–9318 (1990) (cit. on p. 19).

109. Aoki, T. & Yokoyama, T. Mapping the surface electrostatic potentials of Au(111) by using barrier-height measurements. *Physical Review B* **89,** 155423 (2014) (cit. on p. 19).

110. Feenstra, R. M., Stroscio, J. A. & Fein, A. P. Tunneling Spectroscopy of the Si(111)2 x 1 Surface. *Surface Science* **181,** 295–306 (1987) (cit. on p. 20).

111. Koslowski, B., Dietrich, C., Tschetschetkin, A. & Ziemann, P. Evaluation of scanning tunneling spectroscopy data: Approaching a quantitative determination of the electronic density of states. *Physical Review B* **75,** 035421 (2007) (cit. on p. 20).

112. Bardeen, J. Tunneling From a Many-Particle Point of View. *Physical Review Letters* **6,** 57–59 (1961) (cit. on pp. 20, 21).

113. Chen, C. J. Theory of scanning tunneling spectroscopy. *Journal of Vacuum Science & Technology A* **6,** 319 (1988) (cit. on p. 21).

114. Blatter, G. & Greuter, F. Carrier transport through grain boundaries in semiconductors. *Physical Review B* **33,** 3952–3966 (6 1986) (cit. on p. 33).

115. Lyon, S. A. Spectroscopy of hot carriers in semiconductors. *Journal of Luminescence* **35,** 121–154 (1986) (cit. on p. 33).

116. Tung, R. T., Levi, A. F. J., Sullivan, J. P. & Schrey, F. Schottky-barrier inhomogeneity at epitaxial $NiSi_2$ interfaces on Si(100). *Physical Review Letters* **66,** 72–75 (1 1991) (cit. on p. 33).

117. Sullivan, J. P., Tung, R. T., Pinto, M. R. & Graham, W. R. Electron transport of inhomogeneous Schottky barriers: A numerical study. *Journal of Applied Physics* **70,** 7403–7424 (1991) (cit. on p. 33).

118. Schmuttenmaer, C. A. Exploring dynamics in the far-infrared with terahertz spectroscopy. *Chemical Reviews* **104,** 1759–1780 (2004) (cit. on p. 33).

119. Seifert, T., Jaiswal, S., Martens, U., *et al.* Efficient metallic spintronic emitters of ultrabroadband terahertz radiation. *Nature Photonics* **10,** 483–488 (2016) (cit. on p. 33).

120. Hale, P. J., Madeo, J., Chin, C., *et al.* 20 THz broadband generation using semi-insulating GaAs interdigitated photoconductive antennas. *Optics Express* **22,** 26358–26364 (2014) (cit. on p. 33).

121. Huber, R., Brodschelm, A., Tauser, F. & Leitenstorfer, A. Generation and field-resolved detection of femtosecond electromagnetic pulses tunable up to 41 THz. *Applied Physics Letters* **76,** 3191–3193 (2000) (cit. on p. 33).

122. Cooke, D. G., MacDonald, A. N., Hryciw, A., *et al.* Transient terahertz conductivity in photoexcited silicon nanocrystal films. *Physical Review B* **73,** 193311 (2006) (cit. on p. 33).

123. Titova, L. V., Cocker, T. L., Xu, S., *et al.* Ultrafast carrier dynamics and the role of grain boundaries in polycrystalline silicon thin films grown by molecular beam epitaxy. *Semiconductor Science and Technology* **31,** 105017 (2016) (cit. on p. 33).

124. Porer, M., Leierseder, U., Ménard, J.-M., *et al.* Non-thermal separation of electronic and structural orders in a persisting charge density wave. *Nature Materials* **13,** 857–861 (2014) (cit. on p. 33).

125. Burgos-Caminal, A., Socie, E., Bouduban, M. E. F. & Moser, J.-E. Exciton and carrier dynamics in two-dimensional perovskites. *The Journal of Physical Chemistry Letters* **11,** 7692–7701 (2020) (cit. on p. 33).

126. Dhillon, S. S., Vitiello, M. S., Linfield, E. H., *et al.* The 2017 terahertz science and technology roadmap. *Journal of Physics D: Applied Physics* **50,** 043001 (2017) (cit. on p. 33).

127. Bloch, F. Über die quantenmechanik der elektronen in kristallgittern. *Zeitschrift für physik* **52,** 555–600 (1929) (cit. on p. 33).

128. Dagotto, E. Complexity in strongly correlated electronic systems. *Science* **309,** 257–262 (2005) (cit. on p. 34).

129. Vengurlekar, A. S. & Jha, S. S. Terahertz-frequency-resolved transient conductivity of nonthermal electrons photoexcited in GaAs. *Physical Review B* **43,** 12454 (1991) (cit. on p. 34).

130. Beard, M. C., Turner, G. M. & Schmuttenmaer, C. A. Transient photoconductivity in GaAs as measured by time-resolved terahertz spectroscopy. *Physical Review B* **62,** 15764 (2000) (cit. on pp. 34, 35).

131. Kübler, C., Ehrke, H., Huber, R., *et al.* Coherent structural dynamics and electronic correlations during an ultrafast insulator-to-metal phase transition in VO_2. *Physical Review Letters* **99,** 116401 (2007) (cit. on p. 34).

132. Cocker, T. L., Titova, L. V., Fourmaux, S., *et al.* Phase diagram of the ultrafast photoinduced insulator-metal transition in vanadium dioxide. *Physical Review B* **85,** 155120 (2012) (cit. on pp. 34, 147).

133. Kindt, J. T. & Schmuttenmaer, C. A. Theory for determination of the low-frequency time-dependent response function in liquids using time-resolved terahertz pulse spectroscopy. *The Journal of Chemical Physics* **110,** 8589–8596 (1999) (cit. on p. 34).

134. Nozik, A. J. Quantum dot solar cells. *Physica E: Low-dimensional Systems and Nanostructures* **14,** 115–120 (2002) (cit. on p. 34).

135. Semonin, O. E., Luther, J. M. & Beard, M. C. Quantum dots for next-generation photovoltaics. *Materials Today* **15,** 508–515 (2012) (cit. on p. 34).

136. Mak, K. F., He, K., Lee, C., *et al.* Tightly bound trions in monolayer MoS_2. *Nature Materials* **12,** 207–211 (2013) (cit. on p. 34).

137. Butler, S. Z., Hollen, S. M., Cao, L., *et al.* Progress, challenges, and opportunities in two-dimensional materials beyond graphene. *ACS Nano* **7,** 2898–2926 (2013) (cit. on p. 34).

138. Poellmann, C., Steinleitner, P., Leierseder, U., *et al.* Resonant internal quantum transitions and femtosecond radiative decay of excitons in monolayer WSe_2. *Nature Materials* **14,** 889–893 (2015) (cit. on p. 35).

139. Ivanov, I., Hu, Y., Osella, S., *et al.* Role of edge engineering in photoconductivity of graphene nanoribbons. *Journal of the American Chemical Society* **139,** 7982–7988 (2017) (cit. on p. 35).

140. Möbius, W. Über die Dispersion von Wasser und Äthylalkohol zwischen 7 und 35 mm Wellenlänge und Vorversuche zur Verwendung noch kürzerer elektrischer Wellen. *Annalen der Physik* **367,** 293–322 (1920) (cit. on p. 35).

141. Nichols, E. F. & Tear, J. D. Joining the infra-red and electric wave spectra. *The Astrophysical Journal* **61,** 17 (1925) (cit. on p. 35).

142. Auston, D. H., Cheung, K. P. & Smith, P. R. Picosecond photoconducting Hertzian dipoles. *Applied physics letters* **45,** 284–286 (1984) (cit. on p. 35).

143. Lee, Y.-S. *Principles of terahertz science and technology* (Springer Science & Business Media, 2009) (cit. on pp. 35, 42, 51, 54).

144. Martin, M. & Brown, E. R. *Critical comparison of GaAs and InGaAs THz photoconductors* in *Proc. SPIE 8261, Terahertz Technology and Applications V* **8261** (2012), 15–21 (cit. on p. 35).

145. Benicewicz, P. K., Roberts, J. P. & Taylor, A. J. Scaling of terahertz radiation from large-aperture biased photoconductors. *Journal of the Optical Society of America B* **11,** 2533–2546 (1994) (cit. on p. 35).

146. Furch, F. J. A., Witting, T., Osolodkov, M., *et al.* High power, high repetition rate laser-based sources for attosecond science. *Journal of Physics: Photonics* (2022) (cit. on p. 36).

147. Frédéric, D., François, B. & Georges, P. New laser crystals for the generation of ultrashort pulses. *Comptes Rendus Physique* **8,** 153–164 (2007) (cit. on p. 36).

148. Auston, D. H. Subpicosecond electro-optic shock waves. *Applied Physics Letters* **43,** 713–715 (1983) (cit. on pp. 36, 42).

149. Auston, D. H., Cheung, K. P., Valdmanis, J. A. & Kleinman, D. A. Cherenkov radiation from femtosecond optical pulses in electro-optic media. *Physical Review Letters* **53,** 1555 (1984) (cit. on pp. 36, 42).

150. Wu, Q. & Zhang, X.-C. Ultrafast electro-optic field sensors. *Applied physics letters* **68,** 1604–1606 (1996) (cit. on p. 40).

151. Said, A. A., Sheik-Bahae, M., Hagan, D. J., *et al.* Determination of bound-electronic and free-carrier nonlinearities in ZnSe, GaAs, CdTe, and ZnTe. *Journal of the Optical Society of America B* **9,** 405–414 (1992) (cit. on p. 40).

152. Hoffmann, M. C., Yeh, K.-L., Hebling, J. & Nelson, K. A. Efficient terahertz generation by optical rectification at 1035 nm. *Optics Express* **15,** 11706–11713 (2007) (cit. on p. 40).

153. Nelson, D. F. & Turner, E. H. Electro-optic and piezoelectric coefficients and refractive index of Gallium Phosphide. *Journal of Applied Physics* **39,** 3337–3343 (1968) (cit. on p. 40).

154. Kittel, C. & McEuen, P. *Introduction to solid state physics* (Wiley New York, 2005) (cit. on p. 40).

155. Ridah, A., Bourson, P., Fontana, M. D. & Malovichko, G. The composition dependence of the Raman spectrum and new assignment of the phonons in $LiNbO_3$. *Journal of Physics: Condensed Matter* **9,** 9687–9693 (1997) (cit. on p. 40).

156. Peller, D. *High-field terahertz source for ultrafast scanning tunneling microscopy* Bachelor (Regensburg University, 2014) (cit. on pp. 40, 44).

157. Pálfalvi, L., Hebling, J., Kuhl, J., *et al.* Temperature dependence of the absorption and refraction of Mg-doped congruent and stoichiometric $LiNbO_3$ in the THz range. *Journal of Applied Physics* **97,** 123505 (2005) (cit. on p. 40).

158. Koehl, R. M., Adachi, S. & Nelson, K. A. Direct Visualization of Collective Wavepacket Dynamics. *The Journal of Physical Chemistry A* **103,** 10260–10267 (1999) (cit. on p. 42).

159. Koehl, R. M., Adachi, S. & Nelson, K. A. Real-space polariton wave packet imaging. *The Journal of Chemical Physics* **110,** 1317–1320 (1999) (cit. on p. 42).

160. Wang, Z., Su, F. & Hegmann, F. A. Ultrafast imaging of terahertz Cherenkov waves and transition-like radiation in $LiNbO_3$. *Optics Express* **23,** 8073–8086 (2015) (cit. on pp. 42, 98).

161. Trebino, R., Bowlan, P., Gabolde, P., *et al.* Simple devices for measuring complex ultrashort pulses. *Laser & Photonics Reviews* **3,** 314–342 (2009) (cit. on p. 48).

162. Teo, S. M., Ofori-Okai, B. K., Werley, C. A. & Nelson, K. A. Invited Article: Single-shot THz detection techniques optimized for multidimensional THz spectroscopy. *Review of Scientific Instruments* **86,** 051301 (2015) (cit. on p. 48).

163. Hegmann, F. A., Ostroverkhova, O. & Cooke, D. G. Probing organic semiconductors with terahertz pulses. *Photophysics of Molecular Materials: From Single Molecules to Single Crystals,* 367–428 (2005) (cit. on p. 48).

164. Marple, D. T. F. Refractive index of ZnSe, ZnTe, and CdTe. *Journal of Applied Physics* **35,** 539–542 (1964) (cit. on p. 51).

165. Cheville, R. A. & Grischkowsky, D. Far-infrared foreign and self-broadened rotational linewidths of high-temperature water vapor. *Journal of the Optical Society of America B* **16,** 317–322 (1999) (cit. on p. 53).

166. Sitnikov, D. S., Romashevskiy, S. A., Ovchinnikov, A. V., *et al.* Estimation of THz field strength by an electro-optic sampling technique using arbitrary long gating pulses. *Laser Physics Letters* **16,** 115302 (2019) (cit. on pp. 54, 55, 83).

167. Gallot, G. & Grischkowsky, D. Electro-optic detection of terahertz radiation. *Journal of the Optical Society of America B* **16,** 1204–1212 (1999) (cit. on p. 55).

168. Brodeur, A. & Chin, S. L. Ultrafast white-light continuum generation and self-focusing in transparent condensed media. *Journal of the Optical Society of America B* **16,** 637–650 (1999) (cit. on p. 55).

169. Yang, G. & Shen, Y. R. Spectral broadening of ultrashort pulses in a nonlinear medium. *Optics letters* **9,** 510–512 (1984) (cit. on p. 55).

170. Hasegawa, A. Soliton-based optical communications: An overview. *IEEE Journal of Selected Topics in Quantum Electronics* **6,** 1161–1172 (2000) (cit. on p. 56).

171. Fork, R. L., Martinez, O. E. & Gordon, J. P. Negative dispersion using pairs of prisms. *Optics letters* **9,** 150–152 (1984) (cit. on p. 56).

172. Boyd, R. W. *Nonlinear Optics* (2008) (cit. on p. 58).

173. Eisele, M., Cocker, T. L., Huber, M. A., *et al.* Ultrafast multi-terahertz nano-spectroscopy with sub-cycle temporal resolution. *Nature Photonics* **8,** 841–845 (2014) (cit. on pp. 60, 68, 132).

174. Huang, Y., Yao, Z., He, C., *et al.* Terahertz surface and interface emission spectroscopy for advanced materials. *Journal of Physics: Condensed Matter* **31,** 153001 (2019) (cit. on p. 62).

175. Shi, J., Li, Y., Li, Y., *et al.* From ultrafast to ultraslow: charge-carrier dynamics of perovskite solar cells. *Joule* **2,** 879–901 (2018) (cit. on p. 62).

176. Lui, C., Frenzel, A., Pilon, D., *et al.* Trion-induced negative photoconductivity in monolayer MoS_2. *Physical Review Letters* **113,** 166801 (2014) (cit. on p. 62).

177. Kirilyuk, A., Kimel, A. V. & Rasing, T. Ultrafast optical manipulation of magnetic order. *Reviews of Modern Physics* **82,** 2731 (2010) (cit. on p. 62).

178. Smallwood, C. L., Jozwiak, C., Zhang, W. & Lanzara, A. An ultrafast angle-resolved photoemission apparatus for measuring complex materials. *Review of Scientific Instruments* **83,** 123904 (2012) (cit. on p. 62).

179. Richter, C. & Schmuttenmaer, C. A. Exciton-like trap states limit electron mobility in TiO_2 nanotubes. *Nature Nanotechnology* **5,** 769–772 (2010) (cit. on p. 62).

180. Kampfrath, T., Perfetti, L., Schapper, F., *et al.* Strongly coupled optical phonons in the ultrafast dynamics of the electronic energy and current relaxation in graphite. *Physical Review Letters* **95,** 187403 (2005) (cit. on p. 62).

181. Zhu, T., Snaider, J. M., Yuan, L. & Huang, L. Ultrafast dynamic microscopy of carrier and exciton transport. *Annual Review of Physical Chemistry* **70,** 219–244 (2019) (cit. on p. 62).

182. Abdo, M., Sheng, S., Rolf-Pissarczyk, S., *et al.* Variable repetition rate THz source for ultrafast scanning tunneling microscopy. *ACS photonics* **8,** 702–708 (2021) (cit. on pp. 62, 68, 105, 109, 142).

183. Martiín Sabanés, N., Krecinic, F., Kumagai, T., *et al.* Femtosecond Thermal and Nonthermal Hot Electron Tunneling Inside a Photoexcited Tunnel Junction. *ACS Nano* **16,** 14479–14489 (2022) (cit. on p. 62).

184. Arashida, Y., Mogi, H., Ishikawa, M., *et al.* Subcycle mid-infrared electric-field-driven scanning tunneling microscopy with a time resolution higher than 30 fs. *ACS Photonics* **9,** 3156–3164 (2022) (cit. on p. 62).

185. Garg, M. & Kern, K. Attosecond coherent manipulation of electrons in tunneling microscopy. *Science* **367,** 411–415 (2020) (cit. on pp. 62, 68, 143).

186. Garg, M., Martin-Jimenez, A., Luo, Y. & Kern, K. Ultrafast photon-induced tunneling microscopy. *ACS Nano* **15,** 18071–18084 (2021) (cit. on pp. 62, 65).

187. Garg, M., Martin-Jimenez, A., Pisarra, M., *et al.* Real-space subfemtosecond imaging of quantum electronic coherences in molecules. *Nature Photonics* **16,** 196–202 (2022) (cit. on p. 62).

188. Linsebigler, A. L., Lu, G. & Yates Jr, J. T. Photocatalysis on TiO_2 surfaces: principles, mechanisms, and selected results. *Chemical Reviews* **95,** 735–758 (1995) (cit. on p. 62).

189. Robel, I., Subramanian, V., Kuno, M. & Kamat, P. V. Quantum dot solar cells. Harvesting light energy with CdSe nanocrystals molecularly linked to mesoscopic TiO_2 films. *Journal of the American Chemical Society* **128,** 2385–2393 (2006) (cit. on p. 62).

190. Imada, H., Miwa, K., Imai-Imada, M., *et al.* Real-space investigation of energy transfer in heterogeneous molecular dimers. *Nature* **538,** 364–367 (2016) (cit. on p. 62).

191. Doppagne, B., Chong, M. C., Lorchat, E., *et al.* Vibronic spectroscopy with submolecular resolution from STM-induced electroluminescence. *Physical Review Letters* **118,** 127401 (2017) (cit. on p. 63).

192. Lee, J., Perdue, S. M., Perez, A. R. & Apkarian, V. A. Vibronic motion with joint angstrom–femtosecond resolution observed through Fano progressions recorded within one molecule. *ACS Nano* **8,** 54–63 (2014) (cit. on p. 63).

193. Macdonald, A. J., Tremblay-Johnston, Y. S., Grothe, S., *et al.* Dispersing artifacts in FT-STS: a comparison of set point effects across acquisition modes. *Nanotechnology* **27,** 414004 (2016) (cit. on pp. 63, 80, 141).

194. Grothe, S., Johnston, S., Chi, S., *et al.* Quantifying many-body effects by high-resolution Fourier transform scanning tunneling spectroscopy. *Physical Review Letters* **111,** 246804 (2013) (cit. on p. 63).

195. Ugeda, M. M., Pulkin, A., Tang, S., *et al.* Observation of topologically protected states at crystalline phase boundaries in single-layer WSe_2. *Nature Communications* **9,** 1–7 (2018) (cit. on p. 63).

196. Zengin, B., Oppliger, J., Liu, D., *et al.* Fast spectroscopic mapping of two-dimensional quantum materials. *Physical Review Research* **3,** L042025 (2021) (cit. on p. 64).

197. Vogel, E. Technology and metrology of new electronic materials and devices. *Nature Nanotechnology* **2,** 25–32 (2007) (cit. on p. 64).

198. Pop, E. Energy dissipation and transport in nanoscale devices. *Nano Research* **3,** 147–169 (2010) (cit. on p. 64).

199. Chang, L., Choi, Y.-K., Kedzierski, J., *et al.* Moore's law lives on [CMOS transistors]. *IEEE Circuits and Devices Magazine* **19,** 35–42 (2003) (cit. on p. 64).

200. Botkin, D., Glass, J., Chemla, D. S., *et al.* Advances in ultrafast scanning tunneling microscopy. *Applied Physics Letters* **69,** 1321–1323 (1996) (cit. on p. 64).

201. Groeneveld, R. H. M. & Van Kempen, H. The capacitive origin of the picosecond electrical transients detected by a photoconductively gated scanning tunneling microscope. *Applied physics letters* **69,** 2294–2296 (1996) (cit. on p. 65).

202. Steeves, G., Elezzabi, A. & Freeman, M. R. Advances in picosecond scanning tunneling microscopy via junction mixing. *Applied Physics Letters* **70,** 1909–1911 (1997) (cit. on pp. 65, 121).

203. Hamers, R. J. & Cahill, D. G. Ultrafast time resolution in scanned probe microscopies: Surface photovoltage on Si (111)–(7×7). *Journal of Vacuum Science & Technology B: Microelectronics and Nanometer Structures Processing, Measurement, and Phenomena* **9,** 514–518 (1991) (cit. on p. 65).

204. Pfeiffer, W., Sattler, F., Vogler, S., *et al.* Rapid communicationPhotoelectron emission in femtosecond laser assisted scanning tunneling microscopy. *Applied Physics B* **64,** 265–268 (1997) (cit. on p. 65).

205. Wu, S. W. & Ho, W. Two-photon-induced hot-electron transfer to a single molecule in a scanning tunneling microscope. *Physical Review B* **82,** 085444 (2010) (cit. on pp. 65, 68).

206. Grafström, S., Schuller, P., Kowalski, J. & Neumann, R. Thermal expansion of scanning tunneling microscopy tips under laser illumination. *Journal of Applied Physics* **83,** 3453–3460 (1998) (cit. on p. 65).

207. Gerstner, V., Thon, A. & Pfeiffer, W. Thermal effects in pulsed laser assisted scanning tunneling microscopy. *Journal of Applied Physics* **87,** 2574–2580 (2000) (cit. on p. 65).

208. Gerstner, V., Knoll, A., Pfeiffer, W., *et al.* Femtosecond laser assisted scanning tunneling microscopy. *Journal of Applied Physics* **88,** 4851–4859 (2000) (cit. on p. 65).

209. Terada, Y., Yoshida, S., Takeuchi, O. & Shigekawa, H. Laser-combined scanning tunnelling microscopy for probing ultrafast transient dynamics. *Journal of Physics: Condensed Matter* **22,** 264008 (2010) (cit. on pp. 65, 68).

210. Bowker, M. & Davies, P. R. *Scanning tunneling microscopy in surface science* (Wiley-VCH, 2009) (cit. on p. 66).

211. Keldysh, L. V. Ionization in the field of a strong electromagnetic wave. *Soviet Physics JETP* **20,** 1307–1314 (1965) (cit. on p. 66).

212. Zheltikov, A. M. Keldysh parameter, photoionization adiabaticity, and the tunneling time. *Physical Review A* **94,** 043412 (2016) (cit. on p. 66).

213. Wang, L., Xia, Y. & Ho, W. Atomic-scale quantum sensing based on the ultrafast coherence of an H_2 molecule in an STM cavity. *Science* **376,** 401–405 (2022) (cit. on pp. 68, 142).

214. Wimmer, L., Herink, G., Solli, D. R., *et al.* Terahertz control of nanotip photoemission. *Nature Physics* **10,** 432–436 (2014) (cit. on pp. 69, 105, 142).

215. Sato, M., Higuchi, T., Kanda, N., *et al.* Terahertz polarization pulse shaping with arbitrary field control. *Nature Photonics* **7,** 724–731 (2013) (cit. on p. 74).

216. Sheng, S., Oeter, A.-C., Abdo, M., *et al.* Launching Coherent Acoustic Phonon Wave Packets with Local Femtosecond Coulomb Forces. *Physical Review Letters* **129,** 043001 (4 2022) (cit. on p. 78).

217. De Vries, R. J., Saedi, A., Kockmann, D., *et al.* Spatial mapping of the inverse decay length using scanning tunneling microscopy. *Applied Physics Letters* **92,** 174101 (2008) (cit. on p. 79).

218. Krane, N., Lotze, C. & Franke, K. J. Moiré structure of MoS_2 on Au(111): Local structural and electronic properties. *Surface Science* **678,** 136–142 (2018) (cit. on p. 81).

219. Björk, J., Hanke, F. & Stafström, S. Mechanisms of Halogen-Based Covalent Slef-Assembly on Metal Surfaces. *Journal of the American Chemical Society* **135,** 5768–5775 (2013) (cit. on p. 87).

220. Simonov, K. A., Vinogradov, N. A., Vinogradov, A. S., *et al.* Effect of Substrate Chemistry on the Bottom-Up Fabrication of Graphene Nanoribbons: Combined Core-Level Spectroscopy and STM Study. *The Journal of Physical Chemistry C* **118,** 12532–12540 (2014) (cit. on p. 87).

221. Grill, L., Dyer, M., Lafferentz, L., *et al.* Nano-architectures by covalent assembly of molecular building blocks. *Nature Nanotechnology* **2,** 687–691 (2007) (cit. on p. 87).

222. Bieri, M., Treier, M., Cai, J., *et al.* Porous graphenes: two-dimensional polymer synthesis with atomic precision. *Nature Nanotechnology* **45,** 6919–6921 (2009) (cit. on p. 87).

223. Hassan, J., Sévignon, M., Gozzi, C., *et al.* Aryl-aryl bond formation one century after the discovery of the Ullmann reaction. *Chemical Reviews* **102,** 1359–1470 (2002) (cit. on p. 87).

224. Massimi, L., Ourdjini, O., Lafferentz, L., *et al.* Surface-assisted reactions toward formation of graphene nanoribbons on Au (110) surface. *The Journal of Physical Chemistry C* **119,** 2427–2437 (2014) (cit. on p. 88).

225. Simonov, K., Generalov, A., Vinogradov, A., *et al.* Synthesis of armchair graphene nanoribbons from the 10,10'-dibromo-9,9'-bianthracene molecules on Ag(111): the role of organometallic intermediates. *The Journal of Physical Chemistry C* **8,** 2045–2322 (2014) (cit. on p. 88).

226. Teeter, J. D., Costa, P. S., Pour, M. M., *et al.* Epitaxial growth of aligned atomically precise chevron graphene nanoribbons on Cu(111). *Chemical Communications* **53,** 8463 (2017) (cit. on p. 88).

227. Talirz, L., Söde, H., Cai, J., *et al.* Termini of Bottom-Up Fabricated Graphene Nanoribbons. *Journal of the American Chemical Society* **135,** 2060–2063 (2013) (cit. on pp. 88, 98, 99).

228. Simonov, K. A., Vinogradov, N. A., Vinogradov, A. S., *et al.* From Graphene Nanoribbons on Cu(111) to Nanographene on Cu(110): Critical Role of Substrate Structure in the Bottom-Up Fabrication Strategy. *ACS Nano* **9,** 8997–9011 (2015) (cit. on p. 88).

229. Ma, C., Xiao, Z., Lu, W., *et al.* Step edge-mediated assembly of periodic arrays of long graphene nanoribbons on Au(111). *Chemical Communications* **55,** 11848 (2019) (cit. on pp. 88, 89).

230. Linden, S., Zhong, D., Timmer, A., *et al.* Electronic Structure of Spatially Aligned Graphene Nanoribbons on Au(788). *Physical Review Letters* **108,** 216801 (21 2012) (cit. on p. 88).

231. Thussing, S., Flade, S., Eimre, K., *et al.* Reaction Pathway toward Seven-Atom-Wide Armchair Graphene Nanoribbon Formation and Identification of Intermediate Species on Au(111). *The Journal of Physical Chemistry C* **124,** 16009–16018 (2020) (cit. on pp. 88, 90).

232. Ishii, A., Shiotari, A. & Sugimoto, Y. Quality control of on-surface-synthesised seven-atom wide armchair graphene nanoribbons. *Nanoscale* **12,** 6651 (2020) (cit. on p. 89).

233. Koch, M., Ample, F., Joachim, C. & Grill, L. Voltage-dependent conductance of a single graphene nanoribbon. *Nature Nanotechnology* **7,** 713–717 (2012) (cit. on pp. 90, 93, 102).

234. Ruffieux, P., Cai, J., Plumb, N. C., *et al.* Electronic structure of atomically precise graphene nanoribbons. *ACS Nano* **6,** 6930–6935 (2012) (cit. on pp. 93, 94, 103, 106).

235. Batra, A., Cvetko, D., Kladnik, G., *et al.* Probing the mechanism for graphene nanoribbon formation on gold surfaces through X-ray spectroscopy. *Chemical Science* **5,** 4419–4423 (2014) (cit. on p. 93).

236. Zhao, S., Barin, G. B., Cao, T., *et al.* Optical Imaging and Spectroscopy of Atomically Precise Armchair Graphene Nanoribbons. *Nano Letters* **20,** 1124–1130 (2020) (cit. on p. 93).

237. Yu, Y.-J., Zhao, Y., Ryu, S., *et al.* Tuning the Graphene Work Function by Electric Field Effect. *Nano Letters* **9,** 3430–3434 (2009) (cit. on p. 94).

238. VandeVondele, J. & Hutter, J. Gaussian basis sets for accurate calculations on molecular systems in gas and condensed phases. *The Journal of Chemical Physics* **127,** 114105 (2007) (cit. on p. 95).

239. Goedecker, S., Teter, M. & Hutter, J. Separable dual-space Gaussian pseudopotentials. *Physical Review B* **54,** 1703–1710 (1996) (cit. on p. 95).

240. Perdew, J. P., Burke, K. & Ernzerhof, M. Generalized gradient approximation made simple. *Physical Review Letters* **77,** 3865–3868 (1996) (cit. on p. 95).

241. Grimme, S., Antony, J., Ehrlich, S. & Krieg, H. A consistent and accurate ab initio parametrization of density functional dispersion correction (DFT-D) for the 94 elements H-Pu. *The Journal of Chemical Physics* **132,** 154104 (2010) (cit. on p. 95).

242. Kolmer, M., Steiner, A.-K., Izydorczyk, I., *et al.* Rational synthesis of atomically precise graphene nanoribbons directly on metal oxide surfaces. *Science* **369,** 571–575 (2020) (cit. on p. 95).

243. Tersoff, J. Method for the calculation of scanning tunneling microscope images and spectra. *Physical Review B* **40,** 11990–11993 (1989) (cit. on p. 96).

244. Van der Lit, J., Boneschanscher, M., Vanmaekelbergh, D., *et al.* Suppression of electron–vibron coupling in graphene nanoribbons contacted via a single atom. *Nature Communications* **4,** 2023 (2013) (cit. on p. 103).

245. Gross, L., Moll, N., Mohn, F., *et al.* High-resolution molecular orbital imaging using a p-wave STM tip. *Physical Review Letters* **107,** 086101 (2011) (cit. on p. 103).

246. Rizzo, D. J., Veber, G., Mccurdy, R., *et al.* Inducing metallicity in graphene nanoribbons via zero-mode superlattices. *Science* **369,** 1597–1603 (2020) (cit. on pp. 103, 118).

247. Shekhirev, M. & Sinitskii, A. Solution synthesis of atomically precise graphene nanoribbons. *Phys. Sci. Rev.* **2,** 20160108 (2017) (cit. on p. 118).

248. Gröning, O., Wang, S., Yao, X., *et al.* Engineering of robust topological quantum phases in graphene nanoribbons. *Nature* **560,** 209–213 (2018) (cit. on p. 118).

249. Soavi, G., Dal Conte, S., Manzoni, C., *et al.* Exciton-exciton annihilation and biexciton stimulated emission in graphene nanoribbons. *Nature Communications* **7,** 11010 (2016) (cit. on pp. 118, 147).

250. Chen, Y., Wang, Y., Claassen, M., *et al.* Observing photo-induced chiral edge states of graphene nanoribbons in pump-probe spectroscopies. *NPJ Quantum Materials* **5,** 84 (2020) (cit. on p. 118).

251. Kwok, Y., Chen, G. & Mukamel, S. STM imaging of electron migration in real space and time: a simulation study. *Nano Letters* **19,** 7006–7012 (2019) (cit. on p. 118).

252. Frankerl, M. & Donarini, A. Spin-orbit interaction induces charge beatings in a lightwave-STM-single molecule junction. *Physical Review B* **103,** 085420 (2021) (cit. on p. 118).

253. Wang, S., Talirz, L., Pignedoli, C., *et al.* Giant edge state splitting at atomically precise graphene zigzag edges. *Nature Communications* **7,** 11504 (2016) (cit. on p. 118).

254. Simmons, J. G. Low-Voltage Current-Voltage Relationship of Tunnel Junctions. *Journal of Applied Physics* **34,** 238–239 (1963) (cit. on p. 120).

255. Savitzky, A. & Golay, M. J. E. Smoothing and Differentiation of Data by Simplified Least Squares Procedures. *Analytical chemistry* **36,** 1627–1639 (1964) (cit. on p. 127).

256. Schiffrin, A., Paasch-Colberg, T., Karpowicz, N., *et al.* Optical-field-induced current in dielectrics. *Nature* **493,** 70–74 (2013) (cit. on p. 143).

257. Rybka, T., Ludwig, M., Schmalz, M. F., *et al.* Sub-cycle optical phase control of nanotunnelling in the single-electron regime. *Nature Photonics* **10,** 667–670 (2016) (cit. on p. 143).

258. Li, S. & Jones, R. R. High-energy electron emission from metallic nano-tips driven by intense single-cycle terahertz pulses. *Nature Communications* **7,** 13405 (2016) (cit. on p. 143).

259. Kang, T., Kim, R., Choi, G., *et al.* Terahertz rectification in ring-shaped quantum barriers. *Nature Communications* **9,** 4914 (2018) (cit. on p. 143).

260. Matte, D., Chamanara, N., Gingras, L., *et al.* Extreme lightwave electron field emission from a nanotip. *Physical Review Research* **3,** 013137 (2021) (cit. on p. 143).

261. Lange, S. L., Noori, N. K., Kristensen, T. M. B., *et al.* Ultrafast THz-driven electron emission from metal metasurfaces. *Journal of Applied Physics* **128,** 070901 (2020) (cit. on p. 143).

262. Zhang, P., Ang, Y. S., Garner, A. L., *et al.* Space–charge limited current in nanodiodes: Ballistic, collisional, and dynamical effects. *Journal of Applied Physics* **129,** 100902 (2021) (cit. on p. 143).

263. Madéo, J., Man, M. K. L., Sahoo, C., *et al.* Directly visualizing the momentum-forbidden dark excitons and their dynamics in atomically thin semiconductors. *Science* **370,** 1199–1204 (2020) (cit. on p. 147).

264. Cavalleri, A., Dekorsy, T., Chong, H. H. W., *et al.* Evidence for a structurally-driven insulator-to-metal transition in VO_2: A view from the ultrafast timescale. *Physical Review B* **70,** 161102 (2004) (cit. on p. 147).

265. Mathias, S., Eich, S., Urbancic, J., *et al.* Self-amplified photo-induced gap quenching in a correlated electron material. *Nature Communications* **7,** 12902 (2016) (cit. on p. 147).

266. Hase, M., Kitajima, M., Constantinescu, A., *et al.* The birth of a quasiparticle in silicon observed in time–frequency space. *Nature* **426,** 51–54 (2003) (cit. on p. 147).

267. Karni, O., Barré, E., Pareek, V., *et al.* Structure of the moiré exciton capture by imaging its electron and hole. *Nature* **603,** 247–252 (2022) (cit. on p. 147).

268. Kuhnke, K., Große, C. & Merino P. Kern, K. Atomic-Scale Imaging and Spectroscopy of Electroluminescence at Molecular Interfaces. *Chemical Reviews* **117,** 5174–5222 (2017) (cit. on p. 147).

269. Hase, M., Kitajima, M., Constantinescu, A., *et al.* Free coherent evolution of a coupled atomic spin system initialized by electron scattering. *Science* **372,** 964–968 (2021) (cit. on p. 148).